UNIVERSITAT DE LES ILLES BALEARS
DEPARTAMENT DE FISICA

Hydrometeorological Numerical Simulations of Western Mediterranean Severe Precipitation Events

Programa Oficial de Postgrau de Ciències Experimentals i Tecnologies (Física)

Doctor per la Universitat de les Illes Balears

Tesi Doctoral

Arnau Amengual Pou

UNIVERSITAT DE LES ILLES BALEARS
DEPARTAMENT DE FISICA

Hydrometeorological Numerical Simulations of Western Mediterranean Severe Precipitation Events

Programa Oficial de Postgrau de Ciències Experimentals i Tecnologies (Física)

Doctor per la Universitat de les Illes Balears

Tesi Doctoral

Arnau Amengual Pou

Amb el vist i plau dels Directors de la Tesi,

Dr. Romualdo Romero March

Prof. Sergio Alonso Oroza

A n'Anna,
Als meus pares i germans,
Als amics

AGRAÏMENTS

El present treball ha estat realizat sota la direcció del Dr. Romu Romero i del Prof. Sergio Alonso, dins del Grup de Meteorologia del Departament de Física de la UIB. Voldria agrair a en Romu i a en Sergio la gran confiança i comprensió que sempre m'han mostrat des que em vaig integrar al Grup. D'en Romu voldria destacar les seves virtuts com a investigador: una gran capacitat de treball i direcció, i l'agudesa mental que demostra a l'hora de proposar i sintetitzar noves idees. Però, indubtablement i per damunt de tot, destaca la seva manera de ser. D'en Sergio voldria destacar el seu ample bagatge científic, que em va permetre encetar la línia d'investigació exposada en aquest treball, i la seva gran capacitat de gestió i direcció, que han permès la cristal.lització de la present Tesi.

No em voldria oblidar de la resta de membres i col.laboradors científics del Grup de Meteorologia. Del Prof. Climent Ramis voldria destacar la seva àmplia experiència investigadora i el suport que em va mostrar quan em vaig integrar al Grup. Agrair al Dr. Víctor Homar les profitoses discussions científiques que hem mantingut i el seu inestimable suport informàtic. Al Prof. Manuel Gómez, del Departament d'Enginyeria Hidràulica, Marítima i Ambiental de la UPC, agrair-li que compartís sense reserves la seva àmplia experiència en el camp de la hidrologia. De forma més general, vull fer extensiva la meva apreciació a tots/es els/les companys/es que formen el Grup de Meteorologia. Amb alguns/es d'ells/es he compartit profitoses tasques de recerca en els diferents projectes d'investigació en els quals hem col.laborat.

Voldria extendre els meus agraïments a en Maurici Ruiz, director del Servei de Sistemes d'Informació Geogràfica i Teledetecció de la UIB, i a tots els membres del seu equip. Sense la seva experiència dins d'aquest camp, juntament amb el suport informàtic del SSIGT, no hauria estat possible la realització d'aquest treball.

Recordar també als diferents investigadors científics amb els quals he pogut treballar o compartir fructíferes converses científiques: els Drs. Tommaso Diomede i Chiara Marsigli (ARPA-SIM, Bologna, Italy); en Thomas A. Evans (Hydrologic Engineering Center, California, USA); el Dr. Charles A. Doswell III (University of Oklahoma, Oklahoma, USA) i el Dr. Kerry Emmanuel (MIT, Massachusetts, USA). A tots ells vull agrair-los la seva aportació en la meva formació científica.

Per suposat, també agrair als companys de l'Agència EFE i als membres del Departament de Física de la UIB, les grans facilitats i excel.lent tracte que han mantingut amb la meva persona.

Per últim, vull expressar la meva gratitud al Centre Territorial de l'INM a les Illes Balears, pel subministrament de les dades meteorològiques tan essencials per a la realització del present estudi. En particular, als Drs. Agustí Llansà i José Antonio Guijarro i a en Miquel Gayà. A en Carlos Garau, n'Alfredo Barón i na Concha González de la Junta d'Aigües de la Conselleria de Medi Ambient del Govern de les Illes Balears els agraeixo la cessió de les dades hidrològiques. També recordar l'Agència Catalana de l'Aigua pel subministrament de dades hidrometeorològiques. Aquest treball no hauria estat possible sense el suport econòmic dels següents projectes: MEDIS, HYDROPTIMET, AMPHORE i PRECIOSO.

CONTENTS

Chapter 1

INTRODUCTION

1.1 Flood events in the Western Mediterranean area: General aspects

The human life, society and property are essentially fragile elements, susceptible to hazardous episodes caused by the environment. Sometimes and more frequently in some areas than others, such hazardous episodes can be so great or can have a big impact in densely populated or developed areas producing important damages. These natural impacts can be of many several kinds and they can have special features in the different climatological and geomorphologic regions of the world. About the 60% of these disasters are related to hurricanes and to floods. Flooding events in low lands due to large rivers have return periods of many decades and flood-prone areas are quite easily identified. In addition, floods occur over periods of several days and it is possible to attemp damage mitigation. The situation can be quite different in the southern European region, and concretely along the Western Mediterranean coast line (fig. 1.1), where extreme flooding events are experienced in urban areas very frequently in time, but randomly in space, especially during the fall season. The flash-flood episodes are distinguised from the 'ordinary' floods by the time scale of the events: the worst of these can develop in periods of a few hours or less after the rainfall and their occurrence is too rapid to attempt damage mitigation. This makes flash-floods particularly dangerous in terms of human lifes and properties.

A flood is a hydrometeorological event that depends on both hydrological and meteorological factors. The meteorological factors play a basic role when rainfall becomes intense and that intensity is maintained long enough to create the potential for flash-floods. The hydrological factors also play a large role in these kinds of episodes; a given amount of rainfall in a given period of time can or cannot result in a flood owing to factors as: the antecedent precipitation, and therefore, the antecedent moisture condition of the soil; the soil permeability; the terrain slope; the land use or the vegetation cover. As consequence, flood forecasting involves both a hydrological and a meteorological predictions (Doswell, 1994; see figs. 1.2 and 1.3 in order to notice the relationship between the spatio-temporal scales of the atmospheric and the hydrologic processes).

Below, the most relevant physical and social factors are briefly reviewed which together produce a high risk threshold in the Mediterranean area to floods.

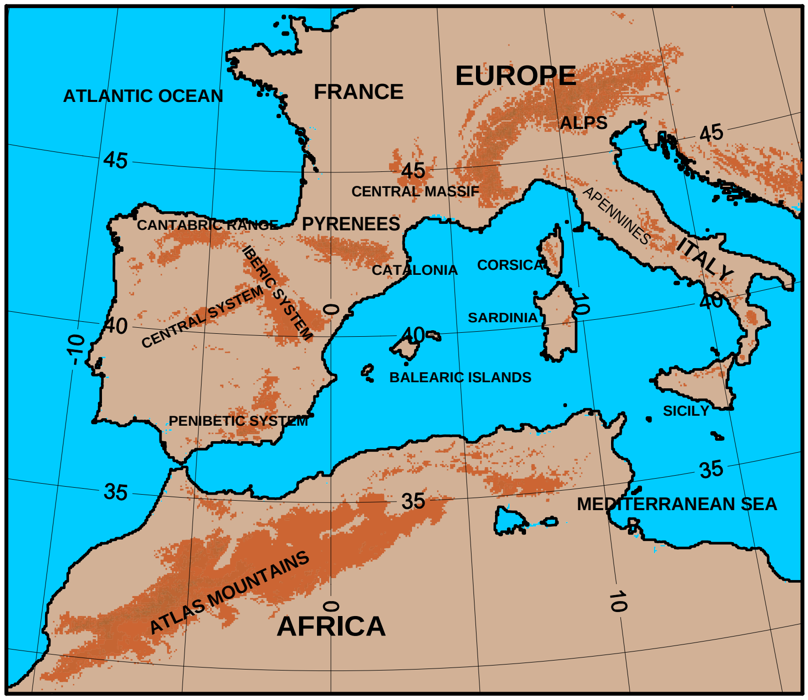

Figure 1.1: Geographical locations and main mountain systems of the Western Mediterranean region. Major topographic features are shown starting at 1000 meters.

1. *The meteorological conditions*

   In the western Mediterranean area, as the summer eastward extension of the Azores high pressure cell moves back towards low latitudes and the pressure drop occurs in the early autumn, a marked increase in the probability of intense precipitation rates rises, certainly favoured by the high sea surface temperature of the Mediterranean Sea. These changes in the synoptic patterns are associated with the early invasion of cold fronts. As described in Doswell et al. (1996), flash-floods are the result of high precipitation rates persisting for a relatively long time (order of a few hours). The minimum amount of rainfall and its duration to create flood conditions depends on the hydrological setting for the episode. It seems clear that the majority of flood-producing rainfall is convective. This is because the rapid upward vertical motion in convection also promotes high precipitation rates. Since not all convective storms produce flash-floods, a major limiting effect is the duration of the relatively intense convective rainfalls. Most convective events do not persist in any given catchment long enough to produce flooding, so the duration of convection is the key issue. In the flash-flood cases, the convection is maintained over a specific location as 'quasi-stationary convective events' (Chappell, 1986). What makes the convection remain geographically fixed for an extended period is the development of new convective cells, forming multi-clusters called mesoscale convective systems (MCSs), so as to nearly cancel the tendency of such cells to drift with the wind.

   Heavy rainfalls can also result from the forced ascent of moist air in stable stratification.

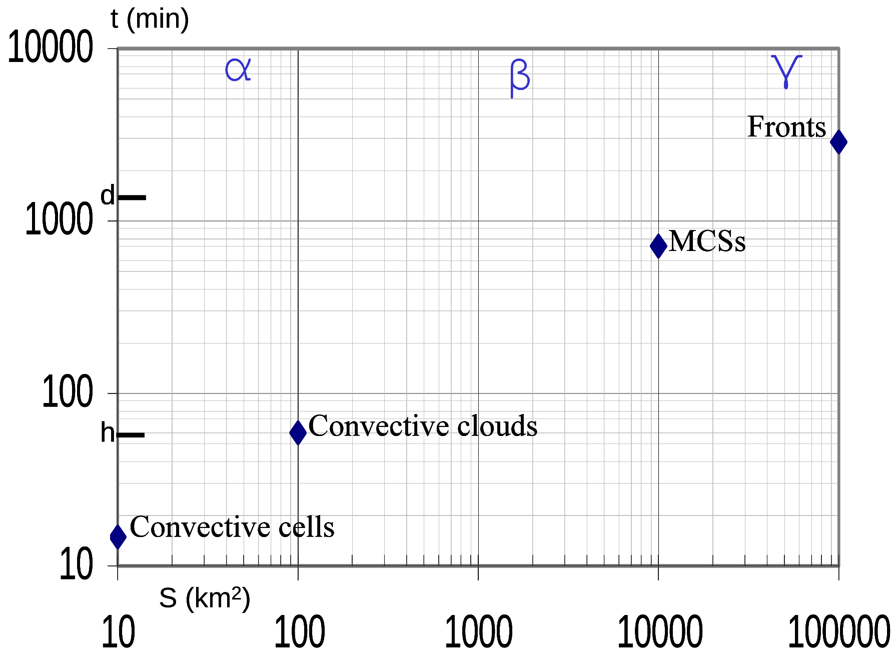

Figure 1.2: Scale subdivision for the atmospheric processes and their orders of magnitude (after Orlanski, 1975).

This is associated with orographically-forced rainfall events and in some cases quasi-stationary convection occurs in situations involving an orographic component where the convective element can develop because ascent tends to reduce the static stability, but convection is not the dominant contributor of rainfall (Romero et al., 1998). Then, into the Mediterranean region, extreme rainfalls often result from the thermal effects induced by relatively high sea surface temperatures in that season together with the incursion of cold air masses leading to convective instabilities along the cold fronts producing interactions between frontal and orographic enhancement (Ramis et al., 1994). The resulting space and time scales of heavy rainfall patterns are highly variable depending on the structure of the large scale circulation and on the local orographic features.

2. *The urban conditions*

   As aforementioned, hydrology plays a major role in the occurence of floods. Of particular significance to flash-floods are: (i) the antecedent precipitation related directly with the moisture of the soil and its infiltration properties; (ii) the terrain, and (iii) the surface runoff characteristics. The last two issues are of crucial importance in the Mediterranean area since the space left for the rivers flowing through the historical cities, sometimes is enough to carry ordinary floods but not the disastrous ones. Furthermore, the high urbanization rate in coastal areas and the absence of a planning capability in all these places increase the risks involved in these kinds of events, most of them owing to the development of the building rate when the knowledge of the involved hydrological risks was rather poor (Siccardi, 1996). In fact, the streams and rivers along the Mediterranean coast are usually dry for most part of the year, but develop floods during storms with the

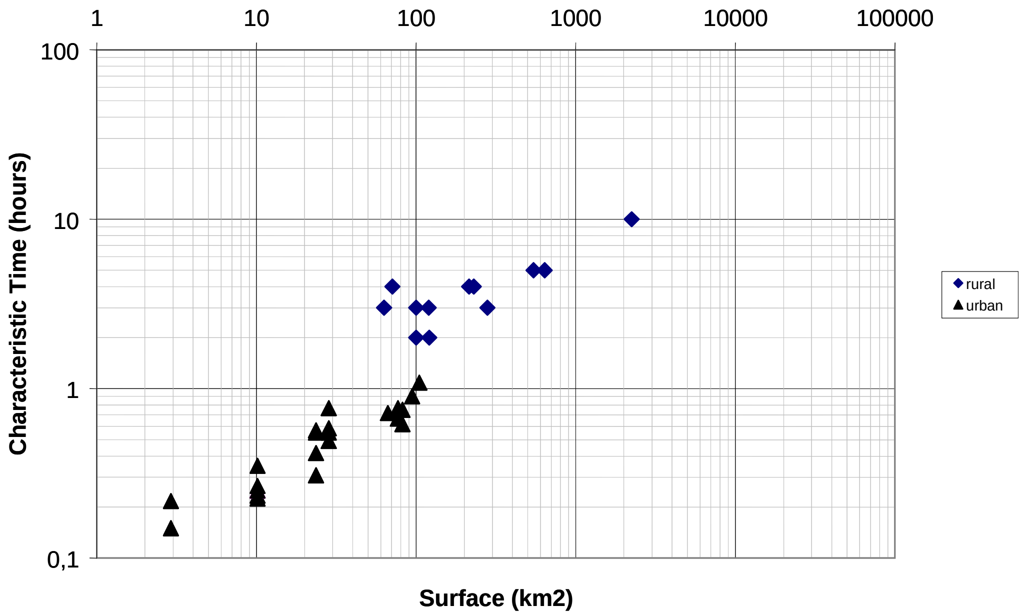

Figure 1.3: Flash-flood domain for rural and urban areas.

associated hydrograph peaks in short periods of time ($\sim$ some hours; see figs. 1.3 and 1.4 in order to notice the effect of urbanization on storm runoff).

The combination of all these factors can be summarized for the Spanish Mediterranean area as follows:

- Its topography makes it especially prone to flood events: mountain systems near the coast usually act as natural barriers to the warm moist mediterranean air, inducing the generation of intense rainfall rates that show high variability in space and time.
- Serious damage can occur when intense convective rainfall events combine with short hydrological response times, characteristic of steep streams and increasing urbanization rates in coastal areas. Furthermore, in this semiarid environment many small and medium steep streams are ephemeral, which can cause unexpected and extensive flood damage. Increased flows over short periods, high flow velocities and large volumes of sediment constitute threats to property and human life (Martín-Vide et al., 1999).

1.2 Numerical modelling in hydrometeorology

Global circulation models of the atmosphere (GCMs), as they are operationally run by meteorological offices can provide suitable weather predictions with a lead time up to 48-96 hours. GCMs parameterize rainfall over spatial windows of the order of $\sim 10^4$ km^2, the size of the elementary grid for the numerical solution of the governing equations. The orography is accordingly resolved at the same space scale. As consequence, many of the watersheds of the

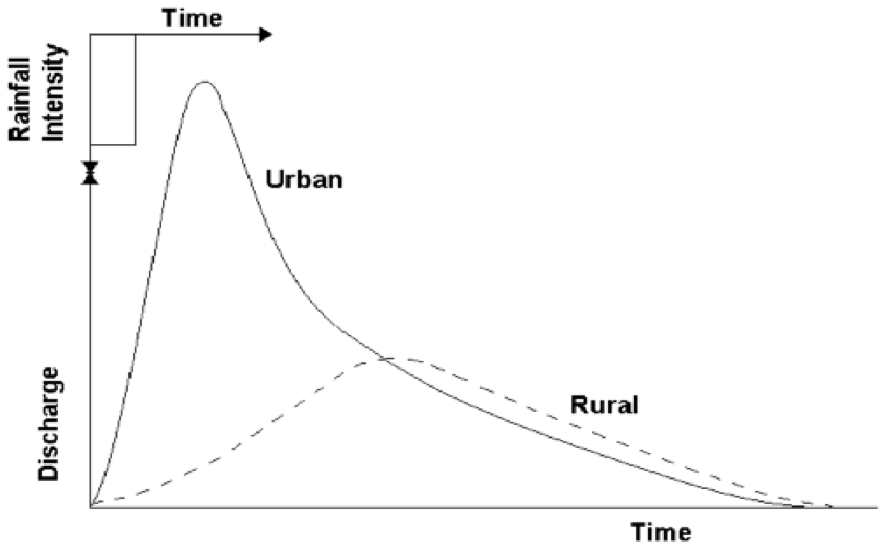

Figure 1.4: Flood hydrographs for urbanized and natural basins.

Mediterranean coastline are lost for these coarse resolutions. In order to address these issues, nowadays, the limited area models (LAMs) –nested inside the GCMs– provide a better space discretization, and research and operational LAM simulations and forecasts are run with space windows of tenths of km^2. This enables them to be used for hydrological purposes, as well as a trigger for flood warning systems targetting large regions within the Western Mediterranean area. In fact, many studies dealing with the coupling of meteorological and hydrological models have shown that the scale compatibility does not seem to represent any longer a serious problem for a successful model coupling. These studies show that non-hydrostatic mesoscale models, run either in a research or operational mode, are able to provide realistic rainfall distributions for hazardous heavy precipitation episodes and aim at supplying a useful support for flood forecasting based on deterministic rainfall forecasts (Todini, 1995; Butts, 2000; Gerlinger and Demuth, 2000; Ranzi et al., 2000; Ducrocq et al., 2002; Bacchi and Ranzi, 2003; Benoit et al., 2003; Kunstmann and Stadler, 2003; Tomassetti et al., 2005). Other studies propose to use a coupled atmospheric-hydrological model system as an advanced validation tool for the mesoscale simulated rainfall amounts (Benoit et al., 2000; Jasper and Kaufmann, 2003; Chancibault et al., 2006).

All the aforementioned experiences show that, despite current limitations, such approach has a great potential in flood forecasting and water resource management, representing also an additional level of verification useful for the improvement of atmospheric models. Most of the operational runoff forecasting systems are based on deterministic hydrometeorological chains, which do not quantify the uncertainty in the outputs. But, the flood forecasting process comprises several sources of uncertainty, which lies in the hydrological and meteorological model formulations, including the initial and boundary conditions, and in the gap which is still present between the scales resolved by the two systems as well. Furthermore, high-resolution precipitation simulations in extreme events is a remarkably arduous task because many factors concur in their determination and of the convective nature of most of the precipitation. Numerical

Weather Prediction (NWP) models have problems in triggering and organizing convection over the correct locations and times due to the small-scale nature of many responsible atmospheric features (Kain and Fritsch 1992, Stensrud and Fritsch 1994a,b). On the other hand, it must be also taken into account the part of the uncertainties coming from the hydrological models formulations including their structures. For example, the physical description of the soil infiltration influences the simulated basin's response strongly, since it determines the modeled soil moisture content. Time to peak flow uncertainties are mainly related with the dynamical formulation. Therefore, an accurate quantification of the initial soil moisture content or the timing to the maximum peak before the occurrence of a flood event is fundamental for an accurate hydrological model simulation.

Taking into account all these factors, two issues of maximum interest have been evaluated in this work. First, to explore the possibility of obtaining as much as possible accurate simulations of the rising flows and their peaks, or at least, whether runoff forecasts could be able to reach suitable thresholds so as to cause the appropriate directives to be enacted for use in emergency management. Second, to assess the impact of the aforementioned uncertainties in the hydrometeorological chain. Chapter 2 presents the numerical tools employed for hydrological numerical modeling purposes. It includes a detailed account of the main features of the physically-based Hydrologic Engineering Center's Hydrologic Modeling System (HEC-HMS) model used for the characterization and the hydrologic modeling of the basins under study. Furthermore, the principal characteristics of the fifth-generation Pennsylvania State University-NCAR Mesoscale Numerical (MM5) model are briefly discussed. MM5 has been used to simulate the intense rainfall episodes under study with appropriate space and time scales to force the hydrological model in a one-way mode. Some meteorological tools used to study the impact of the external-scale uncertainties into the hydrometeorological chain are also introduced.

1.3 Intense precipitation events resulting in flood episodes over the Western Mediterranean area

1.3.1 The June 2000 flash-flood event over Catalonia, Spain

The 10 June 2000 flash-flood event is a good example of the catastrophic effects of a rapid and sudden flow increase in a short time period. This episode was produced by a mesoscale convective system which remained quasi-stationary over many internal catchments of Catalonia. Maximum precipitation amounts above 220 mm were observed within these basins. The subsequent rise of the internal river flows produced serious material and human damages (e.g. El Llobregat, El Besós, El Francolí and La Riera del Bisbal; see fig. 1.5 for locations). The study is centered on the Llobregat basin, with a drainage area of 5040 km^2. Some of the most notable disasters within this catchment consisted of the partial destruction of the infrastructure of Montserrat's Monastery (720 m) and some roads connecting with this mountainous area; the collapse of some bridges and sections in the plain roadway; and the flooding of residential zones with the attendant destruction of some dwellings, especially in the tourist municipality of El Vendrell (fig. 1.5). As a consequence, about 500 people had to be evacuated from the monastery and the episode caused five fatalities and material losses estimated at about 65 million euros.

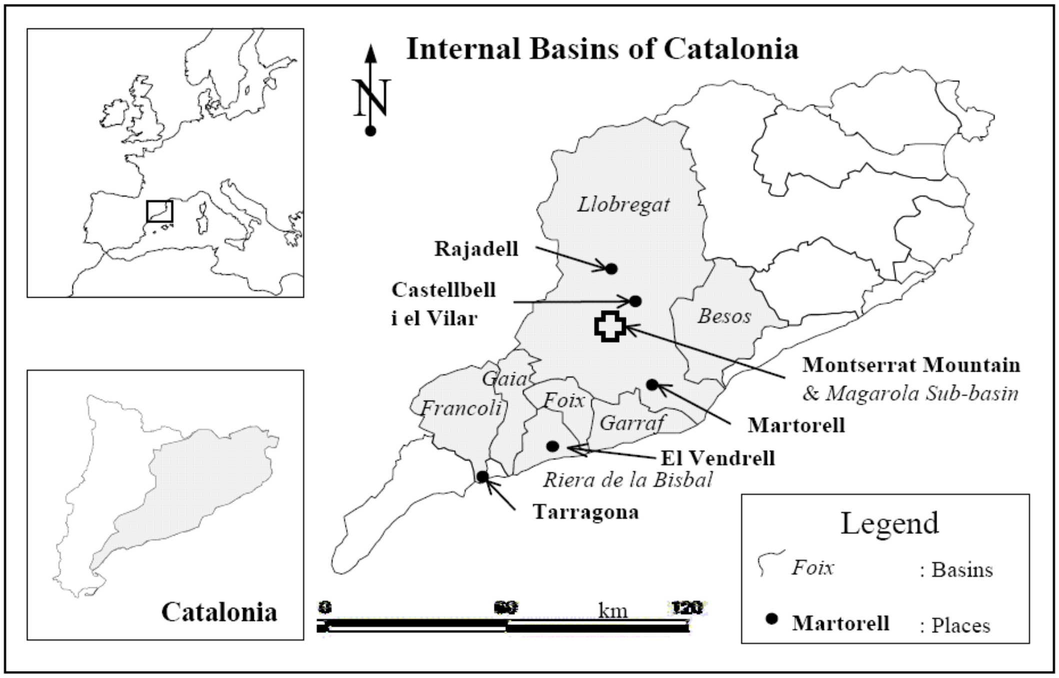

Figure 1.5: Geographical location of the Internal Basins of Catalonia (IBC) where the Montserrat flash-flood event was produced. Several catchments (shaded) and locations affected by the episode are indicated (extracted from Llasat et al., 2003).

Chapter 3 presents as the first objective the reproduction of the hydrological response to the flash-flood event using the HEC-HMS runoff model. An independent sample of events is used to calibrate the HEC-HMS in terms of soil behaviour (losses and imperviousness), which exerts a fundamental role over the runoff volume for the episode, and flood wave celerity in the main channels of the catchment, an important factor owing to the high flow velocities. In order to optimize the rainfall-runoff model set-up, the effects of diverse spatial and temporal scales of the rainfall field on the simulated basin response have been quantified. The second objective aims to test the appropriateness of the atmospheric driven runoff simulations as a methodology for obtaining 12-48 hours forecasts of these extreme events, which would greatly expand the time necessary for emergency management procedures. In particular, the HEC-HMS runoff model is forced with mesoscale rainfall forecasts derived from MM5 simulations initialized with meteorological grid analyses from the American Center for Environmental Prediction (NCEP) and the European Center for Medium Range Weather Forecasts (ECMWF). The third objective consists of assessing the sensitivity of the Llobregat basin to the inherent uncertainties of some aspects of the hydrometeorological forecasting chain (Ferraris et al., 2002; Castelli, 1995; Murphy, 1993). An ensemble of MM5 simulations with small shifts and variations of intensity of the precursor upper-level synoptic scale trough is designed for this purpose. With this method, it is possible to assess the effects on the hydrological response due to relatively moderate spatial and temporal errors of the simulated rainfall fields.

1.3.2 The October 1990, November 2001 and April 2002 intense precipitation events over Majorca Island, Spain

The intense precipitation episodes under study were selected among the flood events of highest magnitude since the late eighties affecting the Albufera river basin in Majorca, when the automatic stations of the Spanish Institute of Meteorology (INM) were installed (fig. 1.6). These are associated with general northerly or north-easterly surface winds produced by low pressure centers to the east of the Islands and troughs or cut-off cyclones aloft over the Western Mediterranean. The *7-10 October 1990 first* and *second phases*, *10-11 November 2001* and *3-4 April 2002* cases are a sample of different heavy rainfall episodes which resulted in floods of diverse spatial and temporal scales. The first two events produced exceptional and sudden rising flows owing to their convective nature; the last ones were an example of more sustained, stratiform-like precipitation rates over longer periods but which also drove to notable discharges at the Albufera basin outlet (fig. 1.6).

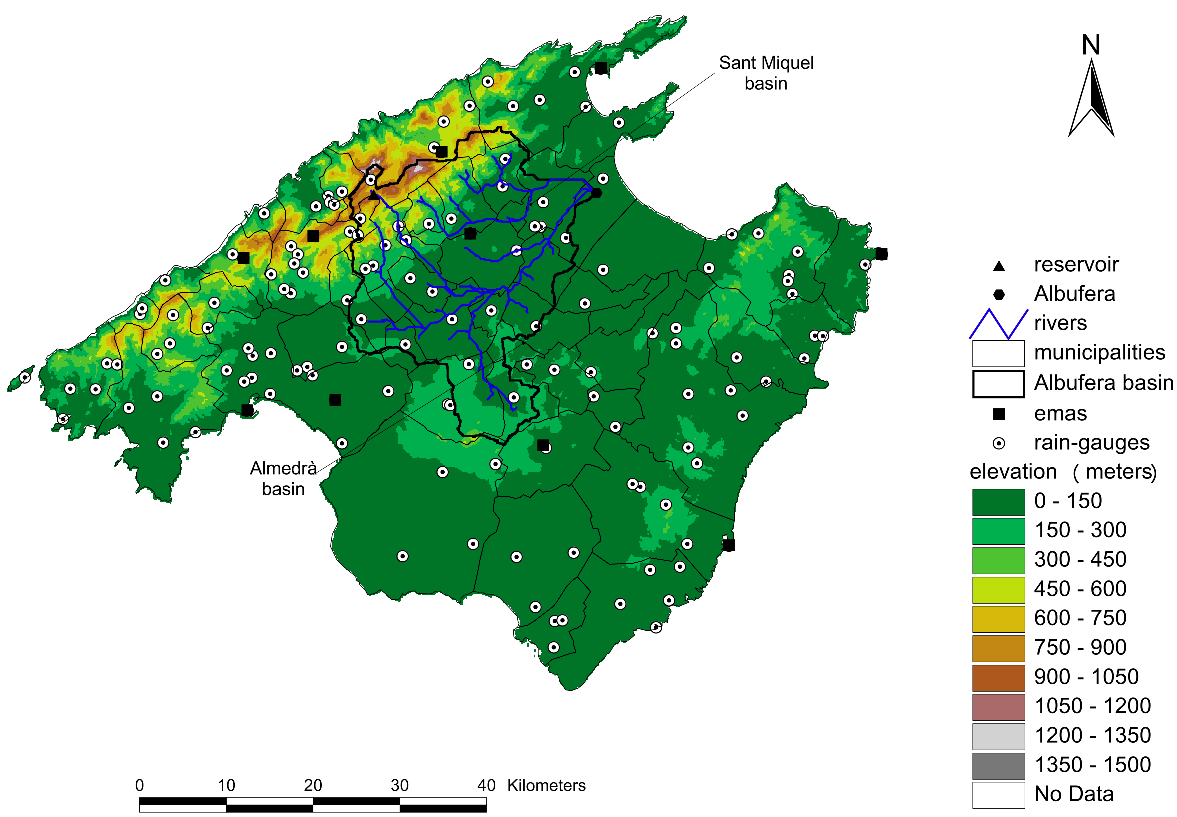

Figure 1.6: Spatial distribution of the rain-gauge network from the Spanish Institute of Meteorology (INM) in the Majorca Island. It includes 100 stations which provide 24-h accumulated values (dotted circles) and 10 automatic stations (emas, black squares). The Almedrà and Sant Miquel rivers which compose the Albufera basin are highlighted, as well as the basin outlet (black circle) and the reservoir mentioned in the text (black triangle). The digital terrain model of the watershed has a cell size of 50 meters.

Many studies have analysed the problem of hydrologic modeling and forecasting of extreme floods using radar rainfall data for small size basins ($\sim$ hundreds of km^2; e.g. Pessoa et al., 1993, Dolciné et al., 2001, Giannoni et al., 2003, Zhang and Smith, 2003). But similar analyses using high-resolution rainfall simulations or quantitative precipitation forecasts provided by mesoscale numerical models are comparatively uncommon in the literature. This is a challenging task given the small hydrological scales involved, their associated uncertainties and the external-scale errors found in the weather numerical models. The feasibility of hydrometeorological forecasting model strategies, under a best guess of the large-scale atmospheric circulation, will be examined for these events. Specifically, the study is centered over the Albufera river basin, with a drainage area of 610 km^2 (Fig.1.6). Chapter 4 presents as the first objective to test the appropriateness of the atmospheric driven runoff simulations for that small size basin as an initial step towards expanding the lead times associated with runoff forecasting of these extreme events. In particular, the HEC-HMS runoff model will be forced with rainfall forecasts derived from MM5 mesoscale simulations initialized with meteorological grid analyses from the European Center for Medium Range Weather Forecasts (ECMWF) and, for one of the cases, also from the American National Center for Environmental Prediction (NCEP).

An ensemble of MM5 experiments combining different parameterizations of cloud microphysics, moist convection and boundary layer parameterizations has been adopted using large-scale analyses as initial and boundary conditions. Then, it is expected that the influence on the hydrological response of the Albufera basin exerted by spatial and temporal errors of the simulated rainfall fields emerging from the physical parameterizations can be addressed. Furthermore, to study the impact of the large-scale uncertainties in the mesoscale model performance, MM5 has been forced by using different initial and boundary conditions for one of the case studies. The value of probabilistic hydrometeorological chains versus deterministic approaches when dealing with flood situations in the area will also be determined from the ensemble of MM5 driven HEC-HMS simulations.

1.3.3 The November 2003 heavy precipitation episode over the Emilia-Romagna region, Italy

On November 6, about 00 UTC, an upper level deep trough at the level of 500 hPa, located over the Balcanic area, evolved into a cut-off low. On 00 UTC 7 November, this cyclonic vortex cut-off moved backward from the Adriatic sea and, in the following 36 hours reached the Alpine region, causing intense precipitations over the central part of the Apennines chain, especially over the Reno river basin, with presence of large amounts of snowfall over the western Apennine even at moderate altitude (less than 500 m; see Fig. 1.7 for locations). During the whole 48-h event, a widespread precipitation was observed over northern Italy. Intense rainfall interested the whole Emila-Romagna Region and the north-eastern part of Italy, with several station recording values up to 100 mm. Maximum values of about 150-200 mm were reached over the upper part of the Reno river basin with a whole extension of 1051 km^2.

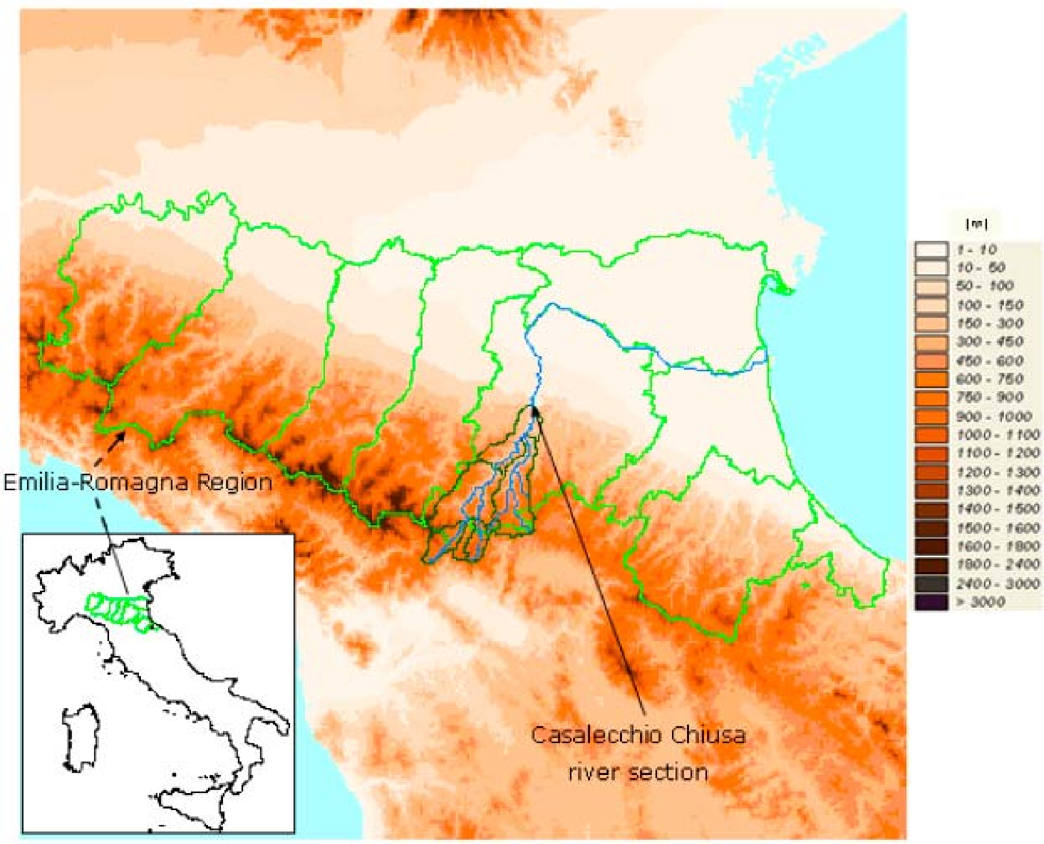

Figure 1.7: Geographical location of the Reno river basin area in the Emilia-Romagna Region, northern Italy. The Reno river subcatchments and the flow-gauge location at Casalecchio Chiusa, which is the outlet of the upper Reno river basin, are shown.

Chapter 5 provides, firstly, a hydrological analysis performed for this intense precipitation event by implementing two different hydrological models over the basin and by driving them with precipitation observations. Secondly, this chapter aims at highlighting some meteorological and hydrological factors which could enhance the hydrometeorological modeling of such hazardous events. At this purpose, we evaluate through a model intercomparison the uncertainties owing to two different sources which directly affect hydrometeorological modeling: one arising from the errors in the QPFs provided by a mesoscale meteorological model and the other arising from the errors in the hydrological model formulation. In order to take into account the meteorological model error, two different non-hydrostatic limited-area mesoscale models have been used: (i) the COSMO model and; (ii) the MM5 model. On the other hand, in order to consider also the part of the uncertainty coming from the hydrological model formulation, the HEC-HMS and TOPKAPI rainfall-runoff models have been coupled to the meteorological models. These models differ particularly in their physical parameterizations and structure.

1.4 The role of hydrometeorological modeling in climate change scenarios

The vulnerability to droughts and the decrease in water availability present particular problems in catchments of the Mediterranean. Numerous and varied reasons exist to deserve a special attention to this area –and, in particular, to the Spanish Mediterranean– such as: (a) the large dependence on the availability, timing and quantity of precipitation, together with the fact that the amount of rainfall has steadily decreased, and the main precipitation period has shortened over the last few decades as a consequence of the climate change at least in some parts of the Mediterranean area; (b) an extensive and unsustainable over-exploitation of superficial and groundwater reservoirs and an expected increase in the demand for water; (c) agriculture and tourism, on some of the regions and/or seasonally, are the predominant consumers of water leading to serious stakeholder conflicts. Moreover, agricultural activities not only threaten the availability (quantity) but also the quality of water due to the extensive use of fertilisers and pesticides. This will further reduce the amount of potable water. Particularly interesting as important indicators of global warming appears to be trends of climate variables such as temperature and rainfall (Easterling et al., 1997 and 2000; Groissman et al., 1999). Regarding to precipitation, although total annual rainfall shows increasing trends in many regions due to global warming, in particular over mid- and upper latitude regions (Dai et al., 1997), upon the Mediterranean area several regional studies show a dominant decreasing trend (Ben Gai et al., 1993; Piervitali et al., 1997; Steinberger and Gazit-Yaari, 1996; Steinberger, 1999; Xopalki, 2000) and also it has been reported a paradoxical increase of extreme daily rainfall in despite of decrease in total values (Alpert et al., 2002).

General circulation models (GCMs) are the primary tool available today for climate simulation and future climate change assessment (IPCC, 2001). Although they incorporate the main characteristics of the general circulation pattern, the performance for the simulation of present climate is rather poor when their projections are applied to regional scale. This is mainly due to the typical horizontal resolution of the GCMs (1^0-3^0), largely imposed by computational restrictions, sufficient to resolve the large-scale forcings but not the impact of the local effects. The large-scale circulation is itself modified by the upscale energy transfer from shorter scale motions, and at least some kind of parameterization of the local forcings (e.g. mesoscale mountain-induced drag) is necessary to obtain realistic results on the large-scale. However, the lack of explicit representation of local circulations prevents the accurate simulation of subregional spatial gradients of the meteorological variables, necessary to characterize the climate of the region.

In the Spanish Mediterranean area (Fig. 1.8), local effects exert a particularly strong influence on the distribution of meteorological variables. This is due to the characteristic complex distribution of land and sea (both the Atlantic ocean and Mediterranean sea are important sources of moisture and thermal regulators), orography (dominated by prominent coastal mountain systems) and even vegetation and soil characteristics. As it has been mentioned, among all surface meteorological parameters, precipitation is undoubtedly the most critical variable for past, present and future social and economic impacts on Mediterranean Spain.

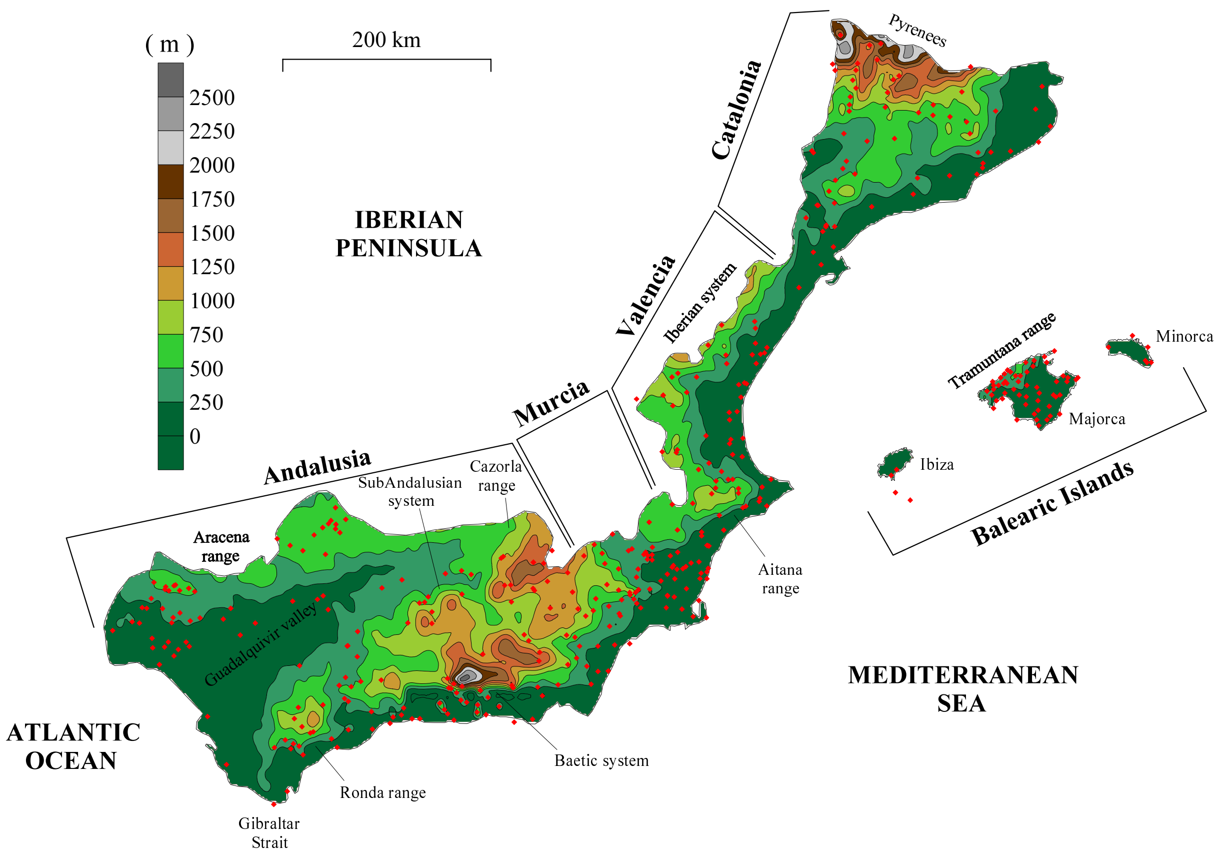

Figure 1.8: The Spanish Mediterranean area. It includes a smoothed version of its orography and the position of the stations included in the daily rainfall data base (410 in total).

Dynamical downscaling applied to GCM outputs attempts to account for the effects of mesoscale forcings by nesting a higher resolution limited area model over the specific area of interest (Giorgi, 1990; Giorgi and Mearns, 1999). This idea was originally based on the concept of the one-way nesting, in which large-scale meteorological fields from general circulation model runs provide initial and time-dependent meteorological lateral boundaries conditions (LBCs) for high-resolution regional climate models (RCMs) simulations. In spite of the rapidly-growing computing power during the last decade, the global nature of future climate simulation efforts and the wide range of greenhouse gas emission scenarios to consider still pose serious challenges for existing and foreseen computational capability. Current GCMs represent a balance among sufficiently realistic physical parameterizations, well-behaved numerical schemes, and grid resolution. Any effort directed toward enhancing the value of the GCMs downscaling results should consider the relative benefits expected from improvement of each of these model aspects. An increase of horizontal grid resolution and temporal frequency of GCM output data ingested by limited area models seems to be a reasonable strategy to follow, but it is not clear whether this is the optimum approach, especially in areas with such a dominant orographic role as the Mediterranean Spain.

Denis et al. (2003) explored for north-eastern America the issue of the sensitivity of a one-way nested RCM to the spatial resolution and to the temporal updating frequency of the LBCs. The one-way nesting aproach was found to produce satisfactory results for most of the fields investigated with a combination of up to T30 (roughly 5^0) spatial resolution and up to 12 h temporal update interval. Antic et al. (2004) addressed the downscaling ability over the west coast of North America, a region with complex topography. Orography and coastline were found to have a positive impact on the quality of the downscaled fields in comparison with the results of Denis et al. (2003). In particular, the nesting technique produced significantly improved cold season precipitation fields over the Rocky Mountains area. Dimitrijevic and Laprise (2005) extended the previous study to the summer season, in which the physical processes of local convective origin exert a predominant role. They found lower skill than during the winter, where precipitation generation is dominated by the large-scale dynamical processes and orographic forcing. The sensitivity of the downscaled precipitation to the spatial and temporal resolution of the LBCs was found to be weaker in summer than in winter, owing to the different nature of the responsible physical mechanisms. On the other hand, some studies have found a relative insensitivity of mesoscale model forecasts to the precise structure of initial and boundary conditions in areas with complex terrain (see, for example, Mass and Kuo, 1998).

Chapter 6 evaluates the sensitivity of mesoscale numerical simulations of rainfall for Mediterranean Spain to large-scale model input data resolution, to help to answer the question whether GCM higher resolution would provide improved dynamically downscaled information in that region in the context of climate change research. The chapter is organized in three main parts: first, results for the whole Mediterranean Spain are presented and discussed; second, the subdomain spatial variability is examined; and third, the results are evaluated as a function of six characteristic circulation types derived in earlier works (Romero et al., 1999b; Sotillo et al., 2003). The main characteristics of the HIgh Resolution Limited Area Model (HIRLAM) –used to perform the numerical mesoscale simulations– are described in chapter 2.

1.5 Objectives

The general motivation of our research is the development of new understanding about those environmental problems of the Western Mediterranean area –and more concretely, the Spanish Mediterranean region– that have been described in sections 1.3 and 1.4. In section 1.3, the impact of intense precipitation events over three Mediterranean catchments of different sizes (ranging, roughly, from 600 to 5000 km^2) and resulting in hazardous flood episodes has been analysed. Then, a major issue for the present research has been to gain insight the hydrometeorological modeling factors which can lead to an enhancement in the study and forecasting of such flood events. The feasibility of runoff simulations driven by numerical weather prediction mesoscale models over these basins has been assessed in an attempt to further extend the lead times for warning and emergency procedures before flood situations. The inaccuracies found in the mesoscale models to the small-scale features of the quantitative precipitation forecasts have also been addressed through different approximations such as: (i) by introducing small shifts and variations of intensity of the precursor upper-level synoptic scale trough; (ii) by using different formulations of the physical processes (i.e. cloud microphysics, moist convection and boundary layer schemes) included within the mesoscale models and (iii) by using different limited area model initializations and configurations. These issues are aimed to take into account the impact of diverse external-scale uncertainties found, nowadays, in the NWP models. With this methodology, it is possible to assess the effects due to relatively moderate spatial and temporal errors of the QPFs on the hydrological responses.

In section 1.4, it has been highlighted that precipitation is undoubtedly the most critical variable in terms of present and future social and economic impacts for the Mediterranean area. Its scarcity during the summer months along with the increasing touristic activity is reflected in strong stress on the water resources, especially after abnormally dry years. On the other hand, extreme precipitation events are common in the region and damaging flash-flood events occur virtually every year. Therefore, it is also important to gain knowledge in the dynamical downscaling of precipitation from General to Regional Climate Models –as the fundamental previous step to the one-way coupling between meteorological and hydrological models– focussed on climate simulation and future climate change assessment. Hence, this issue has been examined in terms of its sensitivity to the spatial and temporal resolution of GCM input fields over the Spanish Mediterranean –a highly vulnerable region according to most of the climate change precipitation scenarios (Meteorological Office, 2001; Watson and Zinyowera, 2001)–.

Chapter 2

NUMERICAL TOOLS

2.1 Geographic Information System tools

Digital Elevation Models (DEMs) are collections of elevation values at equally spaced points of the terrain. They are stored in grid o raster format owing to their matrix nature. This format composes the data structure in square cells or pixels of equal size, arranged in rows and colums. The suitability of DEM-based modeling of gravity-driven flow has been widely addressed in the literature. Consequently, raster-based algorithms for hydrologic analysis have been developed (Jensen and Domingue, 1988; Jensen, 1991), and functions to delineate streams and watersheds based on them are included in many available Geographic Information System (GIS) softwares. Therefore, GISs have become the fundamental cornerstone for hydrologic and hydraulic modeling as a result of the research in geospatial data usage.

The advances in GIS have opened many opportunities for enhancing hydrologic modeling of watershed systems by means of the coupling of the spatial information together with the aforementioned spatial algorithms. The ability of performing spatial analysis for the development of lumped and distributed hydrologic parameters improves the accuracy over traditional methods, as for example, the use of spatial overlays of information to compute lumped or grid-based parameters in order to estimate the basin parameters. These advanced modeling techniques have become feasible because the consuming data manipulations can now be generated efficiently with GIS spatial operations.

2.1.1 Methodology

ArcView version 3.2 has been the GIS selected for the development of this work, since it is used for the Service of Geographical Information Systems and Teledetection at the University of the Balearic Islands (SSIGT). It is a powerful application developed by the Environmental Systems Research Institute (ESRI; further information at: http://www.esri.com), which allows the manipulation and visualitation of point, linear and polygonal elements related among them. For the achievement of the hydrologic modeling, it is necessary to complement the use of ArcView 3.2 program with two additional extensions. First, the ESRI's Spatial Analyst tool (ESRI, 1996) which allows to this GIS software the possibility to further extend the use of vectorial elements to raster files. And second, it must be also used the HEC-GeoHMS geospatial hydrologic modeling extension developed by the Hydrologic Engineering Center's

(USACE-HEC, 2003). This latter program allows to visualize spatial information, document watershed characteristics, perform spatial analysis, delineate subbasins and streams and build inputs to hydrologic modeling systems. Next, a brief summary –step by step– of the methodology followed in some of the applications for DEM-based stream and watershed delineation, hydrologic parameter estimation, and linkage to hydrologic modeling systems (i.e. HEC-HMS in our study cases, see next sections for further information) are expounded in order to derive the aforementioned hydrological model inputs for the Albufera river basin (Olivera, 2001; USACE-HEC, 2003):

- **Depresionless DEM**. The depresionless DEM is created by filling the depressions or pits by increasing the elevation of the pit cells to the level of surrounding terrain in order to determine flow directions of the original Digital Terrain Model (DTM; see figs. 2.1 and 2.2).
- **Flow Direction**. This step defines the direction of the steepest descent for each terrain cell following an eight-point pour algorithm which specifies eight possible directions (figs. 2.1 and 2.2).
- **Flow Accumulation**. This step determines the number of upstream cells draining to a given cell. Upstream drainage area at a given cell can be calculated by multiplying the flow accumulation value by the cell area (figs. 2.1 and 2.3).

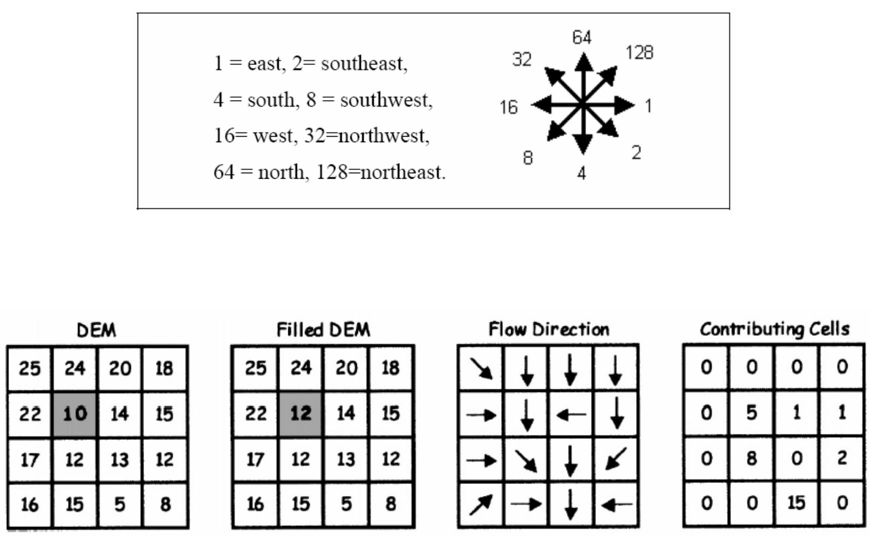

Figure 2.1: From up to down and left to right: Flow directions for each terrain cell and DEM, Filled DEM, Flow Direction and Contributing Cells Grids (shaded cell in DEM grid corresponds to terrain pit).

- **Stream Definition**. This step classifies all cells with flow accumulation greater than an user-defined threshold as cells belonging to the stream network. Typically, cells with high flow accumulation, greater than this threshold value are considered part of the stream network. The user-specified threshold is defined as an area in distance units squared (i.e. square meters) or as a number of cells. The flow accumulation for a particular cell must exceed the user-defined threshold for a stream to be initiated

- **Stream Segmentation**. This step divides the stream into segments. Stream segments or links are the sections of a stream that connect two successive junctions, a junction and an outlet, or a junction and the drainage divide (fig. 2.4).

- **Watershed Delineation**. This step delineates a subbasin or watershed for every stream segment.

- **Watershed Polygon** and **Stream Segment Processing**. These steps convert sub-basins and streams in the grid representation into a vector representation (fig. 2.5).

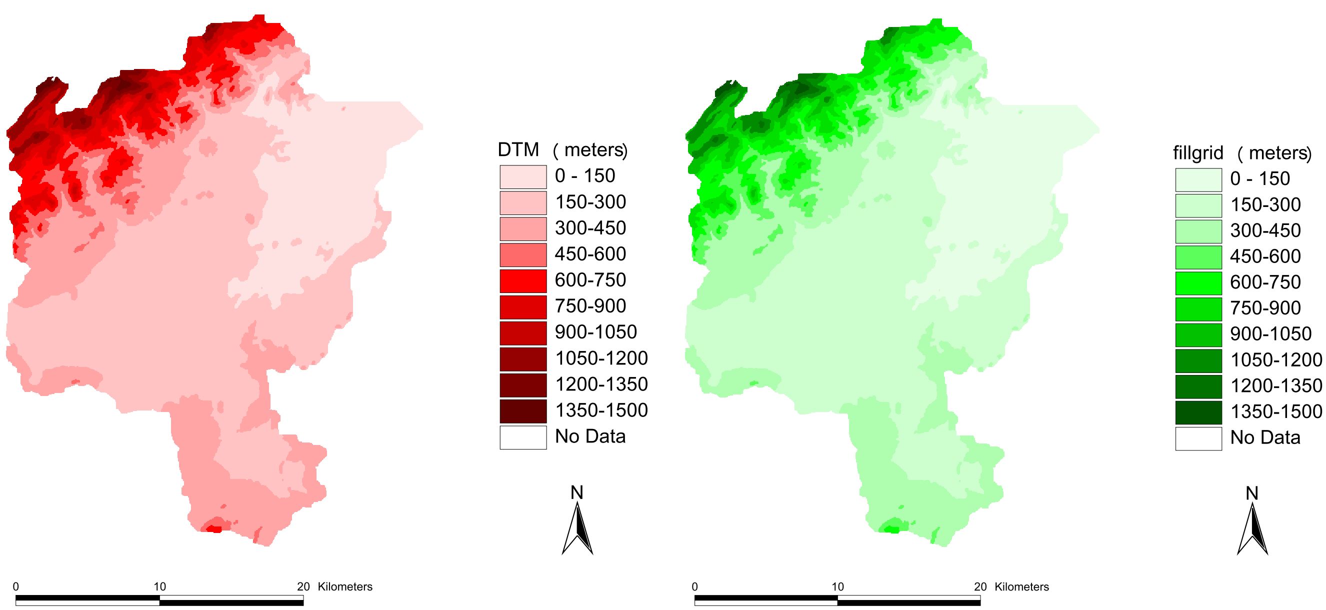

Figure 2.2: From left to right: original and depresionless DTMs.

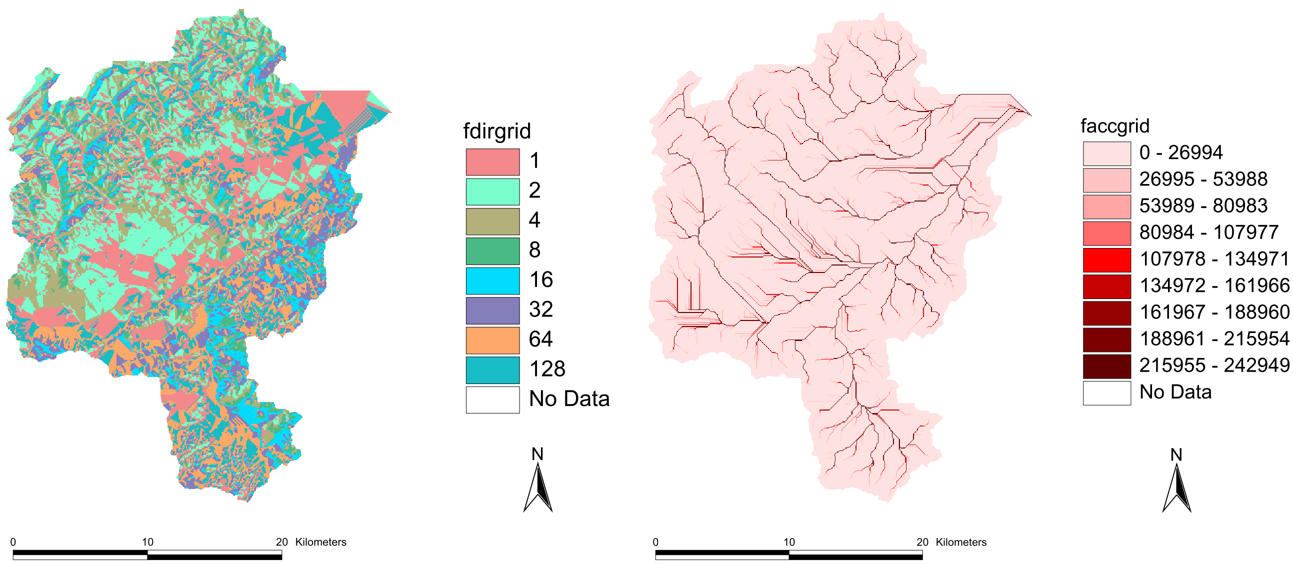

Figure 2.3: From left to right: Flow directions for each terrain cell and the flow accumulation operation output.

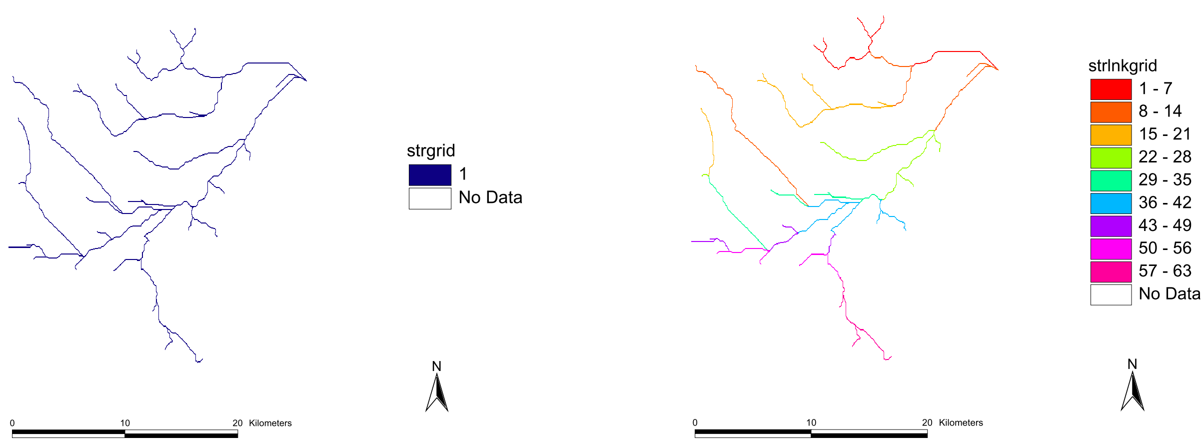

Figure 2.4: From left to right: stream definition and stream segmentation operation results.

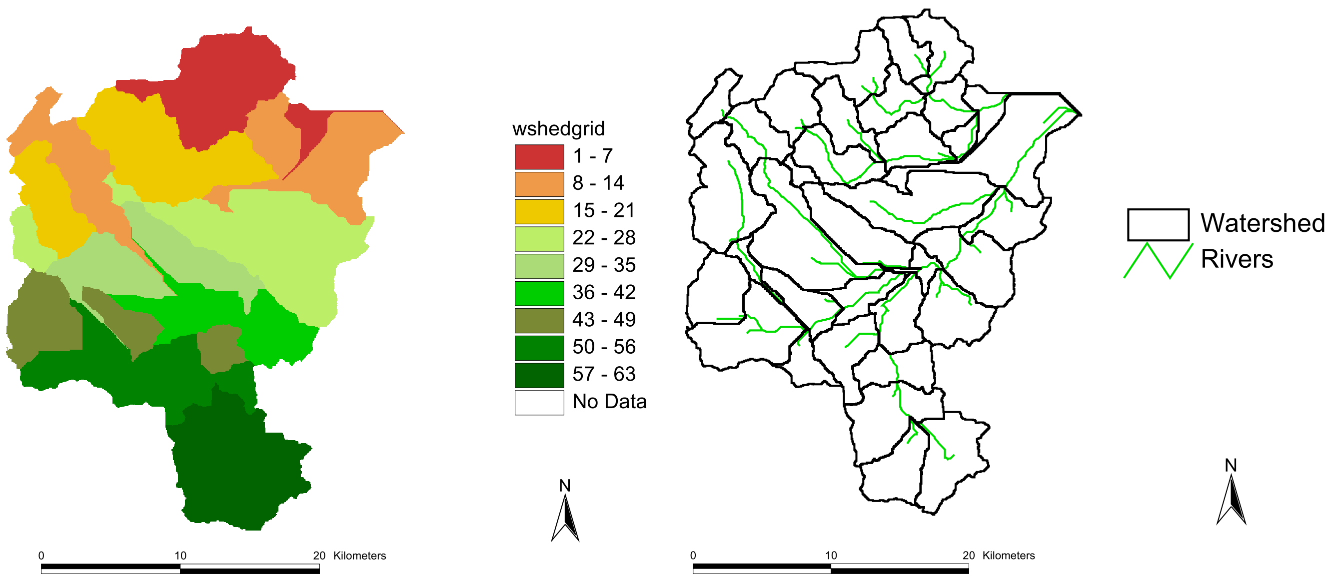

Figure 2.5: From left to right: basin delineation and watershed polygon and stream segmentation operation results.

2.1.2 Computation of hydrologic parameters: an example

Different options are supported by the HEC-HMS model for runoff calculation, subbasin and reach routing. The Soil Conservation Service Curve Number (SCS-CN; see next section for further details) for the calculation of abstractions is now discussed in order to illustrate the automatic implementation of this method within a GIS environment. From the hydrological model set-up adopted in this work (further details in next section), the only parameter necessary is the subbasin average curve number for implementing this method, and it is briefly summarized herein for its automatic extraction. A more extensive discussion of the derivation of this and other hydrological parameters can be found, for example, in Olivera (2001) and USACE-HEC (2003).

The U.S. Department of Agriculture (1972) has published curve number lookup tables, which consist of recommended CN values for unique combinations of hydrologic soil group (i.e. **A**, **B**, **C** and **D**) and land use. The hydrologic soil group is a soil classification based on infiltration rate, so that **A** is more permeable and **D** is less permeable. A curve number map can be estimated using soil and land-use spatial data as inputs (fig. 2.6), and relating this information to the curve number tables. The spatial soil and land-use databases (fig. 2.6) are divided into map units represented by polygons in the map. Therefore, the intersection of the soil and the land-use polygons create a map in which each resulting polygon is related to a unique combination of soil and land use (fig. 2.7). After assigning curve values to each polygon, the curve number and the subbasin polygons have to be intersected before averaging. Then, the average curve number values for each subbasin are calculated, and their values are added to a subbasin table. The subbasin area is calculated automatically when vectorizing the watershed.

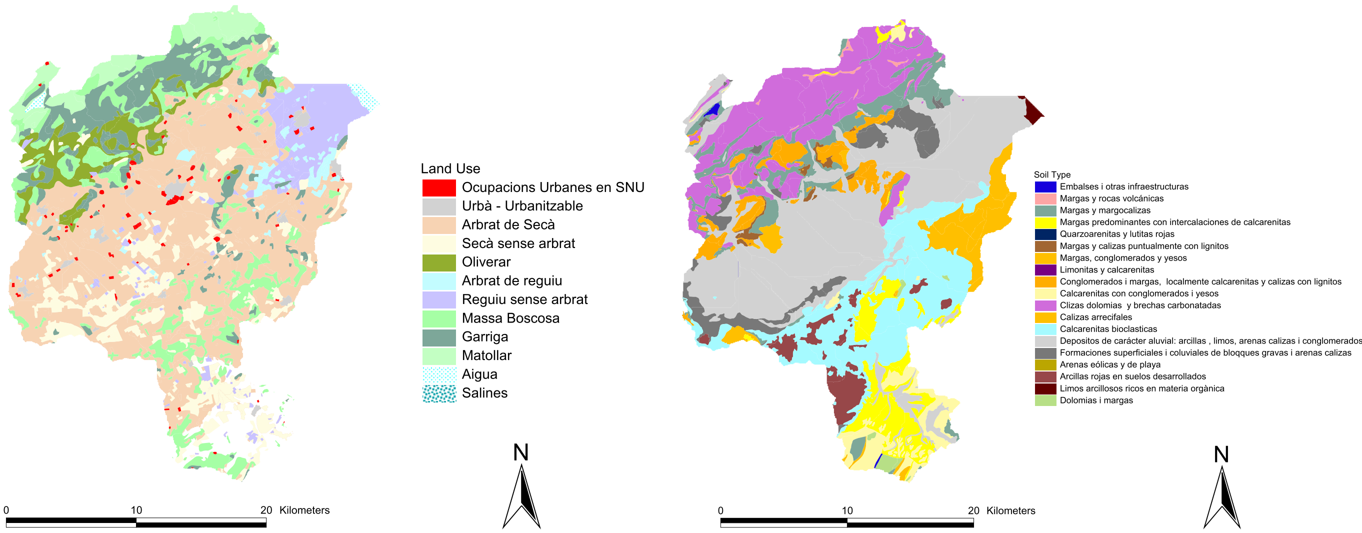

Figure 2.6: From left to right: land uses and hydrologic soil types polygons for the watershed map.

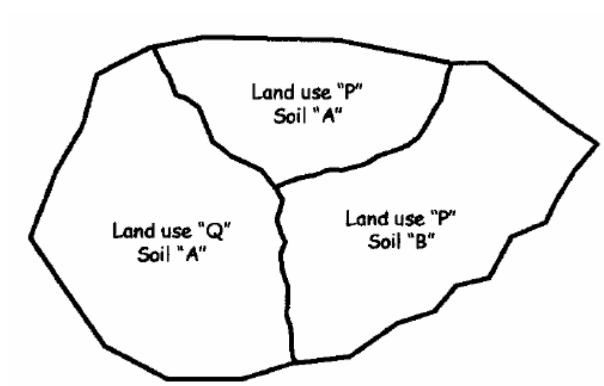

Figure 2.7: After intersecting land-use and soil properties polygons, each resulting polygon is a unique combination of these atributes and a CN can be calculated for it.

2.2 Hydrological model

The numerical model used for our research is the physically-based Hydrologic Engineering Center's Hydrologic Modeling System (HEC-HMS) model developed by the US Army Corps of Engineers (USACE-HEC, 1998). The model simulates precipitation-runoff and dynamical routing processes, both natural and controlled. It provides capabilities for semi- and distributed modeling as well as event-based and continuous simulations. Furthermore, it is able to simulate the rainfall-runoff at any point within a basin given its physical characteristics. In fact, the model has been used as a valuable tool in a broad spectrum of studies: as a tool of watershed management in order to account and determine the human impacts (e.g. basin urbanization) on magnitude, quantity, and timing of runoff at points of interest; and passing through analyses of water availability, urban drainage, flood damage reduction and flow forecasting in geographical areas ranging from small urban or natural catchments to large river basins. HEC-HMS requires three input components: (i) the *basin model*, which describes the different elements of the hydrologic system (i.e. subbasins, reaches, junctions, sources, sinks, reservoirs, and diversions) including their hydrologic parameters and topology; (ii) the *meteorological model*, which describes –in space and time– the precipitation event to be modeled as well as the evapotranspiration processes; and (iii) the *control specifications*, which define the time window for the simulation. This hydrological model utilizes a graphical interface to build a watershed model and to set-up the rainfall and control variables for the simulation. Next subsections describe in detail the mathematical models that have been used within the model to parameterizate the diverse runoff processes at local scale for the performance of the hydrological experiments (fig. 2.8). Briefly, the hydrological model provides the following components for precipitation-runoff-routing simulation:

- Loss models which can estimate the volume of runoff, given the precipitation and the properties of the watershed.
- Direct runoff models that can account for the overland flow, storage and energy losses as water runs of the watershed and into stream channels.
- Hydrologic routing models that account for storage and energy flux as water moves through stream channels.
- Models of naturally occurring confluences and bifurcations, as well as, of water-control measures including diversions and storage facilities.
- Automatic calibration procedures in order to estimate certain model parameters and initial conditions, given observations of hydrometeorological data.

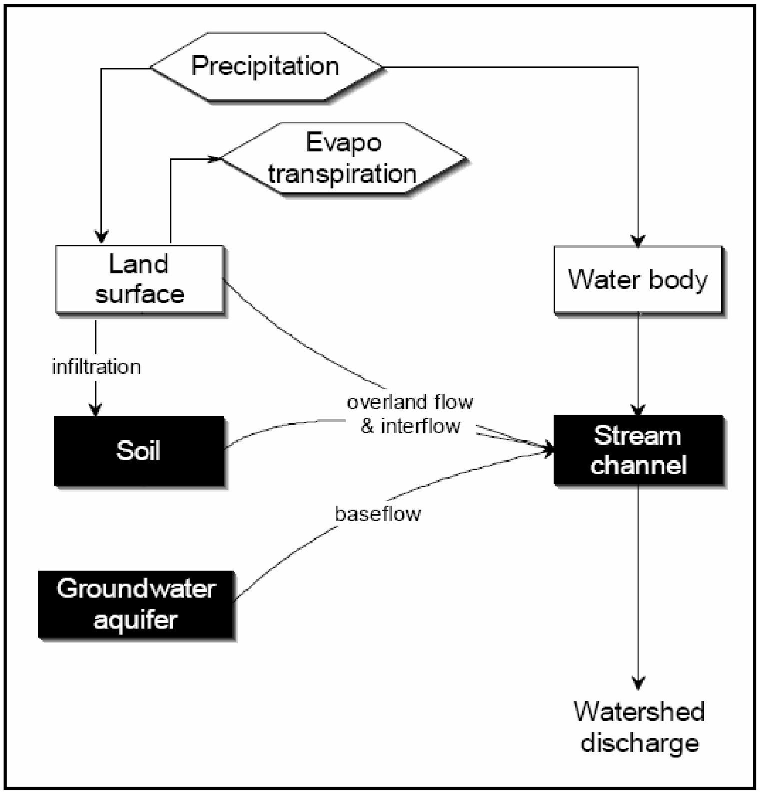

Figure 2.8: Model diagram of the runoff processes at local scale.

2.2.1 Computing runoff volumes: the SCS Curve Number (CN) loss model

The excess rainfall, or effective rainfall, is that rainfall which is neither retained on the land surface nor infiltrated into the soil. After flowing across the basin surface, excess rainfall becomes direct runoff at the basin outlet. The difference between the observed total rainfall hyetograph and the excess rainfall hyetograph is termed abstractions or losses. The hydrologic model calculates the excess precipitation volume by subtracting from rainfall the water volume that is lost through interception, infiltration, storage, evaporation and transpiration. The loss rate is calculated using the Soil Conservation Service Curve Number (SCS-CN; see, for instance, US Department of Agriculture, 1986). This method assumes the storm runoff volumes, P_e, to be proportional to the rainfall volumes, P, exceeding an initial abstraction threshold, I_a, through the ratio of the accumulated infiltration, F_a, to the potential maximum storage capacity, S.

$$P_e = \frac{F_a}{S} \cdot (P - I_a) \text{ for P} > I_a\text{; 0, otherwise.} \tag{2.1}$$

The initial abstraction, I_a, represents the maximum capacity of interception and depression storages. Standard procedures, tested on a wide experimental basis, suggests that $I_a \simeq 0.2 \cdot S$ should be adopted when field measurements for the watershed under study are not available for the initial abstractions. With this assumption together with the continuity equation that for P>I_a states that

$$P = P_e + I_a + F_a \tag{2.2}$$

the cumulative volume of stormflow becomes nonlinearly related to the excess rainfall volume (P-I_a):

$$P_e = \frac{(P - 0.2S)^2}{P + 0.8S} \tag{2.3}$$

which is a function of cumulative rainfall, soil cover, land use and antecedent moisture (see fig. 2.9; Chow et al., 1988; Bacchi et al., 2002).

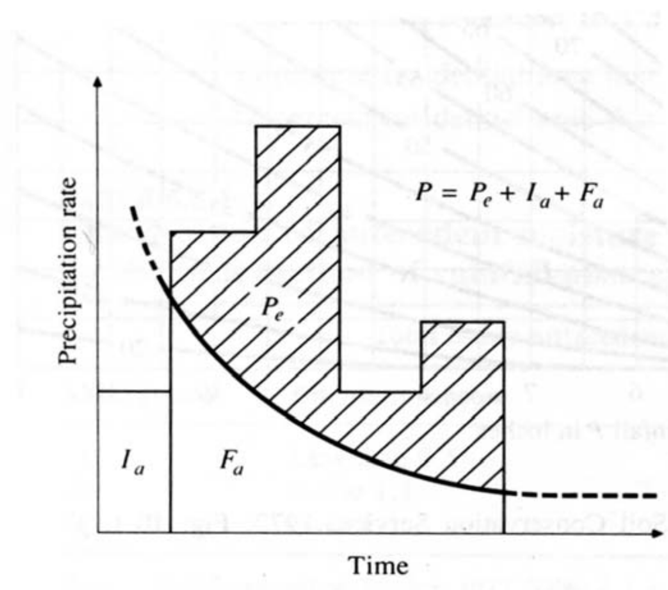

Figure 2.9: Variables in the SCS method of rainfall abstractions.

The maximum retention and the basin characteristics are related through an intermediate parameter, the curve number (CN) and according the SCS formulation for normal antecedent moisture conditions:

$$S = \frac{25400 - 254CN}{CN} \tag{2.4}$$

where the CN values can range from 100 for water bodies to approximately 30 for permeable soils with high infiltration rates (fig. 2.10). The SCS-CN model has been tested on several experimental areas and river basins worldwide and, in Catalonia has been adopted by ACA in their technical studies (ACA 2001, 2003). The SCS-CN model has the advantage that with a single parameter (the storage capacity) it reproduces two phenomena that are systematically observed during floods: an initial loss of rain and an increase in the efficiency of the basin in producing runoff as a response to the rainfall input (Ranzi et al., 2003).

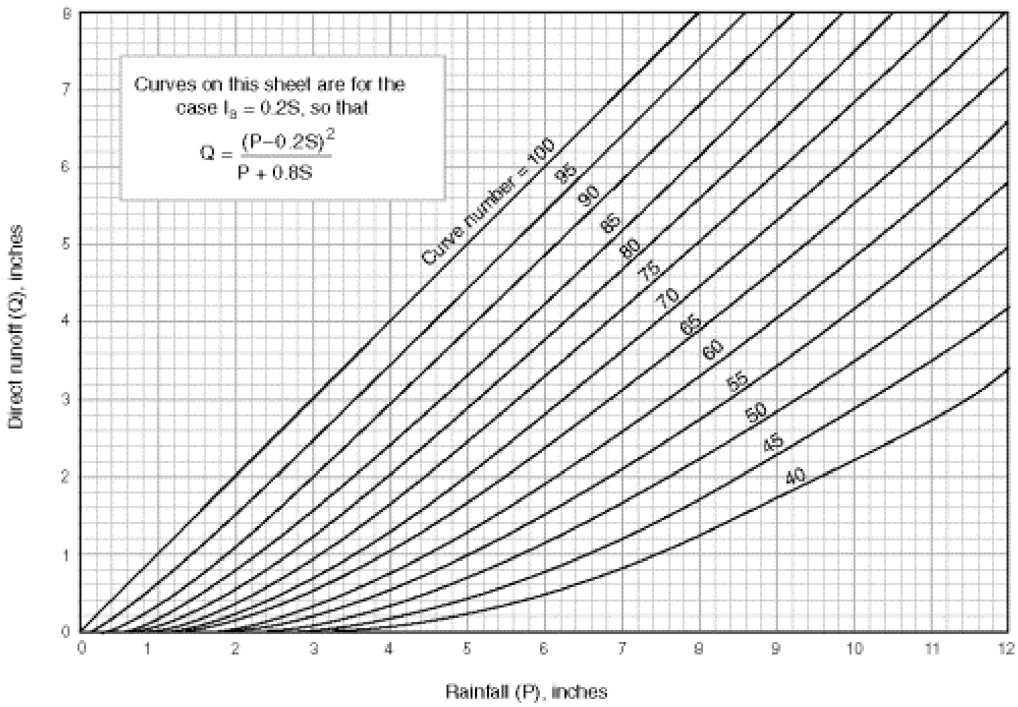

Figure 2.10: Graphical solution for the SCS runoff equations.

For a watershed that consists of several soil types and land uses (see previous section), a composite CN must be calculated as:

$$CN_{composite} = \frac{\sum A_i CN_i}{\sum A_i} \tag{2.5}$$

in which $CN_{composite}$ is the composite CN used for runoff volume computations; i is an index of subbasins divisons of uniform land and soil type (see fig. 2.7 in previous section; CN_i is the CN for the subdivion i; and A_i is the drainage area of subdivion i.

2.2.2 Modeling direct runoff: the Unit Hydrograph model

In order to convert rainfall excess into direct runoff, it is applied the fundamental assumption that the watersheds respond as linear systems. Then, the relationship between storage, inflow and outflow is such that it leads to a linear differential equation. The hydrologic response of such systems can be expressed in terms of an impulse response function (IRF) through a so-called Convolution Equation. This implies that the proporcionality principle applies so that effective rainfall intensitities of different magnitude produce basin responses that are accordingly scaled. It also implies that the superposition principle applies so that the responses of several different storms can be superimposed to obtain the composite response of the catchment, which are implicit in the convolution equation (see fig. 2.11).

The IRF of a linear system represents the response of the system to an instantaneous impulse of unit volume applied at the origin in time (t=0). The response of continuous linear

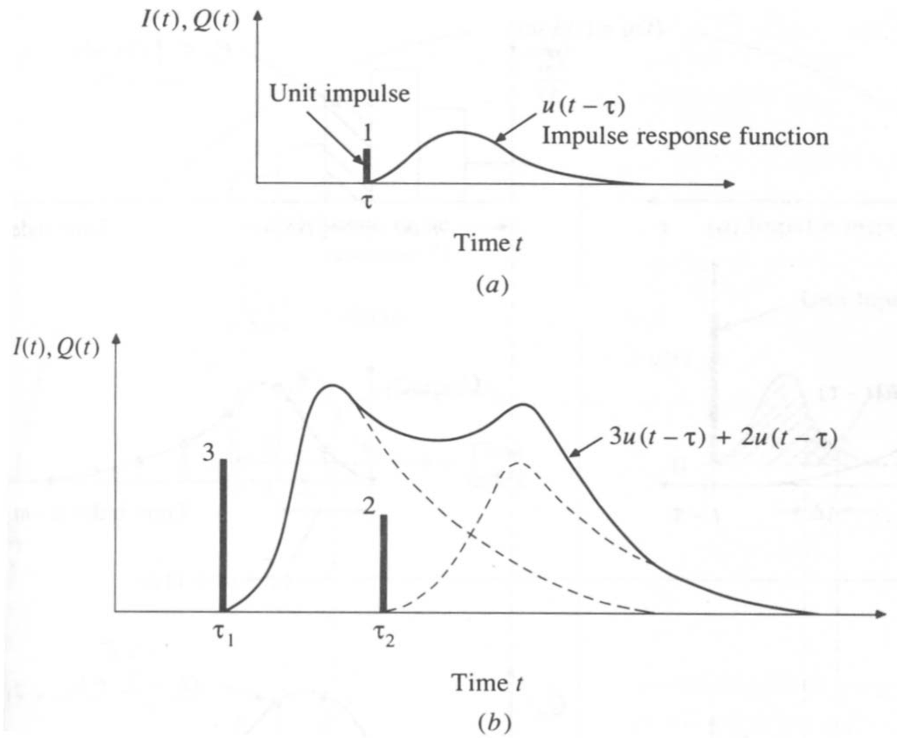

Figure 2.11: Responses of a linear system to impulse inputs. (a) Unit impulse response function. (b)The response to two impulses is found by summing the individual response functions.

systems can be expressed, in the time domain, in terms of the impulse response function via the convolution integral as follows,

$$Q(t) = \int_0^t I_e(\tau)u(t-\tau)d\tau \tag{2.6}$$

where $u(t)$ is the impulse response function of the system.

When dealing with hydrologic systems, $u(t)$ represents the instantaneous unit hydrograph (IUH), and Q_t and $I_e(t)$ represent direct runoff and excess precipitation, respectively. Thus, an unit hydrograph represents the response of a watershed –the discharge at its outlet as a function of time– to a unit volume of precipitation occurring instantaneously at time t=0.

The unit step response function (SRF) is the theoretical counterpart to the S-curve hydrograph concept. It represents the runoff hydrograph from a continuous effective rainfall of unit intensity and it is the convolution integral with $I_e(\tau) = 1 \; for \; \tau \geq 0$, and obtained as,

$$g(t) = \int_0^t u(t)dt \tag{2.7}$$

The unit pulse response function (PRF) is the theoretical counterpart to the UH concept. It represents the runoff hydrograph from a constant effective rainfall of intensity $1/\Delta t$ and of duration Δt:

$$h(t) = \frac{1}{\Delta t}\Big[g(t) - g(t-\Delta t)\Big] = \frac{1}{\Delta t}\int_{t-\Delta t}^{t} u(\tau)d\tau \tag{2.8}$$

From its definition, the PRF can be seen as the normalized difference between two lagged SRF's (S-curve hydrographs), lagged by an amount Δt.

When the effective rainfall is given as a hyetograph, that is, as a sequence of M rainfall pulses of the same duration, Δt, the corresponding direct runoff hydrograph can be expressed as the discrete convolution equation of the rainfall hyetograph and a Unit Hydrograph (figs. 2.12a and b),

$$Q_n = \sum_{m=1}^{m*} P_m U_{n-m+1} \quad \text{m*=min(n,M)} \tag{2.9}$$

$$Q_n = Q(n\Delta t) \quad \text{n=1,2,...,N} \tag{2.10}$$

$$P_m = \int_{(m-1)\Delta t}^{m\Delta t} I(\tau)dt \quad \text{m=1,2,...,M} \tag{2.11}$$

where P_m is the volume of the m^{th} effective rainfall pulse. The value of the system output, Q_n, in the n^{th} time interval ($t = n\Delta t$) is the instantaneous value of the flow rate at the end of the n^{th} time interval. The effect of an input pulse duration Δt beginning at time $(m-1)\Delta t$ on the output time $t = n\Delta t$ is measured by the value of the unit pulse response function which can be represented on a discrete time domain as a sample function U_{n-m+1}. Then, the discrete convolution equation allows the computation of direct runoff Q_n given excess rainfall P_m and the unit hydrograph U_{n-m+1} (Chow et al., 1988; Ramírez, 2000). The Unit Hydrograph ordinates corresponds to the area under the IUH between two consecutive time intervals and are given by,

$$U_{n-m+1} = h\Big[(n-m+1)\Delta t\Big] = \frac{1}{\Delta t}\int_{(n-m)\Delta t}^{(n-m+1)\Delta t} u(\tau)d\tau \tag{2.12}$$

For the derivation of unit hydrographs, sets of simultaneous observations of effective rainfall and direct runoff are required. Thus, the resultant UH is specific to the particular watershed defined by the point on the stream where the direct runoff observations were made. When no direct observations are available, Synthetic Unit Hydrograph procedures must be used. Synthetic Unit Hydrographs procedures can be categorized as (Chow et al., 1988): (i) those based on models of watershed storage (e.g. Nash, 1959; Dooge, 1959), (ii) those relating hydrograph characteristics (time to peak, peak flow, etc.) to watershed characteristics (Snyder, 1938; Geomorphologic Instantaneous Unit Hydrographs) and (iii) those based on a dimensionless unit hydrographs.

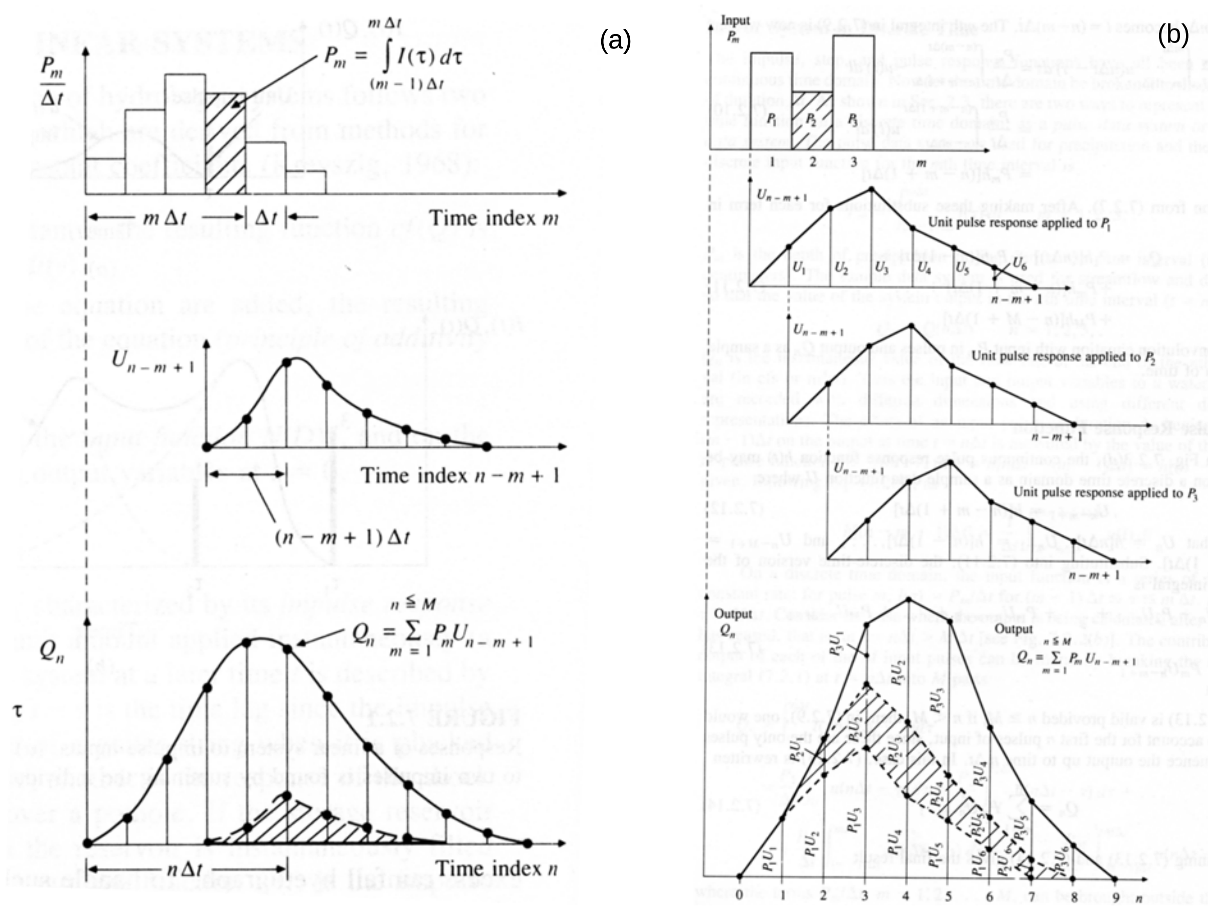

Figure 2.12: (a) Scheme of the discrete convolution and (b) Application of the discrete convolution equation to the output from a linear system.

A synthetic unit hydrograph (UH) provided by SCS (US Department of Agriculture, 1972) is used to convert rainfall excess into direct runoff on a watershed. The discharge is expressed by the dimensionless SCS-UH as the ratio of discharge, U_t, to peak discharge, U_p, and the time by the ratio of time t to the time of rise of the unit hydrograph, T_p. Given the peak discharge and the lag time for the duration of the excess rainfall, the unit hydrograph can be estimated from the synthetic dimensionless hydrograph for the given basin. Figure 2.13 shows such a dimensionless hydrograph prepared from the unit hydrographs of a variety of watersheds where the time is in hours and the discharge in $\mathrm{m^3 s^{-1} cm^{-1}}$. It can be shown that

$$U_p = C \frac{A}{T_p} \tag{2.13}$$

in which C is a constant and A is the drainage area in square kilometers. The time of peak is related to the duration of excess precipitation as

$$T_p = \frac{\Delta t}{2} + t_{lag} \tag{2.14}$$

in which Δt is the excess rainfall duration and t_{lag} is the basin lag, defined as the time difference between the centroid of rainfall excess and the UH peak discharge. Following CEDEX recommendations, based on previous SCS,

$$t_{lag} = 0.35T_c \tag{2.15}$$

where the time of concentration of the basin, T_c (in hrs). The time of concentration is defined as the time of flow from the farthest point on the watershed to the outlet. The travel time of flow from one point on a watershed to another, t, can be deduced from the flow distance and the velocity. If two points on a stream are a distance L apart and the velocity along the path connecting them is $v(l)$, where l is distance along the path, then the travel time is given by

$$t = \int_0^L \frac{dl}{v(l)} \tag{2.16}$$

If the velocity can be assumed constant at v_i in an increment of time of length, Δl_i; i=1,2,...,I, then

$$t = \sum_{i=1}^{I} \frac{\Delta l_i}{v_i} \tag{2.17}$$

Therefore, T_c is the time at which all the watershed begins to contribute to surface water flow and can be estimated by using a diversity of empirical formulas (e.g. Kirpich, California Culverts Practice, Izzard, Morgali and Linsley, SCS lag equation). In Spain, the Témez formula (Témez, 1978) has been widely adopted and shows suitable results. It takes the following expressions depending on the urbanization of the watershed:

$$T_c = \begin{cases} 0.3 \cdot (\frac{L}{j^{0.25}})^{0.76} & \text{for rural basins} \\ \frac{1}{1+\sqrt{\mu(2-\mu)}} \cdot 0.3 \cdot (\frac{L}{j^{0.25}})^{0.76} & \text{for urbanized basins} \\ \frac{1}{1+3\sqrt{\mu(2-\mu)}} \cdot 0.3 \cdot (\frac{L}{j^{0.25}})^{0.76} & \text{for urban basins} \end{cases} \tag{2.18}$$

in which L is the channel length (in km), j the channel mean slope (in m/m) and μ the urbanization rate of the basin (in km^2/km^2). When the lag time is specified, it can be obtained the time of UH peak and the UH peak (Chow et al., 1988; USACE-HEC, 2000).

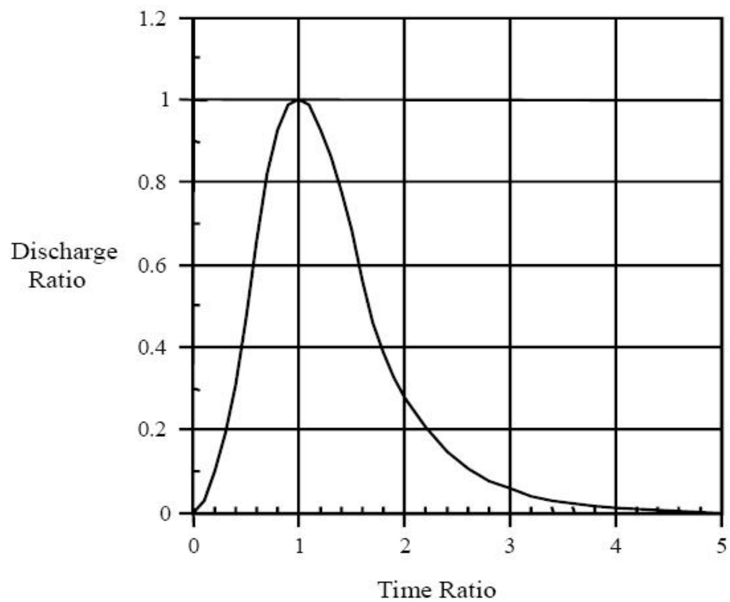

Figure 2.13: Soil Conservation Service dimensionless unit hydrograph.

2.2.3 Modeling baseflow runoff: the exponential recession model

Two distinguishable components of a streamflow hydrograph are the direct, quick runoff of precipitation, and the baseflow. Baseflow is composed by the flow which contributes to the channel from groundwater and the delayed subsurface runoff from the current rainfall. Some conceptual models of watershed processes account explicitly for this storage and for the subsurface movement. The exponential recession model has been used often to explain the drainage from natural storage in a basin (Linsley et al., 1982). It defines the relationship of $Q(t)$, the baseflow at any time t, to an initial value as:

$$Q(t) = Q(t_0)e^{-(t-t_0)/k} \tag{2.19}$$

where $Q(t_0)$ is a reference baseflow discharge at time t_0 and k is an exponential decay constant having the dimensions of time (Chow et al., 1988). As implemented in the hydrological model, k is defined as the ratio of the baseflow at time t to the baseflow one day earlier. The starting baseflow value, $Q(t_0)$, is an initial condition of the model. In HEC-HMS, the baseflow is applied both at the start of simulation of a storm event, and later, as the delayed subsurface flow reaches the basin channels, as illustrated in figure 2.14. That threshold may be specified as a flow rate or as a ratio to the computed peak flow. At the threshold flow, baseflow is defined by the initial baseflow recession.

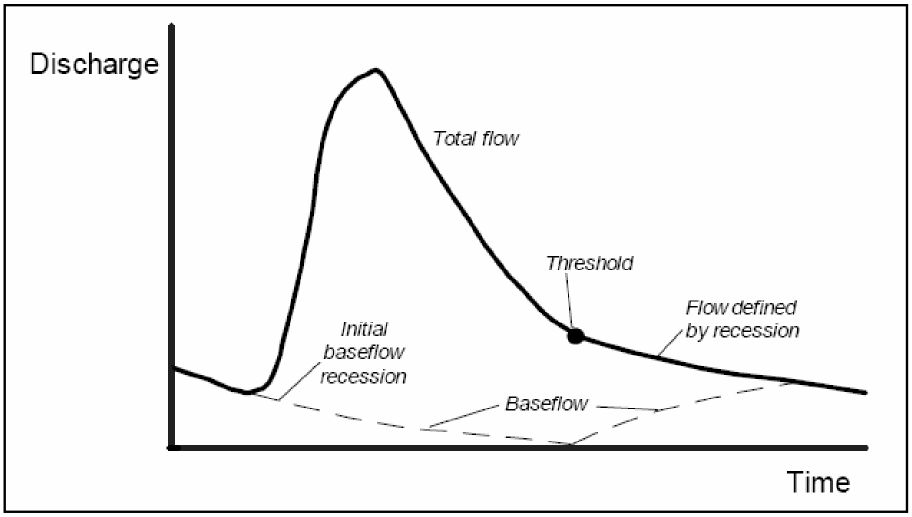

Figure 2.14: Baseflow model illustration.

2.2.4 Modeling channel flow routing: the Muskingum model and the kinematic wave approximation

Flow routing is a procedure to determine the time and magnitude of the flow –the flow hydrograph– at a point in the watercourse from known hydrographs at one o more points upstream, and it is the physical process to define the discharge hydrograph evolution along the river. As flood waves travel downstream they are attenuated and delayed. That is, the peak flow of the hydrograph decreases and the time base and the time to peak of the hydrograph increases. The shape of the outflow hydrograph depends on diverse factors such as: the channel geometry and roughness, the bed slope, the length of the channel reach, and the initial and the boundary flow conditions (fig. 2.15). The propagation of flood waves in a channel is a gradually varied unsteady flow process, which is governed by conservation of mass and momentum equations.

For the hydrologic routing, the inflow at the upstream end, I(t) and the outflow at the end of the watercourse, Q(t), are related by the principle of mass conservation:

$$\frac{dS(t)}{dt} = I(t) - Q(t) \tag{2.20}$$

which requires that the difference between the two flows has to be equal to the time rate of change of the storage within the reach, $S(t)$. The continuity equation can be integrated over a given Δt to obtain

$$S(t+1) - S(t) = \int_{S(t)}^{S(t+1)} dS(t) = \int_{t}^{t+1} I(t)dt - \int_{t}^{t+1} Q(t)dt \tag{2.21}$$

Assuming a linear variation of input and output fluxes during the Δt leads to,

$$S(t+1) - S(t) = \frac{\Delta t}{2}\Big[I(t+1) + I(t)\Big] - \frac{\Delta t}{2}\Big[Q(t+1) + Q(t)\Big] \tag{2.22}$$

Here $Q(t)$ and $S(t)$ are unknown. Thus, a second relationship –the storage function– is needed to relate $I(t)$, $Q(t)$ and $S(t)$. In general the storage function may be written as a

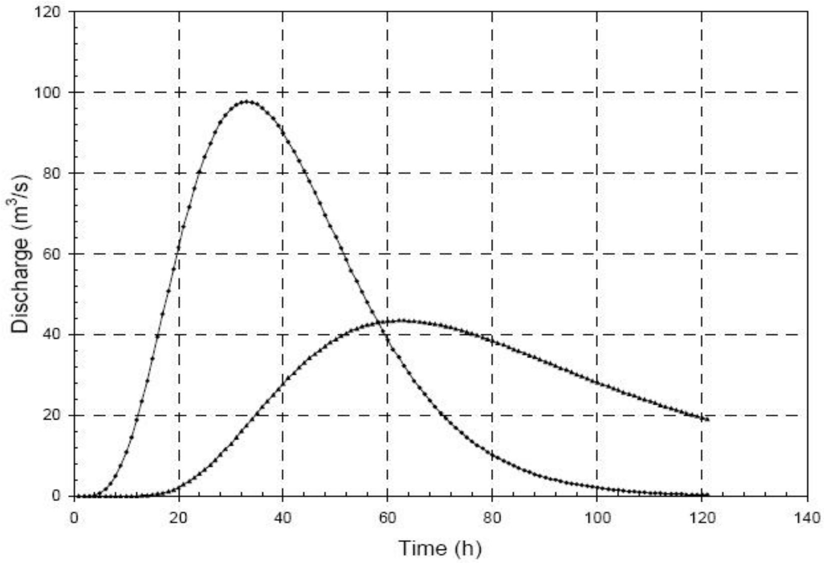

Figure 2.15: Inflow and outflow hydrographs for the Muskingum routing.

function of $I(t)$, $Q(t)$ and their derivatives (although it also depens on the characteristics of the channel reach):

$$S(t) = f(I(t), \frac{dI(t)}{dt}, \frac{d^2I(t)}{d^2t}, ..., Q(t), \frac{dQ(t)}{dt}, \frac{d^2Q(t)}{d^2t}, ...) \tag{2.23}$$

The Muskingum model is used as hydrologic routing method and assumes a linear storage discharge relationship (Chow et al., 1988; USACE-HEC, 2000; fig. 2.15). It models the storage function in a river channel by a combination of a wedge and a prism storages (fig. 2.16). The storage is defined as:

$$S(t) = K[\chi I(t) + (1 - \chi)Q(t)] \tag{2.24}$$

where K is the travel time of the flood wave through the routing reach (in s) and χ a dimensionless weight ($0 \leq \chi \leq 0.5$). Storage in the reach is modeled as a sum of prism and wedge storage.

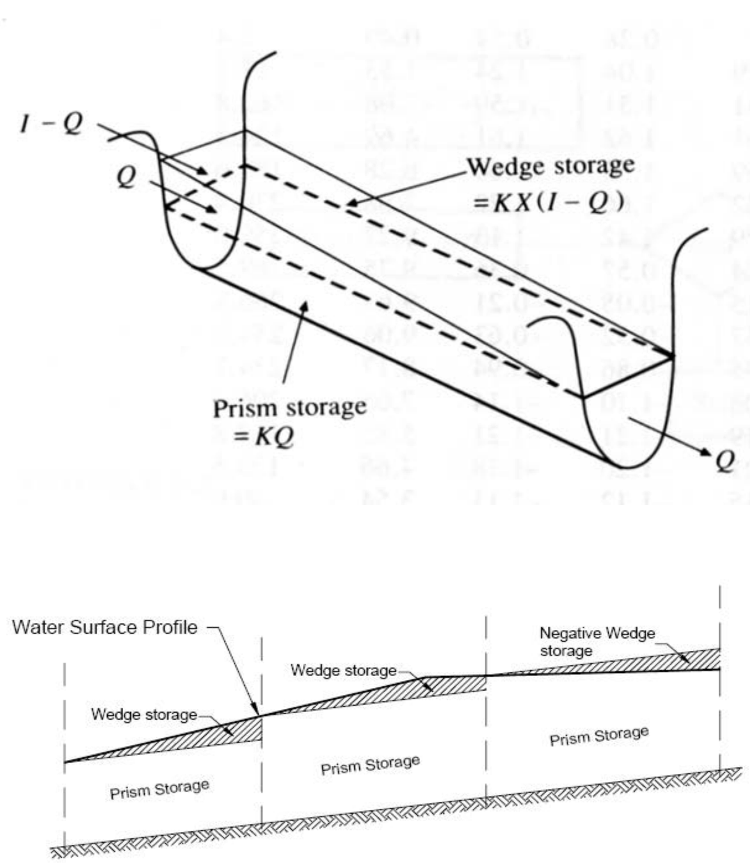

Figure 2.16: Prism and wedge storages in a channel reach.

In HEC-HMS, the mass conservation equation is solved using the finite difference method. Incorporating a finite-difference approximation for the partial derivatives yields

$$\Big[\frac{I(t-1)+I(t)}{2}\Big]-\Big[\frac{Q(t-1)+Q(t)}{2}\Big]=\Big[\frac{S(t)+S(t-1)}{2}\Big] \tag{2.25}$$

where $I(t)$ is the inflow rate at the considered reach, $Q(t)$ is the outflow rate and $S(t)$ the storage rate (in $\mathrm{m^3s^{-1}}$). Combining (2.24) and (2.25) equations:

$$Q(t)=C_0I(t)+C_1I(t-1)+C_2Q(t-1) \;\; \text{where} \tag{2.26}$$

$$C_0=\frac{\Delta t-2K\chi}{2K(1-\chi)+\Delta t}$$

$$C_1=\frac{\Delta t+2K\chi}{2K(1-\chi)+\Delta t}$$

$$C_2=\frac{2K(1-\chi)-\Delta t}{2K(1-\chi)+\Delta t}$$

and it is accomplished that $C_0+C_1+C_2=1$

In order to determine the value of K and χ on the basis of channel characteristics and flow rate in the channel must be used the open-channel-flow equations. The fundamental equations of open channel flow are the continuity and momentum equations. Together the two equations are known as the Saint-Venant equations or the dynamical wave equations. The continuity equation accounts for the volume of water in a reach of an open channel, including the flowing into the reach, the flowing out of the reach, and the stored in the reach. In one dimension, the conservative form of the equation is applicable at a channel cross section:

$$\frac{\partial Q}{\partial x} + \frac{\partial A}{\partial t} - q_l = 0 \tag{2.27}$$

where Q is the flow entering at the upstream end of the channel, q_l is the lateral inflow per unit length of channel, x is the distance along the flow path, A is the average cross-sectional area and v_{lx} is the x-component of the mean velocity for the lateral inflow. Each of the terms in this equation describes inflow to, outflow from or storage in a reach of channel, a lake or pond, or a reservoir. The terms can be described as: $\partial Q/\partial x$ is the rate of change of channel flow with distance and $\partial A/\partial t$ the rate of change of mass stored.

The momentum equation accounts for the forces that act on a body of water in a open channel. In simple terms, it equates the sum of the gravitational, pressure and friction forces to the product of fluid mass and acceleration. In one dimension, the equation is written for the conservative form as:

$$\frac{1}{A}\frac{\partial Q}{\partial t} + \frac{1}{A}\frac{\partial}{\partial x}(\frac{Q^2}{A}) + g\frac{\partial y}{\partial x} - g(S_o - S_f) - q_l v_{lx} = 0 \tag{2.28}$$

where $(1/A)(\partial Q/\partial t)$ is the local acceleration; $(1/A)(\partial(Q^2/A)/\partial x)$ is the convective acceleration; $g(\partial y/\partial x)$ is the pressure force term; gS_f is the friction force term; gS_o the gravity force term and $q_l v_{lx}$ is the momentum entering the main channel with the lateral inflow.

Althought the solution of the full equations is appropriate for all one-dimensional channel-flow problems, approximations of the full equations are adequade for typical flood routing needs. These approximations combine the continuity equation with a simplified momentum equation that includes only relevant and significant terms. For flood events, the momentum equation can be simplified to only contain the gravity and friction force terms. If this simplified momentum equation is combined with the continuity equation, the result is the kinematic wave approximation.

Kinematic waves govern the flow when inertial and pressure forces are not important, then these terms are negligible in the momentum equation and the movement is described principally by the equation of continuity. The gravity and friction forces are balanced, so the flows does not accelerate appreciably. The energy grade line is parallel to the channel bottom and the flow is steady and uniform for a differencial length, dx. Then, the kinematic wave model is defined by the following equations, assuming that the lateral inflow is insignificant:

$$\frac{\partial Q}{\partial x} + \frac{\partial A}{\partial t} = 0 \tag{2.29}$$

$$S_o = S_f \tag{2.30}$$

The above momentum equation can also be expressed in the form,

$$A = \alpha Q^{\beta} \tag{2.31}$$

By combining (2.29) and (2.31) equations:

$$\frac{\partial Q}{\partial t} + c_K \frac{\partial Q}{\partial x} = 0 \tag{2.32}$$

which is the kinematic wave equation and it is accomplished that

$$K = \frac{\Delta x}{c_K} = \frac{\Delta x}{dQ/dA} = \frac{\Delta x}{1/(\alpha\beta Q^{\beta-1})} \tag{2.33}$$

$$\chi = \frac{1}{2}(1 - \frac{Q}{Bc_K S_o \Delta x}) \tag{2.34}$$

where c_K is the celerity corresponding to Q and B, and B is the width of the water surface. The energy gradient can be estimated with the Manning equation, which satisfies (2.31),

$$Q = \frac{S_f^{1/2} A^{5/3}}{nP^{2/3}} \tag{2.35}$$

where n is the Manning roughness coefficient and P is the wetted perimeter of the cross section. The Manning equation together with the kinematic wave approximation can be shown to yield,

$$K = \frac{3}{5} T_R \tag{2.36}$$

where T_R is the travel time through the subbasin and it is calculated using the Témez formulation. Finally, to avoid instabilities in the computation iterations, it is required that $0 \leq \chi \leq 0.5$ ($\chi \approx 0.2$ in natural streams) and it must be imposed to the iteration time the following condition:

$$2K\chi \leq \Delta t \leq K \tag{2.37}$$

2.2.5 Modeling water-control facilities: Reservoir modeling

A reservoir or detention pond mitigates adverse impacts of excess water by holding that water and releasing it at a rate that will not cause damage downstream. The structure stores water temporarily and releases it, either through the outlet pipe or over the emergency spillway. Thus, it limits the release of water during a flood event and it provides a method of emptying the pond after the event so that the reservoir can store future runoff. Outflow can be computed with the level-pool routing model (or also known as Modified Puls routing model). Level-pool routing refers to flood routing for systems whose storage and outflow are related by a function of the type $S(t) = f[Q(t)]$ which is one-to-one (i.e. unique, non-hysteric). Such systems have a pool that is wide and deep compared to its length in the direction of the flow, low flow velocities, and horizontal water surfaces or negligible backwater effects (Ramírez, 2000).

The solution procedure involves rearranging the continuity equation (2.22) such that all unknown quantities are on the left hand side of the equation,

$$\frac{2S(t+1)}{\Delta t} + Q(t+1) = \Big[I(t+1) + I(t)\Big] + \Big[\frac{2S(t)}{\Delta t} - Q(t)\Big] \tag{2.38}$$

The values of $I(t)$ and $I(t+1)$ are the inflow hydrograph ordinates. The values of $Q(t)$ and $S(t)$ are known at the t^{th} time interval. At $t = 0$, these are the initial conditions, and at each subsequent interval, they are known from calculation in the previous interval. Therefore the quantity $[(2S(t+1)/\Delta t) + Q(t+1)]$ can be calculated with the latter equation. For an impoundment, storage and outflow are related, and with this storage-outflow relationship (figs. 2.17), the corresponding values of $Q(t+1)$ and $S(t+1)$ can be found. The computations can be repeated for successive intervals yielding the required outflow hydrograph ordinates (USACE-HEC, 2000).

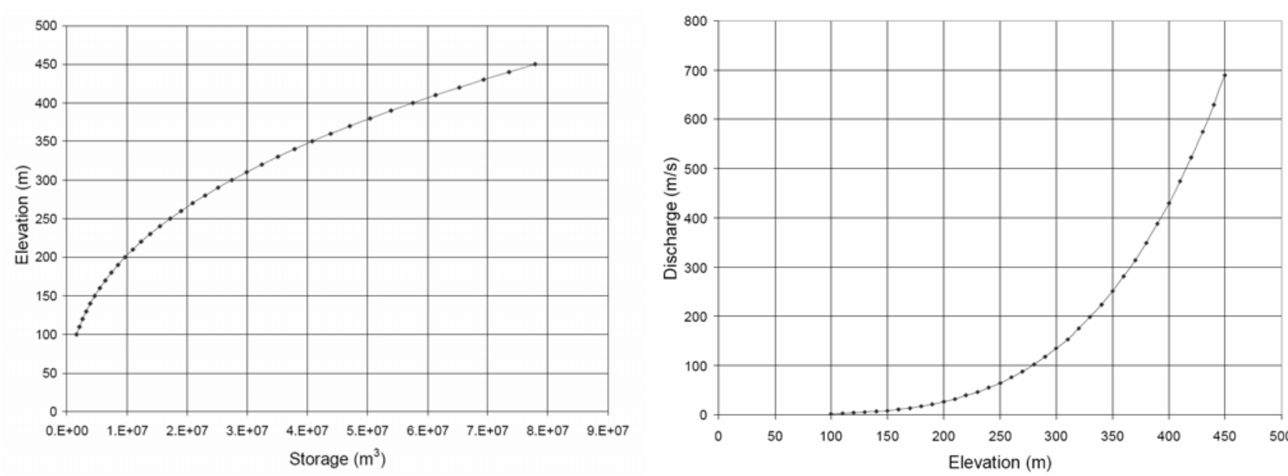

Figure 2.17: From left to right: storage versus elevation and elevation versus discharge relationships.

2.2.6 The calibration procedure

The last subsections have exposed some physical schemes used to model several hydrological processes at local scale in HEC-HMS. The values of the parameters involved in these physical schemes can be obtained from several theoretical frameworks, and various basin and channel properties. However, some of them cannot be easily estimated by observations or field measurements. Furthermore, the high spatial and temporal variability associated with the infiltration mechanism plays a fundamental role in the great uncertainties which arise in the setting of the rainfall-runoff model's initial conditions. This implies that in order to maximize the model performance, the model should be carefully optimized before any application is carried out. This optimization process is best conducted by using rainfall observations as boundary conditions to drive the model and comparing results with observed discharges. It is important to remark that the choice of the optimum model parameters is carried out on physically sound bases and it is designed to optimize the model representation of observed physical processes. This indeed increases both the model performance and its applicability to different studies.

Therefore, if rainfall and streamflow observations are available, a calibration task must be done. Calibration uses observed hydrometeorological data in a systematic search of parameters that yield the best fit of the computed results to the observed runoff in an optimization process. Once the initial best estimation of the parameters is selected, the physical schemes included in HEC-HMS can be used with the observed boundary conditions (rainfall and upstream flow) to compute the output and to compare the computed and observed hydrographs. If the model does not fit the real hydrologic system in a realistic way, the parameters can be adjusted using determined algorithms, running the simulation and applying some methods of comparison again. The process is reiterative until the fit is satisfactory and then HEC-HMS will have obtained the optimal parameter values (fig. 2.18).

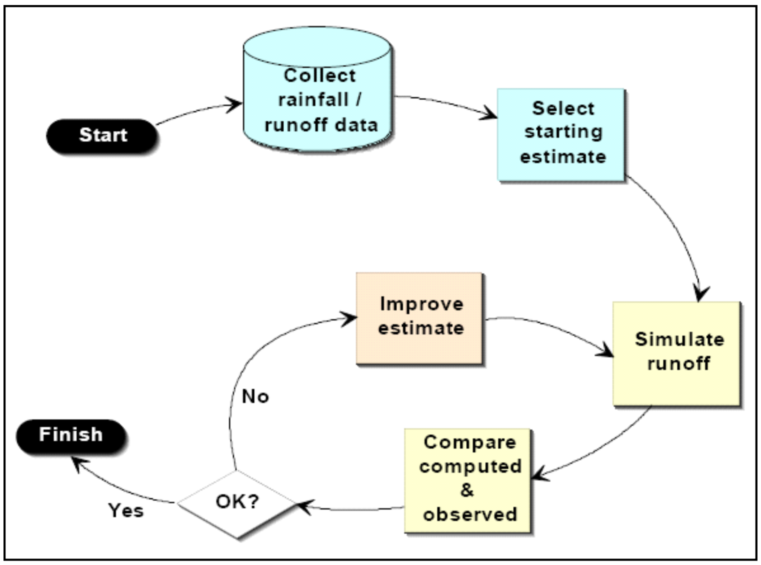

Figure 2.18: Schematic of calibration procedure.

Calibration of the different hydrologic parameters usually combines a manual procedure –when it is possible to derive them from field measurements–, and an automatic procedure. It has been used as an objective function the peak-weighted root mean square error and it has been applied the univariate-gradient search algorithm method (USACE-HEC, 2000). The objective function, Z, is an index of goodness-of-fit to compare the computed and the observed hydrograph and it is defined as:

$$Z = \sqrt{\frac{1}{NQ}\Big[\sum_{i=1}^{NQ}\Big(q_o(i) - q_s(i)\Big)^2\Big(\frac{q_o(i) + q_o(mean)}{2q_o(mean)}\Big)\Big]} \tag{2.39}$$

where NQ is the number of computed hydrograph ordinates; $q_o(i)$ the observed flow at time i; $q_s(i)$ the simulated flow at time i, computed with a selected set of model parameters; and $q_o(mean)$ the mean of observed flows. Mathematically, it corresponds to searching for parameters that minimize the value of the objective function. The search is a trial-and-error search.

Initial parameters are selected, the model is run and the errors are computed. If the error in not acceptable, the hydrological model changes the initial parameters and reiterates. The decisions about these changes rely on the univariate gradient search algorithm.

The univariate-gradient search algorithm makes successive corrections to the parameter estimate. That is, if x^k represents the parameter estimate with objective function $f(x^k)$ at iteration k, the search defines a new estimate x^{k+1} at iteration *k+1* as

$$x^{k+1} = x^k + \Delta x^k \text{ in which } \Delta x^k\text{= the correction to the parameter} \tag{2.40}$$

The goal of the search is to select Δx^k so the estimates move toward the parameter that yields the minimum value of the objective function. If the correction does not reach the minimum value, this equation is applied recursively. The gradient method is based upon Newton's method, which combined with (2.40) derive to

$$\Delta x^k = -\frac{df(x^k)/dx}{d^2 f(x^k)/dx^2} \tag{2.41}$$

The process continues until additional adjustments will not decrease the objective function by at least 1%.

2.3 Meteorological models

2.3.1 Description of the MM5 mesoscale model

The non-hydrostatic MM5 numerical model is used to perform the meteorological simulations. The obtained simulated rainfall fields are then used to drive in a one-way mode the hydrological model. MM5 is a high-resolution short-range weather forecast model developed by the Pennsylvania State University (PSU) and the National Center for Atmospheric Research (NCAR; Dudhia, 1993; Grell et al., 1995). The main characteristics of the model are briefly summarized:

(a) Vertical and horizontal grids

The mesoscale model processes the data on pressure surfaces and this information has to be interpolated to the vertical coordinate of the MM5. The dimensionless vertical coordinate (σ) is defined as

$$\sigma = \frac{p - p_t}{p_s - p_t} \tag{2.42}$$

where p is the pressure, p_t is a constant top pressure, p_s is the surface pressure and each model level is defined by a value of σ ($0 \leq \sigma \leq 1$). This vertical coordinate is a terrain following variable: the lower grid levels follow the terrain while the upper surface is flat (fig. 2.19). Thus, the model vertical resolution is defined by a list of values between 0 and 1 not necessarily even spaced, and commonly, the resolution in the boundary layer is much finer than above.

The horizontal grid has an Arakawa-Lamb B-staggering of the velocity variables with respect to the scalars (fig. 2.20). Therefore, the scalars are defined at the center of the grid square, while the eastward (u) and northward (v) velocity components are located at the corners. All the variables are defined in the middle of each model vertical layer referred to as half-levels. Vertical velocity is carried at the full levels including levels at 0 and 1.

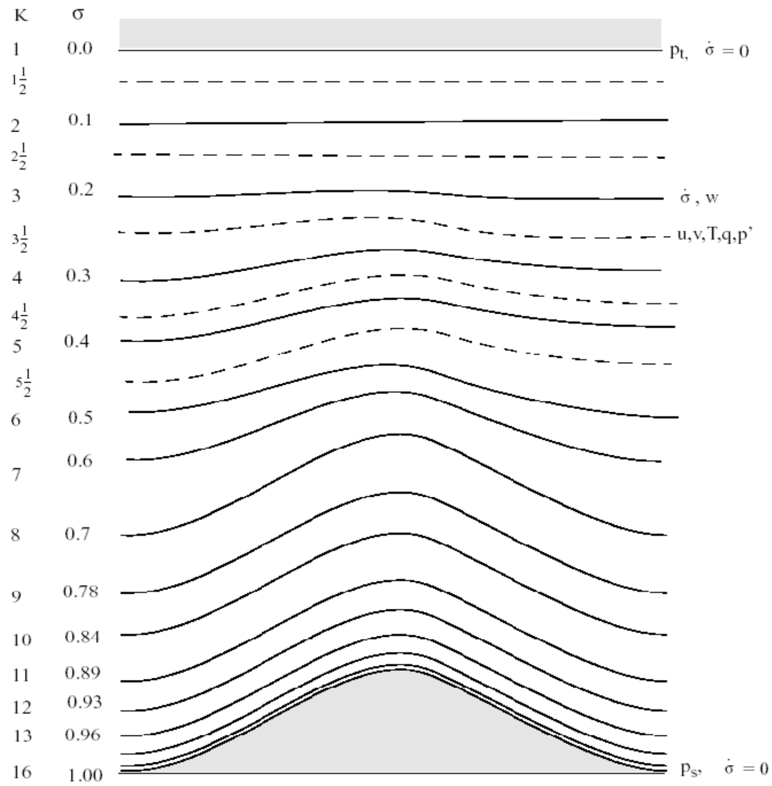

Figure 2.19: Schematic representation of the vertical structure of the model. The example is for 15 vertical layers. Dashed lines denote half-sigma levels, solid lines denote full-sigma levels.

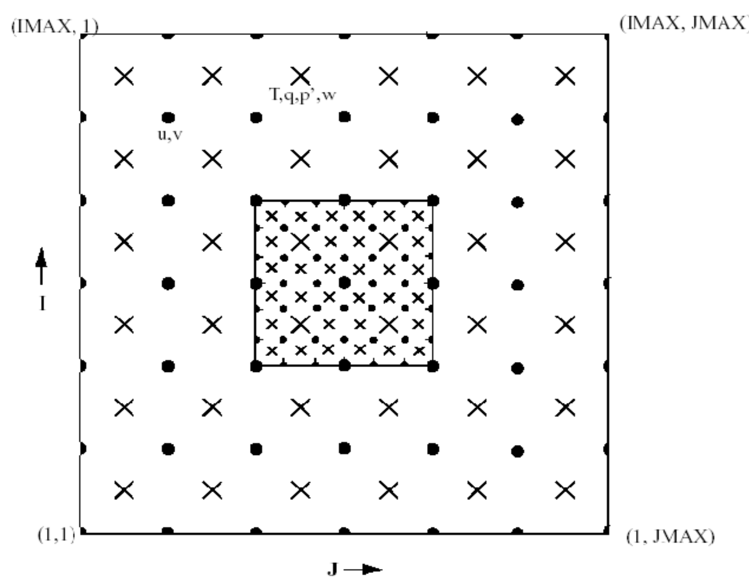

Figure 2.20: Schematic representation showing the horizontal Arakawa B-grid staggering of the dot and cross grid points. The smaller inner box is a representative mesh stagerring for a 3:1 coarse-grid distance to fine-grid distance ratio.

(b) Nesting capability

The MM5 model contains a capability of multiple nesting with several domains running at the same time and completely interacting (see fig. 2.21 as a possible configuration). Furthermore it permits a two-way interaction, thus the input data from a coarse to a fine domain come via its boundaries, while the feedback to the coarser mesh occurs over the interior nest. Each sub-domain has a 'mother domain' in which is completely embedded. There are three ways of doing a two-way nesting: (i) nest interpolation, where the nest is initialized by interpolating the coarse-mesh fields; (ii) nest analysis input, which permits the inclusion of high-resolution topography and initial analyses in the nest and (iii) nest terrain input, where the meteorological fields are interpolated from the coarse mesh and vertically adjusted to a new topography. It is also possible the one-way nesting in MM5. The model is run to create the output fields which are interpolated to the fine domain and an additional boundary field is also created once the one-way nested domain location is specified. Therefore the one-way nesting differs from the two-way nesting in having no feedback and a coarser temporal resolution at the boundaries.

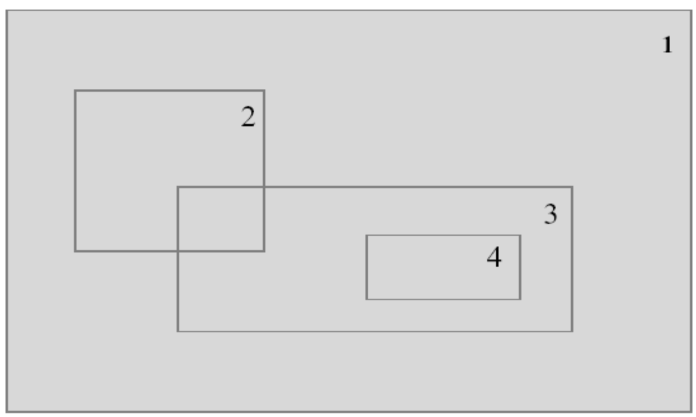

Figure 2.21: Example of a nesting configuration. The shading shows three different levels of nesting.

(c) Lateral boundary conditions

The regional numerical weather prediction models require lateral boundary conditions to run. In MM5 all lateral boundaries have specified horizontal winds, temperature, pressure and moisture fields and these can have specified microphysical fields (e.g clouds) whether are available. Before to running a simulation, the boundary conditions have to be set in addition to the initial values for these fields. The boundary values can come from Global Climate Models (GCMs) at different spatial and temporal resolutions. As an example, the NCEP and ECMWF centers issue these daily outputs at 1.125^0 - 0.5^0 and each 12 - 6 hours respectively and these can be used for weather prediction. Furthermore, the boundary and initial values can come from analyses which are generated from observations for a determined geographical region. The abovemetioned centers can also provide these analyses at different spatial and temporal resolutions. From the observations and by mean of various numerical interpolation methods it can be generated these tridimensional atmospheric fields in order to initialize the mesoscale model. The MM5 ingests these discrete-time analyses or forecasts by linearly interpolating them into its own time-step. Then, the analyses or forecasts completely specify the behaviour of the lateral boundaries of the domain. Very close to the edge domain, the model is nudged towards the boundary conditions and these are also smoothed, since the strength of this nudging decreases linearly away from the boundaries. The 2-way nest boundaries are similar but are updated every coarse-mesh time-step and have no relaxation zone.

(d) Non-hydrostatic dynamics

The mesoscale models are hydrostatic when the typical horizontal grid sizes are comparable with or greater than the vertical depth of features of interest. Then it is accomplished that

$$dp = -\rho_0 g dz \tag{2.43}$$

and when the hydrostatic approximation holds, the pressure is completely determined by the overlying mass of air. However, when the scale of resolved features in the model have aspect radios nearer unity, or when the horizontal scale becomes shorter than the vertical scale, non-hydrostatic dynamics must be considered.

The additional term in non-hydrostatic dynamics is the vertical acceleration that contributes to the vertical pressure gradient and the hydrostatic balance is no longer exact. Pressure perturbations from a reference state together with vertical momentum become extra three-dimensional predicted variables that have to be initialized.

(e) Reference state in the non-hydrostatic model

The reference state is an idealized temperature profile in hydrostatic equilibrium described by the equation:

$$T_0(p_0) = T_{s0} + Alog_e(\frac{p_0}{p_{00}}) \tag{2.44}$$

where T_0 is specified by the sea-level pressure, p_{00}, taken to be 10^5 Pa, the reference temperature T_{s0} at p_{00} and a measure of lapse rate, A, equal to 50 K and representing the temperature difference between p_0 and $p_0/e = 36788Pa$. T_{s0} needs to be selected based on a typical sounding in the domain.

The surface reference pressure, therefore, depends entirely upon the terrain height. Using (2.43) and (2.44),

$$Z = -\frac{RA}{2g}(ln\frac{p_0}{p_{00}})^2 - \frac{RT_{s0}}{g}(ln\frac{p_0}{p_{00}}) \tag{2.45}$$

that can be solved for p_0 given Z, the terrain elevation. The heights of the model, the σ levels, are found from

$$p_0 = p_{s0}\sigma + p_{top} \text{ where} \tag{2.46}$$

$$p_{s0} = p_0(\text{surface}) - p_{top} \tag{2.47}$$

and this expression is used to find Z from p_0.

(f) Land-use categories

The MM5 model has the option of three sets of land-use categorizations. These have 13, 16 or 24 categories (e.g. type of vegetation, desert, urban, water, ice,...). To each grid cell of the model is assigned one of the categories, and this determines surface properties such as albedo, roughness length, longwave emissivity, heat capacity and moisture availability. The values are also variable according to summer or winter season.

(g) Basic equations

The MM5 numerical model solves the following non-hydrostatic basic prognostic equations (moisture equation is omitted in this brief presentation). These are summarized in terms of terrain following coordinates (x, y, σ):

1. *Pressure tendency equation*

$$\frac{\partial p'}{\partial t} - \rho_0 g\omega + \gamma p \nabla \cdot \mathbf{V} = -\mathbf{V} \cdot \nabla p' + \frac{\gamma p}{T}(\frac{\dot{Q}}{c_p} + \frac{T_0 D_\theta}{\theta_0}) \tag{2.48}$$

   where p' is the non-hydrostatic perturbation of the hydrostatic pressure, p; ρ_0 is the density of the air; $\gamma = c_p/c_v$ where c_p is the calorific heat of the air at constant pressure and, c_v, at constant volume; $\dot{Q}$ the heat exchange with the environment; T_0 the temperature of the buoyancy term; θ_0 the reference potential temperature and D_θ the heat loss owing to friction and turbulence. This equation relates the temporal variations of the pressure with the rising and subsidence motions of the fluid, the pressure changes due to convergences or divergences, the pressure advection term and the variations of pressure by heat exchanges.

2. *Momentum equations*

$$\frac{\partial u}{\partial t} + \frac{m}{\rho}(\frac{\partial p'}{\partial x} - \frac{\sigma}{p^*}\frac{\partial p^*}{\partial x}\frac{\partial p'}{\partial \sigma}) = -\mathbf{V} \cdot \nabla u + v(f + u\frac{\partial m}{\partial y} - v\frac{\partial m}{\partial x}) - e\omega cos\alpha - \frac{u\omega}{r_{earth}} + D_u \tag{2.49}$$

   where the terms are referred to: the map-scale factor (m); $p^* = p_{surf} - p_{top}$; the Coriolis force terms (f, $e = 2\Omega cos\lambda$, $\alpha = \phi - \phi_c$ where λ is the latitude and ϕ, ϕ_c are the longitude and the central longitude); the curvature effect terms ($u\partial m/\partial y, v\partial m/\partial x, r_{earth}$); and D_u the heat losses term. The x-component momentum variations are related to the spatial variations of the pressure field, the advection of the x-component velocity, the effects owing to the curvature changes and the Coriolis force. The expressions for the y and z components follow as

$$\frac{\partial v}{\partial t} + \frac{m}{\rho}(\frac{\partial p'}{\partial y} - \frac{\sigma}{p^*}\frac{\partial p^*}{\partial y}\frac{\partial p'}{\partial \sigma}) = -\mathbf{V} \cdot \nabla v - u(f + u\frac{\partial m}{\partial y} - v\frac{\partial m}{\partial x}) + e\omega sin\alpha - \frac{v\omega}{r_{earth}} + D_v \tag{2.50}$$

$$\frac{\partial \omega}{\partial t} - \frac{\rho_0}{\rho}\frac{g}{p^*}\frac{\partial p'}{\partial \sigma} + \frac{g}{\gamma}\frac{p'}{p} = -\mathbf{V} \cdot \nabla \omega + g\frac{p_0}{p}\frac{T'}{T_0} - g\frac{R_d}{c_p}\frac{p'}{p} + e(ucos\alpha - vsin\alpha) + \frac{u^2 + v^2}{r_{earth}} + D_\omega \tag{2.51}$$

   where R_d is the universal constant of the dry air.

3. *Thermodynamic equation*

$$\frac{\partial T}{\partial t} = -\mathbf{V} \cdot \nabla T + \frac{1}{\rho c_p}(\frac{\partial p'}{\partial t} + \mathbf{V} \cdot \nabla p' - \rho_0 g \omega) + \frac{Q}{c_p} + \frac{T_0}{\theta_0} D_\theta \qquad (2.52)$$

where the temperature rate change is related to the termic advection and the variations of the temperature owing to dinamical effects, heat exchanges and heat losses.

(h) Cumulus parameterizations

Several schemes are available within the model to describe the moist convective effects (fig. 2.22). The MM5 group at NCAR center recommends the no inclusion of a cumulus parametrization at grid sizes less than 5-10 km. Next, these are briefly enumerated:

1. *Anthes-Kuo*: This scheme is based on moisture convergence and it is mostly applicable to large grid sizes (> 30 km). It tends to produce much convective rainfall, less resolved-scale precipitation, an specified heating profile and moistening depends upon relative humidity.

2. *Grell*: This parameterization is based on rate of destabilization or quasi-equilibrium. It is a single-cloud scheme with updraft and downdraft fluxes and it accounts for a compensating motion determining a heating/moistering profile. It is applicable to small grid sizes (10-30 km) and it tends to allow a balance between resolved scale and convective rainfall. It also considers the shear effects on precipitation efficiency (Grell et al., 1995).

3. *Arakawa-Schubert*: It is a multi-cloud scheme similar to the Grell one. It is based on cloud population that allows for entrainment into up- and downdrafts. It is suitable for large scales (> 30 km). The shear effects on precipitation efficiency are considered as well (Grell et al., 1995).

4. *Fritsch-Chappell*: It is based on a relaxation to a profile owing to up-, downdraft and subsidence region properties. The convective mass flux removes the 50% of the available buoyant energy in the relaxation time. It maintains a fixed entrainment rate. It is suitable for 20-30 km scales due to the single-cloud assumption and local subsidence. This scheme predicts both up- and downdraft properties and detrains cloud and precipitation, as well as, the shear effects on precipitation efficiency (Fritsch and Chappell, 1980).

5. *Kain-Fritsch* and *modified Kain-Fritsch*: This parameterization is similar to the previous one, but using a sophisticate cloud-mixing scheme to determine entrainment and detrainment, and removing all the available buoyant energy in the relaxation time. This scheme also predicts both up- and downdraft properties, detrains cloud and precipitation and accounts for the shear effects on precipitation efficiency as well (Kain and Fritsch, 1993). The modified Kain-Fritsch scheme is an improved version of Kain-Fritsch that includes shallow convection (Kain, 2004).

6. *Betts-Miller*: Based on a relaxation adjustment to a reference post-convective thermodynamic profile over a given period. The scheme is suitable for grid sizes large than 30 km. It does not account for explicit downdraft, and therefore, it may not be suitable for severe convection (Betts and Miller, 1986).

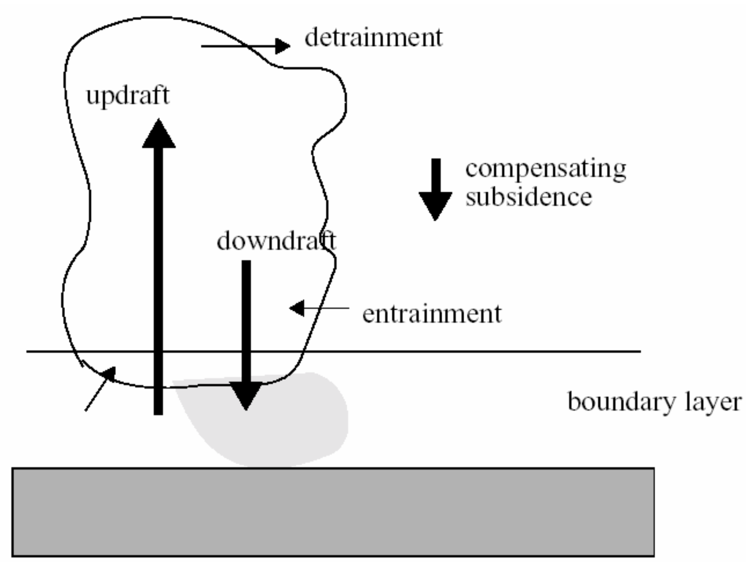

Figure 2.22: Illustration of the cumulus processes.

(i) Planetary Boundary Layer schemes

The Planetary Boundary Layer (PBL) physics can be formulated by using varied surface layer parameterizations (fig. 2.23). MM5 have available several formulations of these which are next summarized:

1. *Bulk*: This scheme is suitable for coarse vertical resolution in the boundary layer vertical grid sizes (> 250 m). It considers two stability regimes.

2. *Blackadar*: This parameterization is suitable for high-resolution PBL (e.g. 5 layers in lowest km, surface layer < 100 m thick). It considers four stability regimes including a free convective mixed layer. Furthermore, it uses split time-steps for stability.

3. *Burk-Thompson*: It is a scheme suitable for coarse and high-resolution PBL. It predicts turbulent kinetic energy (TKE) for use in vertical mixing based on Mellor-Yamada formulas (Burk and Thompson, 1989) and has its own force-restore ground temperature prediction.

4. *Eta*: This is the Mellor-Yamada scheme as used in the Eta model (Janjic, 1990 and 1994). It predicts TKE and has vertical local mixing. This scheme uses the land surface models (SLABs) available in MM5 for calculating the surface temperature (Grell, 1994). Before using SLABs, it calculates exchange coeffcients using similarity theory, and after using SLABs, it calculates the vertical fluxes with an implicit diffusion parameterization.

5. *MRF*: This parameterization is also known as the Hong-Pan scheme and it is suitable for high-resolution discretizations in the PBL. It has an efficient scheme based on Troen-Mahrt representation of the countergradient term and the K profile in the well mixed PBL (Hong and Pan, 1996). The scheme also uses the SLABs models and the vertical diffusion has an implicit scheme to allow longer time-steps.

6. *Gayno-Seaman*: Based on Mellor-Yamada TKE prediction equations as well. It is distinguished from the other schemes by the use of a liquid-water potential temperature as a conserved variable. This fact allows the PBL to operate more accurately in saturated conditions (Ballard et al., 1991; Shafran et al., 2000).

7. *Pleim-Chang*: This PBL scheme is a derivative of the Blackadar parameterization called the Asymmetric Convective Model (Pleim and Chang, 1992) and it employs a variation of the Blackadar's non-local vertical mixing.

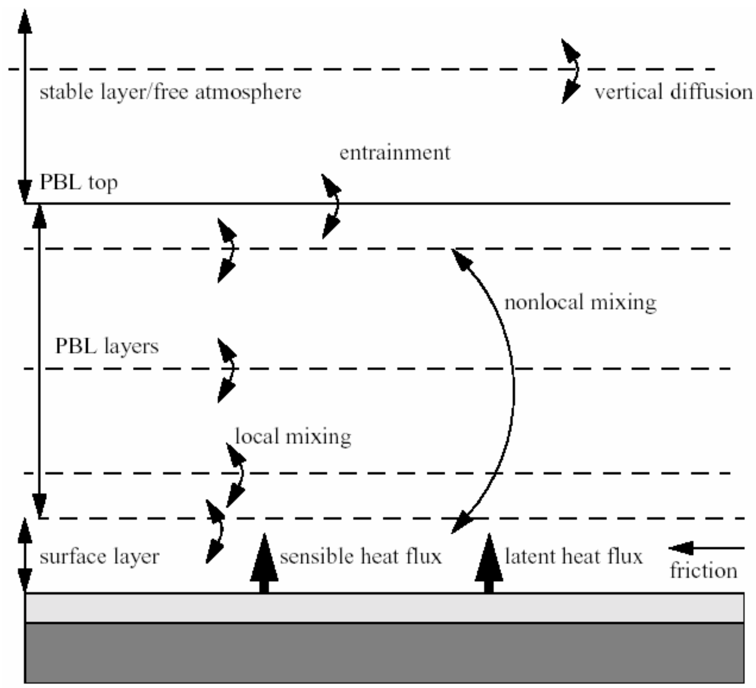

Figure 2.23: Illustration of the PBL processes.

(j) Explicit moisture schemes

The explicit microphysics are represented in MM5 with varied prediction equations for cloud and rainwater fields, cloud ice and snow in all the numerical domains used for the simulations or forecasts (fig. 2.24). Obviously, a dry explicit moisture scheme would correspond to no moisture prediction and no water vapor. Next, the rest of the parameterizations are briefly enumerated:

1. *Stable precipitation*: It represents no convective precipitation. The large-scale saturation are removed and rained out immediately. It does not account for rain evaporation or explicit cloud prediction.

2. *Warm rain*: The cloud and rain water fields are predicted explicitly with microphysical processes, but it does not consider ice phase processes.

3. *Simple ice (Dudhia)*: This scheme adds ice phase processes to the previous scheme, but no considers supercooled water and the snow is immediately melted below the freezing level.

4. *Mixed-phase (Reisner 1)*: The parameterization adds supercooled water to the Dudhia scheme. Furthermore, it allows for slow melting of the snow. It does not take into account graupel or riming processes (Reisner et al., 1998).

5. *Goddard microphysics*: It includes an additional equation for the prediction of graupel and includes graupel and hail properties. It is suitable for cloud-resolving models (Lin et al., 1983; Tao et al., 1989 and 1993)

6. *Reisner graupel (Reisner 2)*: Based on a mixed-phase scheme but including the graupel and ice number concentration prediction equations. It is also suitable for cloud-resolving models.

7. *Schultz microphysics*: This is a highly efficient and simplified scheme and contains ice and graupel/hail processes. It has been designed for running fast and it can be easily tuned for real-time forecast systems (Schultz, 1995).

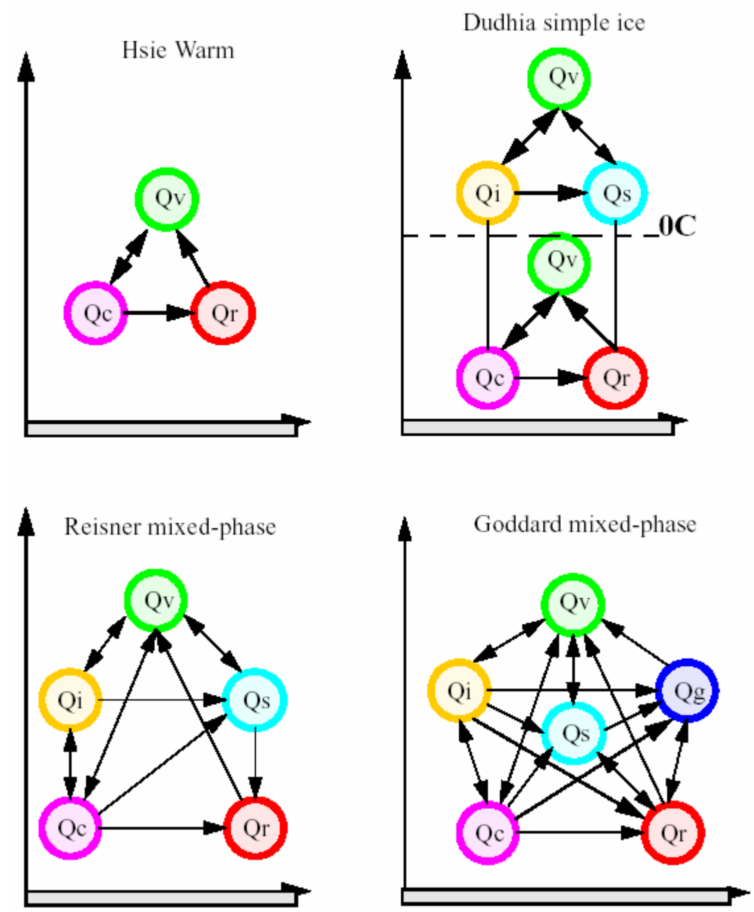

Figure 2.24: Illustration of the microphysics processes.

In addition to the aforementioned physical options, the meteorological model also accounts for radiation and surface schemes. The *radiation schemes* parameterize such processes as: the reflection and absorption of long- and shortwave radiation by the clouds; the atmospheric scattering and absorption; and the surface emissivity and albedo (fig. 2.25). The available radiation schemes are: (i) Surface radiation, (ii) Surface radiation and simple cooling, (iii) Cloud-radiation scheme, (iv) CCM2 radiation scheme and (v) RRTM longwave scheme (PSU/NCAR Mesoscale Modeling System, 2005). The *surface parameterizations* account for the interaction between the atmosphere and the land-surface and outline processes such as: the sensible and latent heat exchanges; the net long- and shortwave exchanges; evaporation processes and the snow cover; and absorption processes, ground fluxes and soil diffusion among different soil layers (fig. 2.26). The available surface schemes are: (i) Fixed surface temperature, (ii) Blackadar scheme, (iii) Five-layer soil model, (iv) NOAH land-surface model, (v) Pleim-Xiu land-surface model, (vi) Bucket soil moisture model, (vii) Snow cover model and (viii) Polar mods (PSU/NCAR Mesoscale Modeling System, 2005). Figure 2.27 shows the direct interactions among all the abovementioned parameterizations.

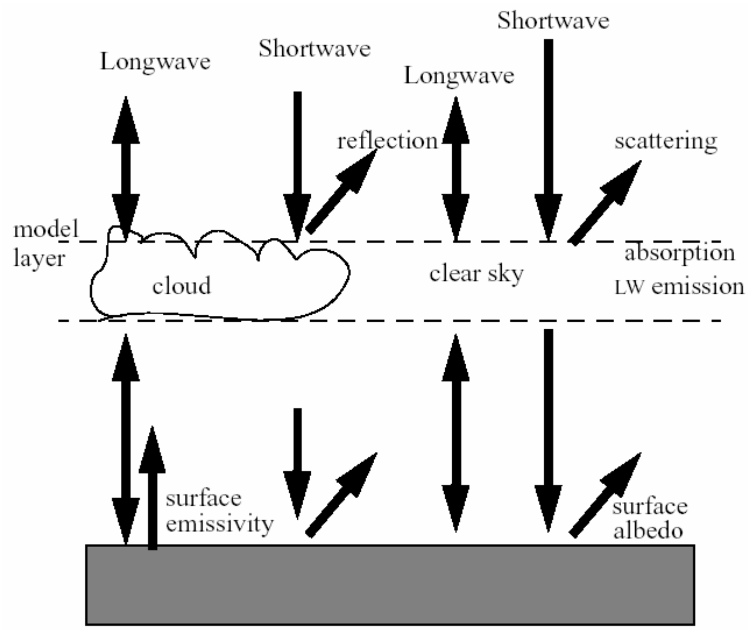

Figure 2.25: Illustration of the radiation processes.

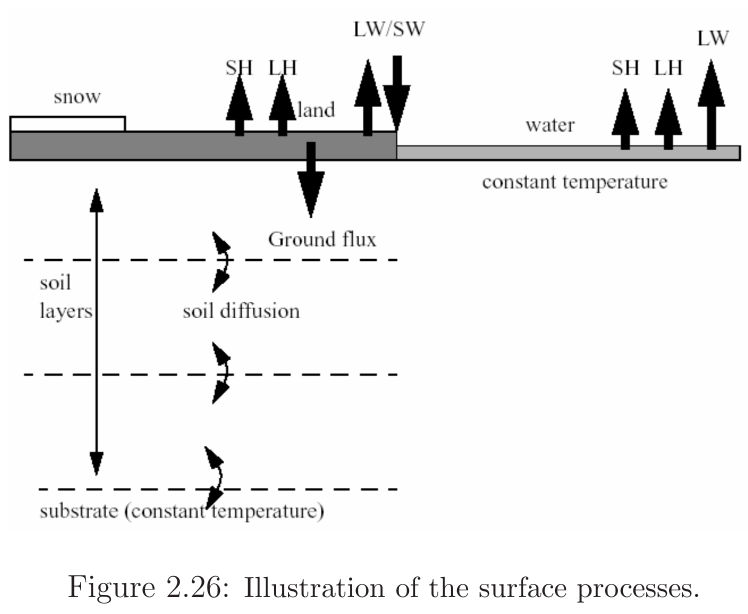

Figure 2.26: Illustration of the surface processes.

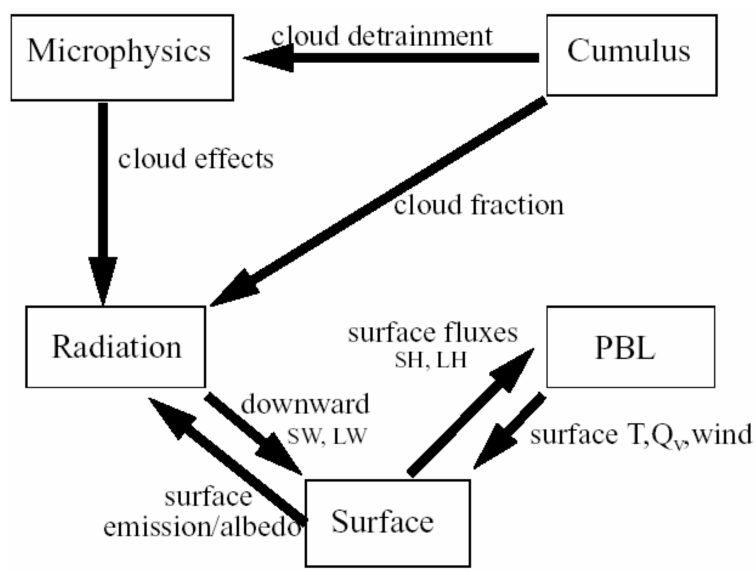

Figure 2.27: Direct interactions of the parameterizations.

2.3.2 The piecewise Potential Vorticity (PV) Inversion tool

External-scale uncertainties are found in the hydrometeorological chain owing to uncertainties in the simulated meteorological fields. In order to study these errors, a very useful methodology has arisen in recent years by applying the PV inversion scheme. This methodology has been widely explained in Romero (2001) and Romero et al. (2005) and, next, it is shortly presented. It allows to study the sensitivity of the mesoscale simulations to changes in the upper-level precursor trough. It requires the calculation of a balanced flow associated with the trough-related PV anomaly at simulation start time. The piecewise PV inversion technique of Davis and Emmanuel (1991) is used for this purpose: it starts with the calculation of the total balance flow –described by the geopotential (ϕ) and the streamfunction (ψ)– from the instantaneous distribution of Ertel's potential vorticity (q). This is defined as:

$$q = \frac{1}{\rho}\boldsymbol{\eta} \cdot \boldsymbol{\nabla}\theta \tag{2.53}$$

where ρ is the density, η is the absolute vorticity vector and θ is the potential temperature. The balance assumption made herein follows the Charney (1955) non-linear balance equation:

$$\nabla^2\phi = \boldsymbol{\nabla} \cdot f\boldsymbol{\nabla}\psi + 2m^2\left[\frac{\partial^2\psi}{\partial x^2}\frac{\partial^2\psi}{\partial y^2} - \left(\frac{\partial^2\psi}{\partial x\partial y}\right)^2\right] \tag{2.54}$$

where f is the Coriolis parameter and m is the map-scale factor of the Lambert conformal projection (x, y) used to define the MM5 model domain. The other diagnostic relation necessary for the inversion of ϕ and ψ is given by the approximate form of Eq. 2.53 resulting from the hydrostatic condition and the same scale analysis used to derive Eq. 2.54, namely, that the irrotational component of the wind is negligible against the non-divergent wind:

$$q = \frac{g\kappa\pi}{p}\left[(f + m^2\nabla^2\psi)\frac{\partial^2\phi}{\partial\pi^2} - m^2\left(\frac{\partial^2\psi}{\partial x\partial\pi}\frac{\partial^2\phi}{\partial x\partial\pi} + \frac{\partial^2\psi}{\partial y\partial\pi}\frac{\partial^2\phi}{\partial y\partial\pi}\right)\right] \tag{2.55}$$

where p is the pressure, g is the gravity, $\kappa = R_d/C_p$ and the vertical coordinate π is the Exner function $C_p(p/p_0)^\kappa$.

Given q, the finite-difference form of the closed system described by Eqs. 2.54 and 2.55 is solved for the unknowns ϕ and ψ, using an iterative technique until convergence of the solutions is reached (see Davis and Emanuel, 1991 for further details). Neumann type boundary conditions ($\partial\phi/\partial\pi = f\partial\psi/\partial\pi = -\theta$) are applied at the top and bottom boundaries, and Dirichlet conditions at the lateral boundaries. The latter are supplied by the observed geopotential and a streamfunction calculated by matching its gradient along the edge of each isobaric surface to the observed normal wind component, which is first slightly modified to force no net divergence in the domain. Owing to the balance condition used, the inverted fields are very accurate even for meteorological systems characterized by large Rossby numbers (Davis and Emanuel, 1991; Davis, 1992).

Later, a reference state must be found from which to define the PV anomalies. As in Davis and Emanuel (1991), this reference state is defined as a time average. Given $\bar{q}$ (the time mean of q), a balanced mean flow ($\bar{\phi}, \bar{\psi}$) is inverted from identical equations to (2.54) and (2.55), except all dependent variables are mean values and the mean potential temperature, $\bar{\theta}$, is used for the top and bottom boundary conditions. The total fields will differ from the time averages by the perturbations (q', ϕ', ψ'):

$$(q, \phi, \psi) = (\bar{q}, \bar{\phi}, \bar{\psi}) + (q', \phi', \psi') \tag{2.56}$$

The PV perturbation field, q', can be considered as a partition of N portions or anomalies,

$$q' = \sum_{n=1}^{N} q_n \tag{2.57}$$

The piecewise inverse scheme determines that part of the balance flow (ϕ_n, ψ_n) associated to each PV portion, q_n, requiring in that process that,

$$\phi' = \sum_{n=1}^{N} \phi_n \text{ and } \psi' = \sum_{n=1}^{N} \psi_n \tag{2.58}$$

As discussed in Davis (1992), there is no a unique way to define a relationship between (ϕ_n, ψ_n) and q_n owing to the non-linearities present in Eqs. (2.54) and (2.55). The linear method of Davis and Emanuel (1991) is here adopted, and it is derived after replacing the expression Eq. (2.56) and the above summations in Eqs. 2.54 and 2.55 and equal partitioning of the non-linear term among the other two linear terms that result from each non-linearity in the above equations (see Davis and Emanuel, 1991 for more details). The resulting closed linear system for the n^{th} perturbation is:

$$\nabla^2\phi_n = \boldsymbol{\nabla} \cdot f \boldsymbol{\nabla} \psi_n + 2m^2 \left(\frac{\partial^2 \psi^*}{\partial x^2} \frac{\partial^2 \psi_n}{\partial y^2} + \frac{\partial^2 \psi^*}{\partial y^2} \frac{\partial^2 \psi_n}{\partial x^2} - 2 \frac{\partial^2 \psi^*}{\partial x \partial y} \frac{\partial^2 \psi_n}{\partial y \partial x} \right) \tag{2.59}$$

$$\begin{aligned} q_n \;=\; & \frac{g\kappa\pi}{p} \left[(f + m^2 \nabla^2 \psi^*) \frac{\partial^2 \phi_n}{\partial \pi^2} + m^2 \frac{\partial^2 \phi^*}{\partial \pi^2} \nabla^2 \psi_n \right. \\ & \left. - m^2 \left(\frac{\partial^2 \phi^*}{\partial x \partial \pi} \frac{\partial^2 \psi_n}{\partial x \partial \pi} + \frac{\partial^2 \phi^*}{\partial y \partial \pi} \frac{\partial^2 \psi_n}{\partial y \partial \pi} \right) - m^2 \left(\frac{\partial^2 \psi^*}{\partial x \partial \pi} \frac{\partial^2 \phi_n}{\partial x \partial \pi} + \frac{\partial^2 \psi^*}{\partial y \partial \pi} \frac{\partial^2 \phi_n}{\partial y \partial \pi} \right) \right] \end{aligned} \tag{2.60}$$

where $()^* = \overline{()} + \frac{1}{2}()'$.

Concretely for the June 2000 flash-flood event over Catalonia, the system (2.59)-(2.60) is solved for the PV anomaly identified above $500hPa$ in relation with the upper-level synoptic trough governing the flash-flood, using homogeneous boundary conditions for θ_n and ψ_n at the top, bottom and lateral boundaries. The shape of the positive PV anomaly on the $330K$ isentropic surface is displayed in Fig. 3.8. The balance flow (θ_n, ψ_n) associated with the anomaly can then be used to alter the model initial conditions without introducing any significant unbalance to the fields. Furthermore, the PV inversion technique attributes components of the mass and wind fields to structures of the PV field. This fact allows to explore the impact of the PV features in the initial conditions on the evolution of the numerical simulations.

2.3.3 Description of the HIRLAM mesoscale model

The hydrostatic HIgh Resolution Limited Area numerical Model (HIRLAM) is used to perform the mesoscale numerical simulations of rainfall for Mediterranean Spain from large-scale model input data resolution, to help answer the question of whether higher resolution GCM output would provide improved dynamically downscaled information over that region in the context of climate change research. HIRLAM was developed within a co-operative project among several European meteorological institutes (Källén, 1996), and it is used operationally at the Spanish Institute of Meteorology (INM). HIRLAM is designed to simulate synoptic and α-mesoscale atmospheric phenomena, whereas the smaller scales effects are included through parameterizations. Next, the main characteristics of the hydrostatic model are briefly summarized:

(a) Vertical and horizontal grids

The model equations are formulated on a geographically oriented (lat-lon) horizontal mesh with a σ-p hybrid vertical coordinate (η). The η is a terrain-following coordinate at the lower levels that gradually reduces with height to pressure coordinate at the top of the model:

$$\eta = h(p, p_s) \;\text{ with }\; h(0, p_s) = 0 \;\text{ and }\; h(p_s, p_s) = 1 \tag{2.61}$$

where p is pressure, p_s is surface pressure and h is a monotonic function of pressure. A spherical-like coordinates are used in the horizontal. The model equations are thus expressed in spherical coordinates without the need of introducing any geographical projection.

(b) Model equations

The model equations are obtained by expressing the basic prognostic equations in the HIRLAM coordinate system:

1. *Continuity equation*

   $$-\frac{d\ln(\partial p/\partial\eta)}{dt} = \nabla_\eta \cdot \mathbf{V} + \frac{\partial\dot{\eta}}{\partial\eta} \tag{2.62}$$

   from this equation and integrating vertically, the pressure vertical velocity can be obtained as:

   $$\omega(\eta) = \frac{\partial p_s}{\partial t} + \int_{\eta'}^{1} \nabla_\eta \cdot (\mathbf{V}\frac{\partial p}{\partial\eta'})d\eta + \mathbf{V}\cdot\nabla p \tag{2.63}$$

   where ω is the pressure vertical velocity, $\mathbf{V}$ is the two-dimensional wind vector and $\dot{\eta}$ is the vertical coordinate velocity.

2. *Momentum equation*

$$\frac{du}{dt} = -\frac{R_d T_v}{a\cos\theta}\frac{\partial \ln p}{\partial \lambda} - \frac{\partial\phi/\partial\lambda}{a\cos\theta} + fv + \frac{uv\tan\phi}{a} + P_u + K_u \tag{2.64}$$

$$\frac{dv}{dt} = -\frac{R_d T_v}{a}\frac{\partial \ln p}{\partial \theta} - \frac{\partial\phi/\partial\theta}{a} - fu + \frac{u^2\tan\phi}{a} + P_v + K_v \tag{2.65}$$

which are the horizontal components in η coordinates. u and v are the zonal and meridional components of the wind, R_d is the gas constant for moist air, T_v is the virtual temperature, a is the Earth mean radius, λ and θ are the longitude and latitude, ϕ is the geopotential, $f = 2\Omega\sin\theta$ is the Coriolis parameter where Ω is the angular velocity of the Earth, P_u are the parameterization terms, and K_u are the diffusive terms.

The vertical component is simplified by neglecting vertical displacements yielding the hydrostatic equation:

$$\frac{\partial\phi}{\partial\eta} = -\frac{R_d T_v}{p}\frac{\partial p}{\partial\eta} \tag{2.66}$$

3. *Temperature equation*

$$\frac{dT}{dt} = \frac{\kappa T_v \omega}{(1+(\delta-1)q)p} + P_T + K_T \tag{2.67}$$

which is obtained by accounting for the water vapor content of the air in the specific heat of moist air at constant pressure (c_p) and assuming the moist ideal gas state equation. T is the temperature, $\kappa = R_d/c_{pd}$ where c_{pd} is the specific heat of dry air at constant pressure, $\delta = c_p/c_{pd}$, and q is the specific humidity.

(c) Discretization and integration schemes

The discrete set of η levels used in HIRLAM are defined as:

$$p_k(x, y, \eta) = A_k(\eta) + B_k(\eta)p_s(x, y) \tag{2.68}$$

where A and B are parameters chosen to distribute in a suitable way the vertical η levels along the vertical domain, with higher density at low levels.

The differential nature of the aforementioned conservation relations motivates the vertical staggering of the model layers, thus increasing the effective resolution by a factor of two (Pielke, 1984). In particular, vertical coordinate (η), vertical velocity ($\dot{\eta}$) and pressure are defined over half levels, located between the full levels, in which winds and thermodynamic quantities are prognosticated (u, v, T, q and m -the cloud water-). In the horizontal, an Arakawa-C staggered grid (Arakawa and Lamb, 1977) is used in HIRLAM (fig. 2.28).

Time discretization is performed by using an Eulerian semi-implicit time integration scheme in HIRLAM (Simmons and Burridge, 1981). The Eulerian approach to the temporal evolution considers the evolution of the fluid from fixed points in the space, on which the physical variables are considered. The semi-implicit algorithm integrates the linear terms of the model equations using an implicit method, although the non-linear terms are integrated explicitly.

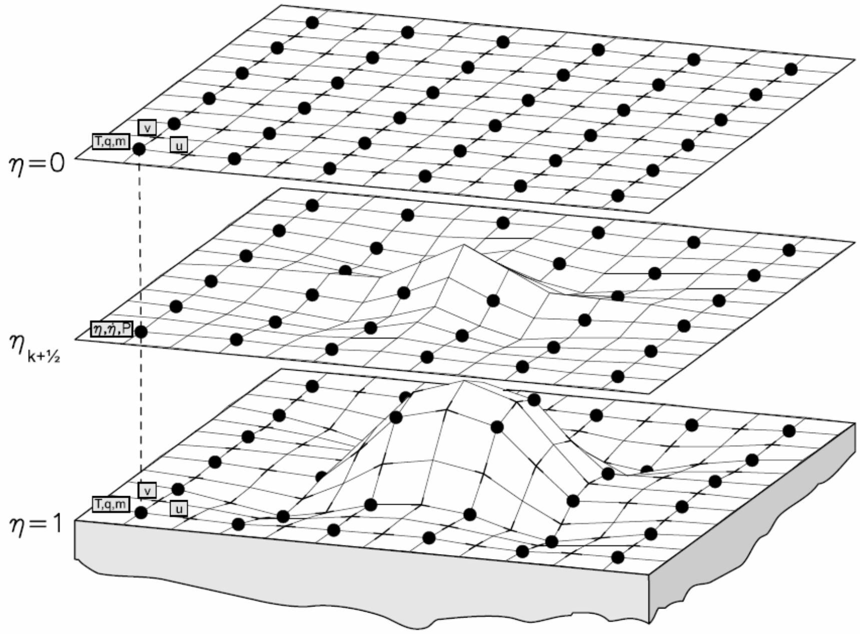

Figure 2.28: Schematic view of the HIRLAM grid (extracted from Homar, 2001). Arakawa-C staggered grid is used in the horizontal, whereas a vertical staggering is also used for the η, $\dot{\eta}$ and p variables.

(d) Physical parameterizations

1. *Condensation and precipitation schemes*: The convective effects on the scales solved by HIRLAM are parameterized by the Sundqvist scheme (Sundqvist et al., 1989) which is based on modifications of the Kuo scheme. This last scheme (Kuo, 1974) is modified by including the water vapor as a resolved and forecasted field, the definition of moisture accesion, and the efficiency of the environmental humidity to condense (Raymond and Emmanuel, 1993). The Sundqvist scheme includes microphysical processes which are used in both, the convection and stratiform parameterizations.

2. *Microphysical scheme*: Microphysics are treated separately from the convective and stratiform parameterizations. This fact allows its application in both regimes using different parameters. The main purpose of the microphysics formulation is to complete the aforementioned schemes by obtaining realistic precipitation fields with a correct mass-energy balance by using the cloud water and cover deduced from the large scale convection and stratiform processes.

3. *Radiation scheme*: In HIRLAM, the aim of the radiative parameterization scheme is to create a net radiative flux profile and add it to the physical parameterization term of the temperature equation (P_T in Eq. 2.67). The Savijärvi scheme is the radiation parameterization used in HIRLAM (Savijärvi, 1990) and distinguishes between short- and longwave radiation contributions to the temperature equation. The shortwave radiation accounts for the absorption by the clear and cloudy air of the radiation, whereas the longwave radiation is due to the thermal radiation emited by the Earth and the atmosphere itself.

This radiation scheme also accounts for the ground energy flux due to longwave which is used in the surface scheme.

4. *Soil processes*: The soil and surface parameterization calculates the surface temperature and humidity which govern the ground properties and its interaction with the atmosphere. The scheme implemented in HIRLAM follows the mosaic approach (Avisssar and Pielke, 1989). This approach considers the fractional composition of each grid square in five surface types: water, ice, bare land, forest and agricultural terrain. The scheme couples, in an independent way, each land-use patch of the grid element to the atmosphere, and the patches interact among them only through the atmosphere. A monthly constant climatic value of the surface temperature is considered over sea water. A simple one-dimensional three-layer diffusive model with constant heat capacity and diffusivity is applied over the areas covered by ice. For the land-surface types, a scheme based on the 2-level Noilhan and Planton (1989) parameterization is used. This scheme solves the soil temperature and the soil water variations over land by using a force-restore model (Blackadar, 1976).

5. *Vertical difussion*: The turbulent motions are sub-grid scale motions and they are essential in the energy budget calculation in the atmosphere. The vertical turbulent fluxes are determinant for the total energy fluxes of energy, since the resolved scales vertical motions are not considered to calculate the vertical transport of momentum, heat and humidity. In HIRLAM, the CBR turbulent scheme is used (Cuxart et al., 2000). The CBR is a diffusive scheme that computes the turbulent kinetic energy (TKE) as a prognostic variable and considers as difussed variables the u, v, potential temperature (θ) and specific humidity (q).

Chapter 3

THE JUNE 2000 FLASH-FLOOD EVENT OVER CATALONIA, SPAIN

3.1 Introduction

In this chapter[1], we study the 10 June 2000 episode presented in subsection 1.3.1. First, it is described the characterization of the Llobregat watershed hydrological response to this flash-flood event based on rain-gauge data and HEC-HMS runoff model. The HEC-HMS model has been calibrated using five episodes of similar torrential characteristics, and the effects of the spatial segmentation of the basin and of the temporal scale of the input rainfall field have been examined.

These kind of episodes present short recurrence intervals in Mediterranean Spain and the use of mesoscale forecast driven runoff simulation systems for increasing the lead times of the emergency management procedures is a valuable issue to explore. Therefore, we have used NCEP and ECMWF analyses to initialize the MM5 non-hydrostatic mesoscale model in order to simulate the 10 June 2000 flash-flood episode with appropriate space and time scales to force the runoff model. We have also analysed the sensitivity of the catchment's response to the spatial and temporal uncertainty of the rainfall pattern based on an ensemble of perturbed MM5 simulations. MM5 perturbations are introduced through small shifts and changes in intensity of the precursor upper-level synoptic scale trough.

In section 3.2, we present a brief description of the Llobregat basin and the observational network available for this study. Section 3.3 describes the flash-flood event. Sections 3.4 and 3.5 present the hydrological and meteorological tools used, respectively. The study and main results of this episode are presented in section 3.6. Finally, section 3.7 contains the conclusions.

[1]The content of this chapter is based on the paper Amengual, A., R. Romero, M. Gómez, A. Martín and S. Alonso, 2007: A hydrometeorological modeling study of a flash-flood event over Catalonia, Spain., *J. Hydrometeor.*, **8**, 282-303.

3.2 The study area

3.2.1 Overview of the Llobregat basin

The Llobregat basin is the most important of the internal hydrographic catchments in Catalonia (fig. 1.5) in terms of size, river length, mean flow and population living inside. It is composed of the Llobregat river and its main tributaries, the Anoia and the Cardener. Llobregat basin extends from the Pyrenees, with heights over 3000 meters, through the Pre-Pyrenees, constituted by a band of folded mesozoic materials, and crossing the central depression, formed by tertiary materials more or less eroded, with a height transition from 750 meters in the Pre-Pyrenees to 200 meters in the pre-coastal range. The last section of the river crosses the Mediterranean orographic systems, formed by two mountainous alignments almost parallel to the coast line: the pre-coastal range formed by varied morphological mounts (e.g. Montseny (1712 m), Montserrat (1236 m) and Serra del Cardó (942 m)) and the coastal range, consisting of small altitude mountains (e.g. Montnegre (759 m), Collserola (512 m) and Garraf (660 m)) (fig. 3.1). The basin has a drainage area of 5040 km^2 and a maximum length close to 170 km.

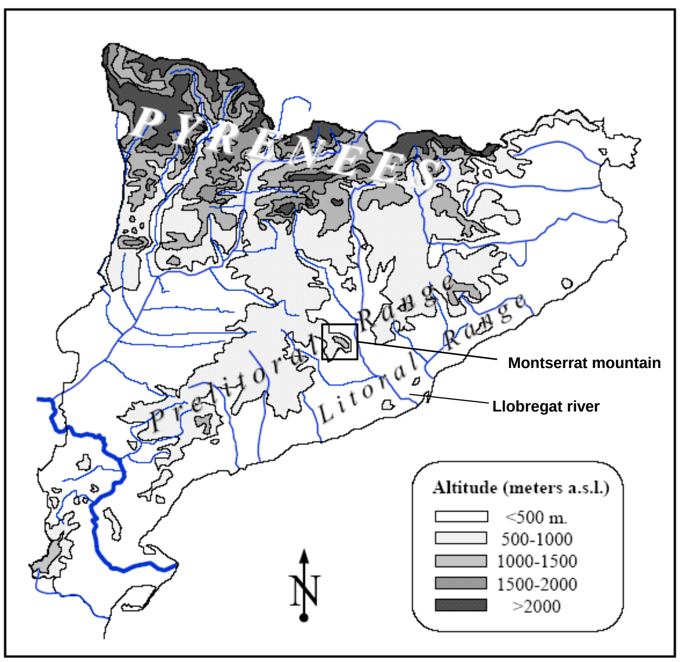

Figure 3.1: The Catalan topography with a depiction of the main mountainous systems and rivers (Montserrat mountain and Llobregat river are indicated. Extracted from Llasat et al., 2003)

Furthermore, the hydrographic catchment is divided into a wide range of climatic areas owing to the diversity of the pluviometric records depending on the altitude. Annual accumulated rainfall in the Llobregat basin can range from quantities exceeding 1000 mm in the Pyrenees (over 1000 meters), 700 mm over Pre-Pyrenees (with elevations comprised between 600-1000 meters) and 500 mm for altitudes below 500 meters. The rainfall regime is typical of the mediterranean areas, with most of heavy rainfall episodes occuring mainly in autumn, with occassional episodes in the spring and the summer. These daily rainfall episodes can represent a large fraction of the annual amounts.

3.2.2 The rain and stream gauge networks

On 10 June 2000, heavy rainfall took place over the northeastern part of Spain and the most intense episode affected the whole of the Internal Basins of Catalonia (IBC; fig. 1.5). The analysis of the pluviometric evolution of the episode used 5-minute rainfall data recorded at 126 stations inside the IBC and distributed over an area of 16000 km^2 (fig. 3.2). These stations belong to the Automatic Hydrological Information System (SAIH) network of the Catalan Agency of Water (ACA). Out of the 126 stations, about 40-50 lie inside the Llobregat basin or near its boundaries.

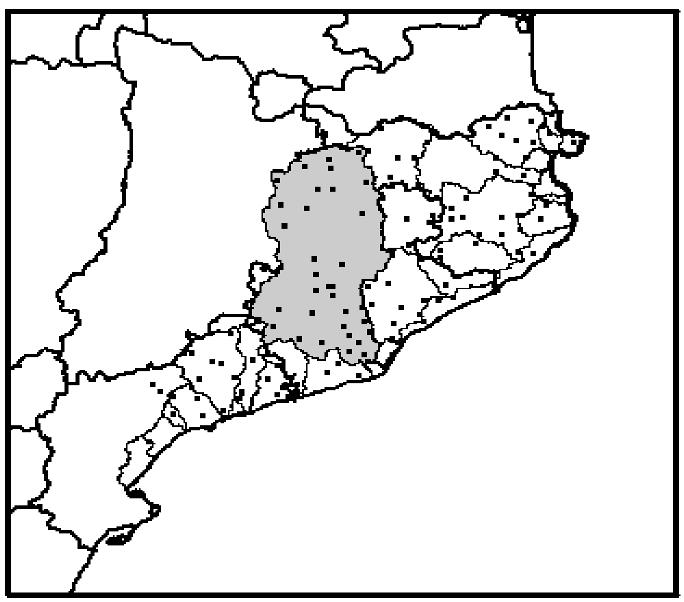

Figure 3.2: Distribution of the rain-gauges from the Automatic Hydrological Information System (SAIH) in the IBC. It includes a total of 126 automatic rainfall stations distributed over an area of 16000 km^2 (Llobregat basin is enhanced).

Runoff in the Llobregat basin was recorded in five flow gauges (fig. 3.3) located in: (i) Súria town, on the Cardener river, with a dranaige area of 940 km^2 and elevation from 250 m at gauge level to 2350 m in the Pyrenees; (ii) Sant Sadurní d'Anoia city, on the Anoia river, with a drainage area of 736 km^2 and elevations from 125 m at gauge level to 850 m at headwater; and (iii) Castellbell (3340 km^2), (iv) Abrera (3587 km^2) and (v) Sant Joan Despí (4915 km^2) towns along the Llobregat river. During the episode, 5-minute runoff measurements were collected, jointly with the rainfall records, for the SAIH database.

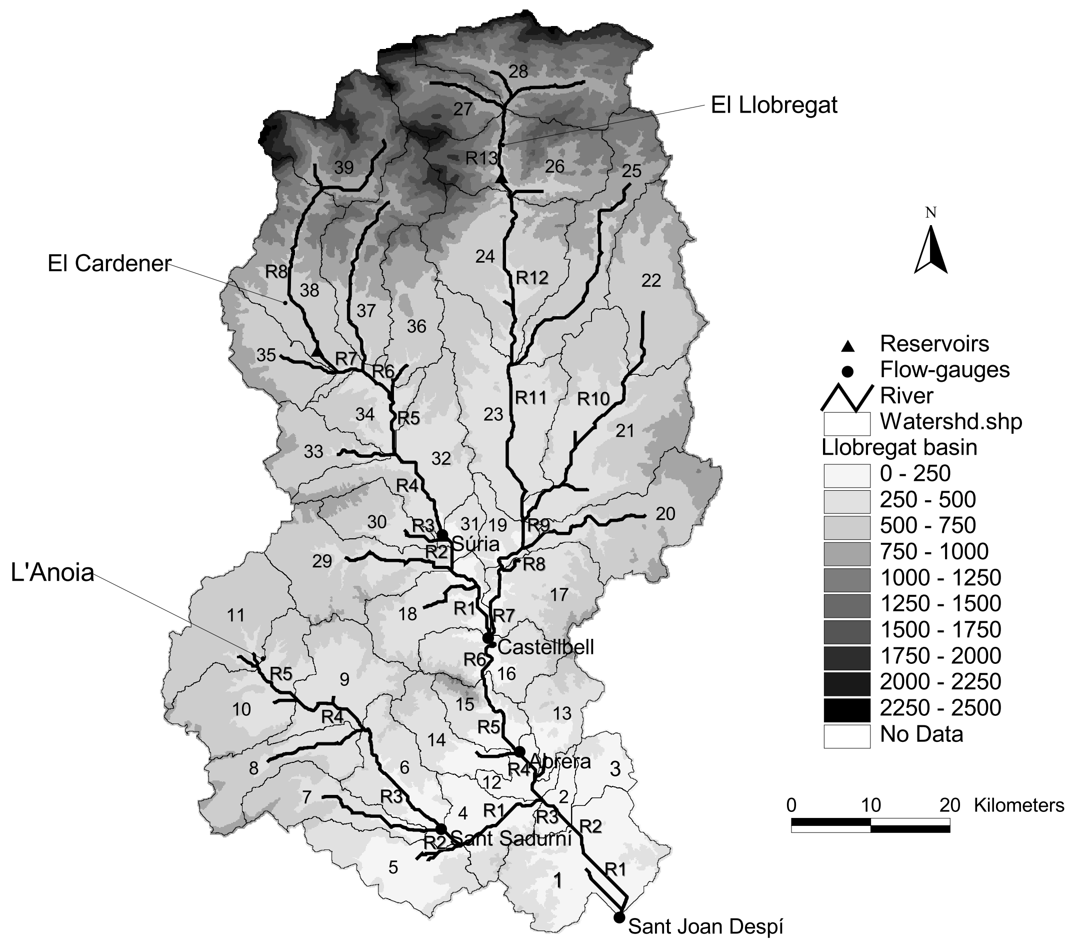

Figure 3.3: Digital terrain model of Llobregat river basin. It has a cell size of 50 m and displays the basin division (numbered), tributaries, stream-gauges (circles) and reservoirs (triangles) mentioned in the text.

3.3 Description of the Montserrat flash-flood episode

As widely described in Martín et al. (2006), this episode was characterized by the entrance of an Atlantic low-level cold front and an upper-level trough that contributed to the generation of a mesoscale cyclone in the Mediterranean Sea east of mainland Spain. This mesoscale cyclone advected warm and moist air toward Catalonia from the Mediterranean Sea. Then, the convergence zone between the easterly flow and the Atlantic flow, as well as the complex orography of the region, were shown to be involved in the triggering and organization of the convective systems which remained quasi-stationary (fig. 3.4). Therefore, heavy rainfall on 10 June 2000 lasted about six hours, from 02 to 08 local time (LT corresponds to UTC plus 2h). Convective systems bearing heavy rainfall remained quasi-stationary over many internal Catalonian catchments (e.g. El Llobregat, El Besós, El Francolí and La Riera del Bisbal; see fig. 1.5 for locations) and lasted about six hours, from 02:00 to 08:00 LT. The subsequent extraordinary rise of the Catalonia internal river basin flow regimes produced the aforementioned serious damages.

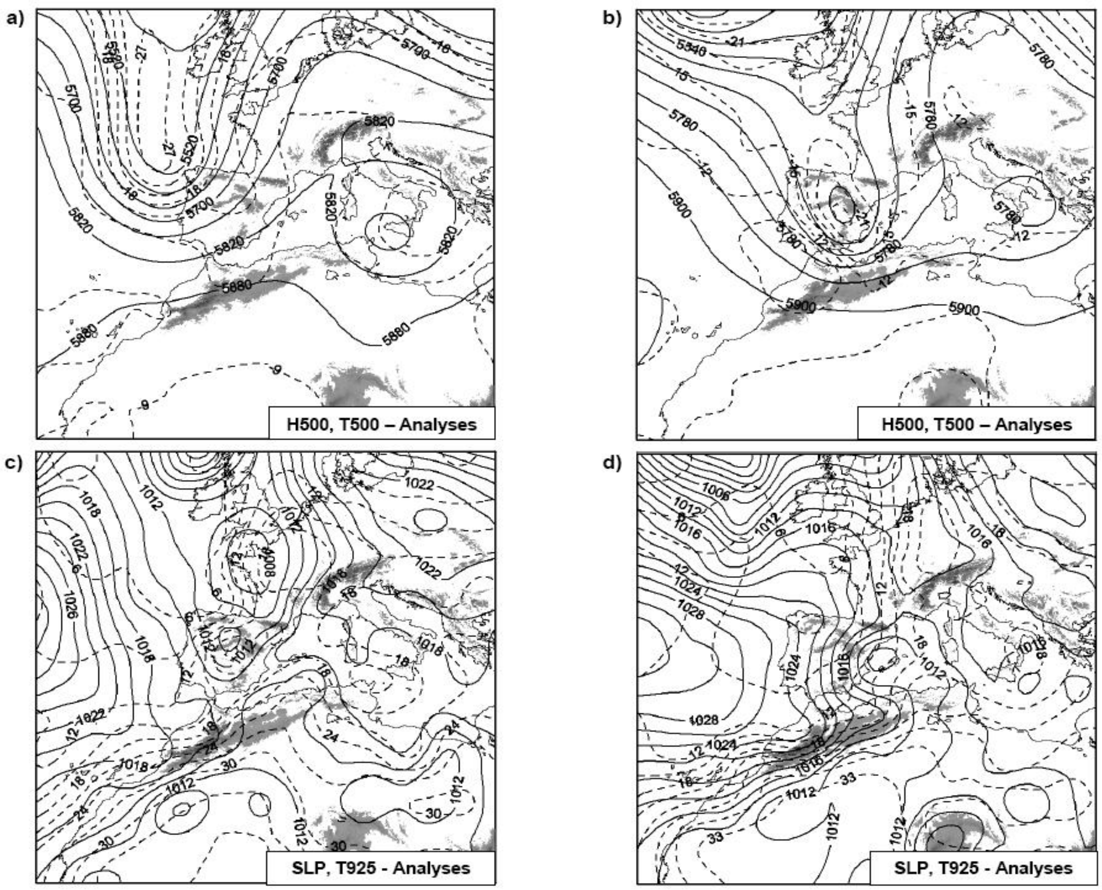

Figure 3.4: NCEP analyses maps. **(Top)** Geopotential height at 500 hPa (continuous line, in gpm) and temperature at 500 hPa (dashed line, in ^{0}C): **(a)** at 0000 UTC 9 June 2000; and **(b)** at 0000 UTC 10 June 2000. **(Bottom)** Sea level pressure (continuous line, in hPa) and temperature at 925 hPa (dashed line, in ^{0}C): **(c)** at 0000 UTC 9 June 2000; and **(d)** at 0000 UTC 10 June 2000. Main orographic systems are highlighted.

The most remarkable hydrometeorological feature of this case, known as the 'Montserrat' flash-flood event for its impact upon Montserrat's mountain, was the high intensity of the sustained rainfall, which accumulated hourly quantities above 100 mm and a six-hour maximum up to 200 mm. Figures 3.5a and b depict, respectively, the radar image of the lowest CAPPI (constant altitude plan position indicator) at 04:00 LT and the cumulative rainfall distribution in the internal catchments from 23:00 LT on 9 June to 23:00 LT on 10 June. The maximum amounts were observed in the basin of the Llobregat river, with 224 mm in the town of Rajadell. Up to 134 mm were observed at Bisbal del Penedés town, in the basin of the Riera de Bisbal, of which above 100 mm occurred in less than 2 hours. Values exceeding 100 mm were also observed in the basins of the Francolí, Gaià, and Foix (Llasat et al., 2003; see fig. 1.5a for locations).

Focusing on the Llobregat basin (fig. 3.3), the maximum flow discharge observed at Súria was 260 m^3 s^{-1} at 12:25 LT with a time to peak of 6h (fig. 3.6a, black solid line). In the Anoia

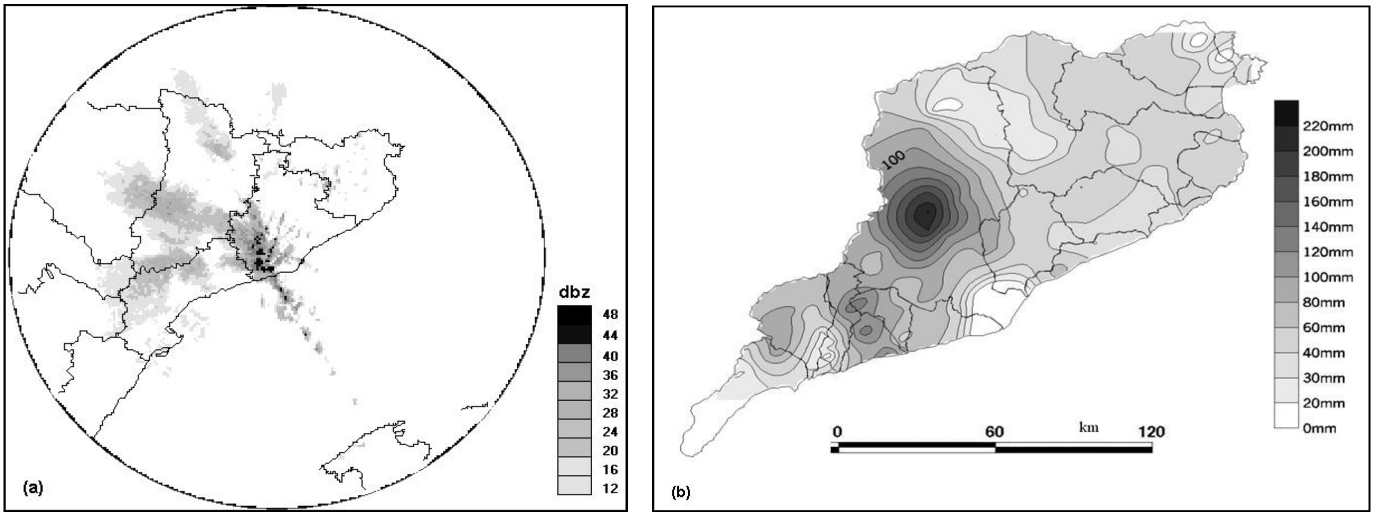

Figure 3.5: (a) CAPPI reflectivity at 1.2 km altitude recorded by the Barcelona radar at 04:00 LT on 10 June 2000. (b) SAIH-derived analysis of accumulated rainfall over the IBC during the 'Montserrat' episode (extracted from Llasat et al., 2003).

affluent, the maximum observed flow stage was close to 2.7 meters, with an associated peak discharge of 270 m^3 s^{-1} at 06:45 LT, and a time to peak of about 2 hours (fig. 3.6b). This was the first river which received the consequences of the event from 01:30 until 06:00 LT on 10 June. Around 03:00 LT, the rainfall extended to the entire Llobregat river basin, lasting for four hours. As a consequence, 5-minute intensites exceeded 120 mm per hour from 03:00 to 05:30 LT, with the highest values over the Llobregat basin occurring between 04:00 and 07:00 LT (fig. 3.5a). In Castellbell town, an increase on the flow stage was observed above 4.5 meters with several peak discharges, the maximum of these reaching 1000 m^3 s^{-1} at 08:00 LT with an associated time to peak close to 1h and 40 minutes (fig. 3.6c). In Abrera, a town sited approximately 15 km downstream, the maximum peak discharge was close to 1200 m^3 s^{-1} (at 12:50 LT; fig. 3.6d). Finally, at Sant Joan Despí city, near the Llobregat river mouth where the last river gauge is installed, the maximum peak discharge was up to 1400 m^3 s^{-1} at 10:15 LT with a timing close to 2h and 20 minutes (fig. 3.6e). These short response times shown by the hydrographs (see figure 5) indicate substantial flow velocities in the subbasins induced by the high rainfall rates, and discharge that propagated very rapidly downstream (9 km h^{-1} on average).

The Spanish Center for Studies and Experimentation on Public Works (CEDEX) has issued, in the framework of a report on flood plain management, the return periods corresponding to certain runoff thresholds for several national catchments. For the Llobregat basin, the associated return period for an outflow of 1025 m^3 s^{-1} is 10 years, whereas for a peak discharge of 1600 m^3 s^{-1} the recurrence interval is 20 years (Menéndez, 1998). These estimations emphasize the notable magnitude of the Montserrat event (1400 m^3 s^{-1}). The probability of suffering a similar catastrophic episode in the Llobregat basin is relatively low, but it must be emphasized that several hazardous episodes of different magnitudes and spatial scales are produced every year over the Spanish Mediterranean regions. In addition, future climate change scenarios and their possible impact on these types of events have to be taken into account. Some authors have indicated an increase in the probability of heavy rainfall episodes in several parts of the world (Groisman et al., 1999), and a paradoxial increase of extreme daily rainfall in spite of a decrease in total values has been observed already in the Mediterranean basin (Alpert et al., 2002).

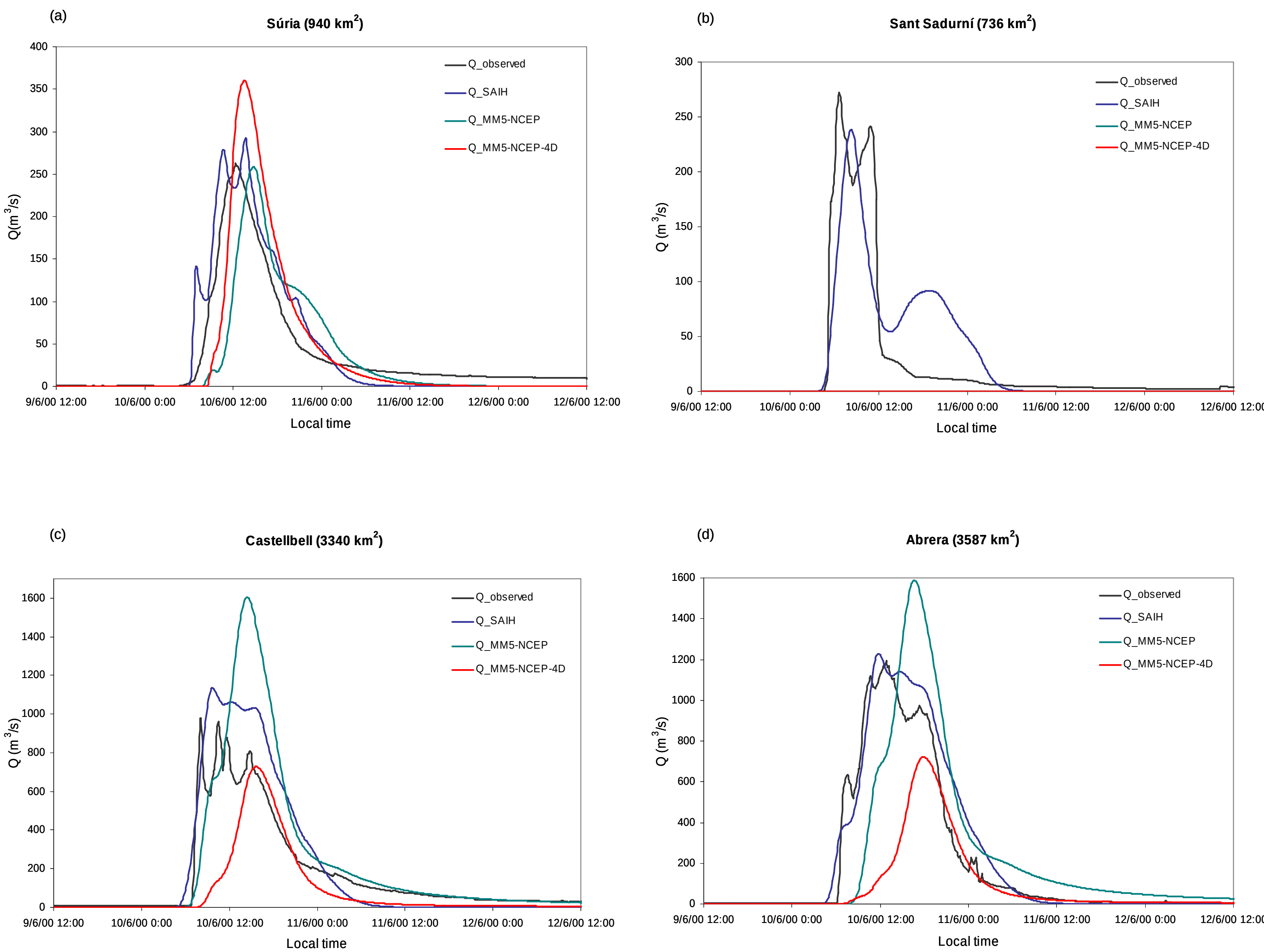

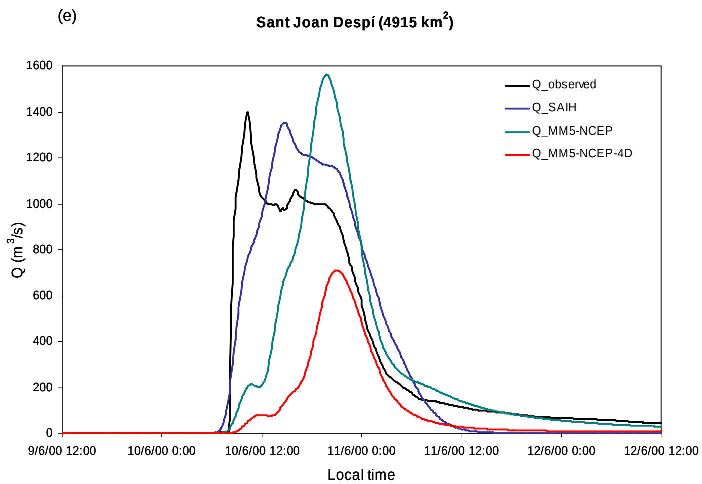

Figure 3.6: Observed, SAIH rain-gauge driven, and MM5-NCEP simulation driven runoff discharge at: (a) Súria, (b)Sant Sadurní, (c) Castellbell, (d) Abrera and (e) Sant Joan Despí.

3.4 Hydrological tools

3.4.1 Rainfall-runoff model implementation

As it has been widely explained in section 2.2, the study is carried out using the HEC-HMS rainfall-runoff model. Figure 3.3 depicts the digital terrain model for the Llobregat basin –with a cell resolution of 50 meters– together with the main watercourses and its tributaries, the considered division in subbasins and the location of the available river gauges. After the analysis presented in this section, the basin is divided in 39 subwatersheds with an average size of 126 km^2 and an extension of 4915 km^2 upstream from Sant Joan Despí, where the last flow-gauge is installed.

HEC-HMS is forced using a single hyetograph for each subbasin. Rainfall spatial distributions were first generated from 30-min, 1-h and 3-h accumulated values at SAIH rain-gauges (see next subsection) using the kriging interpolation method with a horizontal grid resolution of 1 km. Then, temporal rainfall series were calculated for each subbasin as the areal average of the gridded rainfall within the subcatchment. The same methodology is used to assimilate forecast rainfall fields in HEC-HMS (section 3.5), except that atmospheric model grid point values are used instead of SAIH observations.

The hydrologic model calculates runoff volume by using the SCS Curve Number. The SCS-UH is used to convert rainfall excess into direct runoff. The flood hydrograph is routed using the Muskingum method (further details in section 2.2). Llobregat basin contains two reservoirs located in the upstream areas of the Cardener affluent and the Llobregat river (fig. 3.3). Therefore, these watercourses can not be modeled under the natural regime since the dams have an important hydrograph diffusion effect in the flood wave. The technical characteristics of both reservoirs -storage capacity, maximum outflow, maximum elevation and initial level- have been obtained from the technical reports by ACA (2001 and 2003). The detention ponds are modeled in HEC-HMS introducing a reservoir (section 2.2).

The calibration of the rainfall-runoff model is carried out using five episodes of similar extraordinary characteristics to our Montserrat case of study, selected from the period comprised between the deployment of the SAIH system (in 1996) and 2004 (table 3.1). Owing to the malfunction of the flow-gauge network for some of these episodes, the stream-gauges at Abrera and Sant Joan Despí are not available for all the cases (table 3.1), limiting to some extent the calibration of the lower Llobregat basin. Calibration of the infiltration parameters for each independent episode are obtained as explained in section 2.2.6. The SCS curve numbers are derived from field measurements and normal antecedent moisture conditions (ACA, 2001). In addition, the flood wave celerity for the main streams is also considered as a calibration index –by means of K parameter– owing to the nature of these kind of episodes characterized by very high flow velocities. With the intention of capturing as well as possible the flow wave celerities involved in the Montserrat extreme episode, the maximum propagation velocities obtained among the previous calibration episodes were used. The calibrated parameters were then used to run HEC-HMS for the 'Montserrat' case –in a single evaluation event– during a 96h simulation, from 9 June 2000 at 00:00 LT to 12 June 2000 at 24:00 LT, with a 10 minute time-step. This period completely encompasses the flood event and the subsequent hydrograph tail.

Flood events	***Simulation periods***	***Maximum observed rainfall (mm)***	***Maximum observed flow (m^3 s^{-1})***
16-19 Nov 1996	96 h	102.1	1250.0 (Despí)
16-19 Dec 1997	96 h	232.0	502.7 (Castellbell)
17-20 Oct 2001	96 h	84.5	254.4 (Despí)
03-06 Dec 2003	96 h	63.6	436.9 (Castellbell)
29-31 Aug 2004	72 h	178.3	313.5 (Castellbell)

Table 3.1: Summary of the episodes used for the calibration of the hydrologic model. Note that the observed flow at the basin outlet in Sant Joan Despí is not available for some of the cases.

The previous calibration process and subsequent rain-gauge driven runoff simulations have been repeated for three spatial disaggregations of the catchment (21, 39 and 60 subbasins) with 1h accumulated rainfall discretization and varying temporal resolutions of the incoming rainfall data (30-min, 1-h and 3-h) with a 39 subbasins segmentation, in order to explore the sensitivities of the Llobregat basin and find an optimum configuration of the modelling system. The next subsection is fully devoted to this issue.

3.4.2 Sensitivity analysis to the spatial and temporal rainfall scales

In order to study the effects of the spatial scales of the rainfall field on the total basin response, the sensitivity of the catchment to three different spatial segmentations was evaluated: the basin was broken down into 21, 39 and 60 subbasins and the rainfall-runoff model was forced with hourly accumulated rainfall. The skill of the resulting runoff simulations is expressed in terms of the Nash-Sutcliffe efficiency criterion (NSE; Nash and Sutcliffe, 1970), a 'goodness-of-fit' measure widely used in hydrological model validation (Jasper et al., 2003; Dolciné et al., 2001; further details in Appendix). This same index will be used in next sections to evaluate other spatial and temporal series. The performance of the runoff simulations is also checked by means of the relative error of total volume at flow-gauge sites, expressed as percentage ($\%EV$; see Appendix):

Table 3.2 shows the skill indices for the five calibration episodes. The results suggest a choice of 39 subbasins. For the Montserrat flash-flood (table 3.3) the optimum evaluation configuration in terms of model performance corresponds to 39 subbasins, particularly for the smallest watersheds, at Súria and Sant Sadurní gauges (~1000 km^2). For the largest basins, with areas exceeding 3000 km^2, the distinction is not so clear, and in Castellbell the 60 subbasins subdivision appears to be superior. The last two downstream gauges (Abrera and Castellbell) present similar statistical scores among the three discretizations, though the 39 subbasins configuracion is slightly superior (see fig. 3.7a for basin outlet). In general, then, the rainfall-runoff model reproduces better the 'Montserrat' event by dividing the Llobregat basin in 39 subbasins.

Flood events	***NSE 21-sb***	***%EV 21-sb***	***NSE 39-sb***	***%EV 39-sb***	***NSE 60-sb***	***%EV 60-sb***
16-19 Nov 1996	0.27	24.1	0.87	-1.3	0.83	-2.2
16-19 Dec 1997	0.25	57.5	0.84	21.3	0.31	54.0
17-20 Oct 2001	0.67	34.3	0.55	-10.3	0.62	-17.7
03-06 Dec 2003	0.46	30.9	0.77	25.1	0.90	-0.3
29-31 Aug 2004	0.27	27.9	0.43	17.6	0.40	46.2

Table 3.2: NSE efficiency criterion and percentage of error in volume ($\%EV$) for the calibration episodes at the stream-gauges indicated in table 3.1. Three different basin configurations (21, 39 and 60 subbasins) and hourly accumulated rainfall are used.

	NSE 21-sb	***%EV 21-sb***	***NSE 39-sb***	***%EV 39-sb***	***NSE 60-sb***	***%EV 60-sb***
Súria	0.64	23.9	0.84	4.8	0.50	-33.7
Sadurní	0.46	11.6	0.67	12.4	0.50	-23.3
Castellbell	0.64	12.3	0.68	14.5	0.78	-5.4
Abrera	0.91	12.3	0.93	12.6	0.89	-2.1
Despí	0.82	3.6	0.84	1.1	0.76	8.4

Table 3.3: NSE efficiency criterion and percentage of error in volume ($\%EV$) for the Montserrat evaluation event. The SAIH rain-gauge driven simulations are carried out with three different basin segmentations (21, 39 and 60 subbasins) at the five stream-gauges indicated. Hourly accumulated rainfall is used in all cases.

This result appears to be related to the number of rain-gauges lying inside the whole basin

(36), implying an average area per station of 136.5 km^2. This area can be compared with the mean size of the 21, 39 and 60 subcatchments: 241.7 km^2, 126.0 km^2 and 81.9 km^2, respectively. Therefore, for 21 subbasins the model hyetograph tends to overlap information of several rain-gauges per subbasin, smoothing out detailed information of the spatial structure of the rainfall field that the rain-gauge network is able to resolve. On the contrary, for 60 subbasins the rainfall-runoff model does not acquire reliable information of the rainfall field for ungauged catchments. The configuration using 39 subbasins seems to optimize the performance of the simulated basin response, since it represents more adequately the truly resolved spatial variabilities of the rainfall field. It is worth noting that the differences in the outflow characteristics at the flow-gauges among the three watershed discretizations disminishes at larger scales (table 3.3).

In order to study the effects of the temporal scales of the rainfall field on the total basin response, the sensitivity of the catchment using a 39 subbasins segmentation together with 30 minutes, 1h and 3h accumulated rainfall discretizations have been analyzed for the calibration and Montserrat episodes (tables 3.4 and 3.5). Table 3.4 displays weak differences among the three temporal discretizations at the flow gauges indicated in table 3.1. The NSE and $\%EV$ skill scores results in table 3.5 indicate that the hourly discretization optimizes the simulation of the Llobregat basin response to the Montserrat event, since it presents the best performance in three of the five flow sites and a notable reproduction of the observed flow at the remaining gauges. Nevertheless, slightly better accuracy at the basin outlet is exhibited by the 3h rainfall field discretization experiment (fig. 3.7b). With the exception of Sant Joan, the hydrographs computed at the different flow gauges (not depicted) show greater peak discharges for the 30 minutes evaluation experiment and faster response times for the 3h discretization when compared with observed. This result agrees with the notion that the higher the temporal variability of rainfall the greater the peak discharges, and also that a 3h temporal discretization may be inappropriate for strong storms and/or watersheds with fast response times (Singh, 1997).

Flood events	***NSE 30-min***	***%EV 30-min***	***NSE 1-h***	***%EV 1-h***	***NSE 3-h***	***%EV 3-h***
16-19 Nov 1996	0.90	3.0	0.87	-1.3	0.89	3.3
16-19 Dec 1997	0.87	17.6	0.84	21.3	0.84	21.2
17-20 Oct 2001	0.70	-8.0	0.55	-10.3	0.70	-6.7
03-06 Dec 2003	0.88	10.7	0.77	25.1	0.89	14.2
29-31 Aug 2004	0.50	-0.1	0.43	17.6	0.50	-3.1

Table 3.4: NSE efficiency criterion and percentage of error in volume ($\%EV$) for the calibration episodes at the stream-gauges indicated in table 3.1. Three different temporal discretizations (30-min, 1-h and 3-h) and 39 subbasins segmentation are used.

	***NSE* 30-min**	**%*EV* 30-min**	***NSE* 1-h**	**%*EV* 1-h**	***NSE* 3-h**	**%*EV* 3-h**
Súria	0.91	-12.7	0.84	4.8	0.80	-9.9
Sadurní	0.58	23.5	0.67	12.4	0.64	12.3
Castellbell	0.62	18.5	0.68	14.5	0.39	16.0
Abrera	0.91	16.0	0.93	12.6	0.87	13.0
Despí	0.73	-0.5	0.84	1.1	0.90	2.4

Table 3.5: NSE efficiency criterion and percentage of error in volume ($\%EV$) for the Montserrat evaluation event. The SAIH rain-gauge driven simulations are carried out with three different time-scale discretizations (30-min, 1-h and 3-h) at the five stream-gauges indicated. 39 subbasins segmentation is used in all cases.

From the set of the evaluation experiments analyzed, it seems that the most appropriate coherence between the spatial and temporal scales of the flash-flood event that the raingauge network is able to resolve, is reached for 39 subbasins combined with 1h input rainfall data in the hydrological model (tables 3.3 and 3.5). This is the configuration of the model that will be used for the mesoscale model driven runoff simulations. Tables 3.6 and 3.7 report the main hydrological model parameters: curve numbers, initial abstractions, times of concentration and routing parameters.

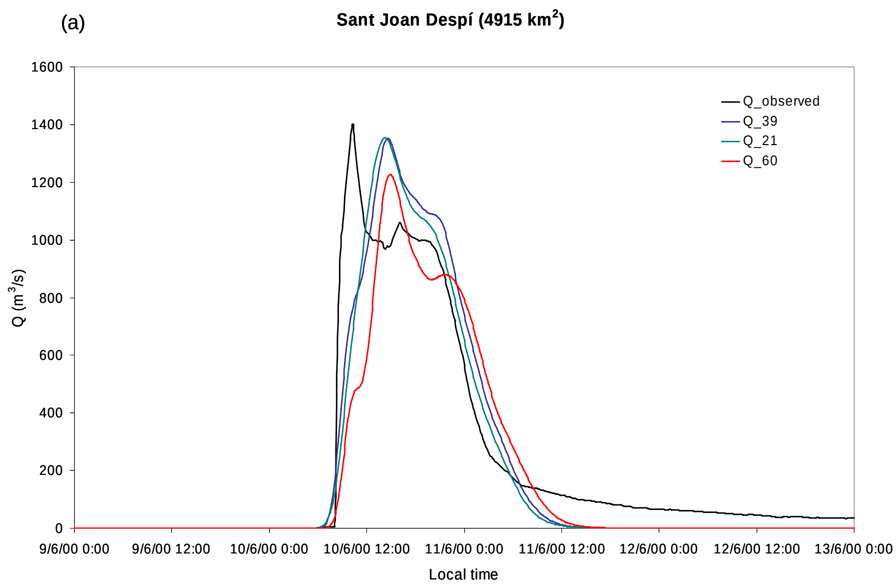

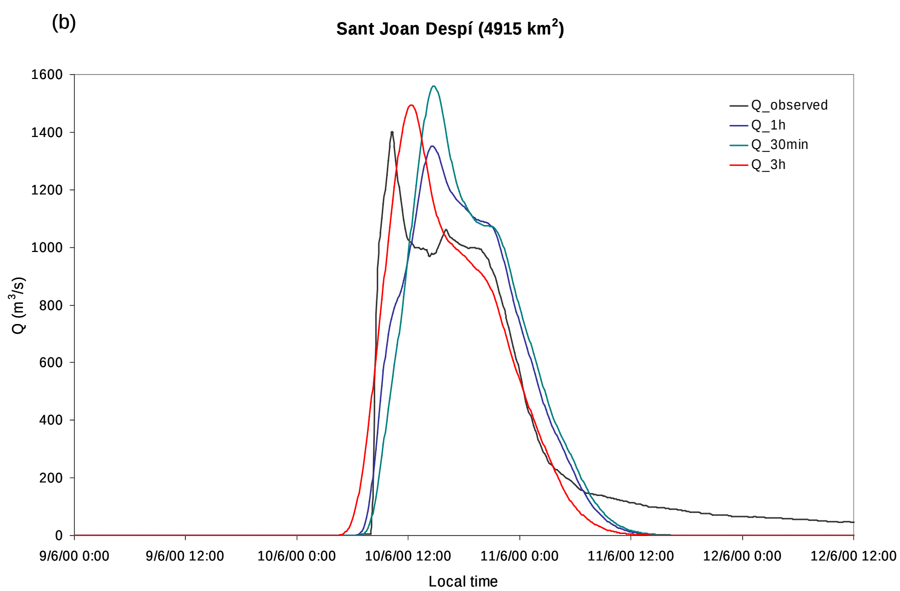

Figure 3.7: SAIH rain-gauge driven runoff discharge at Sant Joan Despí for the different (a) spatial and (b) temporal discretizations.

subbasin	***CN***	I_a***(mm)***	***Tc(h)***	***subbasin***	***CN***	I_a***(mm)***	***Tc(h)***
1	71.6	21.5	3.1	21	60.7	41.1	3.0
2	75.5	23.0	1.4	22	60.4	43.0	2.6
3	78.3	20.8	1.3	23	63.4	29.7	3.0
4	69.0	29.6	2.8	24	63.1	51.0	2.2
5	72.1	22.4	2.0	25	66.1	46.2	3.0
6	59.5	64.5	1.6	26	61.8	42.0	1.8
7	58.8	38.0	2.0	27	67.1	31.0	1.6
8	64.5	34.1	2.3	28	69.4	33.6	2.0
9	62.6	59.9	1.7	29	63.6	45.6	2.2
10	63.4	50.4	2.0	30	63.6	35.5	1.6
11	52.8	43.6	1.6	31	68.1	37.8	2.0
12	69.1	19.6	1.1	32	60.3	79.7	0.6
13	71.0	26.0	1.5	33	56.7	76.2	1.9
14	71.6	32.2	1.8	34	63.5	62.8	1.6
15	70.9	27.9	1.6	35	54.0	77.1	2.2
16	67.0	28.4	1.7	36	56.1	61.1	2.2
17	68.6	33.0	2.2	37	56.8	74.4	1.6
18	62.1	37.1	2.1	38	59.1	85.1	2.0
19	67.5	26.1	1.0	39	55.6	77.4	2.1
20	62.7	28.9	2.4				

Table 3.6: Curve numbers, initial abstractions (in mm) and times of concentration (in h) for the selected basin configuration (displayed in Fig. 3.3).

reach	***K(h)***	χ	***reach***	***K(h)***	χ	***reach***	***K(h)***	χ
	Llobregat			Cardener			Anoia	
R1	1.4	0.20	R1	1.4	0.25	R1	1.6	0.20
R2	0.8	0.20	R2	0.6	0.30	R2	0.3	0.25
R3	0.3	0.20	R3	0.4	0.20	R3	1.4	0.25
R4	0.6	0.25	R4	2.0	0.25	R4	1.2	0.30
R5	1.2	0.25	R5	1.6	0.30	R5	1.0	0.35
R6	1.0	0.25	R6	1.0	0.35			
R7	1.0	0.25	R7	0.8	0.35			
R8	1.4	0.25	R8	3.0	0.35			
R9	1.4	0.25						
R10	3.1	0.25						
R11	3.0	0.25						
R12	3.2	0.30						
R13	2.7	0.30						

Table 3.7: Muskingum parameters for the selected basin configuration. Numeration of the river reaches follows the upstream direction (see Fig. 3.3).

3.5 Meteorological tools: application to the Montserrat flash-flood event

The non-hydrostatic MM5 numerical model is used to perform the meteorological simulations (further details in section 2.3). These simulations are designed using 24 vertical σ-levels and three spatial domains with 82×82 grid points (fig. 3.8). Their respective horizontal resolutions are 54, 18 and 6 km, with integration time-steps of 162, 54 and 18 seconds. The domains are centered in northeast Spain where the convective episode developed. In particular, the finest domain spans the entire Catalan territory and contiguous land and oceanic areas, and is used to supply the high-resolution rainfall fields to drive the hydrologic simulations. The interaction between the domains follows a two way nesting strategy (Zhang and Fritsch, 1986; see section 2.3).

To initialize the model and to provide the time-dependent boundary conditions, NCEP and ECMWF meteorological grid analyses are used. MM5-NCEP simulation uses the analysis from the Global American Center for Environmental Prediction for the large domain, and are updated every 12 hours with a 2.5^0 spatial resolution. MM5-ECMWF simulation uses the analysis of the European Center for Medium Range Weather Forecasts, with a spatial resolution of 0.3^0 and an update frequency of 6 hours. In both cases the first guess fields interpolated from the analyses on the MM5 model grid are improved using surface SYNOP and upper-air RAOB observations with a successive-correction objective analysis technique (Benjamin and Seaman, 1985). The tendencies along the model coarse domain boundaries, specified by differences of the fields between the 12h and 6h apart analyses, respectively, are applied using a Newtonian relaxation approach (Grell et al., 1995).

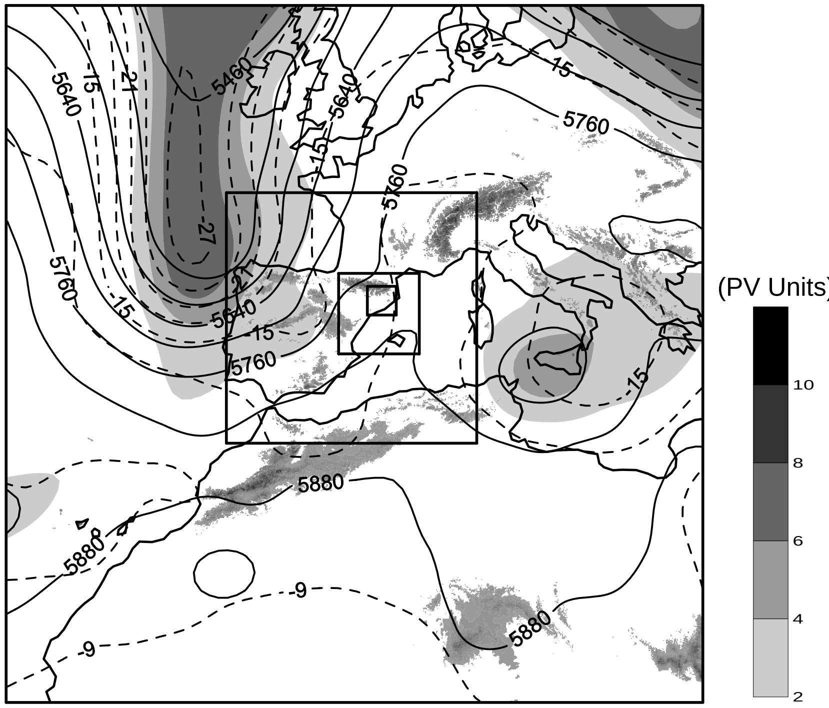

Figure 3.8: Configuration of the four computational domains used for the MM5 numerical simulations (horizontal resolutions are 54, 18, 6 and 2 km, respectively) and MM5-NCEP simulation initial state, showing geopotential height at 500 hPa (continuous line, in gpm), temperature at 500 hPa (dashed line, in ^0C) and isentropic PV on the 330 K surface (shaded, according to scale) at 00 UTC 9 June 2000.

To parameterise moist convective effects the Betts-Miller and Kain-Fritsch cumulus schemes are used in the large domain and the intermediate domain, respectively. No convection scheme is in principle used in the inner one owing to the high horizontal resolution. Explicit microphysics is represented in all domains with prediction equations from the mixed-phase scheme. The planetary boundary layer physics is formulated using the Hong and Pan parameterization. Surface temperature over land is calculated using a force-restore slab (Blackadar, 1979; Zhang and Anthes, 1982) and over sea it remains constant during the simulations. Finally, long and short wave radiative processes are formulated using the RRTM scheme (further details in section 2.3).

Furthermore, since it is debatable whether a 6 km resolution domain can resolve convection appropriately without a convection scheme, an additional experiment has been designed. This simulation, labeled as MM5-NCEP-4D, coincides with MM5-NCEP except that it applies the Kain-Fritsch scheme for the third domain. It also incorporates a fourth domain of 2 km horizontal resolution forced in two way mode, in which convection is fully explicit. The possible benefits of enhanced horizontal resolution in this complex orographic region can thus be assessed.

With the purpose of generating the ensemble of perturbed simulations, the invertibility principle of Ertel potential vorticity (PV) (further details in subsection 2.3.2) is applied. In particular, we are interested in studying the sensitivity of the Montserrat hydrometeorological event to uncertainties in the precise representation of the upper-level precursor trough (shown in fig. 3.8), being aware that small scale aspects of the circulation are propitious to analysis or forecast errors. The piecewise PV inversion scheme is then used as a clean approach to manipulate the upper-level synoptic trough in the model initial conditions. What it is necessary is a simple identification of the PV signature of the trough (shown as shaded in fig. 3.8) and then the balanced mass and wind fields associated with that PV element can be used to alter the meteorological fields in a physically consistent way (effectively, a change in the structure or position of the trough). This method has already shown its value for assessing the predictability of flash-flood events in the western Mediterranean area (e.g. Romero, 2001; Homar et al., 2002; Romero et al., 2005).

Using the NCEP-derived initial conditions, the upper-level trough intensity is perturbed ±5% (simulations -5% PV and +5% PV) and its position is displaced ±54 km along the zonal direction (experiments WEST and EAST). This short ensemble of simulations is a first approximation to the problem of incorporating the spatio-temporal uncertainty of the rainfall forecast into a medium size catchment like the Llobregat basin. The whole set of MM5 simulations comprises a 36 hour period, from 9 June 2000 at 00:00 UTC to 10 June 2000 at 12:00 UTC, after the end of the rainfall event in Catalonia.

3.6 Results and discussion

3.6.1 SAIH rain-gauge driven runoff simulation

SAIH rain-gauge derived rainfall of the 'Montserrat event' is used to drive the calibrated HEC-HMS model in a single evaluation runoff simulation according to the methodology described in section 2.2. Figure 3.9a displays the spatial distribution of the accumulated rainfall upon the entire watershed and figures 3.10 and 3.11 show, respectively, the accumulated volume per subbasin and the temporal sequence of accumulated volume over the entire basin at hourly time-steps. These distributions will be compared against the simulated ones in next sections.

As a general overview, table 3.8 and figure 3.6 show a good HEC-HMS skill for the characterization of the Llobregat basin response to the 'Montserrat' event. NSE exceeds 0.65 in the set of flow-gauges, and particularly at Abrera it exceeds 0.9. Relative errors in volume are reasonably small and only at Castellbell the error is close to 15%, though in all the stream-gauges the volume is overestimated. Therefore, the results indicate a reasonable goodness-of-fit for the main peak discharges, their timing and the volume estimations at the flow-gauges. For small-scale features, however, the rain-gauge driven run shows some inaccuracies: at Súria, multiple peaks are simulated instead of a single one (fig. 3.6a); at Sadurní, Castellbell and Abrera, the opposite case occurs and the model only simulates an envelope of the higher frequency peaks (fig. 3.6b, c and d); at Sant Joan Despí, a significant delay occurs in the time to peak (fig. 3.6e).

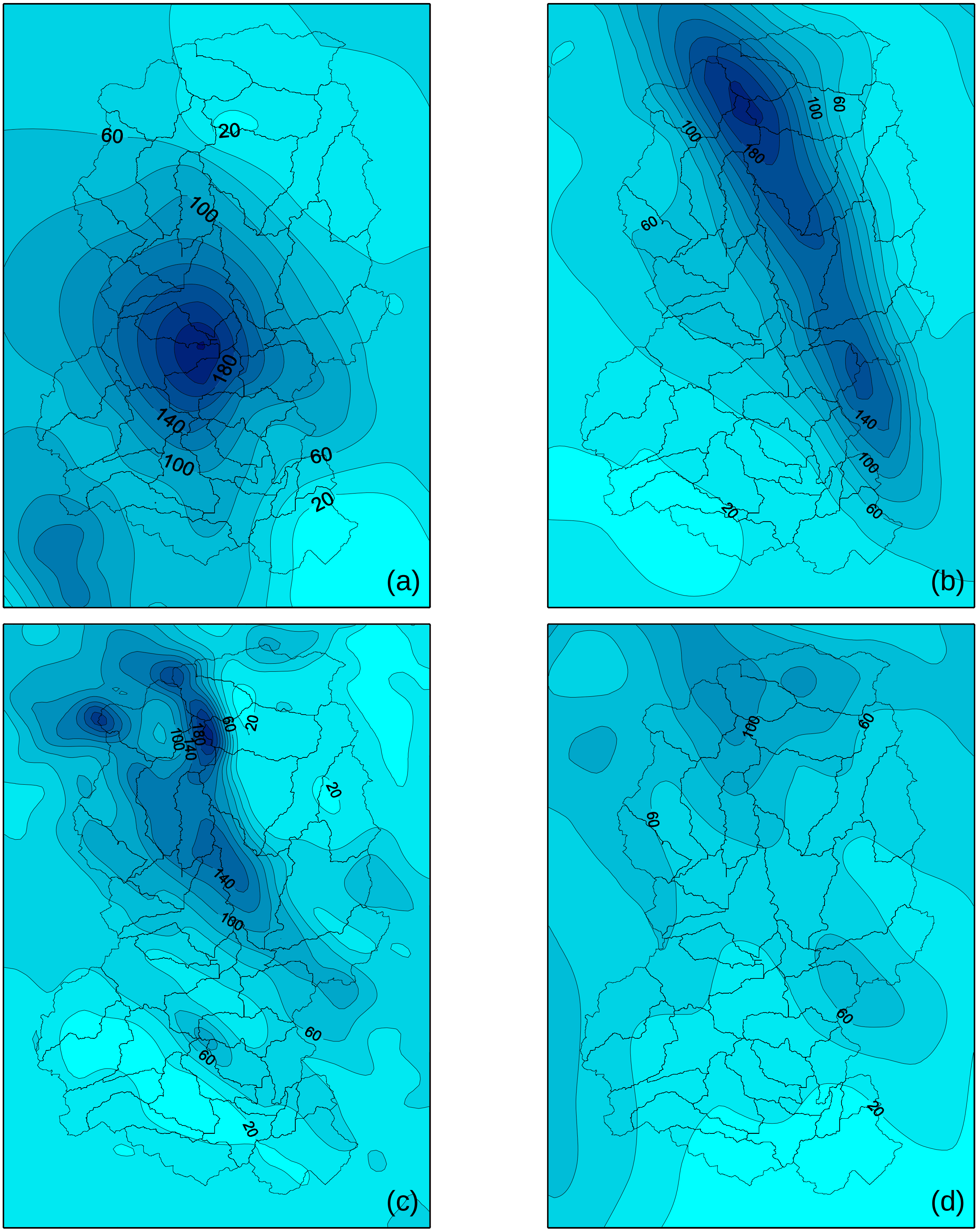

Figure 3.9: Spatial distribution of accumulated rainfall during the 'Montserrat' event in the Llobregat basin, from: (a) SAIH rain-gauges, (b) MM5-NCEP simulation, (c) MM5-NCEP-4D simulation and (d)MM5-ECMWF simulation . Contour interval is 20 mm starting at 20 mm.

	NSE SAIH	***%EV SAIH***	***NSE NCEP***	***%EV NCEP***	***NSE NCEP-4D***	***%EV NCEP-4D***
Súria	0.84	4.8	0.60	-16.9	0.67	-2.3
Sadurní	0.67	12.4	-0.12	-100	-0.12	-100
Castellbell	0.68	14.5	0.19	35.5	0.47	-49.2
Abrera	0.93	12.6	0.58	15.9	0.36	-55.8
Despí	0.84	1.1	0.51	-12.0	0.21	-66.8

Table 3.8: NSE efficiency criterion and percentage of error in volume ($\%EV$) at the five stream-gauges for the SAIH rain-gauge driven and MM5-NCEP driven runoff simulations with three (NCEP) and four domains (NCEP-4D).

3.6.2 MM5-NCEP, MM5-NCEP-4D and MM5-ECMWF driven runoff simulations

To assess the skill of the MM5 mesoscale runs, the spatial and temporal distributions of the simulated rainfall volume are compared against the rain-gauge derived volume pattern. The spatial comparison is done using the 39 subbasins as accumulation units for the whole episode, and the temporal comparison uses hourly accumulations for the whole basin. The degree of agreement between model and observed rainfall distributions is quantified using the NSE and root mean square error (RMSE) statistical indices (table 3.9; see Appendix). With regard to the spatial distribution, the best skill scores are obtained by the MM5-ECMWF and MM5-NCEP-4D experiments. The MM5-NCEP experiment shows a moderately worse behaviour, but on the contrary, it is the best for the temporal distribution.

	NSE spatial	***NSE temporal***	***RMSE spatial***	***RMSE temporal***
NCEP	-1.52	0.74	9.3	11.2
NCEP-4D	-0.36	0.64	6.8	13.2
ECMWF	-0.62	0.51	7.5	15.4
-5%PV	0.39	0.66	4.6	12.7
+5%PV	-2.05	0.56	10.3	14.6
WEST	-0.47	0.39	7.1	17.1
EAST	-2.59	0.56	11.1	14.5

Table 3.9: NSE efficiency criterion and root mean square error (RMSE, in hm^3) of the spatial and temporal rainfall volume distributions yielded by the set of mesoscale numerical simulations.

From a hydrological point of view, the MM5-NCEP simulation is the most suitable, attending to total precipitated water over the Llobregat basin, discharged volume at the basin outlet (table 3.10), and the amount of the maximum hourly precipitated volume in the basin (table 3.11). The superior behaviour in these aspects of the MM5-NCEP rainfall simulation can be appreciated in figures 3.6, 3.10 and 3.11 and table 3.8. MM5-ECMWF driven runoff simulation is not shown owing to its low skill on reproducing the episode, with corresponding statistical scores at the Llobregat basin outlet of $NSE = -0.19$ and $\%EV = -86.3$. Figure 3.9d reveals that the MM5-ECMWF rainfall field is very deficient for this particular case study (compare with fig. 3.9a). In addition, the MM5-NCEP-4D driven runoff simulation exhibits a remarkable underestimation of the peak discharges and volumes at the different stream-gauges, except at Súria (fig. 3.6 and table 3.8). The MM5-NCEP-4D rainfall field contains very fine spatial features owing to the inclusion of the 2 km resolution forcing in the simulation (fig. 3.9c), but the quantitative and spatial rainfall forecast is not better than the MM5-NCEP result (fig. 3.9b). The inclusion of a convective scheme in the third domain appears to have a negative impact on the simulation. Therefore, MM5-NCEP simulation is chosen as the *c*ontrol simulation for this investigation.

The most remarkable deficiency of the control simulation is the north-eastward shift of the rainfall pattern towards higher terrain and a more elongated shape with regard to the observed distribution, although with similar amounts (fig. 3.9). It seems reasonable to argue that the catchment's complex orography, dominated by the Pyrenees, the pre-coastal and coastal ranges is a determinant factor for the mesoscale model to produce that spatial distribution. Nevertheless, the simulated heavy rainfall lies within the Llobregat basin and the simulated timing of the rainfall episode is remarkably good (fig. 3.11), in benefit of the MM5-NCEP driven runoff simulation. Since the MM5 control simulation tends to concentrate the maximum rainfall towards the upper part of the basin, where the two reservoirs are located, then it would be expected a significant effect of hydrograph diffusion in the runoff. For the reservoir located in the Llobregat river, with an initial volume of 95 hm^3 and an inflow volume of 14.0 hm^3, the resulting outflow volume is 12.2 hm^3. The peak discharge disminishes from 560.8 $\mathrm{m^3\ s^{-1}}$ to 145.4 $\mathrm{m^3\ s^{-1}}$ with an attending delay close to 8 hours. The diffusion effect by the reservoir located in the Cardener river is smaller: a decrease from 96.6 $\mathrm{m^3\ s^{-1}}$ to 71.6 $\mathrm{m^3\ s^{-1}}$ with a delay of about 1.5 hours.

	Precipitated volume	***Discharged volume***
SAIH	405.7	72.4
NCEP	378.5	64.5
NCEP-4D	307.0	24.4
ECMWF	252.3	10.1
-5%PV	394.1	75.3
+5%PV	253.8	30.8
WEST	355.7	60.1
EAST	301.2	50.6

Table 3.10: Total precipitated volume (hm^3) in Llobregat basin, and discharged volume (hm^3) at Sant Joan Despí outlet, from SAIH rain-gauges and the set of mesoscale numerical simulations. Observed discharged volume by the SAIH stream-gauge was 73.2 hm^3.

	Maximum volume	***Local time***
SAIH	72.0	06:00
NCEP	71.3	07:00
NCEP-4D	46.9	07:00
ECMWF	53.1	08:00
-5%PV	67.5	08:00
+5%PV	53.8	06:00
WEST	78.5	08:00
EAST	61.5	04:00

Table 3.11: Maximum 1h accumulated volume for the whole Llobregat basin (hm^3) and its corresponding local time (on 10 June, 2000), from SAIH rain-gauges and the set of mesoscale numerical simulations.

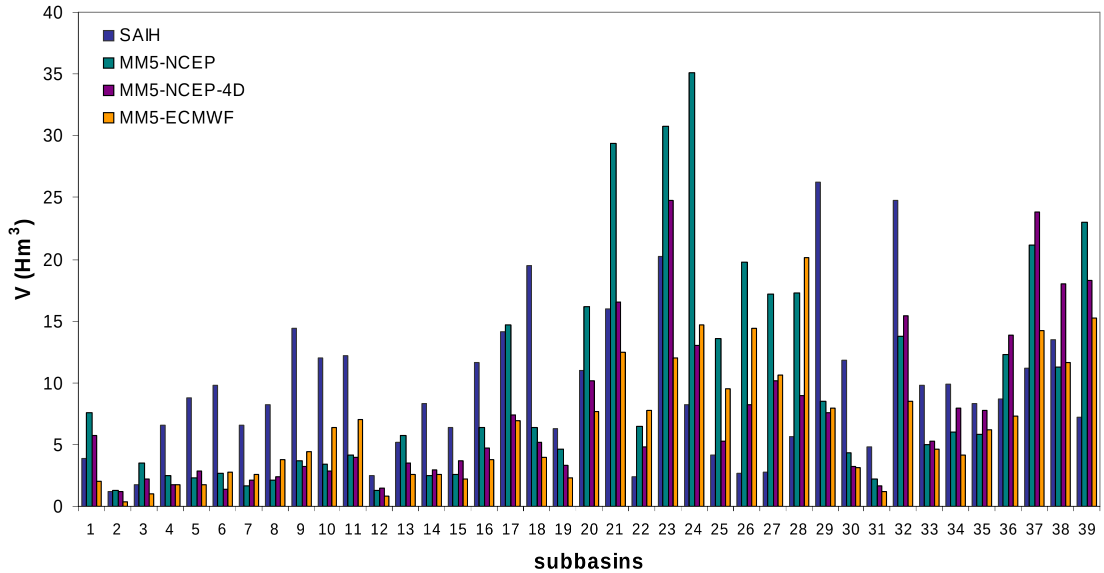

Figure 3.10: Accumulated volume during the 'Montserrat' event, per subcatchment of the Llobregat basin, from SAIH rain-gauge, MM5-NCEP, MM5-NCEP-4D and MM5-ECMWF simulations. See Fig. 3.3 for subcatchment numbering.

The MM5-NCEP driven runoff simulation at Súria site displays a good agreement with the observed peak discharge but not with its timing (fig. 3.6a; table 3.8). At Sant Sadurní site the simulation is very deficient and no runoff is produced (fig. 3.6b; table 3.8): the mesoscale model widely underestimates the rainfall amounts in the Anoia watershed (compare figs. 3.9a and 3.9b and see fig. 3.10). At Castellbell and Abrera sites, runoff is widely overestimated producing a large error in the peak estimation and, consequently, making these results less suitable for use in emergency management directives (figs. 3.6c and d). As the hydrograph is routed downstream, the overestimation of the runoff volume decreases owing to the deficit of the simulated rainfall in the southwestern subbasins which contribute to the inflow. Another characteristic feature of the simulated runoff hydrographs along the Cardener and Llobregat rivers is a lag-time of around 3 hours with respect to the observed flows, which is consistently routed downstream towards the basin outlet (fig. 3.6e). This is due to several factors: the aforementioned hydrograph diffusion by the basin's reservoirs, the fact that the core of the simulated heavy rainfall occurs further upstream and with a certain delay compared with the observations, and the exceptional flood wave propagation for this particular event.

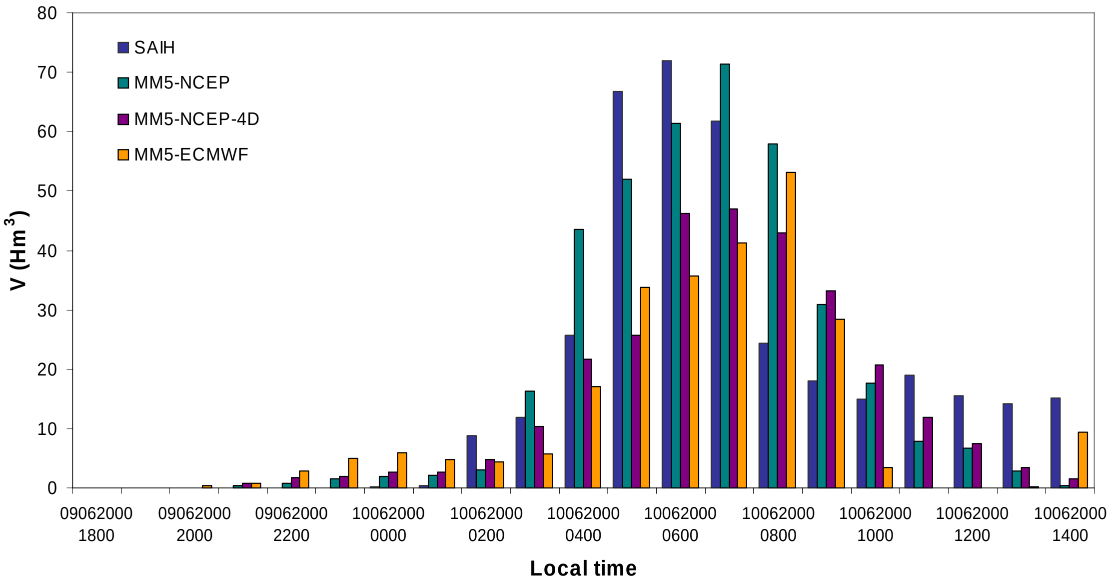

Figure 3.11: Temporal sequence, at 1h time steps, of accumulated volume in the Llobregat basin during the 'Montserrat' event, from SAIH rain-gauge, MM5-NCEP, MM5-NCEP-4D and MM5-ECMWF simulations.

3.6.3 Ensemble of MM5-perturbed driven runoff simulations

Following the PV inversion method described in subsection 2.3.2 and section 3.5, four additional mesoscale runs (-5% PV, +5% PV, WEST and EAST) are performed in order to produce MM5-perturbed driven runoff simulations. These simulations, together with the previously referenced experiments MM5-NCEP, MM5-NCEP-4D and MM5-ECMWF, become a useful experimental dataset to investigate the effects of the uncertainty of the mesoscale model initial conditions on the hydrometeorological chain. It is well-known (e.g. Ferraris et al., 2002) that even slight spatial and temporal errors of the rainfall pattern can have a significant impact on the response of small catchments (up to hundreds of km^2). However, the spatio-temporal gap between operational meteorological model outputs, and the required hydrological model inputs, should be considerably smoothed for a basin of medium size (thousands of km^2). The results in the last section showed that the Llobregat basin was reasonably capable of filtering the forecast rainfall errors as long as the main rainfall nuclei lie within the catchment (tables 3.8 and 3.9). Our hypothesis is that the basin should be relatively insensitive to realistic perturbations of the rainfall field introduced through the PV inversion method, and therefore the predictability of flash-flood events should be appreciable in this medium size catchment. The use of ensemble strategies like the one tested here should provide a very useful probabilistic approach to the problem in the context of real-time operations.

Figures 3.12 and 3.13 display the spatial distributions of accumulated rainfall volume for the perturbed experiments. The -5% PV and WEST simulations (figs. 3.12a and c) are fairly similar to the observed rainfall pattern (fig. 3.9a), such that the spatial goodness-of-fit statistical indices of forecast rainfall outperform the results of the reference MM5-NCEP simulation. On the contrary, the spatial errors of +5% PV and EAST simulations are greater than in the reference experiment (table 3.9). It seems, then, that a weaker or more distant upper-level precursor trough benefits the rainfall forecast of the Montserrat event. Pressumably, the resulting slower-moving surface cyclone is more representative of the actual disturbance.

Furthermore, the whole ensemble of perturbed experiments slightly underestimates the total water collected over the Llobregat basin as it occurred with MM5-NCEP, although the -5% PV slightly improves the control simulation, with only 11.6 hm^3 below the observed value (table 3.10). The underestimation of precipitated volume is particularly severe in the Anoia subcatchment, where only the -5% PV run is able to produce appreciable values of rainfall (fig. 3.12). Even so, the runoff simulation at Sant Sadurní gauge is rather poor, albeit for the rest of the ensemble dataset, runoff is not produced at all (table 3.12). In addition, tables 3.9 and 3.11 and figure 3.14 exhibit a certain uniformity in the temporal distributions of the rainfall volume for the perturbed experiments. Nevertheless, none of these prove to be superior in the temporal evolution to the control simulation. It is interesting to note that the ensemble of simulated rainfall fields exhibits a larger heterogenity in space than in time (compare the respective NSE indices; table 3.9).

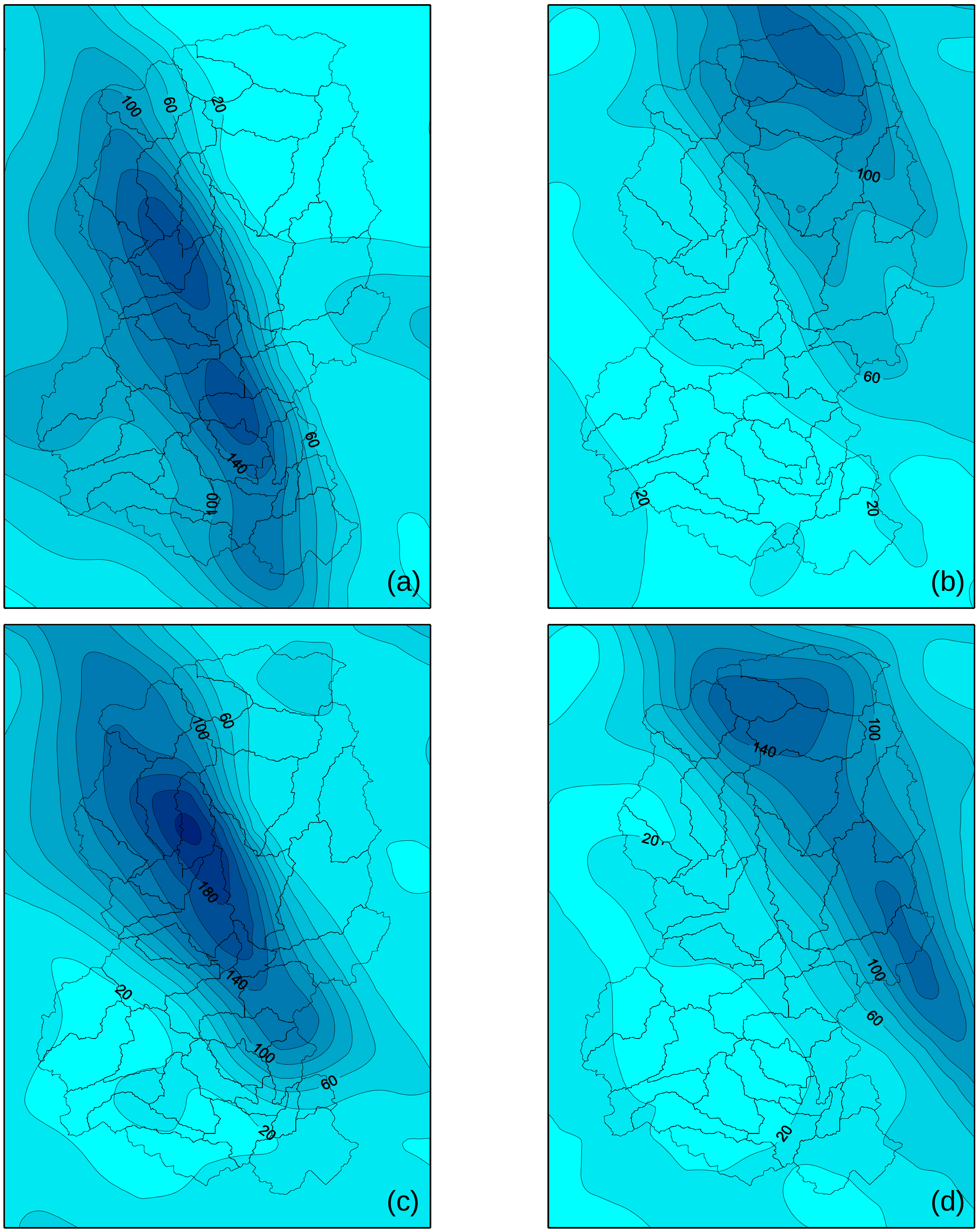

Figure 3.12: Spatial distribution of accumulated rainfall during the 'Montserrat' event in the Llobregat basin, from: (a) -5% PV, (b) +5% PV, (c) WEST, and (d) EAST simulations. Contour interval is 20 mm starting at 20 mm.

(a)

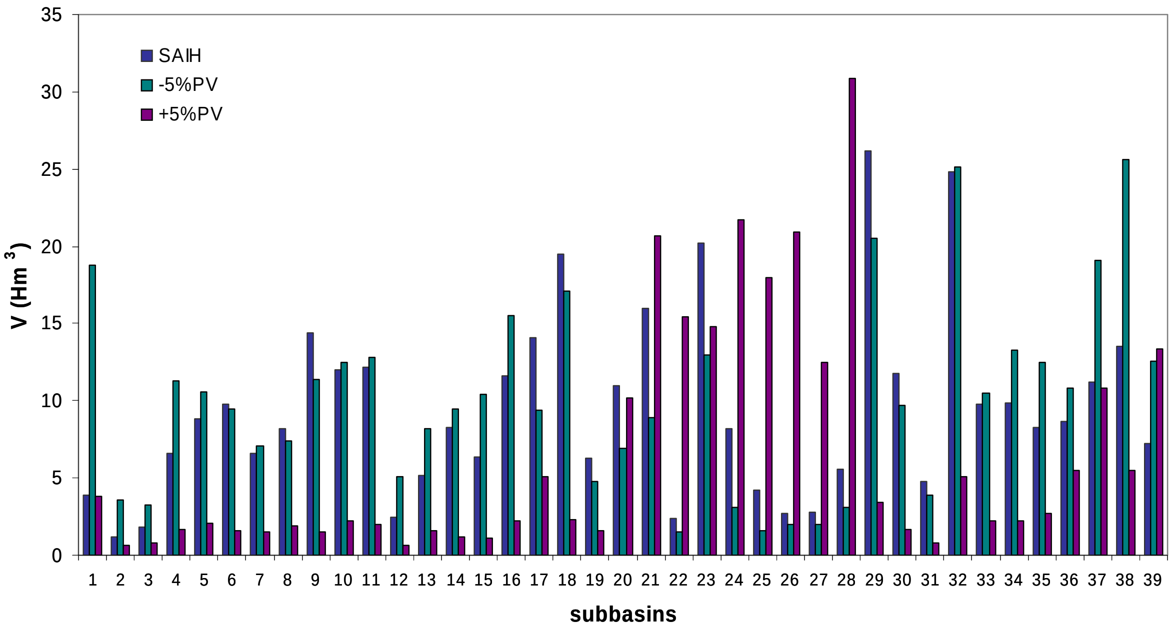

(b)

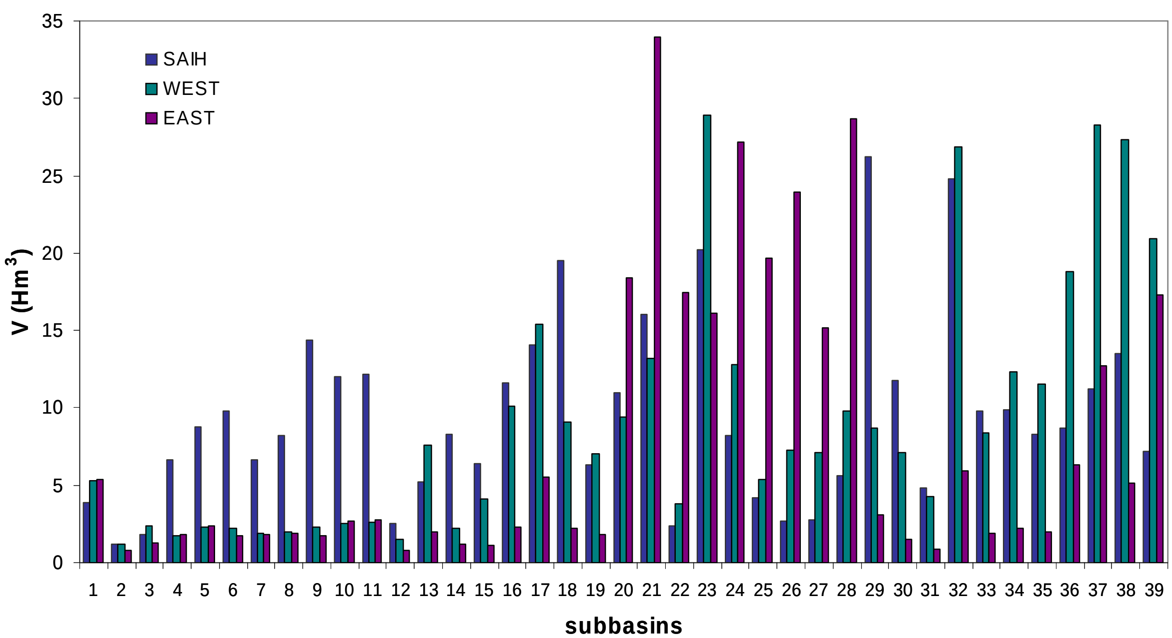

Figure 3.13: Accumulated volume during the 'Montserrat' event, per subcatchment of the Llobregat basin, from: (a) SAIH rain-gauges, -5% PV, and +5% PV simulations, and (b) SAIH rain-gauges, WEST, and EAST simulations.

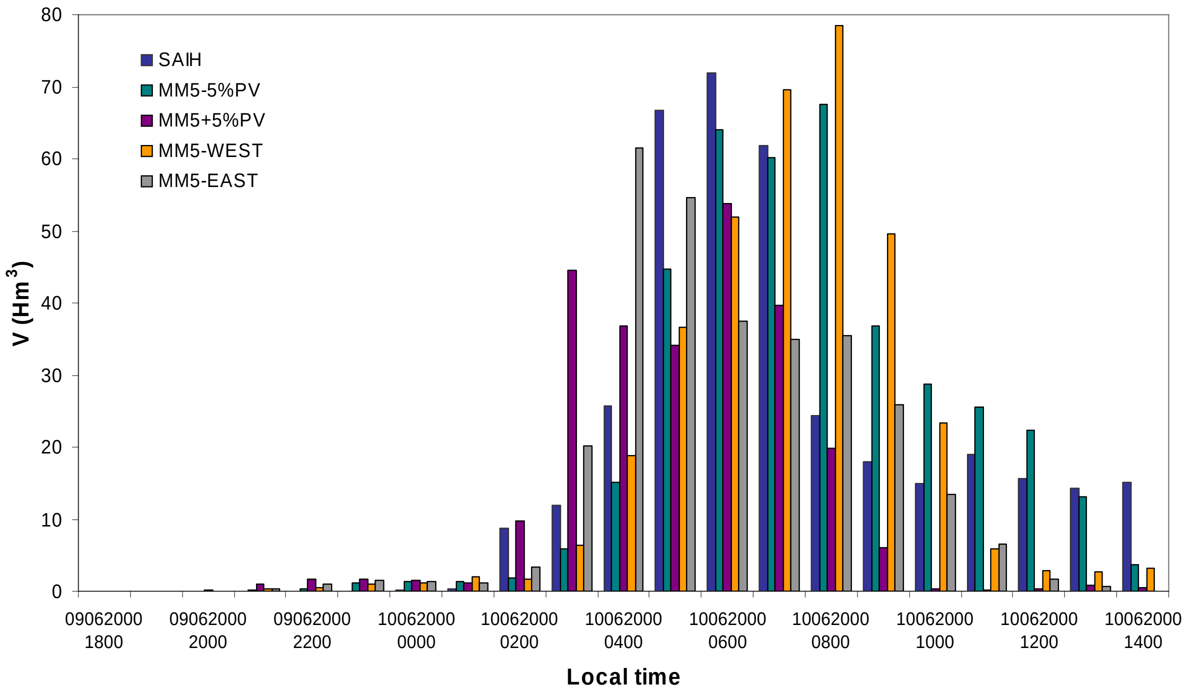

Figure 3.14: Temporal sequence, at 1h time steps, of accumulated volume in the Llobregat basin during the 'Montserrat' event, from: SAIH rain-gauges, -5% PV, +5% PV, WEST and EAST simulations.

Finally, table 3.12 summarizes the statistical indices at the five stream-gauges for the ensemble of perturbed runoff simulations. At small basin scales, the skill is rather low owing to the lack of coherence among the meteorological and hydrological spatio-temporal scales (figures not shown). But at larger scales, the skill of the ensemble to forecast the discharge is considerably improved (figs. 3.15a, b and c), to the extent that different members of the ensemble outperform the control simulation at different stream-gauges (e.g. Castellbell and Abrera). These results demonstrate the value of an ensemble strategy in order to obtain a higher confidence interval in mesoscale model driven rainfall-runoff forecasts and to enact the appropriate emergency directives.

		-5%PV	*+5%PV*	*WEST*	*EAST*
Súria	***NSE***	-0.62	-0.25	-7.97	-0.18
	% EV	75.6	-97.5	191.3	-86.4
Sadurní	***NSE***	-0.17	-0.12	-0.12	-0.12
	% EV	-33.9	-100	-100	-100
Castellbell	***NSE***	0.71	0.48	0.21	0.56
	% EV	-19.5	-31.0	20.1	12.8
Abrera	***NSE***	0.93	0.28	0.72	0.51
	% EV	-5.1	-41.8	7.6	-4.7
Despí	***NSE***	0.53	0.13	0.56	0.34
	% EV	2.8	-58.1	-17.9	-31.1

Table 3.12: NSE efficiency criterion and percentage of error in volume (% EV) at the five stream-gauges, for the set of MM5-perturbed driven runoff simulations.

Essentially, the full set of driven runoff simulations does not exhibit any strong degradation of the forecast skill, not accounting for the ECMWF analysis driven simulation. It appears, then, that this catchment as a whole is relatively insensitive to typical errors of the forecast rainfall, like spatial shifts of a few tenths of kilometers and temporal shifts of not more than 1-2 hours. The relative insensitivity of the Llobregat basin is surely a consequence of its medium size, and it is only lost for the smallest subbasins or when the heavy rainfall affects external hydrographic areas as for the ECMWF experiment. The filtering behaviour of rainfall uncertainty found for the Llobregat basin in this case could also be raised by the moderate urbanization density and the relatively high predictability of the responsible mesoscale convective system. For smaller basins intercepting significant urban areas or with very local thunderstorms the capability of filtering the rainfall uncertainty is generally not found (Gómez et al., 1998).

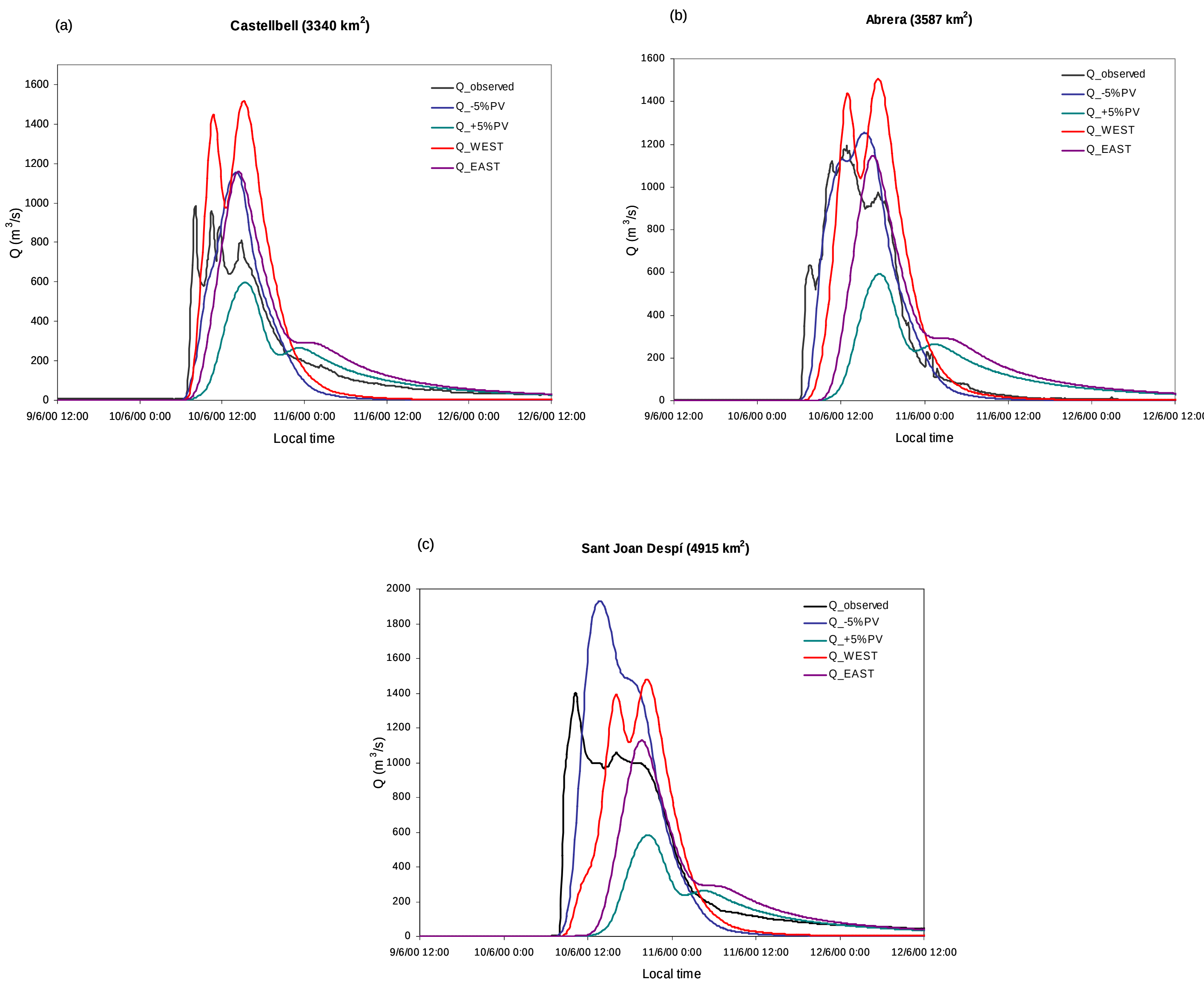

Figure 3.15: Observed, -5% PV simulation driven, +5% PV simulation driven, WEST simulation driven and EAST simulation driven runoff discharge at: (a) Castellbell, (b) Abrera and (c) Sant Joan Despí.

3.7 Conclusions

This chapter has analysed the feasibility of runoff simulations driven by numerical weather prediction mesoscale models over the Llobregat basin, characteristic of the Spanish Mediterranean environment, in an attempt to understand the sensitivity of the basin response to forecast errors, and help to gain additional lead times for warning and emergency procedures before flash flood situations. The effects of different spatial and temporal rainfall field scales on the basin response has been studied by breaking down the basin in three different segmentations and by considering three temporal scales in a set of six experiments. A configuration considering 39 subbasins division together with hourly temporal rainfall field discretization optimizes the basin response for the 'Montserrat' event. It appears that this result is particularly related to the current density of rain gauges available within or very near the catchment. Similar tests and a re-calibration of the runoff model should be applied using a long sample of mesoscale rainfall forecasts rather than rain-gauge information in order to properly optimize the numerical system for operational purposes, but this task is beyond the objectives and capabilities of the present study.

Hazardous events present short recurrence periods in Mediterranean Spain as a whole, and the 'Montserrat' event analysed in this study is a forceful proof of their possible consequences. Using NCEP and ECMWF analyses to initialize the hydrometeorological chain, it was possible to obtain, at least at the basin outlet, reasonable runoff forecasts with up to 12-48 hours lead times in the first case. These control runs were complemented by an ensemble of driven rainfall-runoff simulations which showed to be useful to derive conclusions in depth. With the ensemble of MM5-NCEP perturbed simulations, it was possible to reduce the biases at some sites, as Castellbell and Abrera, where the control simulation would have not produced enough accurate runoff forecasts.

The set of perturbed mesoscale simulations was also introduced to address the effects of the meteorological external-scale uncertainty. This source of uncertainty was reflected on the spatial and temporal distribution of the rainfall pattern in the Llobregat basin, with shifts of tenths of kilometers in the position of the heavy rainfall cores and changes of about 1-2 hours in their timing, in some cases outperforming the control run. Interestingly, the basin rainfall-runoff mechanisms were shown to smooth to a high degree the above spatial and temporal differences, thus enhancing, at least for this case, the predictability of flash floods in the Llobregat basin considering the entire catchment and the typical magnitude of mesoscale rainfall output errors. Nevertheless, one of the simulations of the ensemble –the MM5-ECMWF run– exhibited very poor results, and used in a deterministic hydrometeorological system, would have missed completely the hazardous event and inhibit any standard emergency procedure. This is a good example where a simple multi-analysis ensemble prediction system (EPS) accounting for the forecast variance associated to the initial conditions uncertainty would have been found of great value to trigger special flood warnings. However, to further extend the derived results, rainfall forecast errors found in existing mesoscale models should be examined for their typical magnitude and variability in space and time. Obviously, the higher performance of the NCEP-based simulations is simply a particularity of the 'Montserrat' meteorological situation, and not an inherent aspect of this analysis dataset. It is reasonable to expect that the high resolution of ECMWF analyses would generally benefit nested mesoscale numerical forecasts in the region.

The precise hydrological response of a catchment to rainfall events, in terms of the induced runoff, is strongly determined by the spatial and temporal variability of the soil properties. The infiltration mechanism acts as a highly non-linear filter in the rainfall-runoff transformation and it has been modeled as an integrated process over each subbasin at discrete time-steps. The model parameters related with this mechanism and with the flood wave routing have been calibrated using five events. These events are characterized by important discharges and high velocities of the associated flood waves, but the lack of flow data at some flow-gauges for some of these events has posed difficulties in the basin calibration. In order to improve the reliability and skill of the rainfall-runoff model before such hazardous episodes, it would be desirable to get more information of other flash-flood events affecting the Llobregat basin. The expected future increase of the number of recorded cases in the SAIH database, and a larger number of stream-gauges operating in the basin, will then permit an improvement of the basin configuration and the forecast and alert schemes.

Chapter 4

FOUR INTENSE PRECIPITATION EVENTS OVER MAJORCA ISLAND, SPAIN

4.1 Introduction

As first objective of this chapter[1], a hydrometeorological modeling study is designed in order to assess the feasibility of high-resolution mesoscale model driven runoff simulations for a small-size basin of Majorca, Balearic Islands. Four intense precipitation events which caused flood events of different magnitude over the Albufera basin, with a drainage area of 610 km^2, are analysed. The lack of flow measurements in the basin poses great difficulties to the evaluation of the HEC-HMS rain gauge driven runoff simulations. Therefore, the rainfall-runoff model is run under the assumption that a best estimation of the hydrological model parameters, mainly related with the infiltration properties of the watershed, can be obtained from the high resolution observational campaign developed by the Coordination of Information on the Environment (CORINE) Land Cover (CLC) project. MM5 is used to provide quantitative precipitation forecasts (QPFs) for the events. The MM5 driven runoff simulations are compared against stream-flow simulations driven by the rainfall observations, thus employing the hydrological model as a validation tool.

In the last decade, an important methodology has been implemented in order to improve the short-range QPFs: the use of an ensemble of model forecasts in order to further extend the space of possible outcomes. The aim of ensemble forecasting is to predict the probability of future weather events as completely as possible. This is motivated by the fact that forecasts are sensitive to both uncertainties in the initial and boundary conditions, and model errors. Model contributions to these uncertainties are mainly due to the imperfect representation of the atmospheric physical processes in the model (Tribbia and Baumhefner 1988). This issue is of major importance when the forecast is concerned with the precise locations and amounts of rain at small scales, which are directly affected by the uncertainties in the model parameterization schemes for the convection and moist microphysical processes (Kain and Fritsch 1992, Wang and

[1] The content of this chapter is based on the paper Amengual, A., R. Romero and S. Alonso, 2008: Hydrometeorological ensemble simulations of flood events over a small-size basin of Majorca Island, Spain., *Q. J. R. Meteorol. Soc.*, (conditionally accepted).

Seaman 1997). It appears that the sensitivity of forecast accuracy to model parameterizations must be addressed for short-range forecasts involving convective events (Stensrud et al. 2000). Examples of the use of a multiphysics ensemble strategies in order to take into account the model imperfections are widely described, for example, in Stensrud et al. (2000) and Jones et al. (2007). In this approach, different model physical parameterization schemes are combined to build varied versions of the mesoscale model and to produce an ensemble of simulations that start for the same initial condition. An inherent assumption is that all the mesoscale model configurations are equally skillful. If one of the model configurations is significantly less skillful than the others, then the ensemble members should be weighted unequally to obtain the best results. However, several studies have not found substantial differences in model performance by using different well-tested physical schemes of the MM5 model in simulating diverse meteorological processes (Wang and Seaman 1997; Stensrud et al. 2000; Bright and Mullen 2002; Zhang and Zheng 2004).

Following the aforementioned methodology, the second objective of the paper consists of assessing the sensitivity of the small-scale features of the precipitation simulations to the uncertainties in the approximations of the physical parameterizations included in the MM5 mesoscale model. An ensemble of MM5 experiments combining different parameterizations of cloud microphysics, moist convection and boundary layer parameterizations has been adopted, using large-scale analyses –rather than forecast data– as initial and boundary conditions in order to minimize the synoptic scale errors (further details in section 4.4). Furthermore, to study the impact of the large-scale uncertainties in the mesoscale model performance, MM5 has been forced by using different initial and boundary conditions for one of the case studies. This test is a first approximation to assess the relative importance of these inaccuracies when compared with the errors coming from the model formulation for short-range modeling systems. The value of probabilistic hydrometeorological chains versus deterministic approaches when dealing with flood situations in the area will also be determined from the ensemble of MM5 driven HEC-HMS simulations. In addition to using a best guess for the MM5 initial and boundary conditions, other sources of uncertainty acting in the problem such as the hydrological model configuration will not be considered in the present study. That is, the rainfall-runoff model will be treated under the perfect-model assumption and 'ideal' knowledgement of the synoptic scale dynamical forcing, in order to focus the study exclusively on the impacts of the NWP model formulation errors.

The validation of high-resolution precipitation fields is not straightforward, particularly for extreme events. If rain-gauge networks are not dense enough, these are not able to resolve the small-scale features of the highly variable precipitation fields driving floods. These limitations must be especially considered in this study, since we are dealing with a small size basin –partially located in a mountainous area– with a scarce number of automatic rain-gauge stations and where meteorological radar is not available. Furthermore, a point comparison among the observed and simulated rainfall fields is not always appropriate for hydrological purposes. In this study, the performance of the spatial and temporal distributions of the simulated rainfall fields are examined against the observed rainfall patterns at catchment scale by using a set of continuous and categorical verification indices over the subbasins, which are employed as spatial integrated surfaces. Furthermore, the discharge experiments resulting from the one-way coupling between the meteorological and hydrological models have been compared with the rain-gauge driven runoff simulations, thus employing the hydrological model as an advanced validation tool. This approach has been found especially suitable for the evaluation of high-resolution simulated precipitation fields (Benoit et al. 2000; Jasper and Kaufmann 2003; Chancibault et al. 2006).

Section 4.2, contains a brief description of the study area; section 4.3 describes the selected intense rainfall episodes; sections 4.4 and 4.5 explain, respectively, the meteorological model applied to forecast the events and to design the ensemble of mesoscale simulations, and the hydrological tools used for the basin characterization; section 4.6 presents and discusses the results; and finally, in section 4.7 we provide an assessment of the used methodology.

4.2 The study area

4.2.1 Overview of the Albufera basin

The Albufera basin is the most important of the hydrographic catchments in the Balearic Islands in terms of size, river length, mean flow and socio-economical activities. It is located in Majorca, the biggest of the Islands, and is composed of the Almedrà and Sant Miquel ephemeral river basins. The Albufera basin extends from the Tramuntana range, with heights close to 1500 meters, to the central plain. This central plain constitutes the main agricultural area of Majorca. The last sections of both ephemeral rivers flow into the Albufera's natural park, a natural wetland located in the north-eastern part of the basin, extending over an area of 17 km^2. The main economic activities in the catchment area are: tourism in the basin coast line, which is the leading activity, and agriculture in wide areas of the central plain (MEDIS, 2006). Although the Albufera river basin has a whole extension of 610 km^2, we have modeled the catchment upstream from the junction of the Almedrà and Sant Miquel rivers in the natural wetland, with a drainage area of 607.4 km^2 and a maximum length of 42.1 km (fig. 1.6). The Sant Miquel river basin (141.7 km^2) can be classified as mountainous, characterized by steep streams, short times of concentration and high flow velocities. On the contrary, the Almedrà river basin (465.7 km^2), although in part composed of elevated terrain, mainly flows through the central plain of Majorca, an area with moderate slopes and consequently with higher times of concentration and lower flow velocities.

Furthermore, the hydrographic catchment is divided into several climatic areas owing to the diversity of the pluviometric records imposed by the varying altitude. Annual rainfall in the Albufera basin can range from quantities exceeding 1000 mm in the Tramuntana range (over 900 meters) and 700 mm over pre-mountainous areas (with elevations comprised between 500-900 meters), to about 600 mm in the plain area. The rainfall regime is typical of the Mediterranean regions, with most of the heavy rainfall episodes occurring from September to December, but with occasional events in spring and winter. These extreme daily rainfall episodes can represent a large fraction of the annual amounts.

4.2.2 The rain-gauge network

Raw precipitation data consists of 24-h (0700-0700 UTC) accumulated values at 140 climatic stations from the Spanish Institute of Meteorology (INM) deployed in the Balearic Islands (see fig. 1.6 for the localization of the Majorca stations). Out of the 140 stations, about 40 lie inside or near the watershed boundaries. In addition, precipitation is recorded every 10 minutes in 12 additional automatic rain-gauges of the system (emas in fig. 1.6). The emas located inside or very close to the Albufera basin have been used, first, to accumulate the 10-min series into 1-h series and, second, to build hourly series for the rest of the INM network. Thus, the temporal frequency of the precipitation data has been increased to permit hydrological applications. To downscale the daily accumulations into hourly values using the emas 1-h series, the following inverse-distance weighted equation on each day of the selected flood episodes has been applied:

$$p_{st_j}(t) = \frac{\sum_i \left(\frac{p_{emas_i}(t)}{d_{emas_i,st_j}} \frac{P_{Tst_j}}{P_{Temas_i}} \right)}{\sum_i \frac{1}{d_{emas_i,st_j}}}$$

where $p_{st_j}(t)$ is the derived hourly value at time-step t for the daily j station; $p_{emas_i}(t)$ is the 1-h value at the automatic station i at time-step t; P_{Tst_j} is the 24-h accumulated value at the station j; P_{Temas_i} is the daily accumulation at the emas i; and d_{emas_i,st_j} is the distance between the daily j station and the i emas. Therefore, it has been considered as a reasonable approximation that the rainfall temporal distributions at daily stations and neighbour emas should not differ significantly owing to the typical size of the meteorological disturbances driving to large rainfall amounts (see next section). It is worth to note that the spatial distribution of automatic and daily rain-gauges covers reasonably well the different climatic areas of the basin.

4.3 Description of the intense precipitation episodes

Romero et al. (1999) presented a classification of the atmospheric circulation patterns producing significant daily rainfall in the Spanish Mediterranean area. The study pointed out the synoptic-scale disturbances bearing important rainfall accumulations over the Balearics, as the four intense precipitation episodes under study. These were characterized by low pressure centers to the east of the Islands and cold cut-off lows at mid-upper tropospheric levels. Their circulation at lower levels over northern Majorca had a general southeast-northwest pressure gradient, which imposed a northerly or north-easterly surface wind regime (fig. 4.1). The Albufera river basin was directly affected by substantial rainfall accumulations, specially its upper part (fig. 4.2). Next, a brief description of the synoptic situations and the derived rainfall distributions for each of the cases is provided (figs. 4.1 and 4.2):

- Case 1 (*7-10 October 1990, first phase*): this was a long episode that lasted about 72 h and for practical reasons has been split in two different phases. The first phase consisted of a mid-upper level cold cut-off cyclone located to the south-west of the Balearics. The associated low-level cyclone provided a north-easterly surface current towards Majorca (figs. 4.1a, b). The high rainfall rates observed, with accumulated values above 100 mm from 1600 to 1800 UTC on 8 October and total accumulations during the first 48 h over 240 mm (fig. 4.2a), together with the fact that the heavy rainfall fell over the northern part of the basin, resulted in a flash-flood over the Sant Miquel catchment and the last sections of both rivers, with hazardous effects for the coastal urbanizations.

- Case 2 (*7-10 October 1990, second phase*): during the last stage of this episode, the depression at 500 hPa level remained stationary but weaker (fig. 4.1c). At low levels, the southeast-northwest pressure gradient maintained the north-easterly surface current (fig. 4.1d). This second phase was characterized by a brief duration, a few hours, but with extraordinary rainfall rates which accumulated an hourly maximum close to 115 mm at 2200 UTC on 9 October. The rainfall spatial distribution was quite similar to the first phase of the episode, but with a slight south-westward shift. Thus, the whole north-eastern part of the basin was affected by the sudden event with cumulative rainfall amounts over 235 mm. The heavy precipitation was caused by an intense convective system which remained quasi-stationary over the same specific area. The subsequent flash-flood affected several locations along the rivers, but again, the coastal dwellings were the most damaged (fig. 4.2b).

- Case 3 (*10-11 November 2001*): this case produced accumulated precipitation values close to 240 mm in 24 h, mainly distributed between 10 November 2000 UTC and 11 November 0500 UTC, and total amounts up to 400 mm. During the event, the whole basin collected substantial quantities of precipitation, although the mountainous range was the most affected (fig. 4.2c). At 500 hPa, two embedded depressions in the large-scale trough were located to the south of the Iberian Peninsula (fig. 4.1e). The low level cyclone was placed to the south-east of the Balearics over a zone of marked baroclinicity (fig. 4.1f). The associated strong winds produced a severe sea storm, substantial material losses and four fatalities.

- Case 4 (*3-4 April 2002*): the episode was characterized by accumulated precipitations over 230 mm in 24 h and total amounts in the period near 300 mm. The maximum amounts were recorded upon the Tramuntana range between 03 April 1730 UTC and 04 April 0930 UTC. The observed rainfall pattern is quite similar to the last case, but with lower rainfall collected over the Albufera basin (fig. 4.2d). The mid-upper tropospheric low was sited over the Western Mediterranean very near the Balearics (fig. 4.1g). The associated surface cyclone was located to the east of the Balearic Islands, providing northerly winds over the Albufera river basin. (fig. 4.1h).

The four cases are a sample of different heavy rainfall episodes which resulted in floods of diverse spatial and temporal scales. The first two cases produced exceptional and sudden rising flows owing to their convective nature; the last two cases were an example of more sustained, stratiform-like precipitation rates over longer periods but which also drove to notable discharges at the Albufera basin outlet.

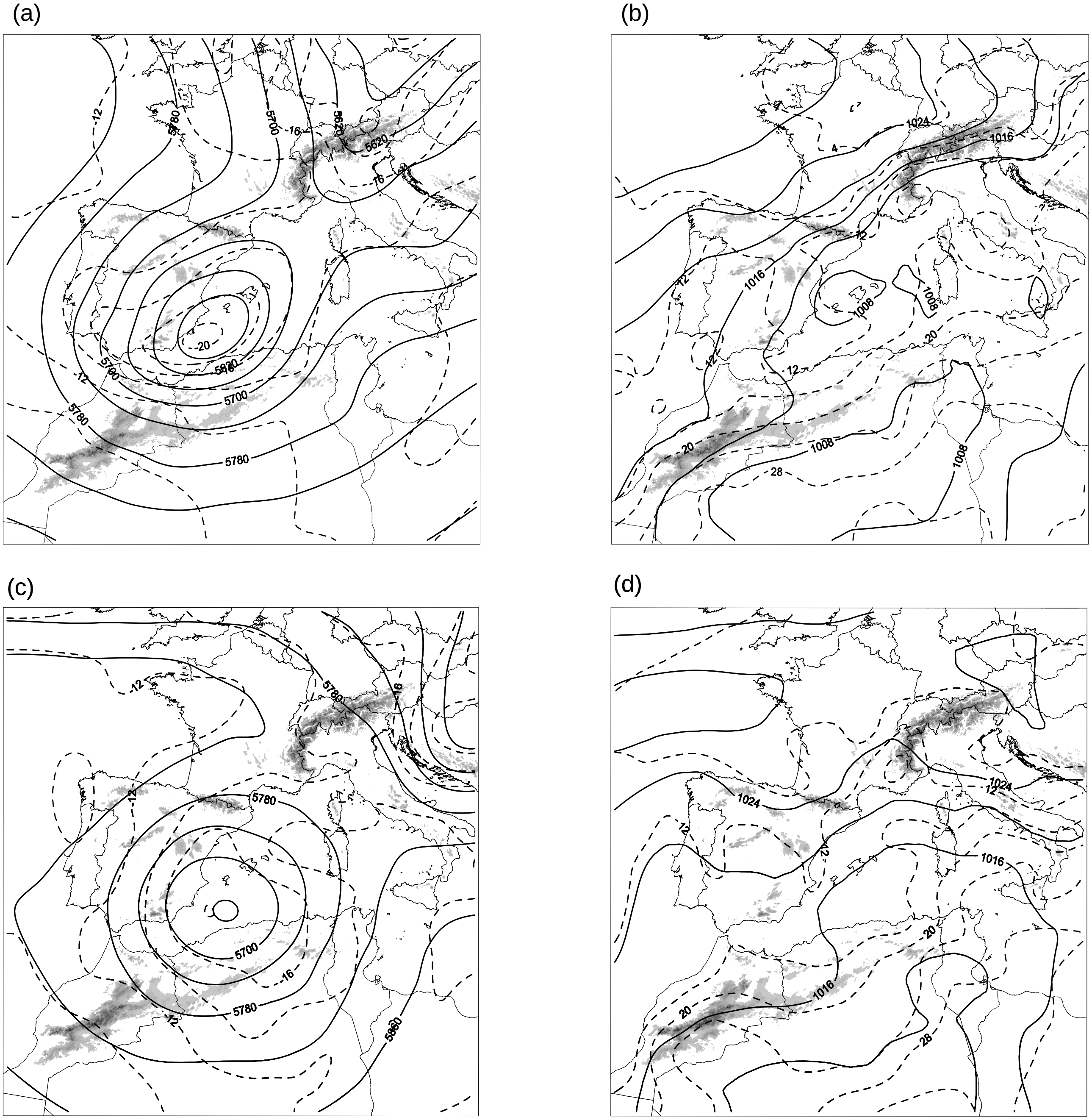

Figure 4.1: ECMWF analyses maps. Geopotential height (continuous line, in gpm) and temperature (dashed line, in ^{0}C) at 500 hPa for: (a) 8 October 1990 at 1200 UTC, (c) 9 October 1990 at 1200 UTC, (e) 11 November 2001 at 0000 UTC and (g) 4 April 2002 at 0000 UTC. Sea level pressure (continuous line, in hPa) and temperature at 925 hPa (dashed line, in ^{0}C) for: (b) 8 October 1990 at 1200 UTC, (d) 9 October 1990 at 1200 UTC, (f) 11 November 2001 at 0000 UTC and (h) 4 April 2002 at 0000 UTC. Main orographic systems are highlighted

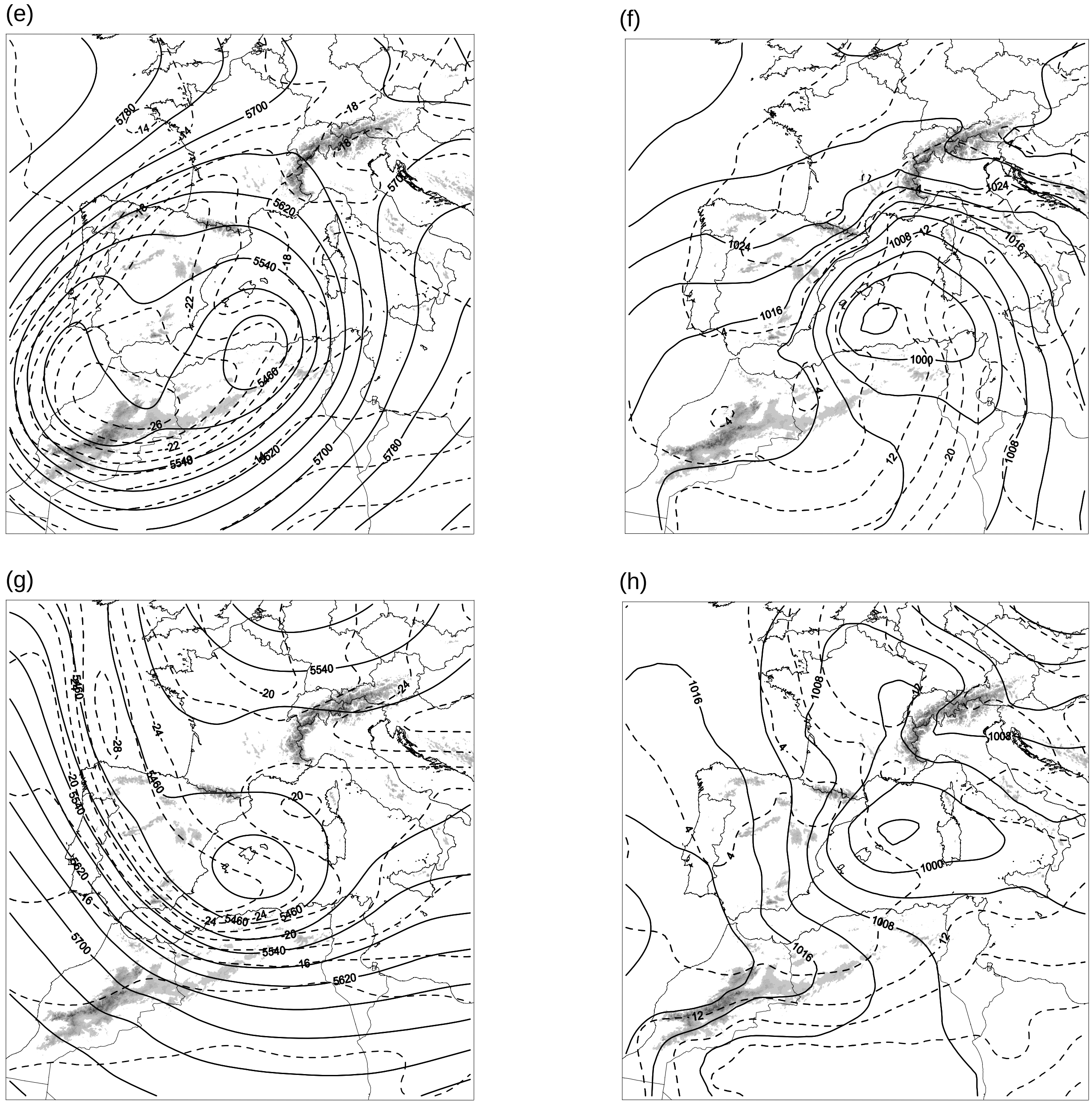
(e)
5780
5700
5620
5540
5460
-14
-18
-22
-26
(f)
1024
1016
1008
1000
4
12
20
(g)
5460
5540
5620
5700
-20
-24
-28
20
16
(h)
1016
1008
1000
4
12

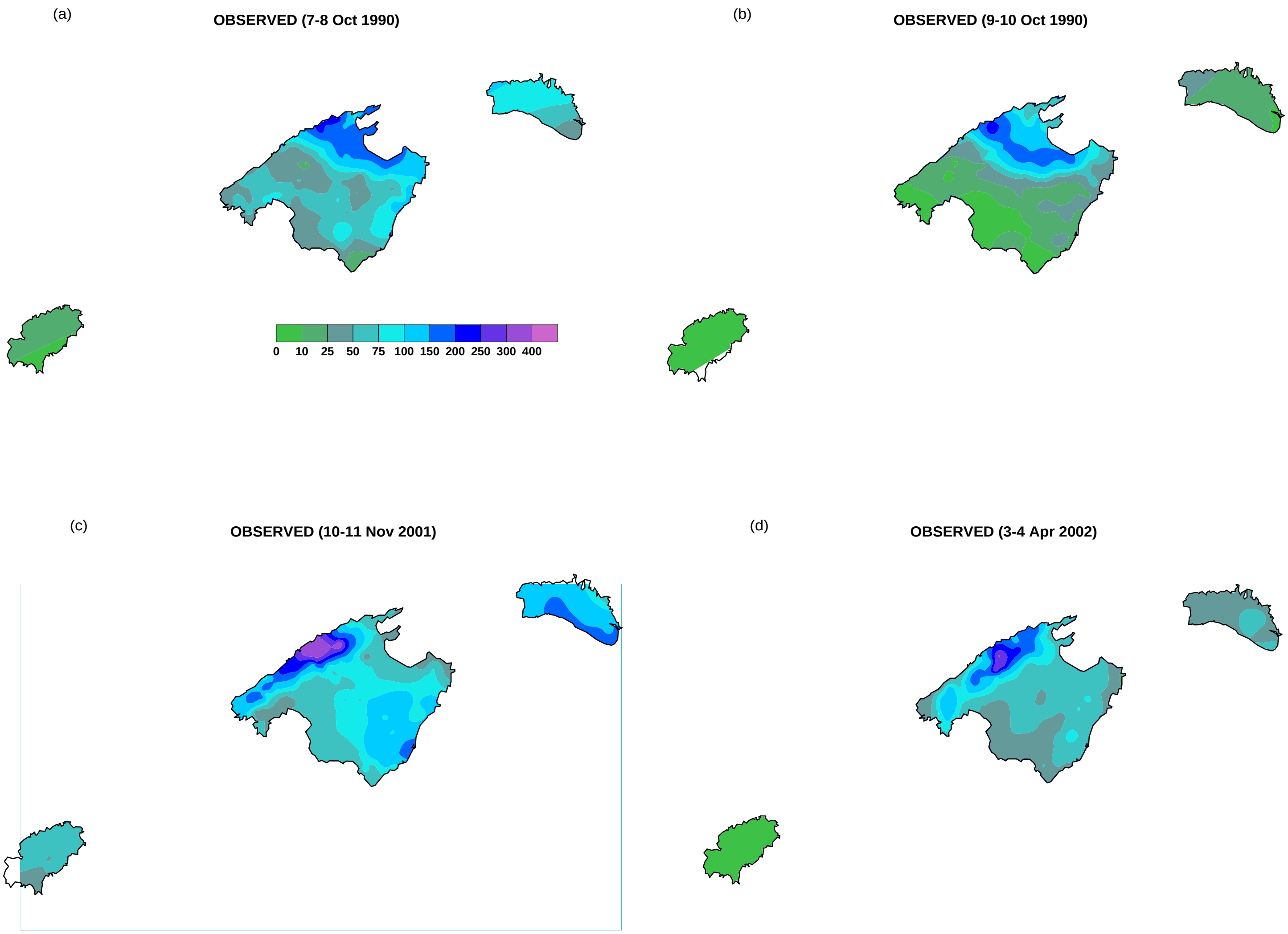

Figure 4.2: Observed accumulated precipitation (in mm according to the scale) for: (a) 7-8 October 1990 (first phase), (b) 9-10 October 1990 (second phase), (c) 10-11 November 2001 and (d) 3-4 April 2002 episodes

4.4 Meteorological tools

MM5 model is used to perform the meteorological simulations (further details in section 2.3). The model domains are configured as in the real-time operational version used at the University of the Balearic Islands (UIB; see http://mm5forecasts.uib.es). Simulations are designed using 24 vertical σ-levels and three spatial domains with 121×121 grid points centered at the Balearic Islands (fig. 4.3). Their respective horizontal resolutions are 22.5, 7.5 and 2.5 km. In particular, the finest domain spans the entire Balearic Islands and the surrounding sea region, and it is used to supply the high-resolution rainfall fields to drive the hydrologic simulations. The interaction between the domains follows a two way nesting strategy.

For the initialization and provision of boundary conditions, large-scale analyses are interpolated to the MM5 coarse domain: ECMWF analyses are used for all the cases and an additional experiment for 10-11 November 2001 episode using NCEP analyses is also included. The latter serves as a test of the sensitivity of high-resolution rainfall simulations to the initial conditions (further details in sections 2.3 and 3.5). The control simulation of the four episodes follows the same physics options as the UIB operational runs. To represent the moist convection effects, the Kain-Fristch parameterization scheme is used in the large domain, while convection is explicitly resolved in the second and third domains owing to the high horizontal resolutions. Explicit microphysics, PBL, surface temperatures over land and sea and long and short wave radiative processes are calculated as explained in sections 2.3 and 3.5. It is worth to highlight that these control simulations are not intended neither to be the most commonly used configuration for the MM5 model nor to have the best model skill for the study cases, but simply to identify the configuration used in the UIB operational runs.

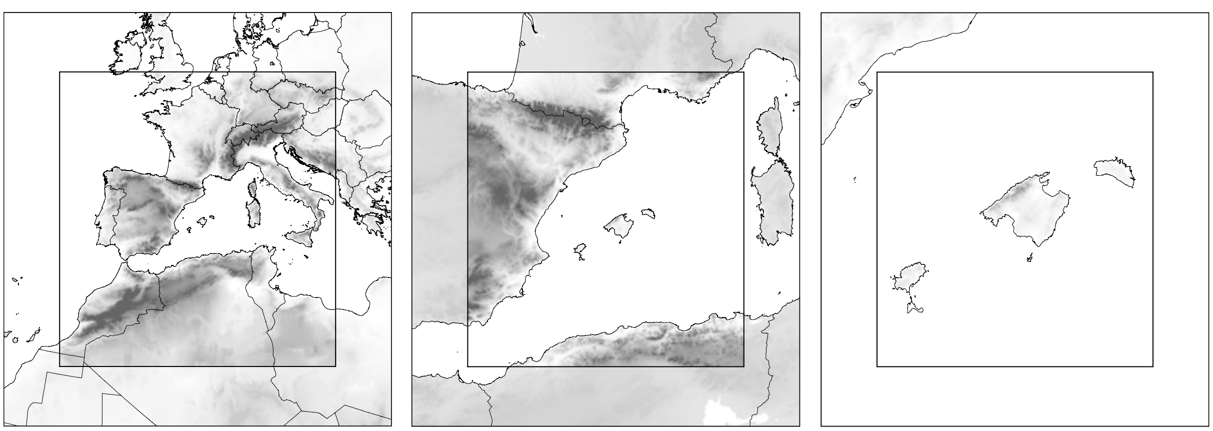

Figure 4.3: Configuration of the three computational domains used for the MM5 numerical simulations (inner square, with horizontal resolutions of 22.5, 7.5 and 2.5 km from left to right, respectively)

In addition to the control MM5 simulations, the multiphysics ensemble is carried out by means of different combinations of three model's physical parameterizations (explicit microphysics, moist convection and boundary layer schemes) trying to better encompass the atmospheric processes leading to the high precipitation amounts. Based on previous research, the Hong-Pan parameterization scheme (option 5 in MM5 model) was selected for the boundary layer turbulence and kept fixed. Then, the multiphysics ensemble is defined as all possible combinations of five well-tested explicit moisture schemes (options 4, 5, 6, 7 and 8 in the model) and the inclusion, or absence, of the Kain-Fritsch convection scheme (option 8 in the MM5 model) in the second domain (section 2.3). That is, since it is uncertain whether a 7.5 km resolution can resolve convection appropriately without a convection scheme, experiments with and without parameterized convection in the second domain have been designed to account for this issue. In summary, the ten resulting experiments are labelled as follows:

1. Microphysics schemes (4, 5, 6, 7 and 8) + Hong-Pan scheme (5) + Kain-Fritsch convection scheme in the first domain: Simple Ice (MM5-4-5), Mixed-phase (MM5-5-5), Graupel (MM5-6-5), Reisner-Graupel (MM5-7-5; **control**), and Schultz (MM5-8-5)

2. Microphysics schemes (4, 5, 6, 7 and 8) + Hong-Pan scheme (5) + Kain-Fritsch convection scheme (8) also in the second domain: MM5-4-5-8, -5-5-8, -6-5-8, -7-5-8 and -8-5-8 respectively

All these MM5 simulations comprise a 48 hour forecast period covering each of the flood episodes under study: three sets of experiments are performed to better encompass the 7-10 October 1990 episode (cases 1 and 2) starting at 0000 UTC on 7, 8 and 9 October 1990; the simulations for case 3 start at 0000 UTC on 10 November 2001; and finally, for case 4, simulations begin at 0000 UTC 3 April 2002.

4.5 Hydrological tools

This study is carried out using the physically-based HEC-HMS rainfall-runoff model and it has been implemented in a semi-distributed and event-based configuration (section 2.2). Figure 1.6 depicts the digital terrain model for the Albufera watershed together with the main watercourses forming the Almedrà and Sant Miquel river basins. The whole watershed has been segmented into 35 subwatersheds with an average size of 17.4 km^2 and a total extension of 607.4 km^2 at the junction of the Almedrà and Sant Miquel rivers (fig. 1.6). HEC-HMS is forced using a single hyetograph for each subbasin. This hyetograph is built in two steps: first, a rainfall spatial distribution is generated from 1-h accumulated values at INM rain-gauges (see subsection 4.2.2 and fig. 1.6) using the kriging interpolation method with a horizontal grid resolution of 250 m; and then, the temporal rainfall series is calculated for each subbasin as the areal average of the gridded rainfall within the subcatchment. The same methodology is used to assimilate forecast rainfall fields in HEC-HMS (section 4.6), except that atmospheric model grid point values are used instead of the INM network observations.

The hydrologic model set-up is identical to this explained in section 2.2 and subsection 3.4.1. The Albufera basin contains one reservoir located in the upstream area of the Almedrà river (fig. 1.6) but with no contribution downstream, and consequently, it has not been modeled. It is important to remark that the lack of flow measurements in the basin has posed great difficulties to the evaluation of the rain-gauge driven runoff simulations. Therefore, it has not been possible to carry out a calibration and verification task for the model. The rainfall-runoff model has been run under the assumption that a best estimation of the initial model parameters can be obtained from the high resolution observational campaign developed by the CORINE Land Cover project (Bossard et al., 2000). Specifically, the curve numbers and thus, the initial abstractions have been assigned for all the subbasins from that experimental database. The whole set of rainfall-runoff model simulations have been run for a 72 hours period with a 2 minute time-step. These periods comprise completely the four flood events and the subsequent hydrograph tails beginning at: 0000 UTC on 7, 8 and 9 October 1990 for cases 1 and 2; 0000 UTC on 10 November 2001 for case 3; and 0000 UTC 3 April 2002 for case 4.

4.6 Results and discussion

4.6.1 Rain-gauge and MM5-control driven runoff simulations

The stream flow simulations are first driven using precipitation observations in order to assess the performance of the model for the selected episodes. The lack of stream-gauges in the river basin poses great difficulties when the hydrological simulations must be evaluated. The only existing information corresponds to field estimations of the 9-10 October 1990 floods on different locations close to the rivers. The estimated peak discharge for the Sant Miquel river was 260 m^3s^{-1} when it overflew and, for the Almedrà river, was 366 m^3s^{-1} (Grimalt, 1992). These estimated peak flows were calculated from the rivers slopes and maximum wet cross sections measured at different locations on the river basins after the flash-flood. It was applied the empirical Riggs equation when the flood waves were contained within the river channels (Riggs, 1976), and the empirical Williams equation at rivers sites where active flood planes were found (Williams, 1978).

Rain-gauge driven simulation yields maximum discharges of 356 m^3s^{-1} and 346 m^3s^{-1} for the Sant Miquel and Almedrà rivers at the basin outlet, respectively. Thus, it seems that the hydrologic model set-up captures satisfactorily the initial basin conditions, at least for its effects on the attained peak discharges linked to this episode. A small simulation peak discharge error of only -5.5 % is obtained for the Almedrà river basin. With respect to the Sant Miquel river, the inaccuracy for the maximum flow at the basin outlet is larger, close to 37 %, but the river overflew and the hydrological model cannot take into account this effect. It is worth to note that the simulated peak discharges of both river basins coincide in time at the basin outlet, yielding a total peak outflow over 700 m^3s^{-1} (fig. 4.4b). This is a remarkable flow considering the small size of the whole watershed.

It is also notable the peak discharge obtained for the 7-8 October simulation, where again both river flows coincided, reaching a maximum value of about 540 m^3s^{-1} on 8 October at 2230 UTC (fig. 4.4a). The rain-gauge driven simulation of 10-11 November 2001 episode shows a signal characterized by several peak discharges, the maximum of which is above 208 m^3s^{-1} (on 11 November 2001 at 1010 UTC) and corresponds, mainly, to the contribution of the Sant Miquel river. The second maximum peak occurs four hours later with a stream flow close to 200 m^3s^{-1} and, owing principally to the Almedrà river discharge (fig. 4.4c). Then, it can be noticed the quicker response of the shorter and steeper Sant Miquel river basin in comparison with the Almedrà watershed when the heavy rainfall does not affect exclusively the last sections of both rivers (contrast for example cases 2 an 3; figs. 4.2b and c). Finally, the 3-4 April 2002 simulation has produced the lowest peak among the set of simulations, with a value up to 100 m^3s^{-1} on 4 April at 1400 UTC, due again to the Sant Miquel river contribution. The Almedrà basin peak contribution is obtained later, at 2000 UTC, with a maximum stream flow above 90 m^3s^{-1} (fig. 4.4d).

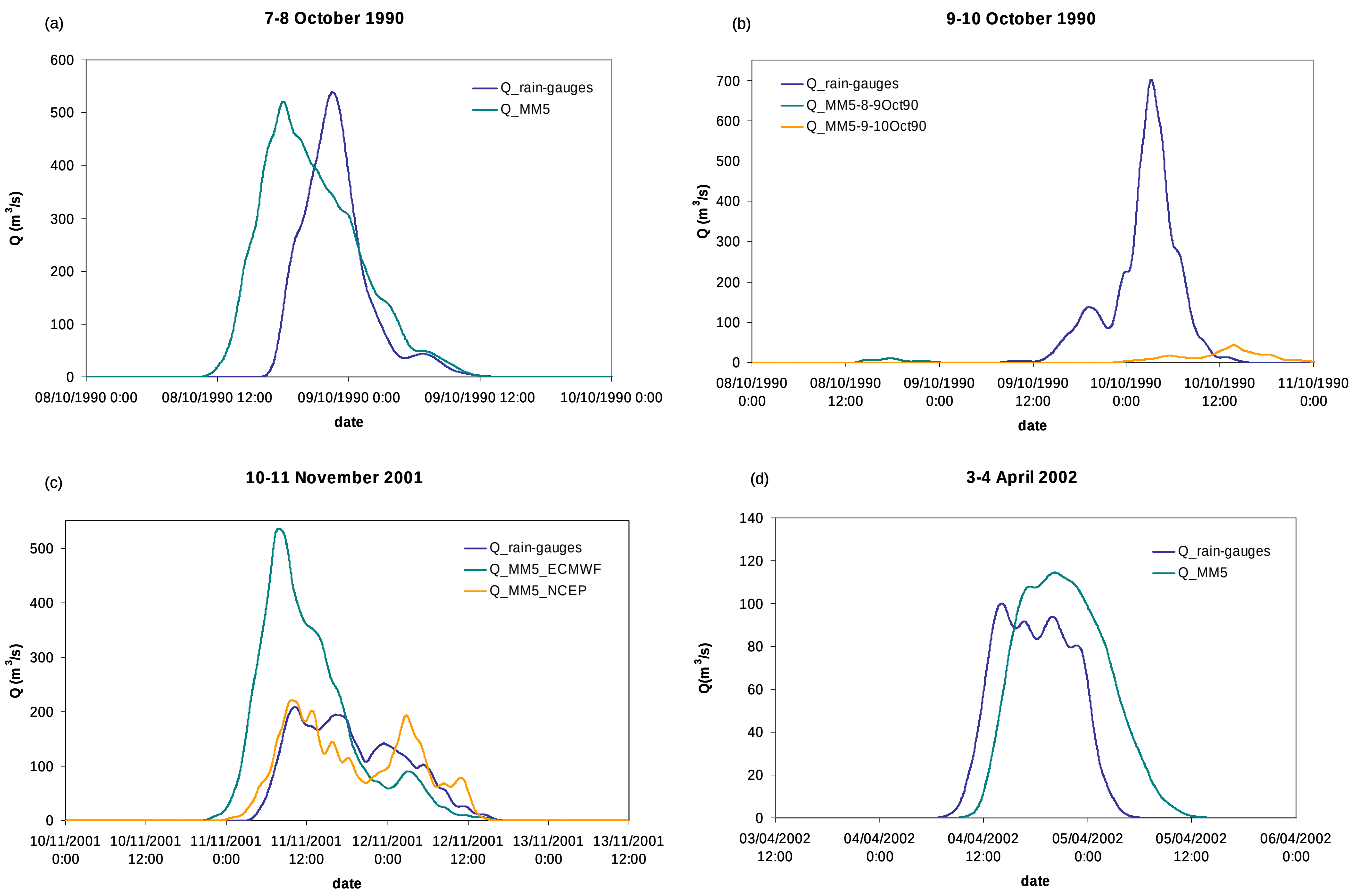

Figure 4.4: Rain-gauge driven and MM5-control driven runoff simulations for: (a) 7-8 October 1990 (first phase), (b) 9-10 October 1990 (second phase), (c) 10-11 November 2001 and (d) 3-4 April 2002 episodes. Figure 4.4b shows the 8-9 and 9-10 October 1990 mesoscale model driven runoff experiments. Figure 4.4c displays the discharge runs for the 10-11 November 2001 mesoscale model simulations driven by ECMWF and NCEP analyses.

The MM5 mesoscale model has provided the QPFs for the episodes (labelled as **MM5-control**; see fig. 4.5). Runoff simulations driven by these QPFs are then compared against the rain-gauge driven runoff simulations. The skill of the resulting runoff forecasts are expressed in terms of the Nash-Sutcliffe efficiency criterion and of the relative error of total volume at the basin outlet expressed as percentage (see Appendix). In addition, to assess the skill of the MM5 mesoscale runs, the spatial and temporal distributions of the simulated rainfall volumes are compared against the rain-gauge derived volume patterns. The spatial comparison is done using the 35 subbasins as accumulation units for each episode, and the temporal comparisons use hourly accumulations for the whole basin. The degree of agreement between simulated and observed rainfall distributions is measured using the NSE efficiency criterion as well as the root mean square error (RMSE; see Appendix).

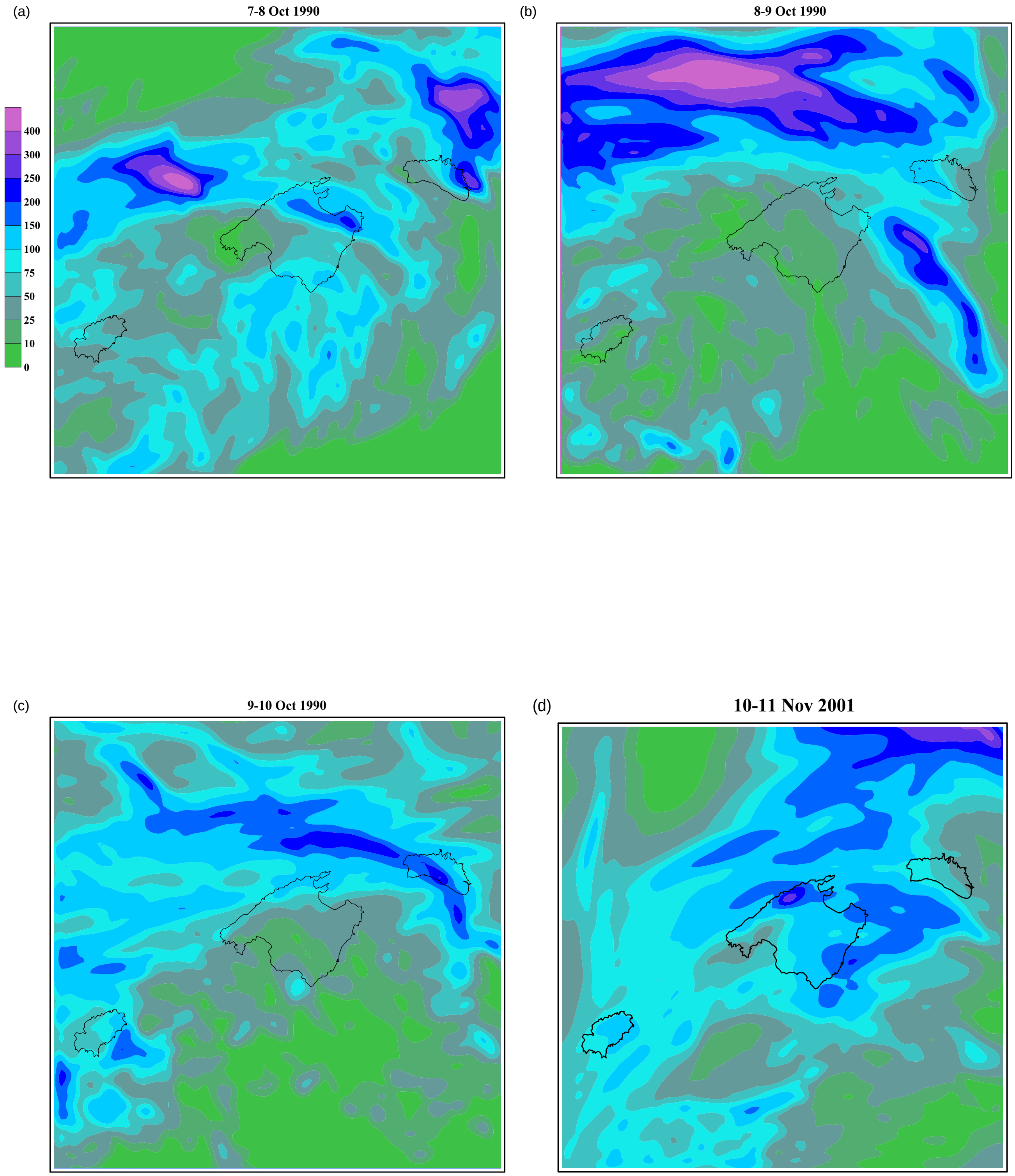

(a)
7-8 Oct 1990
400
300
250
200
150
100
75
50
25
10
0
(b)
8-9 Oct 1990
(c)
9-10 Oct 1990
(d)
10-11 Nov 2001

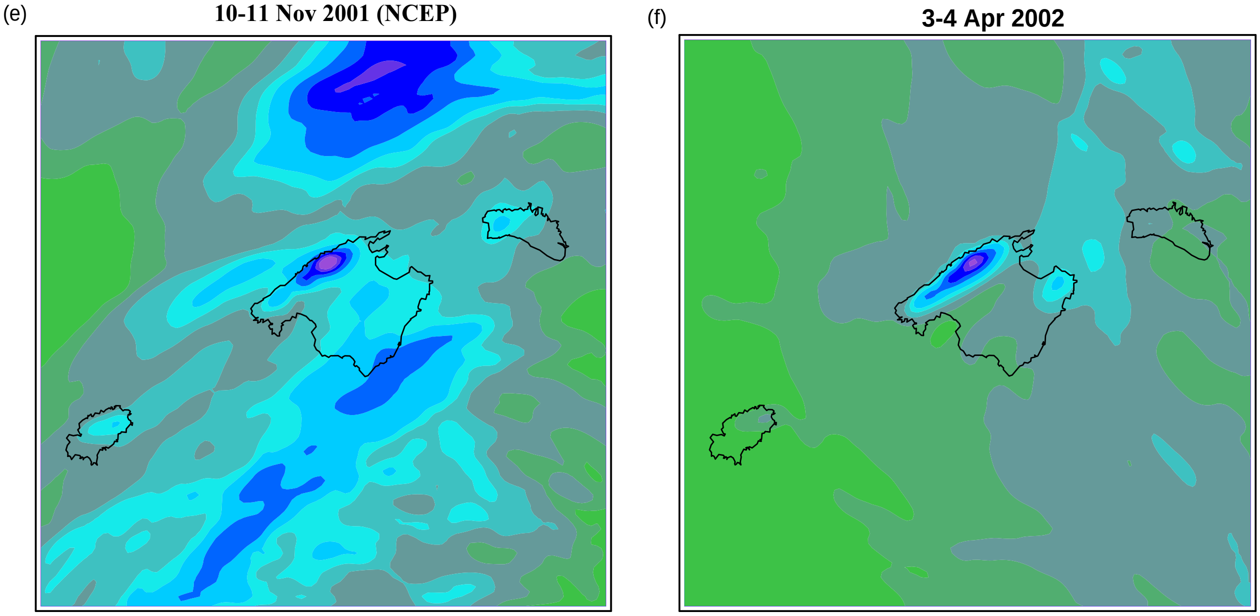

Figure 4.5: Spatial distribution of accumulated precipitation over the Balearics for: (a) 7-8 October 1990, (b) 8-9 October 1990, (c) 9-10 October 1990, (d) 10-11 November 2001, (e) 10-11 November 2001 (NCEP) and (f) 3-4 April 2002 MM5 control 48 h simulations

Tables 4.1 and 4.2 depict the skill of the spatial and temporal rainfall volume distributions for the set of MM5-7-5 (*control*) simulations, and figure 4.5 shows the accumulated rainfall patterns of these simulations (compare with fig. 4.2). With regard to the spatial distributions, the 7-8 October 1990, 10-11 November 2001 using NCEP analysis and 3-4 April 2002 experiments show the best performances, while moderate errors are found for the 10-11 November 2001 MM5-ECMWF simulation. With regard to the timing, only the 10-11 November 2001 MM5-NCEP and the 3-4 April 2002 simulations present a reasonable agreement with the observed rainfall series. Then, the 8-9 and 9-10 October 1990 runs are not able to match neither the spatial nor the temporal precise rainfall distributions of this convective episode, and the 10-11 November 2001 MM5-ECMWF experiment presents an overforecasting of the precipitation amounts over the basin (compare figs. 4.2 and 4.5). It seems that as a general feature, the mesoscale model determines more precisely the spatial than the temporal rainfall distributions for the set of episodes. In addition, a noticeable impact of the November 2001 multianalysis experiment is obtained.

Table 4.3 and figure 4.4 summarize the MM5-control driven runoff simulations in this complex orographic basin. It is found that some of the experiments reproduce reasonably well the rain-gauge driven floods in spite of the small size of the basin, thus allowing the production of valuable discharge predictions. Specifically, for the 7-8 October 1990 episode (fig. 4.4a), MM5 and rain-gauge driven runoff simulations are quite similar in terms of peak discharge –with a slight difference close to 16 m^3s^{-1}– but with an important advance on the time to peak (more than 4 hours). This fact together with the wide overestimation of the runoff volume cause a penalty in the NSE index. Better statistical scores are found for the 3-4 April 2002 event (fig. 4.4f). The MM5 driven runoff simulation shows a moderate error in forecasting the time to peak, with a delay to the first maximum of 3 hours, but better agreement is found in terms of the maximum peak discharge (with a relative error of 14.2%) and the runoff volume. The most suitable results are obtained for the 10-11 November 2001 MM5-NCEP experiment (fig. 4.4e). The simulation has accurately matched the rain-gauge driven hydrograph with a NSE score of 0.84, an error in volume of only 1.7% and a small overestimation of the peak discharge (below 15 m^3s^{-1}), together with a slight advance in time (about 30 minutes). However, the mesoscale model driven runoff runs have been very deficient in the 8-9, 9-10 October 1990 and 10-11 November 2001 MM5-ECMWF experiments. The first two simulations have missed completely the flash-flood event resulting in a severe underestimation of the flow (table 4.3; figs. 4.4b and 4.4c), whereas the last run has largely overestimated the flood at the basin outlet (table 4.3 and fig. 4.4d). Therefore, it remains as an important issue to evaluate whether our multiphysics probabilistic strategy can provide a better short-range prediction guidance when dealing with these unsuccessful flood simulations.

	7-8 Oct 1990		***8-9 Oct 1990***		***9-10 Oct 1990***	
MM5-4-5	**0.72**	**0.58**	-0.10	2.50	-0.12	2.53
MM5-5-5	-0.41	1.30	-0.10	2.50	-0.17	2.59
MM5-6-5	0.51	0.76	-0.01	2.40	-0.12	2.53
MM5-7-5 (control)	**0.80**	**0.49**	-0.73	3.14	-0.45	2.88
MM5-8-5	0.30	0.91	-0.42	2.84	-0.11	2.52
MM5-4-5-8	0.45	0.81	**0.13**	**2.23**	-0.18	2.59
MM5-5-5-8	**0.68**	**0.62**	0.06	2.32	-0.12	2.53
MM5-6-5-8	**0.87**	**0.40**	-0.09	2.50	0.35	1.92
MM5-7-5-8	0.33	0.90	0.01	2.38	0.10	2.26
MM5-8-5-8	**0.75**	**0.55**	0.11	2.26	**0.51**	**1.67**
mean	0.79	0.50	-0.07	2.47	0.02	2.37

Table 4.1: Error indices applied to the spatial rainfall volume distributions produced by the ensemble of MM5 simulations of the episodes under study (left column: NSE criterion; right column: RMSE, in hm^3. In bold, the best simulations according to these indices).

	10-11 Nov 2001		***10-11 Nov 2001 (NCEP)***		***3-4 Apr 2002***	
MM5-4-5	**0.63**	**0.68**	0.50	0.80	0.38	0.70
MM5-5-5	-1.05	1.61	-0.38	1.32	0.55	0.60
MM5-6-5	0.54	0.76	-0.29	1.28	0.41	0.69
MM5-7-5 (control)	0.33	0.92	**0.86**	**0.42**	**0.91**	**0.26**
MM5-8-5	0.59	0.72	**0.76**	**0.55**	**0.76**	**0.44**
MM5-4-5-8	0.52	0.78	0.46	0.82	0.44	0.67
MM5-5-5-8	0.51	0.79	0.41	0.86	**0.71**	**0.48**
MM5-6-5-8	**0.70**	**0.62**	0.40	0.87	0.41	0.69
MM5-7-5-8	0.46	0.83	-0.96	1.58	**0.92**	**0.26**
MM5-8-5-8	-0.63	1.44	-0.26	1.26	**0.81**	**0.39**
mean	0.56	0.75	0.57	0.73	0.85	0.35

(Table 4.1 cont.)

	7-8 Oct 1990		*8-9 Oct 1990*		*9-10 Oct 1990*	
MM5-4-5	**0.03**	**2.87**	-0.19	4.94	-0.09	4.73
MM5-5-5	-1.83	4.90	**-0.10**	**4.75**	-0.22	5.00
MM5-6-5	-0.57	3.66	-0.21	4.99	-0.22	5.01
MM5-7-5 (control)	-0.41	3.47	-0.19	4.94	-0.13	4.81
MM5-8-5	-0.25	3.27	-0.24	5.05	**-0.06**	**4.66**
MM5-4-5-8	-0.28	3.30	-0.23	5.02	-0.19	4.94
MM5-5-5-8	-0.32	3.35	-0.70	5.91	-0.20	4.95
MM5-6-5-8	-0.67	3.76	-0.20	4.96	-0.25	5.06
MM5-7-5-8	-0.83	3.95	-0.22	5.01	-0.20	5.06
MM5-8-5-8	-1.22	4.35	-0.37	5.30	-0.38	5.32
mean	-0.28	3.30	-0.13	4.82	-0.13	4.82

Table 4.2: Error indices applied to the temporal rainfall volume distributions produced by the ensemble of MM5 simulations of the episodes under study (left column: NSE criterion; right column: RMSE, in hm^3. In bold, the best simulations according to these indices).

	10-11 Nov 2001		*10-11 Nov 2001 (NCEP)*		*3-4 Apr 2002*	
MM5-4-5	-0.67	2.38	**0.45**	**1.36**	0.10	1.20
MM5-5-5	-2.03	3.21	0.11	1.74	-0.07	1.31
MM5-6-5	-0.03	1.87	-0.65	2.37	-0.40	1.50
MM5-7-5 (control)	-0.02	1.86	**0.31**	**1.54**	**0.37**	**1.01**
MM5-8-5	-1.21	2.74	0.30	1.54	0.07	1.22
MM5-4-5-8	-0.25	2.06	0.13	1.72	0.12	1.18
MM5-5-5-8	-1.68	3.02	0.20	1.65	0.08	1.21
MM5-6-5-8	**0.11**	**1.74**	0.22	1.63	-0.45	1.52
MM5-7-5-8	0.08	1.77	-0.73	2.43	**0.35**	**1.01**
MM5-8-5-8	-3.15	3.76	-2.77	3.58	0.03	1.25
mean	-0.10	1.93	0.53	1.26	0.13	1.18

(Table 4.2 cont.)

	7-8 Oct 1990		*8-9 Oct 1990*		*9-10 Oct 1990*	
MM5-4-5	**0.75**	-26.9	0.22	-64.0	0.05	-70.2
MM5-5-5	-0.73	118.7	0.06	-70.6	-0.08	-75.3
MM5-6-5	0.31	-51.4	-0.02	-56.0	-0.14	-65.1
MM5-7-5 (control)	0.28	55.4	-0.2	-98.7	-0.15	-91.6
MM5-8-5	0.31	36.5	-0.17	-88.9	-0.13	-60.0
MM5-4-5-8	0.36	-56.0	0.28	-35.8	0.17	-60.5
MM5-5-5-8	**0.63**	**-19.2**	**0.61**	**-4.7**	0.28	-62.7
MM5-6-5-8	0.38	-26.9	**0.53**	-43.3	**0.56**	**-5.2**
MM5-7-5-8	**0.58**	**-19.8**	0.26	-47.8	0.34	-36.5
MM5-8-5-8	-0.21	46.9	0.1	-47.9	**0.69**	50.4
mean	0.68	5.7	0.26	-55.8	0.3	-47.7

Table 4.3: NSE efficiency criterion (left column) and percentage of error in volume (right column, % EV) at the Albufera basin outlet for the ensemble of MM5 driven runoff simulations and the selected episodes. In bold, the best simulations according to these indices.

	10-11 Nov 2001		*10-11 Nov 2001 (NCEP)*		*3-4 Apr 2002*	
MM5-4-5	0.49	41.0	**0.71**	58.8	-2.75	193.1
MM5-5-5	-5.29	190.5	0.51	147.5	-0.89	129.3
MM5-6-5	0.03	59.0	0.52	135.1	-2.82	187.4
MM5-7-5 (control)	-1.53	73.1	**0.84**	**1.7**	**0.60**	27.8
MM5-8-5	-0.46	43.4	**0.74**	**-15.8**	0.50	-42.4
MM5-4-5-8	**0.57**	**18.5**	-1.44	-56.1	-2.38	183.0
MM5-5-5-8	-0.55	48.2	-1.28	-56.3	-0.02	78.8
MM5-6-5-8	**0.71**	**-15.4**	**0.63**	71.8	-2.88	188.8
MM5-7-5-8	**0.62**	-51.8	0.48	169.0	**0.57**	**13.5**
MM5-8-5-8	-9.05	172.6	**0.52**	142.0	**0.55**	-32.5
mean	-0.23	57.9	0.78	59.8	-0.14	92.7

(Table 4.3 cont.)

4.6.2 Multiphysics ensemble of MM5 driven runoff simulations

Following the motivation and methodology explained in sections 4.1 and 4.4, nine additional experiments are performed for each episode in order to produce the MM5 multiphysics ensemble. To evaluate the derived runoff simulations the aforementioned statistical indices are used. These are complemented with an additional set of skill scores widely used to test the quality of hydrometeorological chain forecasts. Specifically, frequency bias score (BIAS), probability of detection (POD), false alarm rate (F) and ROC score have been calculated for different precipitation and runoff volume thresholds (Jolliffe and Stephenson, 2003; Wilks, 2006; more information in Appendix). These skill indices are calculated using the six hydrometeorological experiments in order to increase the statistical significance of the results as follows: (i) the rainfall volumes of the MM5 control simulations are compared against the observed rainfall volumes; (ii) the rainfall volumes of the ensemble means are employed and (iii) the volumes by the members of the ensembles are used for the comparison with the observations. All these rainfall volumes are accumulated at hourly time-steps and using the subbasins as accumulation units. With regard to the discharge volumes, the same methodology is followed but comparing, instead, the hourly runoff volumes produced at each subbasin by the MM5 driven runoff simulations against the rain-gauge driven runoff volume accumulations. In this case, the scores are calculated using only the hourly data that is non-zero in at least one of the two compared series in order to prevent an artificial improvement of the ROC values.

It is worth to remark that the ensemble mean, statistically, provides a better forecast that any individual ensemble member, because errors in the individual forecasts tend to cancel when averaged (Epstein, 1969; Leith, 1974). Moreover, previous research studies have pointed out that despite the computational limitations and burdens for generating large member ensembles, a clear improvement due to the ensemble averaging can be obtained with small ensembles sizes (typically from 8 to 19 members; Du et al., 1997; Stensrud et al., 2000; Jones et al., 2007). Therefore, ROC scores for the ensemble means of rainfall and runoff volumes have also been computed in order to highlight the benefits of a simple ensemble average in comparison with the control experiments.

The probabilistic results provided by the ensemble strategy have been represented as cumulative distribution functions (CDFs) for the maximum peak discharges plotted on a Gumbel chart (Ferraris et al., 2002). Each peak flow value is equally likely as consequence of the equally skillful model configuration assumption. Though no hydrometeorological forecasting chain is currently implemented for civil protection purposes in the Albufera basin, we have considered suitable for the present study the introduction of a hyphotetical warning discharge threshold. This threshold, $Q_{th} = 100\ \mathrm{m^3 s^{-1}}$, is the lowest peak discharge found among the four rain-gauge driven runoff simulations. Next, a brief discussion case by case of the results is presented.

(a) Case 1: the 7-10 October 1990 first phase episode

For this case study, some members of the ensemble have outperformed the control simulation in terms of the spatial and/or the temporal rainfall distributions (tables 4.1 and 4.2; fig. 4.6a), the runoff volume and the time to peak (table 3 and fig. 4.7a). However, the control simulation still shows the best reproduction of the maximum discharge (fig. 4.4a).

From a probabilistic point of view for the runoff ensemble, figure 4.8a shows that the probability of peak discharge exceedence for the rain-gauge driven runoff simulation is close to 0.3

and the probability of exceeding Q_{th} would be 1. This a clear benefit of an ensemble that estimates the range of the atmospheric probability density function (PDF) through the inclusion of the mesoscale model physics uncertainties.

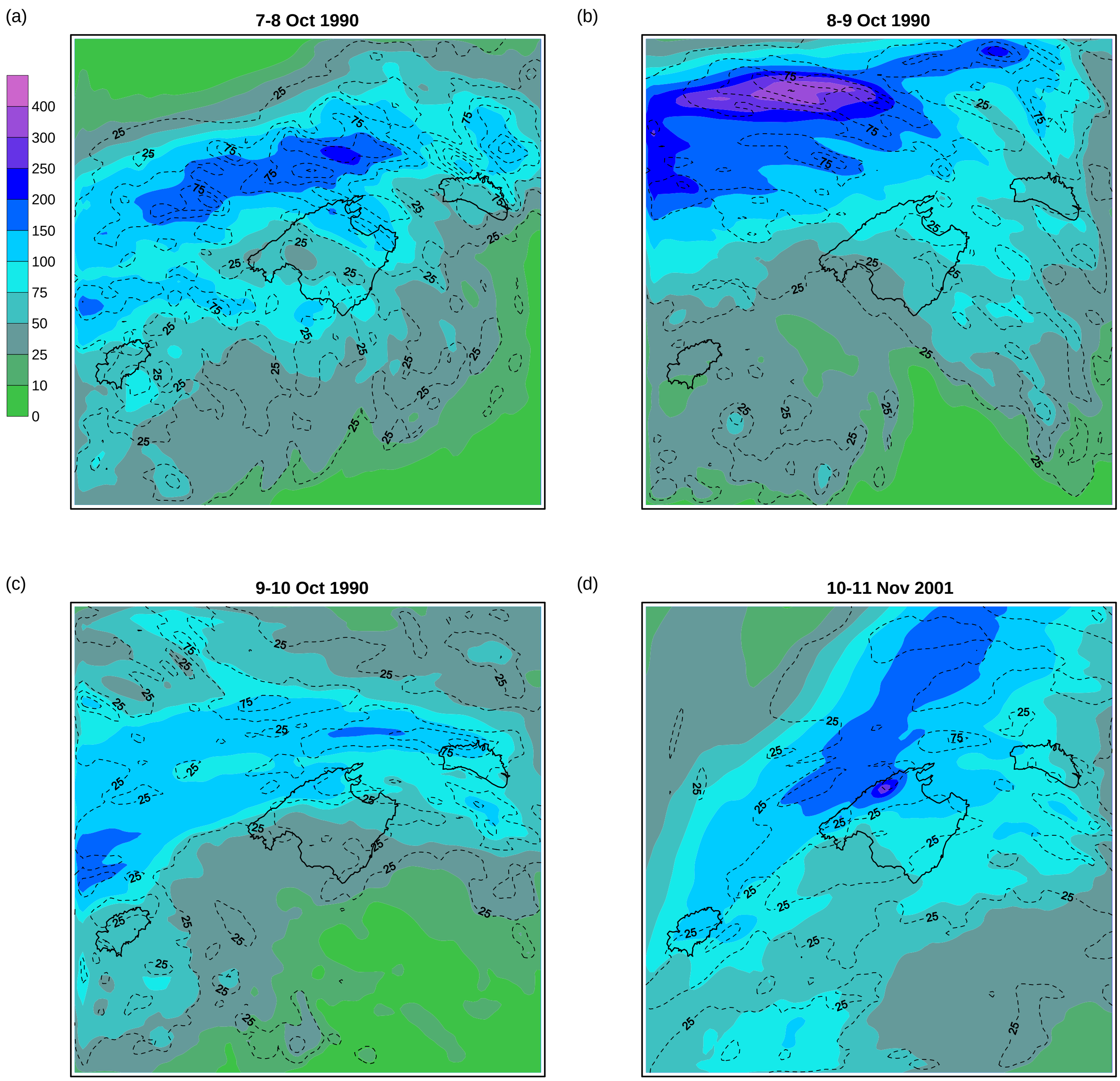

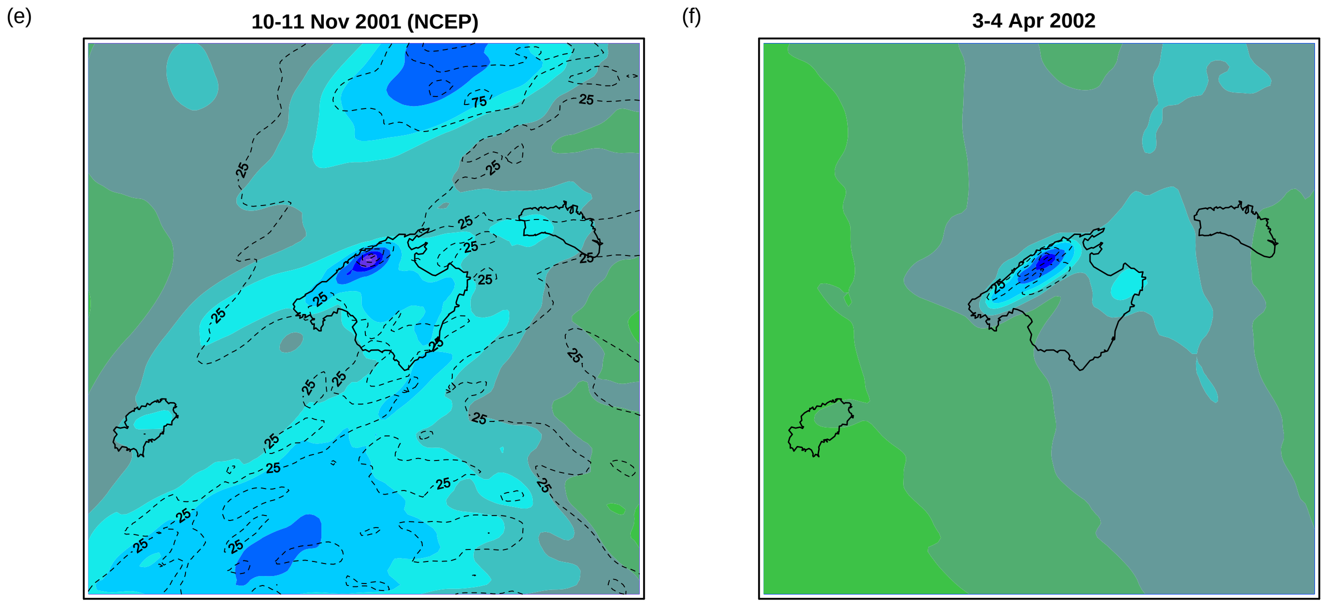

Figure 4.6: Ensemble mean (in mm, shaded contours) and ensemble standard deviation (in mm, discontinuous line at 25 mm intervals) of the accumulated precipitation over the Balearics for: (a) 7-8 October 1990, (b) 8-9 October 1990, (c) 9-10 October 1990, (d) 10-11 November 2001, (e) 10-11 November 2001 (NCEP) and (f) 3-4 April 2002 experiments

(b) Case 2: the 7-10 October 1990 second phase episode

With regard to the 9-10 October 1990 flash-flood episode, both sets of MM5 ensemble simulations (8-9 and 9-10 October 1990 experiments) are rather similar: the maximum rainfall amounts are located in the north-western part of the domain, quite far from the Albufera basin (tables 4.1 and 4.2; figs. 4.6b and c). Only one member is sufficiently accurate to reproduce the rain-gauge driven discharge (figs. 4.7b and c). This member pertains to the 9-10 October 1990 experiment and depicts a peak disagreement of only 30 m^3s^{-1}, but with a remarkable overestimation of the runoff volume (table 4.3). It is also worth to emphasize a member from the 8-9 October experiment, which has approached the rain-gauge driven simulation. However, it is less accurate in terms of peak discharge, with a difference up to 200 m^3s^{-1}, and an advance of the time to peak of 3 h.

Figures 4.8b and c depict a remarkable improvement of the rainfall simulation when using an ensemble strategy: the poor detection of the control simulations are partially alleviated. Even though none of ensembles' members is able to reproduce the rain-gauge driven peak discharge –pointing out the low predictability of this hydrometeorological event– an important improvement is found, and the probability of exceeding Q_{th} would be close or above 0.8 for both ensembles. In agreement with Stensrud el al. (2000), it is found that model physics largely control the evolution of this convectively-driven weather event.

(c) Case 3: the 10-11 November 2001 episode

As explained in section 4.4, the set of simulations for the 10-11 November 2001 episode has consisted of multiphysics ensembles initialized with ECMWF and NCEP analysis. It appears that both ensembles (MM5-ECMWF and MM5-NCEP) present a similar performance with regard to the spatial distribution of rainfall and a great homogeneity among their members (table 4.1, figs. 4.6d and e), as well as for the total precipitated volume over the basin: the observed volume was 60.9 hm^3, whereas the mean volumes obtained by the ECMWF and NCEP experiments are 73.2 hm^3 and 74.0 hm^3 respectively. Nevertheless, the elements of the MM5-NCEP ensemble show a better reproduction of the temporal rainfall distribution together with a higher uniformity of the results (table 4.2), and therefore, the ensemble of MM5-NCEP driven runoff simulations presents more members with a best goodness-of-fit (table 4.3; figs. 4.7d and e). However, some members of the MM5-ECMWF driven runoff ensemble have displayed a reasonable agreement in terms of the peak discharge and the stream flow volume when compared against rain-gauge driven runoff, thus overperforming the control experiment.

In addition, MM5-ECMWF driven runoff ensemble presents a considerable increase of the forecasting skill with respect to the deterministic driven runoff prediction, and the probabilities of exceedence of the rain-gauge driven runoff peak and the threshold peak flow are above 0.9 and up to 1 respectively (fig. 4.8d). Rain-gauge driven peak flow and Q_{th} show a probability of being exceeded superior to 0.8 for the MM5-NCEP driven runoff ensemble (fig. 4.8e). In contrast with the MM5-NCEP deterministic forecast, which is very accurate, there is a clear overestimation of the runoff by the MM5-ECMWF deterministic run. This problem, however, is notably alleviated by most of the MM5-ECMWF ensemble members. It is worth to note that the effects owing to the external-scale uncertainties related to the initial and boundary conditions (as measured by the difference between MM5-ECMWF and MM5-NCEP control runs) are smaller than the effects due to the model physics uncertainties (as measured by the spread found in both ensembles). This notion agrees with the results found by Stensrud et al. (2000), where the variance of a multiphysics experiment exceeded that produced by an initial-condition experiment in a short-range ensemble forecast (SREF) modeling system.

(d) Case 4: the 3-4 April 2002 episode

The atmospheric ensemble for the 3-4 April 2002 case presents the greatest similarities in the simulated rainfall patterns among their members, and some of them accurately match the observed pattern (table 4.1 and fig. 4.6f), but this feature is lost when the temporal distributions are evaluated (table 4.2). Attending to the resulting runoffs, three simulations are clearly the most suitable (table 4.3 and fig. 4.7f) with only small differences in their skill scores. The low temporal skill of the mesoscale model results in a remarkable delay in the timing of the peak discharges. Furthermore, the important overforecasting on the precipitation amounts produces excessive flow volumes. These facts are reflected on the poor performance of the ensemble of simulated hydrographs.

However, the probability of exceedence of the rain-gauge driven peak discharge is above 0.8 (fig. 4.8f). These results would have been found suitable in a hypothetical real-time hydrometeorological forecasting framework owing to the high probability of overpassing Q_{th}. In fact, Anderson et al. (2002) pointed out that runoff predictions for use in emergency management directives may not need to match exactly the peak discharges or the timing, but must reach suitable thresholds so as to cause the appropriate directives to be enacted. Ferraris et al. (2002) argued similar requirements within an operational civil framework for the Tanaro river basin, north-western Italy.

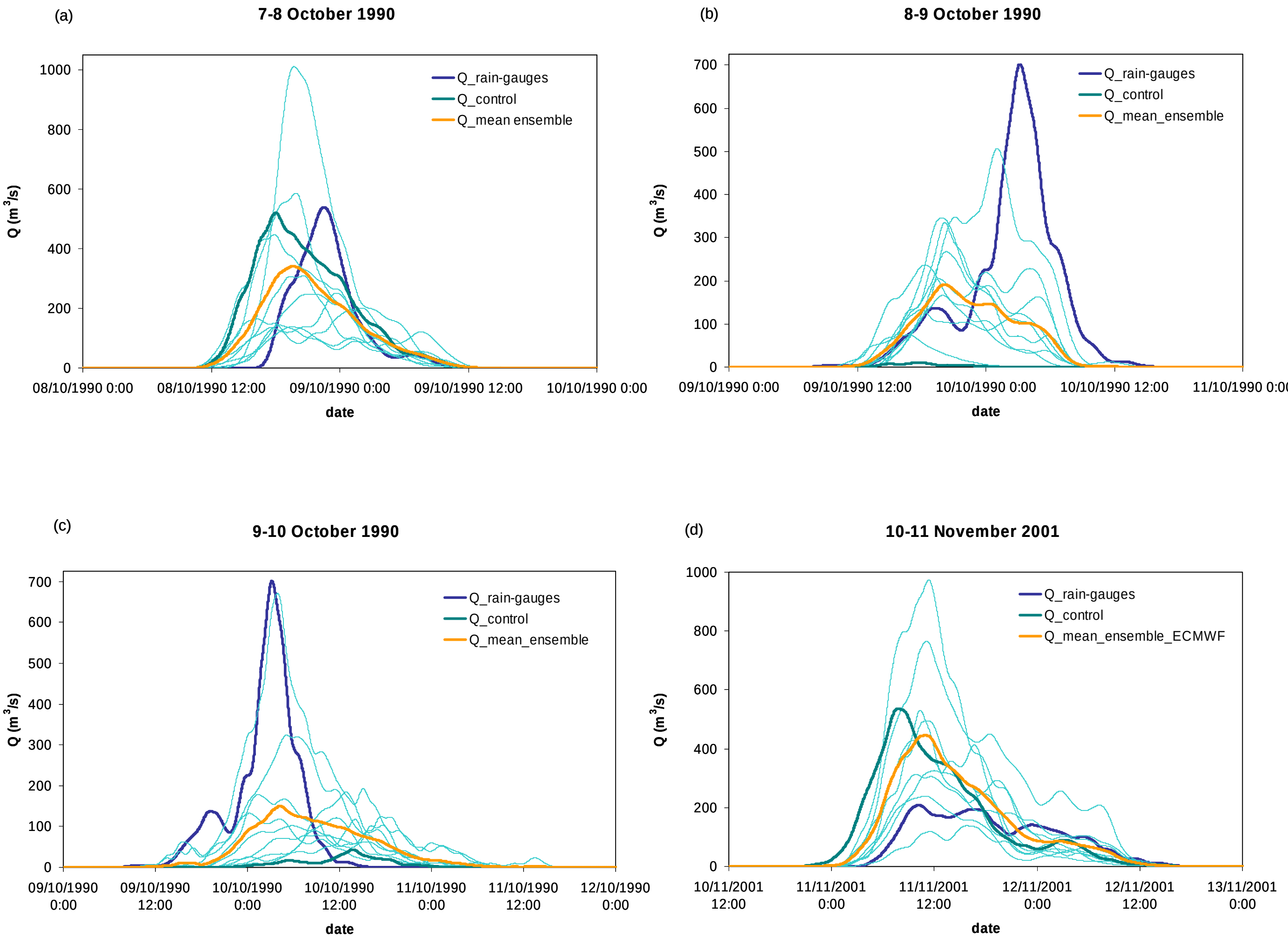
(a)
7-8 October 1990
Q (m³/s)
Q_rain-gauges
Q_control
Q_mean ensemble
08/10/1990 0:00
08/10/1990 12:00
09/10/1990 0:00
09/10/1990 12:00
10/10/1990 0:00
date
(b)
8-9 October 1990
Q (m³/s)
Q_rain-gauges
Q_control
Q_mean_ensemble
09/10/1990 0:00
09/10/1990 12:00
10/10/1990 0:00
10/10/1990 12:00
11/10/1990 0:00
date
(c)
9-10 October 1990
Q (m³/s)
Q_rain-gauges
Q_control
Q_mean_ensemble
09/10/1990 0:00
09/10/1990 12:00
10/10/1990 0:00
10/10/1990 12:00
11/10/1990 0:00
11/10/1990 12:00
12/10/1990 0:00
date
(d)
10-11 November 2001
Q (m³/s)
Q_rain-gauges
Q_control
Q_mean_ensemble_ECMWF
10/11/2001 12:00
11/11/2001 0:00
11/11/2001 12:00
12/11/2001 0:00
12/11/2001 12:00
13/11/2001 0:00
date

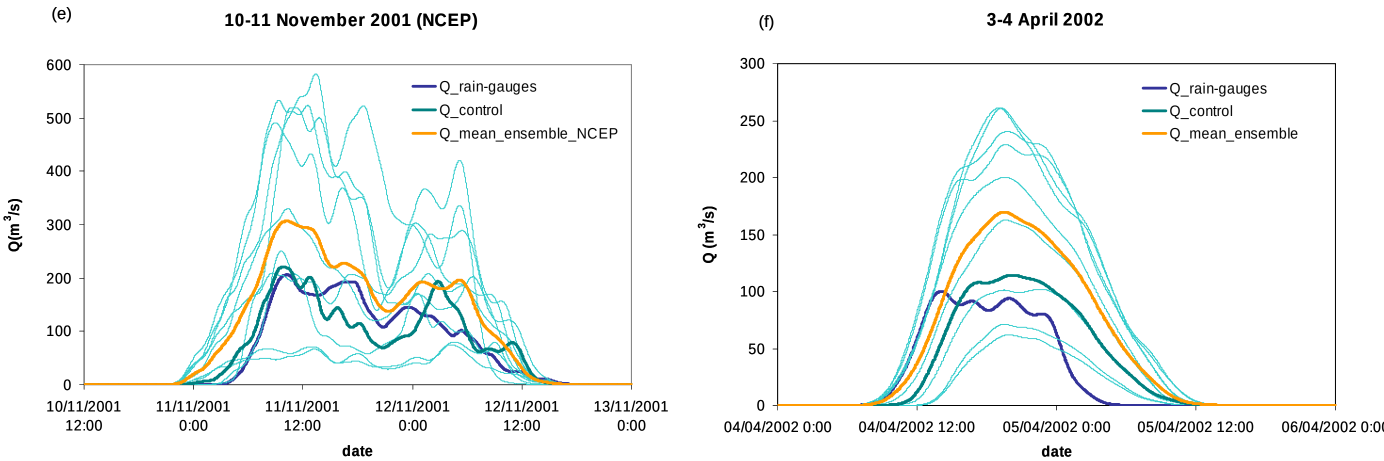

Figure 4.7: Ensemble of the multiphysics MM5 driven runoff simulations for: (a) 7-8 October 1990, (b) 8-9 October 1990, (c) 9-10 October 1990, (d) 10-11 November 2001, (e) 10-11 November 2001 (NCEP) and (f) 3-4 April 2002 experiments. Thin lines correspond to the nine additional ensemble members.

(e) POD, F, BIAS and ROC skill indices

Table 4.4 and figures 4.9a-c and 4.10a-c depict the results for the rest of applied scoring techniques. As it has been aforementioned, the skill indices are applied to all the experimental ensembles in order to increase their statistical significance. With regard to the rainfall accumulations, the ensemble mean proves to be the best for the POD, although the increased skill for the POD induces a rise of the F score, and a moderate overforecasting of the rain amounts at low and medium thresholds can be observed attending to the BIAS index. The ensemble mean presents the highest ROC score as a consequence of the aforementioned smoothing effect produced in averaging the rainfall fields (table 4.4). ROC scores for the control and ensemble simulations are rather similar and higher probability of detections for the ensemble experiments can be appreciated only at low precipitation volumes. Moreover, the set of ensembles depicts higher false alarm rates for all thresholds when compared with the control simulations. These control simulations present a systematic underprediction of the precipitation amounts at all thresholds, which is in part alleviated by the ensemble experiments (fig. 4.9c).

With respect to the driven runoff forecasts, table 4.4 shows again the highest performance in terms of ROC score for the ensemble mean owing to the highest POD scores at small and medium values together with an appreciable tendency in decreasing F at increasing volumes. It can also be noticed the overprediction of low- and mid-thresholds and the underprediction at high thresholds for the ensemble mean (figs. 4.10a-c). Furthermore, an improvement of the ROC scores is found when using the ensembles strategy instead of the deterministic control simulations. It appears that the ensembles depict slightly higher POD and smaller F indices at low thresholds, and a smaller underestimation of runoff volumes from medium to high thresholds.

Finally, it is worth to note that the introduction of a convection scheme in the second domain only results beneficial for some of the high-resolution rainfall simulations (tables 4.1 and 4.2). For example, an improvement in the spatial distribution for the 9-10 October 1990 event is found for one of the experiments, but the reproduction of the heavy rainfall timing is rather deficient. This fact leads to a slight improvement in the simulation of the flash-flood event in terms of runoff (table 4.3). The enhanced representation of the physical processes resulting from the parameterized convection benefits reasonably the 10-11 November 2001 ensemble based on ECMWF analyses, since the wide areas with large rainfall amounts (fig. 4.5d) become better constrained to the Albufera basin (not shown). However, no benefit is obtained for the 10-11 November 2001 ensemble based on NCEP analyses, and only a slight improvement can be noticed for some experiments of the 7-8 October 1990 episode. These results reinforce the previous idea of considering as equally skillful the members of the physics ensemble with and without parameterized convection in the second domain.

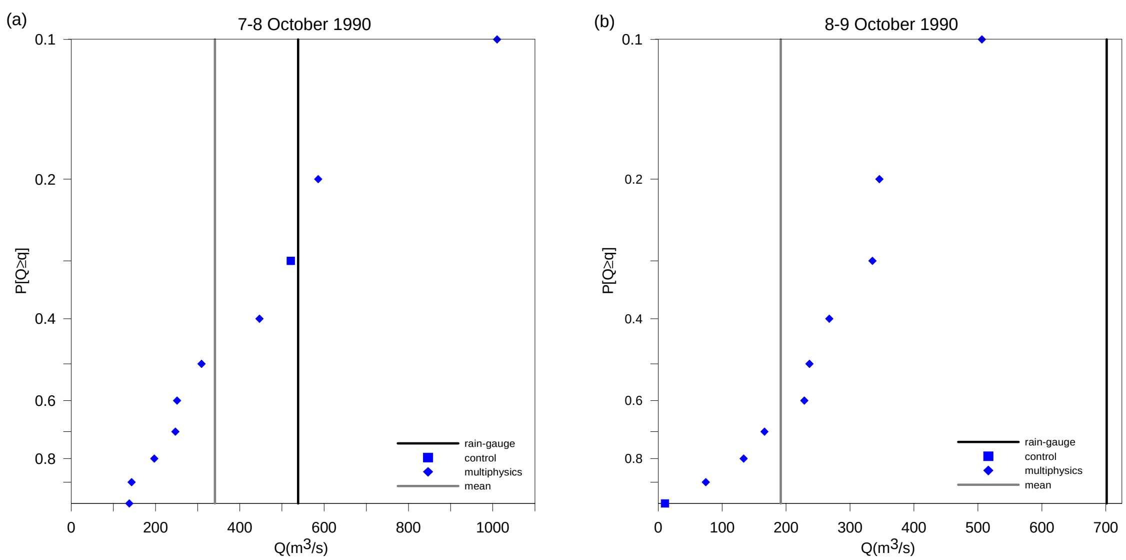

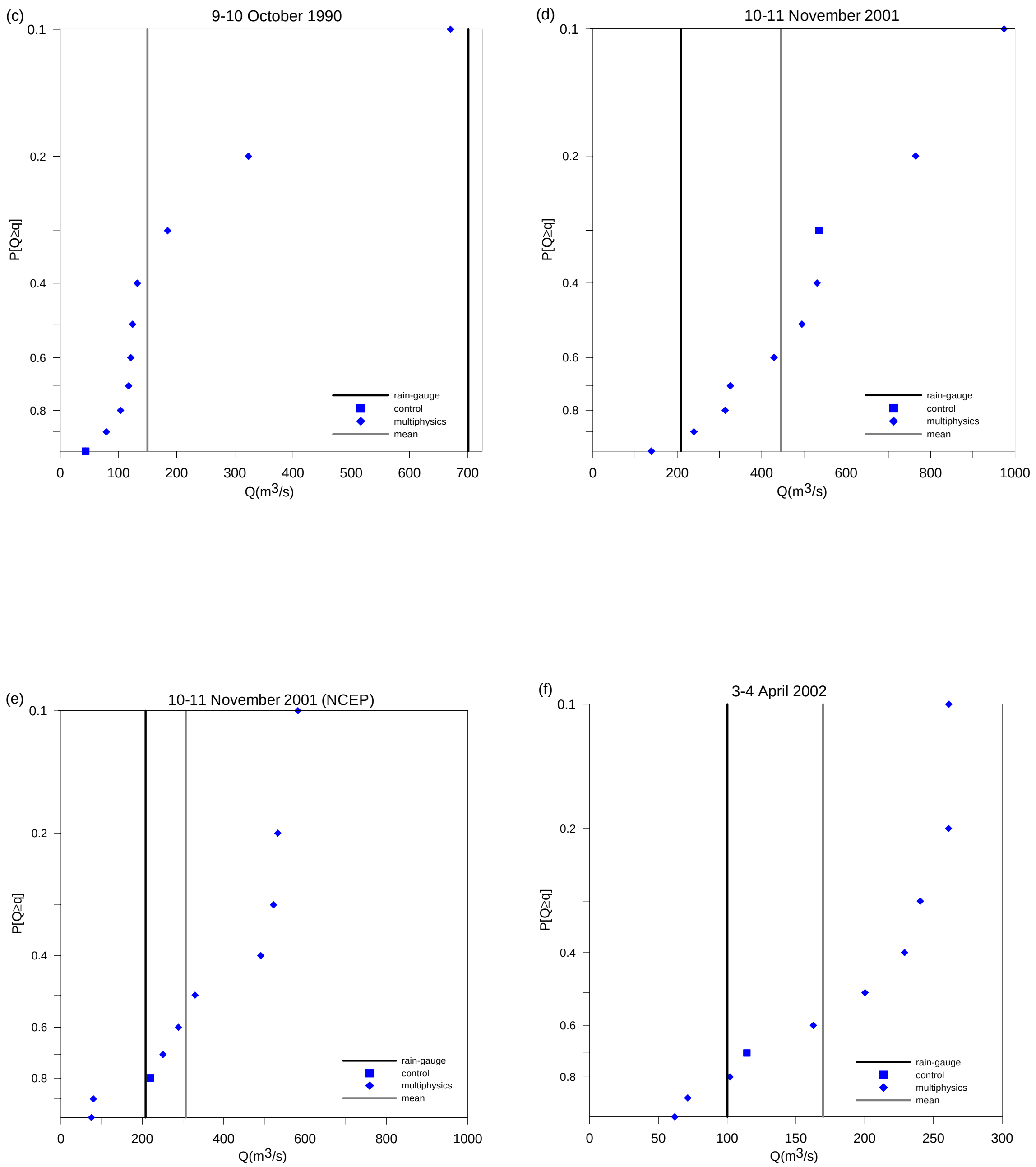

Figure 4.8: Peak discharge exceedence probability plotted on a Gumbel chart for: (a) 7-8 October 1990, (b) 8-9 October 1990, (c) 9-10 October 1990, (d) 10-11 November 2001, (e) 10-11 November 2001 (NCEP) and (f) 3-4 April 2002 hydrometeorological experiments. The cumulative distribution functions of peak discharge are shown at the Albufera river basin outlet. The vertical black line represents the rain-gauge driven maximum peak flow at the Albufera river basin outlet for each of the hydrometeorological events. The additional vertical grey line denotes maximum peak discharge from the ensemble mean.

	control	*mean*	*ensemble*
rainfall volumes	0.67	0.74	0.68
runoff volumes	0.57	0.77	0.72

Table 4.4: ROC scores for the control simulations, ensemble mean and ensemble members of all the hydrometeorological experiments, for hourly rainfall and runoff volumes.

4.7 Conclusions

This chapter has analysed the feasibility of runoff simulations driven by a high-resolution non-hydrostatic mesoscale atmospheric model over the small Albufera river basin of Majorca. By using analyses –instead of forecasts– to drive the model, a best scenario for the synoptic scale environment has been assumed. Four intense rainfall events which resulted in floods of varying spatial and temporal scales have been considered. These kinds of intense precipitation events –often highly localised and convectively driven– present short recurrence periods in Mediterranean Spain as a whole, and therefore, the conclusions drawn could be widely applicable to other territories of the region as well.

Using ECMWF analyses to initialize the hydrometeorological chain, it was possible to obtain reasonable runoff simulations at the basin outlet for some of the episodes. In addition, an ensemble of MM5 experiments with varying microphysical, moist convection and boundary layer parameterizations has been adopted in order to mitigate the low forecasting skill of the deterministic runoff simulations in some events (e.g. 9-10 October 1990 and 10-11 November 2001 using ECMWF analyses). Hence, the use of an ensemble strategy has been able to further extend the short-range prediction guidance when dealing with flood simulation situations for the Albufera river basin.

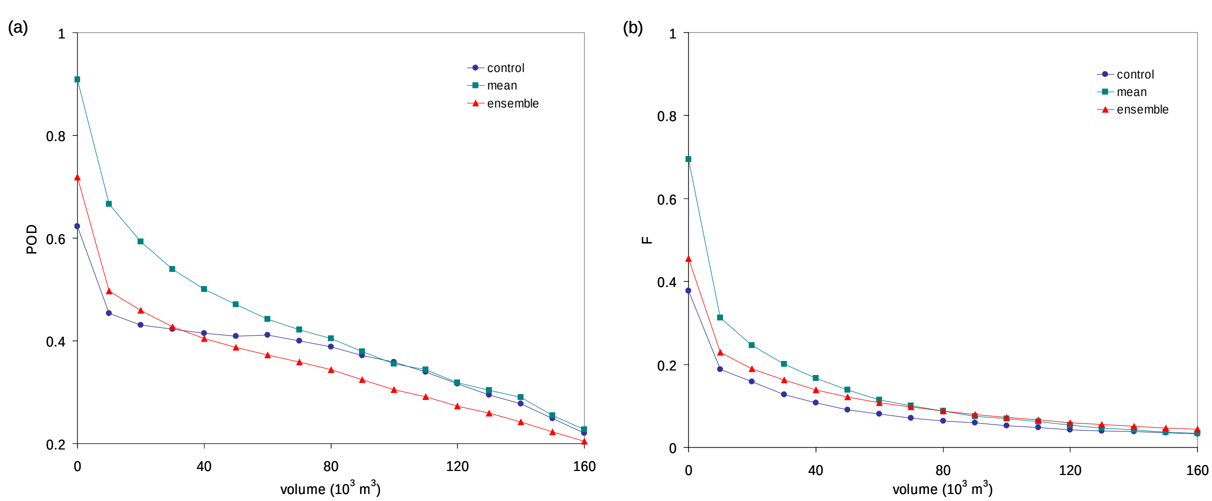

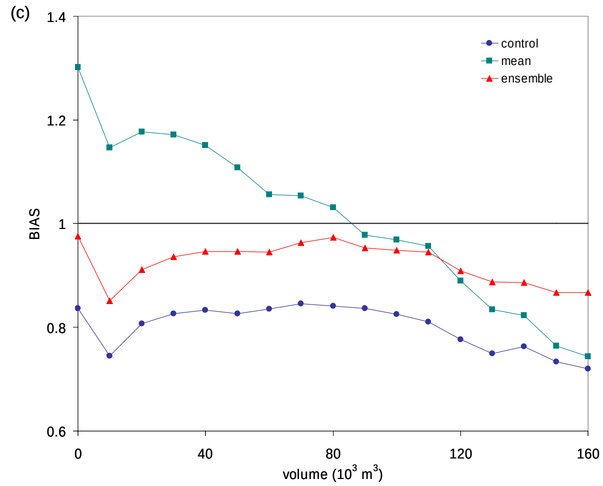

Figure 4.9: POD, F and BIAS skill scores for different precipitation volume thresholds obtained by the ensemble of MM5 driven runoff discharge simulations for all the hydrometeorolgical experiments.

The ensemble of simulated rainfall fields has displayed moderate spatial and temporal variabilities as well as significant changes in the precipitation amounts. Some members of the ensemble outperformed the control simulation and reduced the biases at the Albufera outlet, where the control experiments would have not produced enough accurate runoff simulations. Furthermore, a multianalysis experiment has also been introduced for the 10-11 November 2001 event in order to address the hydrometeorological chain sensitivity to the initial and boundary meteorological conditions. For this particular case, it was found superior to initialize the MM5 mesoscale model with the NCEP analyses, but this result cannot be generalized. Obviously, the higher performance of the NCEP-based simulations in terms of peak discharges and their timing is simply a particularity of this meteorological situation, and not an inherent aspect of this analysis dataset.

The performance of the mesoscale model has been assessed from a comparison of simulated and observed rainfall distributions in space and time over the subbasins, as well as in terms of the MM5 driven runoff discharges. Hence, the one-way coupling between the meteorological and hydrological models has been regarded as a validation tool for the simulated rainfall distributions. The value of a multiphysical model ensemble to convey the uncertainty of the small-scale features in precipitation and thus of the discharge simulations has also been proved. This is a good example of the potential benefits provided by more general short-range ensemble forecast (SREF) modeling systems aimed at accounting for the forecast variance associated to the physical parameterizations and/or to the initial conditions uncertainties.

It has been highlighted that the lack of flow gauge measurements and any estimated runoff peak –except for the 9-10 October 1990 episode– together with the scarcity of automatic pluviometric stations over the Albufera catchment, has entailed great difficulties for constructing a set of reference rain-gauge derived runoff simulations. Nevertheless, the perfect-hydrological model assumption has allowed to consider these unverified rain-gauge driven discharges as 'the observed flows' when evaluating the sets of mesoscale model driven runoff simulations. Obviously, in a hydrometeorological forecasting chain framework, the reliability and skill of the rainfall-runoff model must be improved and it would be highly desirable to get more information of the flood events affecting the Albufera river basin. The expected future increase in the number of automatic stream- and rain-gauges in the catchment will be very helpful to better address the uncertainties related to the spatial and temporal variabilities found in the model's initial conditions (the infiltration mechanism) and to the dynamical formulation (the channel routing). In spite of the current limitations, however, the benefits from hydrometeorological analyses as the present one are of greater significance than its possible weaknesses, given the hazardous consequences and relatively short recurrence periods of these kinds of extreme hydrometeorological events.

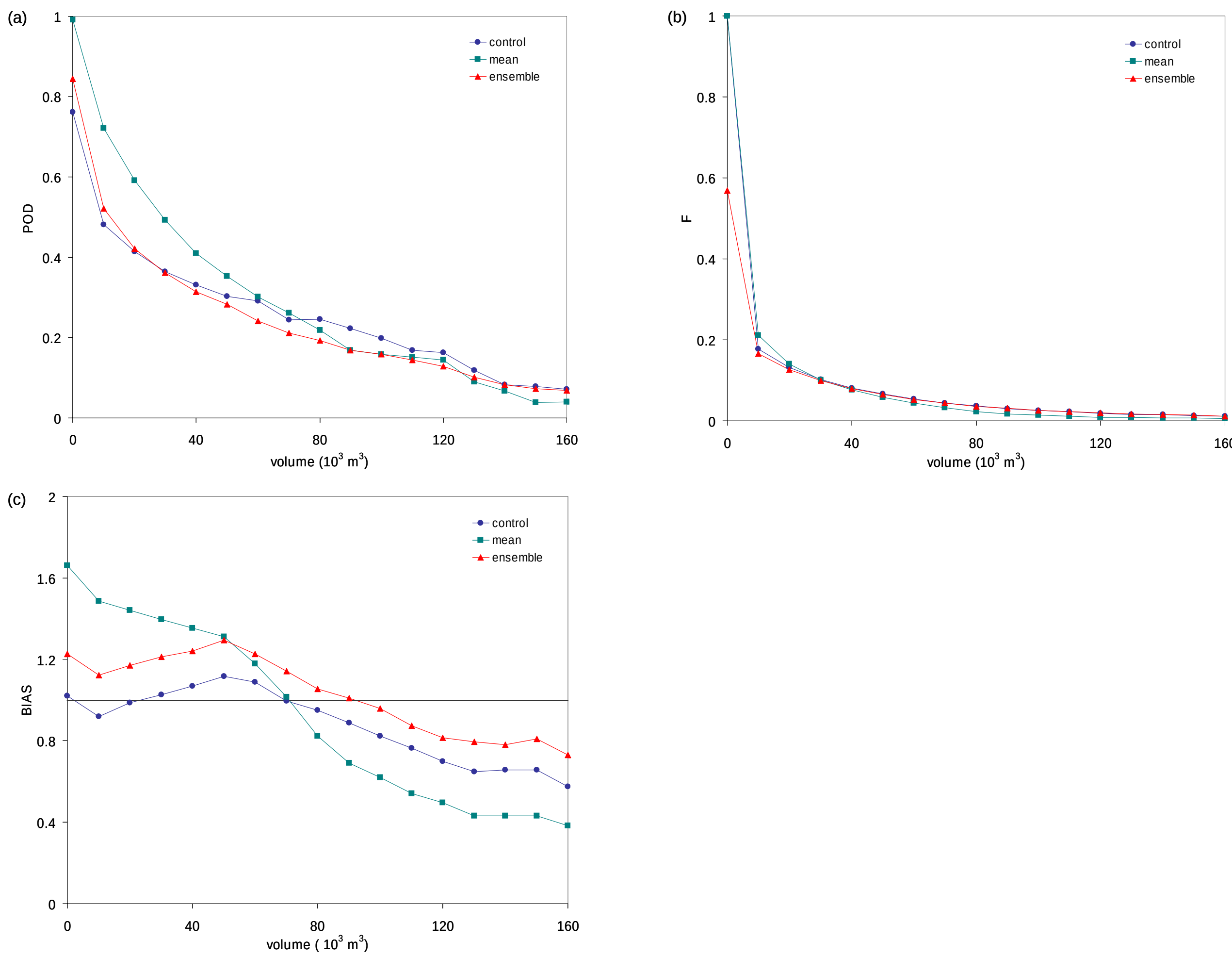

Figure 4.10: POD, F and BIAS skill scores for different runoff volume thresholds obtained by the ensemble of MM5 driven runoff discharge simulations for all the hydrometeorolgical experiments.

Chapter 5

THE NOVEMBER 2003 HEAVY PRECIPITATION EPISODE OVER THE EMILIA-ROGMANA REGION, ITALY

5.1 Introduction

This chapter[1] presents a hydrometeorological model intercomparison carried out by means of a set of hydrometeorological simulations. These experiments have been performed in order to estimate the uncertainty associated with the discharge predictions over the upper Reno river basin, a medium size catchment in the Emilia-Romagna Region. The analysis is performed for an intense precipitation event which affected northern Italy and caused a flood event over the aforementioned river basin.

One of the more important challenges for numerical weather modeling is to improve the quantitative precipitation forecasts (QPFs) for hydrological purposes. Concretely, the reliability and practical use of the flood forecasting system for the upper Reno river basin is strongly connected with the accuracy of QPFs provided by numerical weather prediction (NWP) models. These are useful to extend the desired forecast lead time beyond the concentration time of the basin. In fact, for the upper Reno river basin, rainfall observations are not appropriate to drive the hydrological models, since they do not allow for the timely predictions required to implement an adequate emergency planning. The use of QPFs provided by NWP models is, therefore, fundamental. In general, the required lead times can range from several days ahead (for qualitative early warning) to 1-2 days (for flood warning and alarm) and down to a few hours for crisis management (Obled et al., 2004). This additional gain in lead time can be achieved only by including precipitation information ahead of its occurrence. However, most of the operational runoff forecasting systems are based on deterministic hydrometeorological chains, which do not quantify the uncertainty in the outputs. But, as it has been widely

[1]The content of this chapter is based on the paper Amengual, A., T. Diomede, C. Marsigli, A. Martín, A. Morgillo, R. Romero, P. Papetti and S. Alonso, 2008: A hydrometeorological model intercomparison as a tool to quantify the forecast uncertainty in a medium size basin. Special Issue on 'Propagation of uncertainty in advanced meteo-hydrological forecast systems', *Nat. Haz. and Earth. Syst. Sci.*, (conditionally accepted).

exposed in section 1.2, the flood simulation and forecasting processes comprise several sources of uncertainty.

Some works have been addressed to the study of these uncertainties through a numerical meteorological model intercomparison. For example, Anquetin et al. (2005) analyzed the 8-9 September 2002 flood occurred in the Gard region, France; and Mariani et al. (2005) studied the 9-10 June 2000 flash-flood episode in Catalonia, Spain. The former work aimed at an improvement of QPFs to be relevant for hydrological modeling purposes, and the latter study was devoted to draw more conclusions of the model factors which can give a good forecast for these kinds of events. Both studies pointed out that high-resolution modeling is an important issue to address for a successful prediction of convectively-driven episodes bearing high amounts of precipitation. However, these works also found the aforementioned problems on the precise location and timing of the simulated precipitation patterns and an underestimation on the rainfall amounts by the limited area models as well.

In this context, the present chapter aims at highlighting some meteorological and hydrological factors which could enhance the hydrometeorological modeling of such hazardous events. At this purpose, we evaluate through a model intercomparison the uncertainties owing to two different sources which directly affect hydrometeorological modeling: one arising from the errors in the QPFs provided by a mesoscale meteorological model and the other arising from the errors in the hydrological model formulation. The first is, in turn, due to errors in the initial and boundary conditions, to the limited vertical and horizontal resolutions adopted, to the nesting strategy used to drive the model and to the formulation of the model itself. In order to take into account the meteorological model error, two different non-hydrostatic limited-area mesoscale models have been used: (i) the COSMO model (previously known as Lokal Modell) and; (ii) the MM5 model.

The other sources of error affecting the QPFs have been considered by using different initial and boundary conditions and by changing the models' resolution. Furthermore, it has been used two different nesting techniques: COSMO and MM5 have been run in a one-way and a two-way nesting mode, respectively. In the one-way nesting, the information is interpolated from the coarse to the fine grid without feedback from the fine grid. The two-way nesting allows a feedback upscale of the small-scale features from the fine to the coarse domain, and therefore, it influences the features in the large-scale (Zhang and Fritsch, 1986). Even though a two-way interaction is believed to work better, it may introduce instabilities at the interface between the two grids which may degrade the solution (Zhang et al., 1986). Therefore, both nesting techniques could lead to rather different results on the simulated precipitation fields when applied to a mesoscale episode with marked dynamic forcing and over a region with such complex sea-land and orographic distributions as northern Italy.

On the other hand, in order to consider also the part of the uncertainty coming from the hydrological model formulation, two different rainfall-runoff models have been considered, even though the choice of the one most appropriate model for any specific task is difficult (Todini, 2007). The two models are: (i) the physically-based HEC-HMS model –run in a semi-distributed and event-based configuration– and; (ii) the distributed and physically-based TOPographic Kine-matic APproximation and Integration (TOPKAPI) model –run in a continuous way–. These models have been implemented over the upper Reno river basin and differ in their physical parameterizations and structure. Concretely, their different physical descriptions of the soil infiltration mechanism are of particular interest in this chapter. This aspect influences the simulated basin's response strongly, since it determines the modeled soil moisture content. An accurate quantification of the initial state of this variable before the occurrence of a flood event is fundamental for a reliable hydrological model forecast.

For practical hydrological predictions there are important benefits in exploring different hydrological model structures (Butts et al., 2004). As a matter of fact, this approach enable to examine the impact of model structure error and complexity on the flood forecasting chain and to extend the assessing of modelling uncertainty involved in the meteo-hydrological coupling. In the hydrological literature, recent studies have investigated the use of different models, in particular with respect to the effects of model structure in the context of modelling performance and to consider in a more comprehensive way uncertainty in model structure (Refsgaard and Knudsen, 1996; Atkinson et al., 2002 and 2003; Farmer et al., 2003; Butts et al., 2004; Georgakakos et al., 2004; Koren et al., 2004; Hearman and Hinz, 2007). Regarding the aim of the present chapter, the use of two models with different structures, especially for the modelling of the soil infiltration mechanism, may result beneficial to better understand and describe the rainfall-runoff transformation processes, according to the nature of the rainfall episode which occur over the catchment in question. As a matter of fact, the characteristics of the rainfall event (i.e. spatial-temporal distribution and intensity) may influence the simulated catchment's response depending on the modelled surface runoff generating mechanism (Hearman and Hinz, 2007).

The accuracy of the simulations provided by the proposed hydrometeorological experiments is assessed by means of a threefold approach. First, the experiments have been evaluated by comparing the spatial observed and simulated rainfall accumulations through a point validation methodology using categorical verification statistics. Second, the performance of the spatial and temporal distributions of the QPFs over the upper Reno river basin has been examined by using continuous verification indices. Finally, it has also been analyzed the simulated discharges which result from the one-way coupling with the NWP models in the catchment of interest. Thus, the hydrological models are employed also as a validation tool for the QPFs. To fulfil this aim, the stream-flows obtained by using observed rainfall data as input have been used as reference values for the comparison with the results derived from the mesoscale models driven runoff simulations. In this way, systematic errors of the hydrological models would not affect the comparison.

The chapter is structured as follows: section 5.2 contains a brief description of the study area and of the selected intense rainfall episode; section 5.3 describes the hydrological models used for the basin characterization; section 5.4 describes the numerical meteorological models; section 5.5 presents and discusses the results; and finally, section 5.6 provides an assessment of the proposed methodology.

5.2 Descriptions of the area of interest and the event

5.2.1 The watershed of interest

The Reno river basin is the largest in the Emilia-Romagna Region, northern Italy, measuring 4930 km^2 (Fig. 1.7). It extends about 90 km in the south-north direction, and about 120 km in the east-west direction, with a main river total length of 210 km. Slightly more than half of the area is part of the mountain basin. The basin is divided into 43 subcatchments. The mountainous part, crossed by the main river, covers 1051 km^2 up to Casalecchio Chiusa, where the river reaches a length of 84 km starting from its springs (Fig. 1.7). This upper catchment extends about 55 km in the south-north direction, and about 40 km in the east-west direction. It follows a foothill reach about 6 km long, characterised by a particular hydraulic importance since it has to connect the regime of mountain basin streams with the river regime of the leveed watercourse in the valley. Contributing to the importance of this reach is the fact that it extends practically to within the city limits of Bologna. Then, the valley reach conducts the waters (enclosed by high dikes) to its natural outlet in the Adriatic Sea, flowing along the plain for 120 km. In the valley reach, the transverse section of the Reno river is up to about 150-180 m wide.

The altitude of 44% of the area is below 50 m, 51% is characterized by an altitude from 50 m up to 900 m, and the remaining 5% is between 900 and 1825 m. The concentration time of the watershed is about 10-12 hours at the Casalecchio Chiusa river section and about 36 hours when the flow propagates through the plain up to the outlet. In this chapter, the observed and simulated discharges are evaluated at Casalecchio Chiusa, the closure section of the mountainous basin (hereafter 'Reno river basin' refers only to this upper zone of the entire watershed). In practice, a flood event at such a river section is defined when the water level, recorded by the gauge station, reaches or exceeds the value of 0.8 m (in terms of discharge, a value of about 80 m^3s^{-1}), corresponding to the warning threshold. The pre-alarm level is set to 1.6 m (corresponding to a discharge value of about 630 m^3s^{-1}).

5.2.2 The 7-10 November 2003 event

On November 6, at about 00 UTC, an upper level deep trough at the level of 500 hPa is active over Northern Europe and moves towards south-west interesting the Balcanic area, evolving into a cut-off low in the following hours (not shown). On 00 UTC 7 November this cyclonic vortex moved backward from the Adriatic sea and in the following 12 hours reached the Alpine region (Fig. 5.1). During the evening the cyclone continues to move backward and the upper level winds tend to become southerly. Starting from the evening of the day 7, intense precipitation occurred over the central part of the Apennine chain, especially over the Reno river basin, with presence of large amounts of snowfall over the western Apennine even at moderate altitude (less than 500 m). The persistence of southerly upper level winds determines on the following morning a rapid increase of temperature. On November 8th, thundery cells develop over Tuscany and determine intense precipitation over the central part of the Apennine chain, in particular over the hydrographic basin of the Panaro and Reno rivers.

During the whole 48-h event (Fig. 5.2), a widespread precipitation was observed over northern Italy. Intense rainfall interested the whole Emilia-Romagna Region and the north-eastern part of Italy, with several station recording values up to 100 mm in 48 h. Maximum values of about 150-200 mm/48 h were reached over the central Apennine, on the upper part of the Reno river basin. The maximum water level at Casalecchio Chiusa was 1.75 m (corresponding to a discharge value of about 760 m^3s^{-1}), at 20 UTC, November 8, representing the 13th most critical case in terms of flood event magnitude over a historical archive of 90 events from 1981 to 2004.

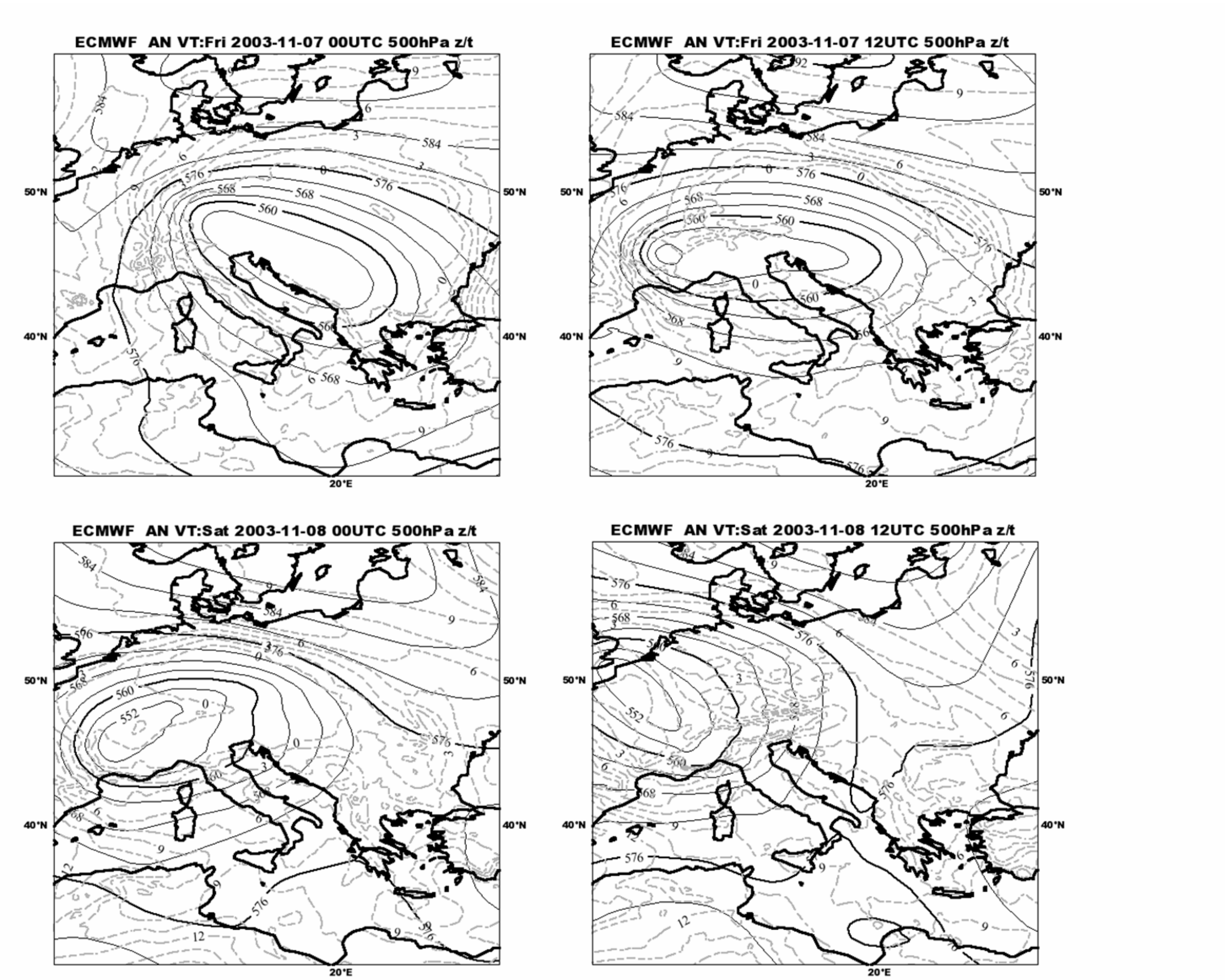

Figure 5.1: ECMWF analyses of the geopotential height at 500 hPa (contours in continuous black line) and of temperature at 850 hPa (contours in dash grey line) every 12 hours from 00 UTC 7 November 2003 to 12 UTC 8 November 2003.

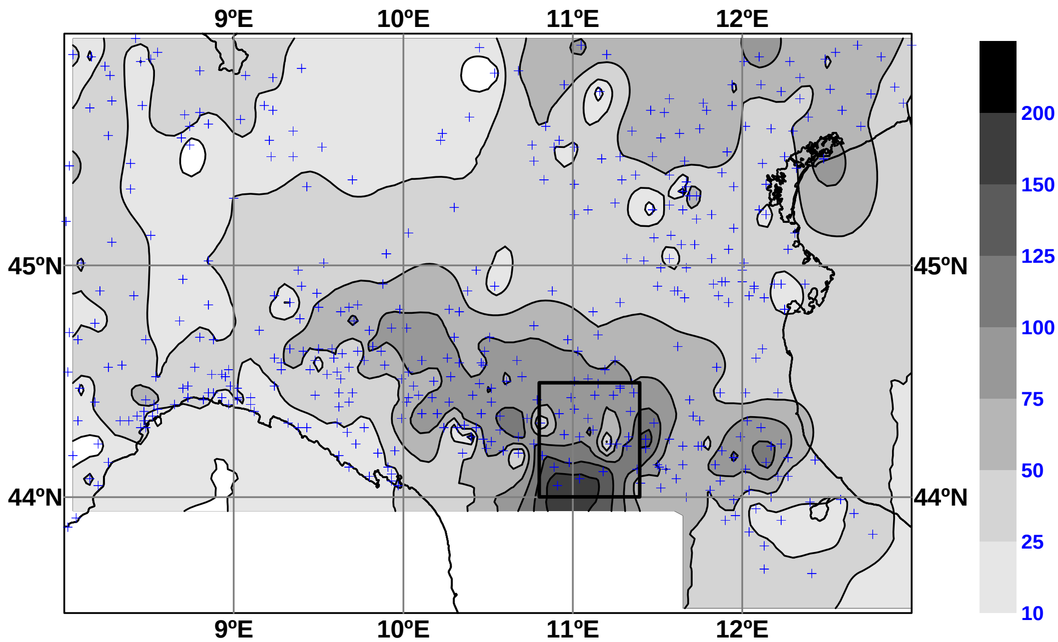

Figure 5.2: Accumulated observed precipitation (in mm according to the scale) from 13 UTC 7 November 2003 to 12 UTC 9 November 2003, over an area covering northern Italy. The area of the upper Reno river basin is included within the black rectangle. Blue crosses denote the 579 rain-gauges available over the domain. Kriged observed precipitation has been blanked in the areas without rain-gauge information in order to avoid artificial rainfall distributions.

5.3 The hydrological models

The hydrometeorological model intercomparison study proposed in the present chapter is carried out by using two different rainfall-runoff models to generate simulated discharges. These are: (i) HEC-HMS (section 2.2) and; (ii) TOPKAPI (Todini and Ciarapica, 2002).

5.3.1 HEC-HMS model

The model has been implemented in a semi-distributed and event-based configuration (section 2.2). Figure 5.3 depicts the digital elevation map (DEM) used, with a cell resolution of 500 meters, and the main watercourses forming the upper Reno river catchment. The whole basin has been segmented in 13 subbasins with an average size of 83.6 km^2. The hydrological model is forced using a single hyetograph for each subbasin. Rainfall spatial distributions were first generated from hourly values recorded at the automatic rain-gauge stations by applying kriging method with a horizontal grid resolution of 500 meters. Then, the hourly rainfall series were calculated for each subbasin as the area-averaged of the grided precipitation within the subcatchment. The same methodology is used to assimilate forecast precipitation fields in HEC-HMS, except the atmospheric model grid points values are used instead of pluviometric observations. The kriging analysis method has been used by applying a linear model for the variogram fit. This minimal error variance method is recommended for irregular observational networks and has been commonly used to compute rainfall fields from rain-gauges (Krajewski, 1987; Bhagarva and Danard, 1994; Seo, 1998).

The hydrological model set-up is identical to this explained in sections 2.2 and 3.4.1. It has also been modeled the baseflow by means of an exponential recession method in order to explain the drainage from natural storage in the watershed (see section 2.2.3). HEC-HMS has been calibrated during the 2002-2003 period. Within this period, three events were considered the most suitable to perform the model calibration owing to their similar characteristics to our case study. The similarity is intended in terms of: the antecedent soil conditions, the convective nature of the rainfall driving to intense precipitation rates in short time scales, and the notable amplitude of the subsequent peak discharges (all of them exceeded 300 m^3s^{-1}). The calibration procedure is widely described in sections 2.2.6 and 3.4.1. Then, for the 7-10 November 2003 event, the rainfall-runoff model is run in a single evaluation simulation. This simulation lasts 84 hours from 12 UTC on 7 November 2003 to 00 UTC on 11 November 2003, with a time-step interval of 1 hour. This period completely encompasses the flood event and the subsequent hydrograph tail. All the mesoscale model driven runoff experiments are run for the same time window.

5.3.2 TOPKAPI model

This model couples the kinematic approach with the topography of the catchment and transfers the rainfall-runoff processes into three 'structurally-similar' zero-dimensional non-linear reservoir equations. Such equations derive from the integration in space of the non-linear kinematic wave model: the first represents the drainage in the soil, the second represents the overland flow on saturated or impervious soils and the third represents the channel flow. The parameter values of the model are shown to be scale independent and obtainable from DEM, soil maps and vegetation or land-use maps in terms of slopes, soil permeabilities, topology and surface roughness. A detailed description of the model can be found in Liu and Todini (2002).

For the implementation of the model over the Reno river basin, the grid resolution is set to 500x500 m. This size of the grid cell, which represents a computational node for the mass and momentum balances, can be considered appropriate to take into account all the hydrological processes that are mainly lead by the slope. As a matter of fact, a correct integration of the differential equations from the point to the finite dimension of a pixel, and from the pixel to larger scales, can actually generate relatively scale independent models, which preserve, as averages, the physical meaning of the model parameters (Liu and Todini, 2002). This consideration is reflected in the TOPKAPI approach.

The calibration and validation runs have been performed forcing the model in a continuous way with the hourly rainfall and temperature data observed from 1990 to 2000 over the Reno river basin. The calibration process did not use a curve fitting process. Rather, an initial estimate for the model parameter set was derived using values taken from the literature. Then, the adjustment of parameters was performed according to a subjective analysis of the discharge simulation results. The simulation runs performed for the present chapter have been carried out exploiting different techniques to spatially distribute the precipitation data (forecasts and rain-gauge observations) onto the hydrological model grid. A Block Kriging technique, developed by Mazzetti and Todini (2004), was applied to interpolate the irregularly distributed surface observations. Within the framework of this approach, once the semi-variogram model has been defined (the Gaussian model in this case), the computation of the parameters of the Semi-variogram function is updated at each time step using a Maximum Likelihood estimator (Todini, 2001). On the other hand, the rainfall fields predicted by COSMO-LAMI were downscaled to each pixel of the hydrological model structure by assigning to the value of the nearest atmospheric model grid point.

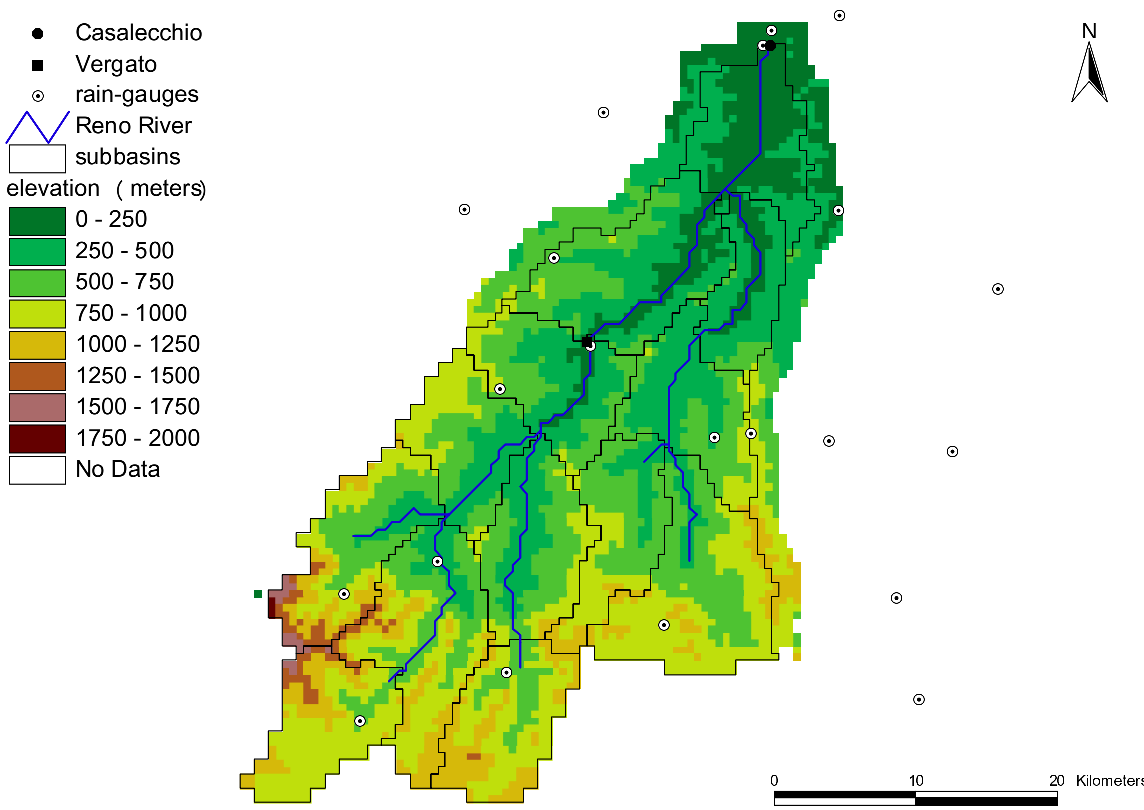

Figure 5.3: Digital elevation model (DEM) of the upper Reno river basin. It displays the basin division defined in the implementation of the HEC-HMS model; the main watercourses; the automatic pluviometric stations nearby the watershed (dotted circles); and the flow-gauge (black circle) closing the basin at Casalecchio outlet.

5.4 The meteorological models

The non-hydrostatic COSMO and MM5 limited-area models are used to perform the meteorological simulations. Table 5.1 briefly summarizes the different models' experiments, with their main characteristics such as initial and boundary conditions, the nesting technique, the number of vertical levels and the models' horizontal resolutions. The model integration domains are shown in Fig. 5.4.

5.4.1 COSMO model

The COSMO model (previously known as Lokal Modell) was originally developed at the DWD (Deutscher WetterDienst) (Steppeler et al., 2003) and it is currently developed and maintained by the COSMO Consortium (COnsortium for Small-scale Modelling), which involves Germany, Italy, Switzerland, Greece, Poland and Romania.

COSMO is a non-hydrostatic model, based on the primitive equations describing fully compressible non-hydrostatic flow in a moist atmosphere, without any scale approximation. The model equations are expressed with 5 prognostic variables: temperature, pressure, humidity, horizontal and vertical velocity components. They are solved numerically using the traditional finite difference method on a Arakawa-C grid. In the vertical, a terrain following hybrid σ-type coordinate is used. The subgrid-scale physical processes described by parameterisation schemes are: radiation (Ritter-Geleyn, 1992, scheme), surface turbulent fluxes and vertical diffusion, soil processes, subgrid-scale clouds, moist convection (Tiedtke, 1989, mass-flux scheme), grid-scale clouds and precipitation. The microphysical scheme includes 5 hydrometeors, for which the prognostic equations are solved: cloud ice, cloud water, rain, snow, graupel. For a complete description of the model, the reader is referred to the COSMO web site (www.cosmo-model.org, mirror site on cosmo-model.cscs.ch).

ARPA-SIM has been using COSMO as the operational forecast model since 2001; COSMO is run twice a day (at 00 UTC and 12 UTC) for 72 hours with a spatial horizontal resolution of 7 km and 40 layers in the vertical. The boundary conditions are supplied (one-way nesting) by the global model of the ECMWF (European Centre for Medium-range Weather Forecasts) every three hours. The initial condition is provided by a mesoscale data assimilation based on a nudging technique. The variables which are assimilated are: temperature, humidity and wind. The model is also operational twice a day at 2.8 km, with 45 vertical layers, nested (one-way) on the 7 km runs starting at 00 and 12 UTC. The forecast range is 48 hours.

For this chapter, the model (version 3.9) has been run in a slightly different configuration, since only 35 vertical layers have been used for both the 7 km and 2.8 km runs. Graupel was not available as a prognostic variable in model version 3.9. Initial and boundary conditions are provided by ECMWF analyses or forecasts for all the models, testing different configurations (Table 5.1). The model integration domains are shown in Fig. 5.4a.

In the *COSMO hind+obs 7* experiment (**control**) the model is driven by ECMWF analyses every 6 hours and observations are assimilated with the nudging technique throughout the whole running period (60 h, referred to as continuous assimilation in Table 5.1), while in the *COSMO hind* experiment no assimilation is performed. In the *COSMO fc 7* experiment, the initial condition is provided by a mesoscale data assimilation with the nudging technique over the preceding 12 hours (referred to as COSMO analysis in Table 5.1), while the boundary conditions are provided every 3 hours by the ECMWF operational model forecasts. In the latter case, therefore, a real time forecast is simulated. In the 2.8 km runs an explicit representation of the deep convection is allowed by switching off the Tiedtke convection scheme. The simulations are 72 h long.

5.4.2 MM5 model

MM5 model is used to perform the meteorological simulations (further details in section 2.3). Simulations are designed using 24 vertical σ-levels, with higher density near the surface to better resolve near-ground processes, and three spatial domains with 151 x 151 grid points centered in north-western Italy (Fig. 5.4b). Their respective horizontal resolutions are 22.5, 7.5 and 2.5 km. Concretely, the second domain spans the entire Italian peninsula as well as important oceanic areas surrounding Italy, including Corsica and Sardinia. The third domain covers a geographical area centered upon the upper Reno river basin. The interaction between the domains follows a two way nesting strategy (section 2.3). The second and third domains are used to supply the high-resolution rainfall fields to drive the hydrologic simulations depending on the runoff experiment. With the 2.5 km resolution driving data it is possible to test whether the enhanced representation of local topographic forcings leads to an improvement of the simulated precipitation fields.

To parameterise moist convection effects in the meteorological simulations, the modified Kain-Fritsch scheme is used for the first and second domains. In the third domain, the convection is explicitly resolved owing to the very high resolution. Moist microphysics, planetary boundary layer physics, surface temperature over land and sea, and finally, long and short wave radiative processes are widely described in sections 2.3 and 3.5.

To initialize the model and to provide the boundary conditions, ECMWF analyses and forecasts are used depending on the experiment (Table 5.1; further details in sections 2.3 and 3.5). For the *MM5 hind+obs* at 7.5 (**control**) and 2.5 km experiments, the first guess fields –interpolated from the ECMWF analyses on the MM5 model grid– are improved using surface and upper-air observations with a successive-correction objective analysis technique. The whole set of MM5 simulations comprise a 48 hour simulation period starting at 12 UTC on 7 November 2003.

Experiment	Model	Horizontal resolution (km)	Grid points	Levels	Initial and boundary conditions	Assimilation	Nesting procedure
COSMO hind+obs 7 (**control**)	COSMO	7	234x272	36	ECMWF analyses	continuous	1-way
COSMO hind 7	COSMO	7	234x272	36	ECMWF analyses	No	1-way
COSMO hind 2.8	COSMO	2.8	265x270	36	COSMO hind 7 analyses and forecasts	No	1-way
COSMO fc 7	COSMO	7	234x272	36	COSMO analysis and ECMWF forecasts	No	1-way
COSMO fc 2.8	COSMO	2.8	265x270	36	COSMO fc 7 analysis and forecasts	No	1-way
MM5 hind+obs (**control** at 7.5 km)	MM5	7.5 2.5	151x151	24	ECMWF analyses	continuous	2-way
MM5 hind	MM5	7.5 2.5	151x151	24	ECMWF analyses	No	2-way
MM5 fc	MM5	7.5 2.5	151x151	24	ECMWF analysis and forecasts	No	2-way

Table 5.1: Summary of the main characteristics for the adopted meteorological models configurations.

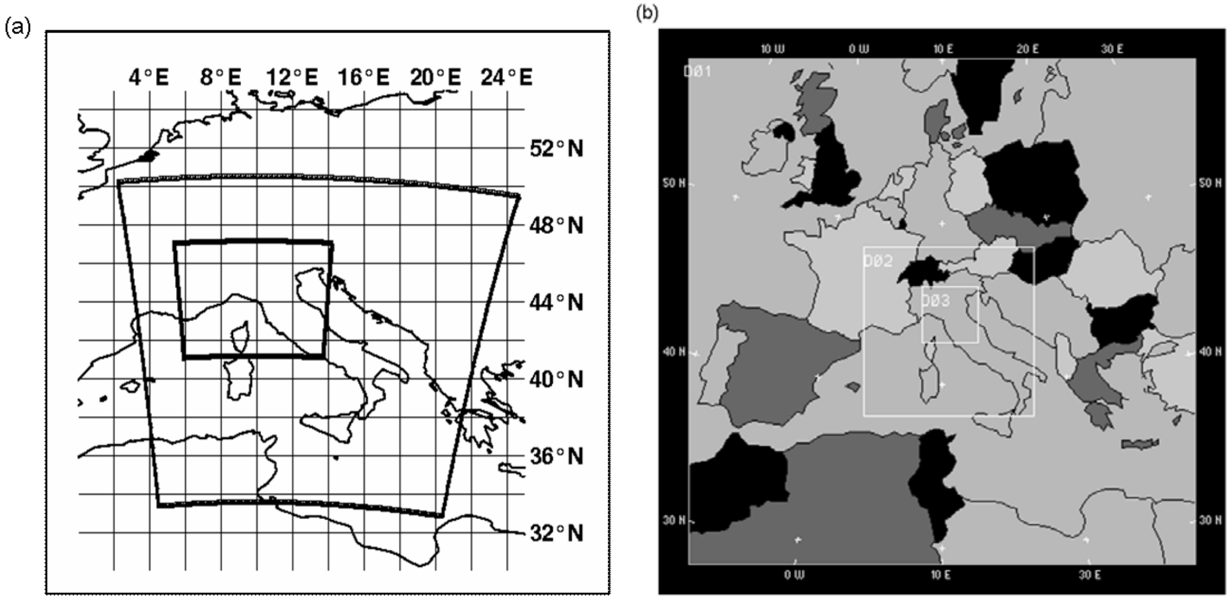

Figure 5.4: (a) Configuration of the domains used for the COSMO simulations with horizontal resolutions of 7 (larger domain) and 2.8 (smallest domain) km and (b) for the MM5 simulations with horizontal resolutions of 22.5, 7.5 and 2.5 km respectively. The Reno river basin is located between 44.0^0-44.5^0 N and 10.8^0-11.4^0

5.5 Results

5.5.1 Runoff simulations driven by rain-gauge data

The streThese rain-gauge driven flows will be used, instead of the observed discharge, for the comparison with the results derived from the meteorological models (sections 5.5.2 and 5.5.3). In such a way, the systematic error of the hydrological model will not affect the comparison. The skill of the resulting runoff simulations are expressed in terms of the NSE, %EV and %EP skill scores at Cassalecchio flow-gauge (further details in Appendix).

The observed hydrograph depicted a maximum discharge of 757.6 m^3s^{-1} on 21 UTC 8 November 2003 (Fig. 5.5). Rain-gauge driven runoff simulations show a similar performance in terms of peak runoff for both models, with a noticeable overestimation of 160.4 m^3s^{-1} and 188.4 m^3s^{-1} for TOPKAPI and HEC-HMS, respectively. This represents an overestimation of the observed peak flow slightly above of the 20% for TOPKAPI and very close to 25% for HEC-HMS, respectively. Otherwise, HEC-HMS reproduces the volume and the time base of the observed hydrograph more accurately than TOPKAPI. Therefore, NSE and %EV result in a better performance for the former than the latter model (Table 5.2 and Fig. 5.5). The time to peak is identical for both models and it is simulated on 22 UTC 8 November 2003 with a delay of only 1 hour.

MODEL	NSE	%EV	%EP
HMS	0.86	13.2	24.9
TOPKAPI	0.77	34.7	21.2

Table 5.2: Performance of the rain-gauge driven runoff simulations for the 7-10 November 2003 episode and for the HEC-HMS and TOPKAPI hydrological models in terms of NSE efficiency criterion, $\%EV$ and $\%EP$ at Casalecchio flow-gauge.

The overestimation of the runoff volumes and the peak discharges for both models can be ascribed to several factors. First, an inaccurate reproduction of the infiltration processes –that might lead to consider the initial soil moisture content slightly superior to the existent–, can produce an overestimation of precipitation available for runoff during the event. Second, the presence of a small hydroelectric reservoir located in the upper catchment –which has not been modeled– can also affect the modeled basin's response, since its impact on the flow regime and the runoff volume cannot be negligible.

On the other hand, both hydrological models fit the dynamical routing and the rising limb of the observed hydrograph quite well, in spite of not reproducing the first bump of runoff observed on 12 UTC 8 November 2003. This bump is due to a short intense raining period comprised within the forecast time steps 18th and 21st (Fig. 5.9), which especially affected the left side of the upper basin. Therefore, this failure could be ascribed to an inaccurate reproduction of the observed rainfall field over the area located in the left side of the upper basin, upstream to the Vergato river section (Fig. 5.3). The scarce presence of rain-gauges in this zone could have affected the accuracy of the rainfall inputs, leading to a slight and localised underestimation of the precipitation amounts. It is also worth to remark the more smoothed recession limb obtained for the TOPKAPI rain-gauge driven simulation, although both models do not reproduce in an accurate way this feature. This result may be ascribed to the several facts, such as: first, TOPKAPI reproduces the dynamics of the overall soil filling and depletion mechanisms and the flood routing in a more unrealistic way (particularly, underestimating the soil depletion mechanism) than HEC-HMS for the current case study, and second; the impact of the reservoir in the models' structure and its hydrograph diffusion effect in the flood wave can have a remarkable role in the aforementioned inaccuracies. Unfortunately, the technical characteristics and the release data for this reservoir are not available. Despite the abovementioned shortcomings, the reproduction of the flood event provided by both rain-gauge driven hydrological models simulations can be considered accurate, especially from the point of view of stakeholders (i.e. end users such as representatives from civil protection authorities for the aims of civil protection), since the timing and the order of magnitude of the event are well simulated.

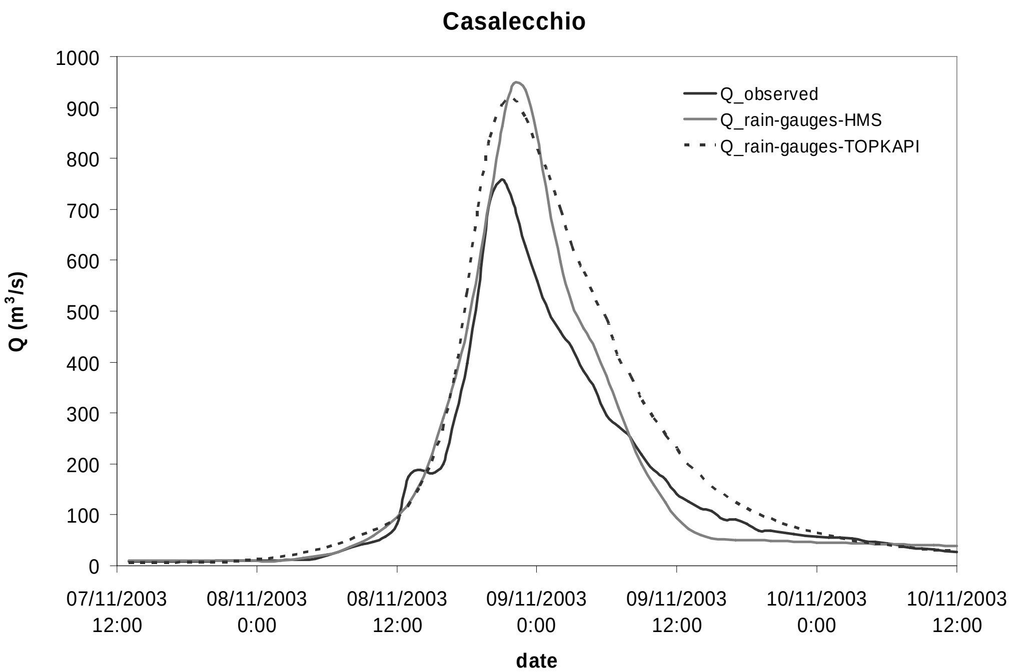

Figure 5.5: Rain-gauge driven runoff simulations provided by HEC-HMS and TOPKAPI models versus the observed discharge

5.5.2 Runoff simulations driven by COSMO and MM5 experiments

The COSMO and MM5 meteorological simulations have been evaluated at a scale larger than the basin by comparing the spatial observed and simulated rainfall accumulations over northern Italy in the 6-h period of maximum precipitation (from 12 to 18 UTC on 8 November 2003; Fig. 5.6a). Therefore, the analysis of the cumulative rainfall fields for this time window provides valuable information of the models' skill to simulate the more intense rainfall period. At this aim, a set of non-parametric statistical scores has been calculated through a point validation methodology. Then, Threat Score (TS), Bias Score (BIAS) and False Alarm Ratio (FAR) have been computed (Appendix). To interpolate the spatial distributions from the models' grid-points into the 579 rain-gauge point locations available over the domain, it has been used the bilinear interpolation method for each experiment. The set of thresholds includes values up to 50 mm/6 h due to the high intensity of the observed rainfall amounts. It is worth to note that it has not been possible for some experiments to compute statistical scores at the largest thresholds, since the forecasts never exceeded these thresholds.

To quantify the skill of the precipitation fields provided by both COSMO and MM5 simulations at catchment scale, the area-averaged spatial and temporal distributions of these patterns are compared against the observed rainfall distribution over the Reno river basin by using two continuous statistical indices: the NSE and the mean absolute error (MAE; Appendix). At this aim, the 13 subbasins segmentation of the catchment –carried out to implement the HEC-HMS runoff model in its semi-distributed configuration– has been used to evaluate the spatial distributions. Each individual subbasin has been used as an areal accumulation unit for the rainfall amounts over a 48 h time window, starting at 13 UTC on 7 November 2003. Thus, the results based on these cumulative rainfall fields provide information of the general performance of the models to simulate the whole event. The temporal distributions are computed by using hourly rainfall amounts over the whole basin and during the same 48 h time period. The hourly discretizations are found suitable in order to evaluate the ability of the mesoscale models of providing enough intense simulated rainfall fields, owing to the short times of concentration of the basin when it is affected by intense rainfall.

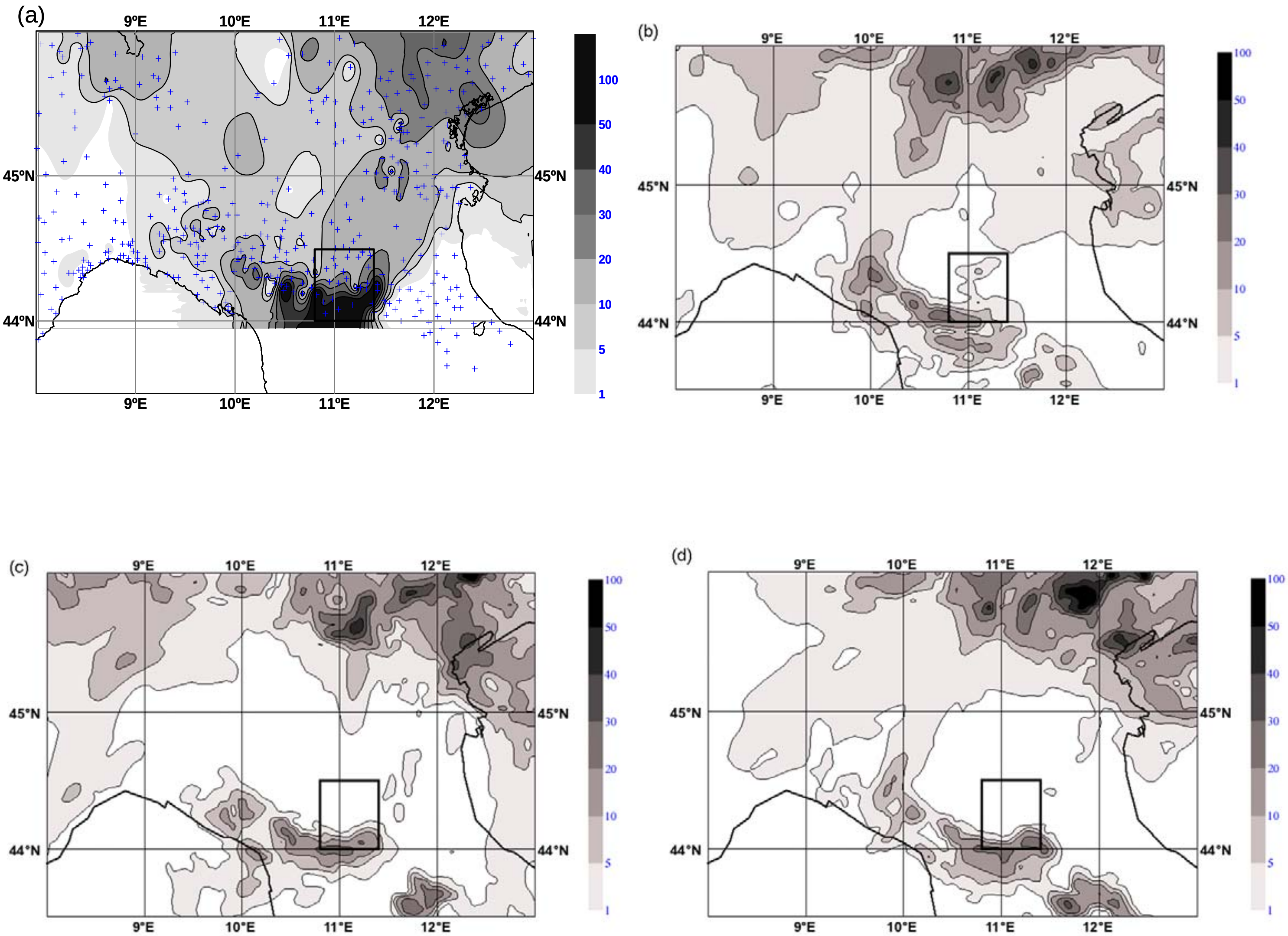

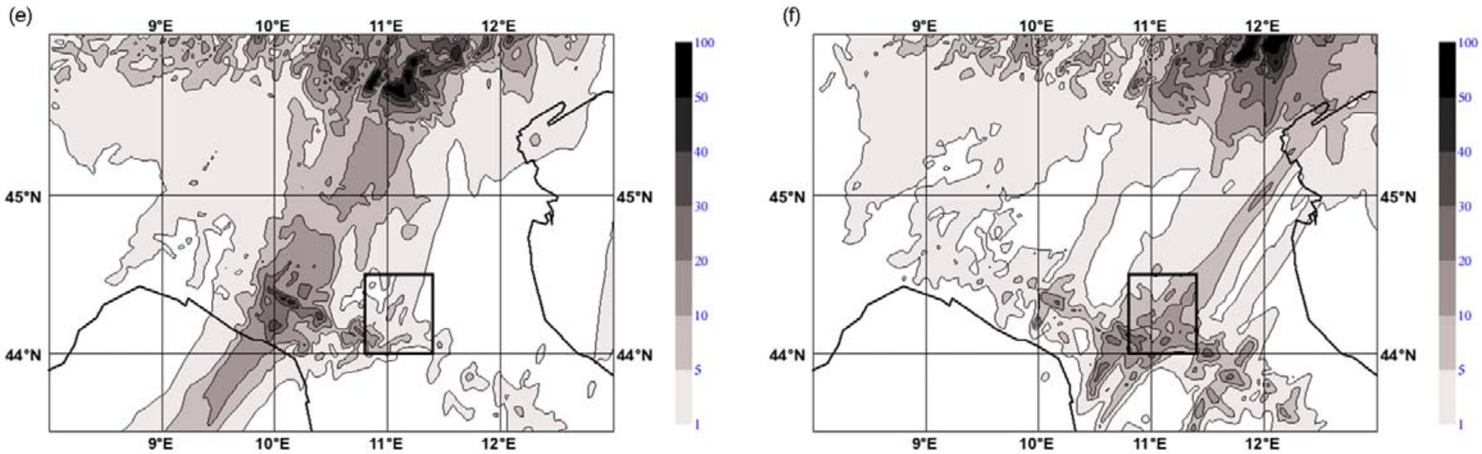

Figure 5.6: Observed (a) and forecasted precipitation accumulated over 6 hours (on 12-18 UTC 8 November 2003) provided by the following COSMO runs: (b) control (*COSMO hind+obs 7)*, (c) *COSMO hind 7*, (d) *COSMO fc 7*, (e) *COSMO hind+obs 2.8*, (f) *COSMO fc 2.8*. Rainfall is shown in mm according to the scale. In Fig. 5.6a the blue crosses denote the rain-gauges, and the kriged observed precipitation has been blanked in the areas without rain-gauges in order to avoid artificial rainfall distributions.

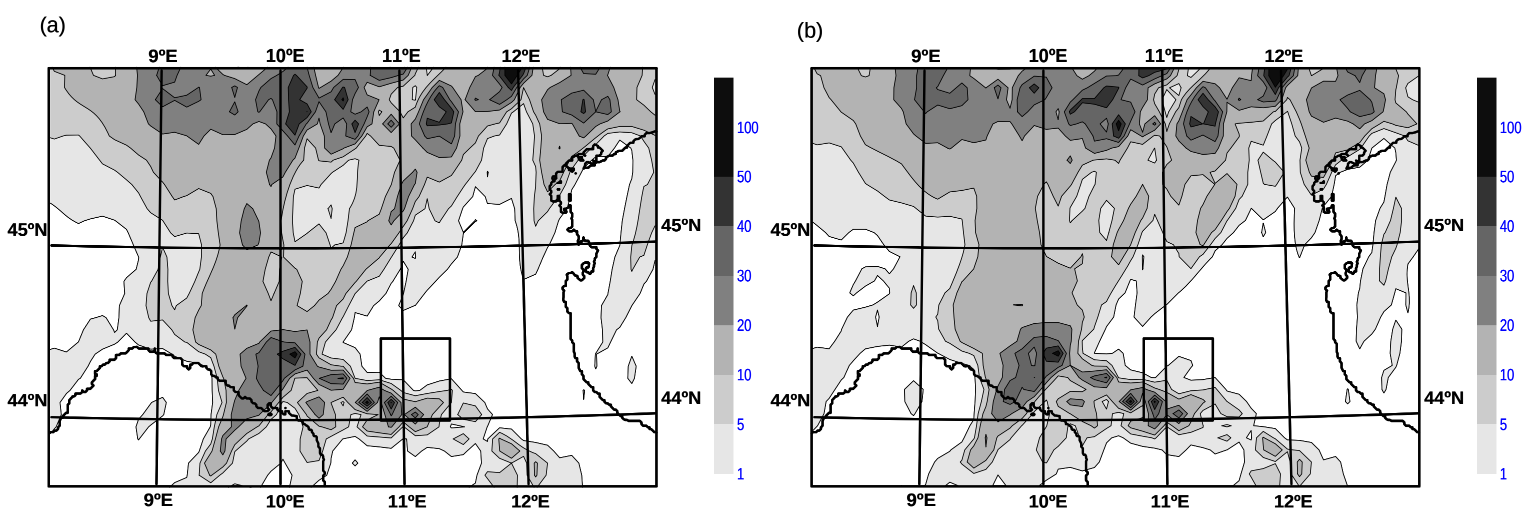

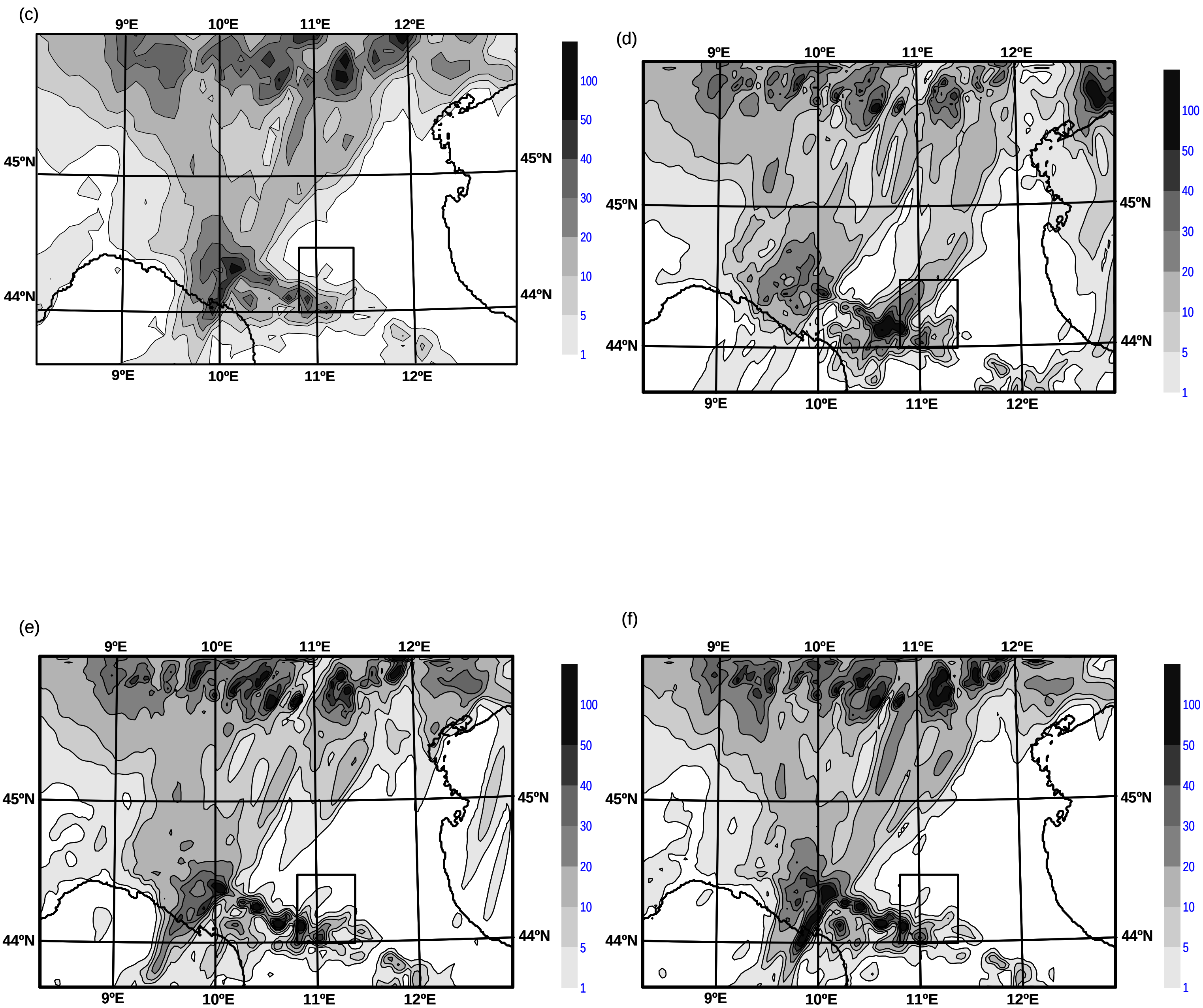

Figure 5.7: Forecasted precipitation accumulated over 6 hours (on 12-18 UTC 8 November 2003) provided by the following MM5 runs: (a) control (*MM5 hind+obs 7.5*), (b) *MM5 hind 7.5*, (c) *MM5 fc 7.5*, (d) *MM5 hind+obs 2.5*, (e) *MM5 hind 2.5* and (f) *MM5 fc 2.5*. Rainfall is shown in mm according to the scale.

(a) COSMO and MM5 control runs

Six hourly accumulated precipitations provided by both COSMO and MM5 control simulations over northern Italy are analysed. The COSMO simulation reproduces quite well the precipitation occurred over the north-eastern Alps, even if the structure is spatially shifted (Fig. 5.6b), whereas the MM5 experiment shows a greater spread in simulating the precipitation field over the Alps, together with a slight overforecasting of the rainfall amounts (Fig. 5.7a). Both models do not forecast correctly the rainfall amounts observed within the Reno river basin, but capture the precipitation pattern over the western part of the Apennines. Therefore, the rainfall amounts inside the catchment are underestimated.

COSMO and MM5 control simulations show the highest TS value at small thresholds, with TS rapidly decreasing for higher thresholds (Figs. 5.8a and b). For medium and high threshold, the MM5 control is better than COSMO in terms of TS. Both experiments underforecast the precipitation amounts over the whole domain (Figs. 5.8c and d), but the MM5 simulations present a better performance with respect to COSMO, the MM5 BS being generally closer to 1. Regarding the FAR (figs. 5.8e and f), both control experiments display a small proportion of incorrect forecasts for the lowest thresholds, but the false alarms increase rapidly for moderate and intense rainfall. At low- and mid-thresholds, the COSMO run is more accurate than the MM5 simulation. It seems that the greater rainfall amounts simulated by the MM5 experiment produce more hits but also more false alarms. It is worth to note that both models are driven by the same initial and boundary conditions and with an assimilation of observational data. Therefore, the aforementioned differences can be ascribed to the different model formulations and, possibly, to the different physical parameterizations. Maybe the convection scheme of the MM5 model is responsible for the enhancement of the rainfall amounts within this complex orographic area. The higher vertical resolution of the COSMO model does not seem to be beneficial for this case.

Tables 5.4 and 5.5 depict the continuous skill scores for the area-averaged spatial and temporal rainfall distributions for both control runs over the catchment. Both the COSMO and MM5 simulations show a low forecasting skill at small scales. The inaccuracies in correctly forecasting the timing and rainfall amount over the upper Reno river basin are depicted in figures 5.9 and 5.10. In particular, the experiments miss the highest precipitation amounts observed around the 25th forecast hour. Therefore, the severe underestimation of the maximum precipitation amounts and the wrong timing are propagated to the subsequent driven runoff hydrographs (Tables 5.6 and 5.7), which exhibit a negative relative error in total volume. The hydrological runs (Figs 5.11 and 5.12) simulate a discharge value exceeding only the warning threshold (i.e. 80 m^3s^{-1}), but not the pre-alarm level (i.e. 630 m^3s^{-1}): COSMO-TOPKAPI and COSMO-HEC driven experiments show a maximum peak discharge slightly superior to 275 m^3s^{-1} (Figs. 5.11a and b) and MM5-TOPKAPI and MM5-HEC driven runoff experiments yield maximum discharges slightly below 200 m^3s^{-1} (Figs. 5.12a and b).

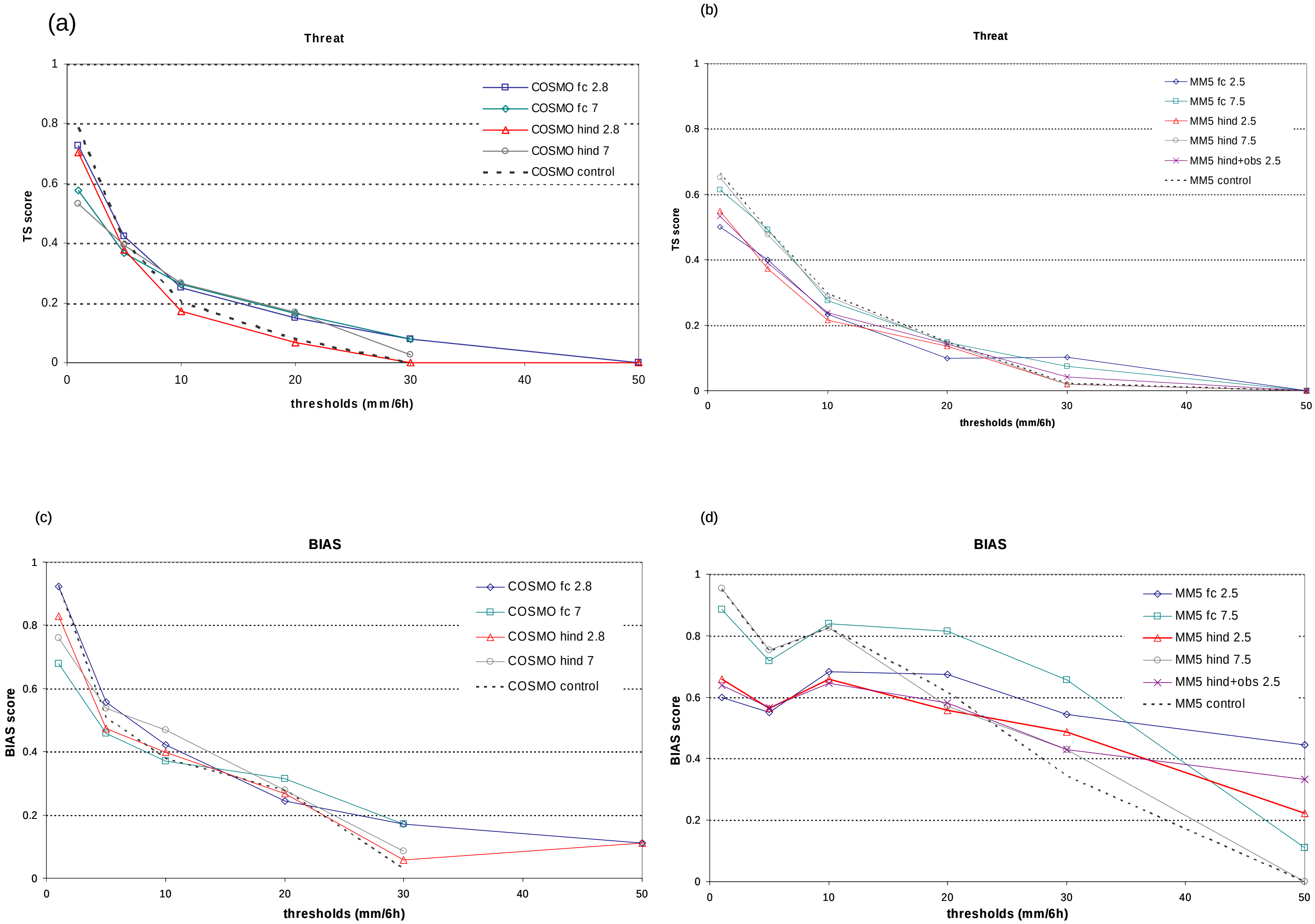
(a)
Threat
TS score
thresholds (mm/6h)
COSMO fc 2.8
COSMO fc 7
COSMO hind 2.8
COSMO hind 7
COSMO control
(b)
Threat
TS score
thresholds (mm/6h)
MM5 fc 2.5
MM5 fc 7.5
MM5 hind 2.5
MM5 hind 7.5
MM5 hind+obs 2.5
MM5 control
(c)
BIAS
BIAS score
thresholds (mm/6h)
COSMO fc 2.8
COSMO fc 7
COSMO hind 2.8
COSMO hind 7
COSMO control
(d)
BIAS
BIAS score
thresholds (mm/6h)
MM5 fc 2.5
MM5 fc 7.5
MM5 hind 2.5
MM5 hind 7.5
MM5 hind+obs 2.5
MM5 control

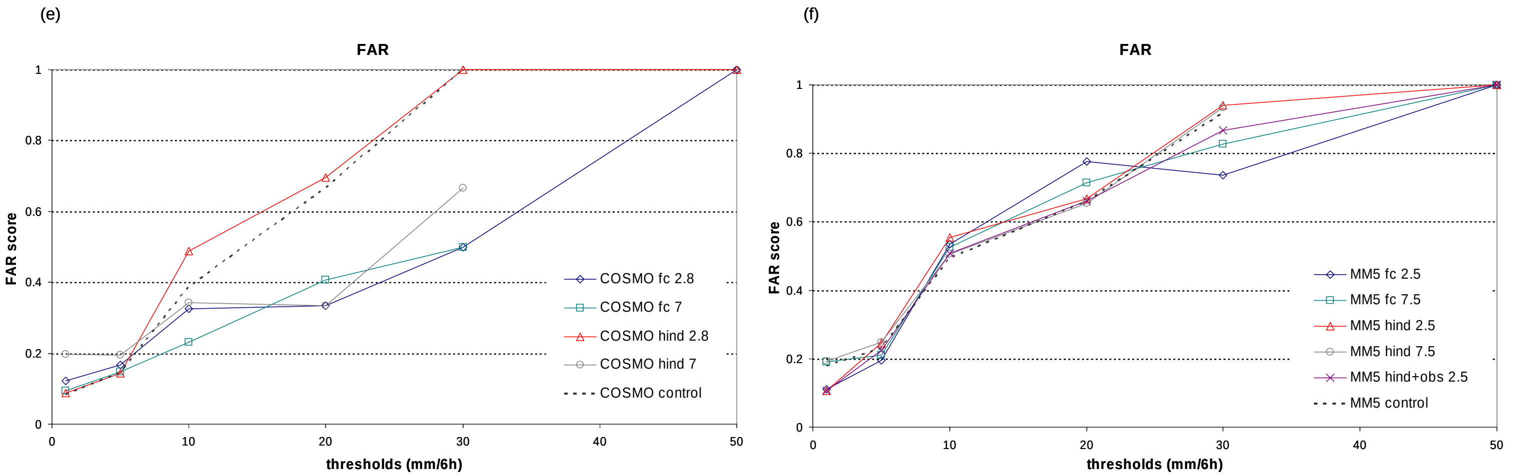

Figure 5.8: TS, BIAS and FAR skill scores for different 6-h rainfall amounts thresholds obtained by the COSMO and MM5 meteorological experiments

experiment	NSE	MAE	experiment	NSE	MAE
COSMO fc 2.8	0.76	1.4	*MM5 fc 2.5*	-1.15	4.5
COSMO fc 7	- 1.33	4.5	*MM5 fc 7.5*	-1.21	4.5
COSMO hind 2.8	-1.52	4.7	*MM5 hind 2.5*	-0.83	4.1
COSMO hind 7	-1.53	4.7	*MM5 hind 7.5*	-0.90	4.2
COSMO control	-0.71	3.7	*MM5 control*	-1.0	4.3
			MM5 hind+obs 2.5	-0.77	4.0

Table 5.3: NSE efficiency criterion and MAE (in mm) of the spatial area-averaged rainfall distributions yielded by the set of mesoscale numerical simulations.

experiment	NSE	MAE	experiment	NSE	MAE
COSMO fc 2.8	-0.11	1.6	*MM5 fc 2.5*	-0.58	2.0
COSMO fc 7	-0.30	1.7	*MM5 fc 7.5*	-0.53	1.9
COSMO hind 2.8	-0.80	2.1	*MM5 hind 2.5*	-0.55	1.9
COSMO hind 7	-0.92	2.3	*MM5 hind 7.5*	-0.52	1.9
COSMO control	-0.46	1.7	*MM5 control*	-0.54	1.9
			MM5 hind+obs 2.5	-0.58	1.9

Table 5.4: NSE efficiency criterion and MAE (in mm) of the temporal area-averaged rainfall distributions yielded by the set of mesoscale numerical simulations.

(b) COSMO and MM5 runs with different configurations

Following the motivation and methodology explained in the previous sections, a set of additional experiments is performed in order to produce the experimental meteorological model runs. Figures 5.6 and 5.7 show the observed and the simulated rainfall accumulations for the remaining COSMO and MM5 experiments over the 6-h period of maximum precipitation.

(b.1) The COSMO based experiments

All the COSMO runs reproduce the observed rainfall structure over the Apennines but underestimate the amounts, especially on the lee side over the Reno river basin (Figs. 5.6 c-f). The tendency to overestimate the rainfall in upwind areas in presence of a mountain range, with a related drying effect in the downwind regions, in case of intense precipitation forecast, has already been recognised as a typical feature of the COSMO model (Elementi et al., 2005). This drawback heavily influences the reliability of the meteo-hydrological forecasting chain implemented for the concerned watershed, resulting in an underestimation of the forecast streamflow (Diomede et. al, 2008). In fact, being located on the north-eastern side of the Apennine barrier, the Reno river basin clearly suffers from such a problem when the flow is from the south-west quadrant.

On the contrary, the precipitation occurred over the Alps is forecasted quite well in terms of rainfall amounts and their spatial distribution (Figs. 5.6c-f). In general, high-resolution experiments produce highest amounts of rainfall for this period; the best forecast is provided by the COSMO fc 2.8 run (Fig. 5.6f). This simulation reproduces the whole rainfall structure quite well within the Reno river basin, but only forecasts moderate amounts of rain. With regard to the Threat Score (Figs. 5.8a), COSMO high-resolution experiments show the highest value at the smallest threshold. At the higher thresholds, no benefits are obtained by the high-resolution runs: *COSMO hind 2.8* has the lower score, while COSMO fc 2.8 has a similar behaviour to the 7 km runs. The underforecasting of the precipitation amounts over northern Italy, expressed by the BS (Fig. 5.8c), remains uncorrected, since no significant differences can be found among the different runs. The False Alarm Ratio is small at the lowest thresholds for all the experiments (Fig. 5.8e). At increasing thresholds, *COSMO hind 2.8* has the worst performance, while *COSMO fc 2.8* has a similar behaviour to the 7 km runs.

At the catchment scale, all the COSMO experiments miss the high precipitation amounts observed around the 25th forecast hour (Fig. 5.9a). However, the *COSMO fc 2.8* experiment provides an underestimation of only about 10% for the total areal amount (Fig. 5.9b), even if this forecast is characterised by a wrong temporal distribution. Tables 5.4 and 5.5 confirm that this experiment exhibits the best forecasting skill in terms of NSE and MAE scores among all the COSMO runs. The aforementioned inaccuracies of the COSMO simulations are propagated to the subsequent set of driven runoff simulations. Figure 5.11 depicts that the amplitudes of the simulated peaks are considerable smaller than the rain-gauge driven maximum discharge, except for the *COSMO fc 2.8* driven experiment. For this experiment, a suitable reproduction can be pointed out for both HEC-HMS and TOPKAPI runs in terms of the peak flows and runoff volumes, although the time to peak is not well fitted. These features are reflected in their statistical scores (Table 5.6), the *COSMO fc 2.8* driven experiments having the smallest values of relative error in volume. Therefore, it is worth to note the usefulness of the *COSMO fc 2.8* driven experiment for the aims of civil protection: the exceeding of the pre-alarm threshold is forecast correctly, and the delay in the time to peak is not crucial with respect to the forecasting lead time.

Experiment	**TOPKAPI**		**HEC-HMS**	
	NSE	**%EV**	**NSE**	**%EV**
COSMO fc 2.8	0.58	-21.9	0.51	-21.4
COSMO fc 7	-0.13	-74.4	-0.10	-71.0
COSMO hind 2.8	-0.40	-77.9	-0.19	-72.6
COSMO hind 7	-0.41	-75.5	-0.23	-70.2
COSMO control	0.15	-65.6	0.05	-63.8

Table 5.5: NSE efficiency criterion and percentage of error in volume for the COSMO driven stream-flow experiments performed by the two hydrological models.

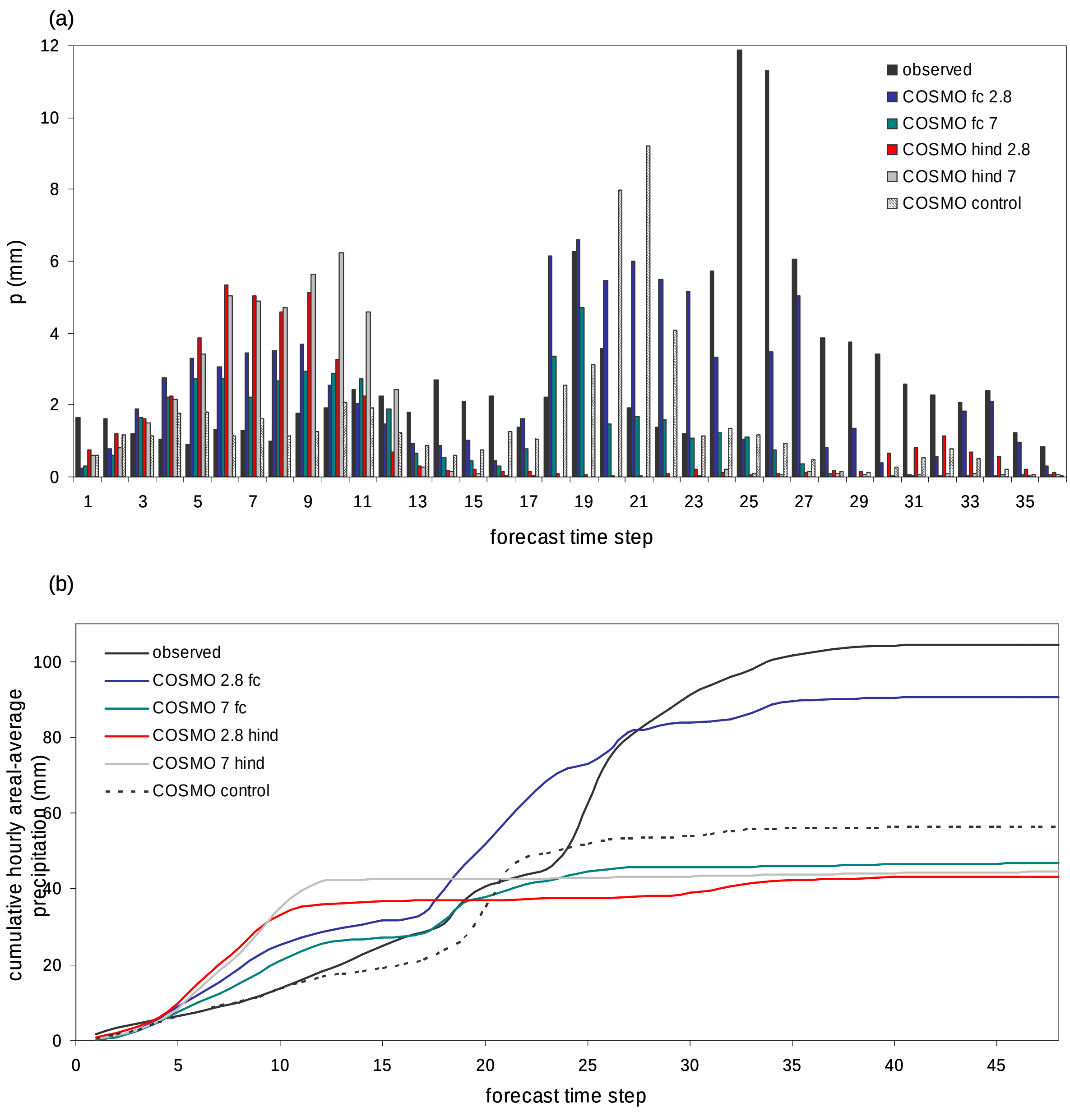

Figure 5.9: (a) Observed and forecasted hourly area-averaged amounts and (b) cumulative hourly area-averaged amounts over the upper Reno river basin provided by the different configurations of COSMO model are displayed from 1300 UTC 7 November 2003 until 00 UTC 09 November 2003.

(b.2) The MM5 based experiments

The maximum cumulative values for the MM5 experiments, in terms of precipitation over northern Italy, range from 66 to 93 mm/6 h. However, the highest values –rather similar to the observations– do not lie inside the basin, but westwards of the catchment in the Apennine range. The precipitation amounts occurred over the eastern part of the Alps are also well simulated, even if all the runs forecast excessive quantities over the western and the central Alps (Figs. 5.7b-f). Threat Score shows a better performance for the low-resolution simulations at small- and mid-thresholds (Fig. 5.8b). At the greater thresholds, higher TS is obtained by the high-resolution experiments, owing to the forecasting of higher rainfall amounts. It is worth to note that low-resolution experiments presents very similar TS values: it appears that the simulated rainfall patterns are rather insensitive to the different initial and boundary conditions used to initialize the MM5 experiments, at least in terms of this index. This feature can be a consequence of dealing with such complex orographic area. In addition, it seems clear that once the low-resolution simulations misplace the correct locations of the precipitation, the high-resolution experiments do not correct these errors due to the two-way nesting strategy. BIAS scores point out an underforecasting of the rainfall amounts over the whole domain for the MM5 runs, but this feature is more moderate than for the COSMO runs (Fig. 5.8d). Again, low-resolution predictions outperform the high-resolution forecasts at small thresholds. At medium thresholds, the *MM5 fc 7.5* run has the best performance, followed by the *MM5 fc 2.5* run, while at the highest threshold the high-resolution runs perform better, since they provide higher rainfall amounts. FAR values indicate small differences among the low- and high-resolution experiments, and the expected continuous rise of the number of false alarms at increasing thresholds is found (Fig. 5.8f).

At the catchment scale, MM5 predictions distribute the maximum rainfall amounts for the upper Reno river basin over the first 12 hours of simulation, completely missing the maximum quantities observed around the 25th forecast hour (Fig. 5.10a). In terms of the cumulative area-averaged precipitation amounts, the event is heavily underestimated by the simulations (about 50%; Fig. 5.10b). This feature is reflected in Tables 5.4 and 5.5: a great homogeneity together with a small skill among all the MM5 simulations are found. These errors are propagated to the MM5 driven runoff simulations. In fact, small differences are found among the low- and high-resolution driven discharge peak flows (Fig. 5.12) and discharge volumes (Table 5.7). Therefore, the flood event is neither simulated in an accurate way by TOPKAPI nor HEC-HMS runoff models.

Experiment	TOPKAPI		HEC-HMS	
	NSE	%EV	NSE	%EV
MM5 fc 2.5	-0.21	-70.2	0.01	-67.9
MM5 fc 7.5	-0.22	-71.6	-0.03	-69.6
MM5 hind 2.5	-0.12	-64.7	0.10	-62.8
MM5 hind 7.5	-0.15	-66.8	0.04	-65.4
MM5 hind+obs 2.5	-0.13	-64.1	0.08	-61.8
MM5 control	-0.20	-68.8	0	-67.3

Table 5.6: NSE efficiency criterion and percentage of error in volume for the MM5 driven stream-flow experiments performed by the two hydrological models.

5.5.3 Further remarks

The comparison among the low-resolution COSMO and MM5 experiments shows the impact of the different model formulation and physical parameterizations (i.e. cloud microphysics, moist convection, boundary layer) on the structure and amounts of the simulated rainfall fields for the investigated event over this complex orographic area. It is found that BIAS scores are closer to 1 for MM5 than for COSMO simulations almost for all the thresholds. The different schemes used for the parameterization of the deep convection in the two models can play a role in determining this result. In fact, this may be due to the fact that the modified Kain-Fritsch scheme of MM5 produces higher precipitation amounts on the domain –rather similar to the observations–, but too much scattered. On the contrary, the Tiedtke moist convection parameterization of COSMO drives to noticeable underestimations of the rainfall amounts, but more constrained to the correct locations.

With regard to the COSMO simulations, the use of different initial and boundary conditions results beneficial, since it appears that a part of the error of the control simulation comes from the inaccuracies found in the boundary conditions. On the contrary for the MM5 simulations, the use of different initial and boundary conditions does not contribute to an improvement of the simulated rainfall fields: low-resolution experiments resemble each other in terms of the forecast hits. Furthermore, the assimilation of mesoscale observations during the hindcast runs does not lead to a significant improvement for both models. The increase of the horizontal resolution –which permits an explicit representation of deep convection– results in an enhancement of the simulated rainfall amounts for the event. One of the high-resolution COSMO simulations shows a significant improvement in the rainfall forecast over the basin, indicating that the explicit representation of the convection plays an important role, in association with more accurate boundary conditions. However, the high-resolution MM5 experiments do not provide an improvement on the location of the simulated rainfall patterns over the Reno river basin.

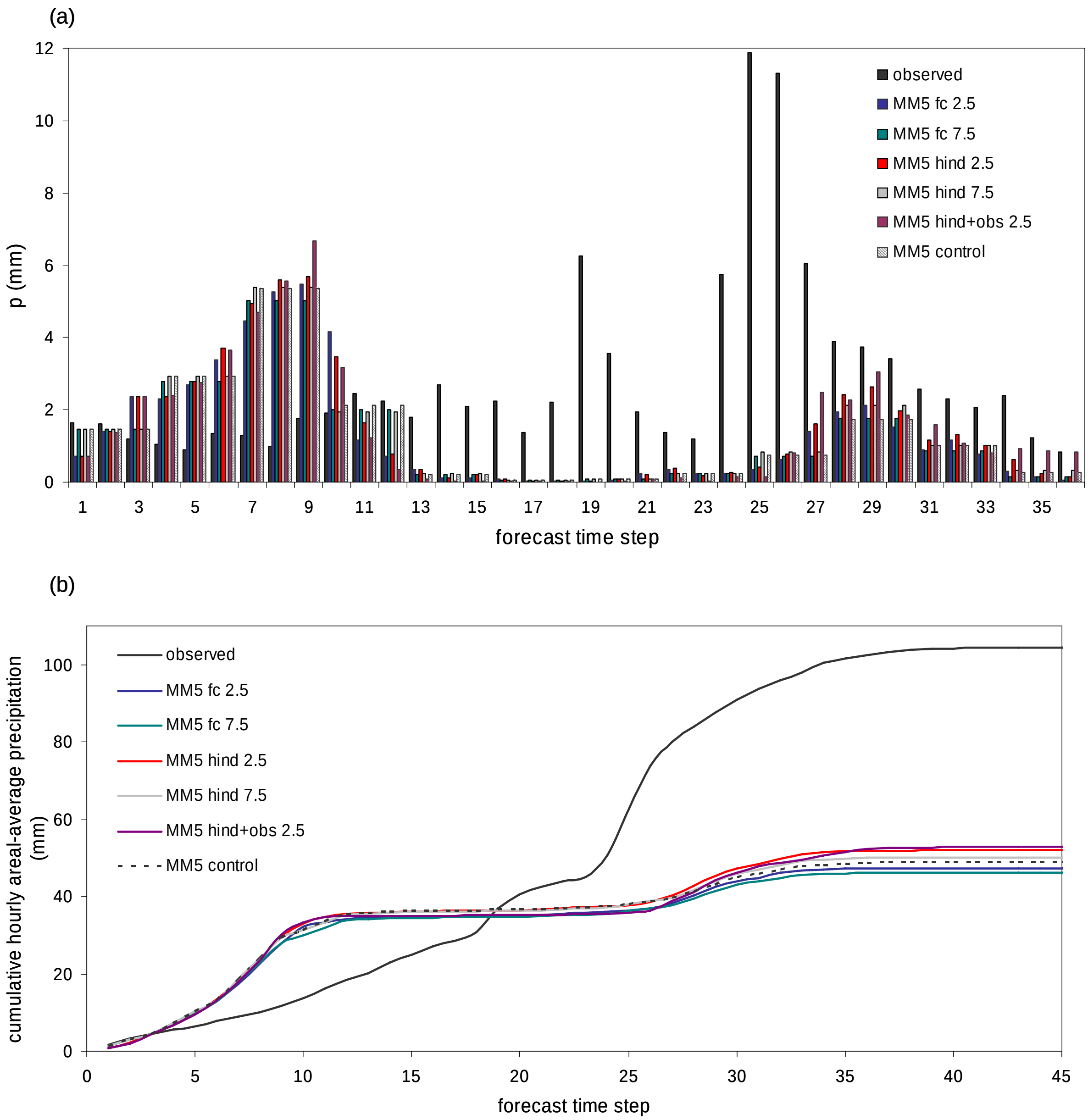

Figure 5.10: (a) TOPKAPI and (b) HEC-HMS runoff simulations driven by the different configurations of COSMO, evaluated at Casalecchio outlet

This fact highlights the impact of the different nesting strategies: the set of COSMO simulations displays a larger spread when compared with the set of MM5 experiments, both in terms of the spatial distributions and of the cumulative hourly area-averaged rainfall amounts throughout the forecasting period. The two-way nesting strategy results in small differences among the low- and high-resolution spatial rainfall patterns. Therefore, the wrong locations of the cores of maximum precipitations remain uncorrected.

It is important to emphasize the different responses of the two hydrological models when driven with the same rainfall forecast. The simulations provided by TOPKAPI show quite similar peak discharges in response to similar raining periods. Otherwise, the experiments provided by HEC-HMS are commonly characterised by a smaller increase of the stream-flow in response to the first raining period, but higher values in response to the later ones. These differences can be mainly attributed to the different infiltration schemes adopted by the two models: TOPKAPI exploits the first hours of the QPFs to saturate the soil –following a dunnian mechanism–, whereas HEC-HMS directly exploits the initial rainfall amounts to calculate the runoff volumes after subtracting an initial abstraction. Then, with the SCS-CN method, once the initial infiltration threshold has been exceeded, the efficiency of the watershed in producing runoff increases while precipitation occurs. The impact of the different calibration procedures –carried out during different time windows– in the optimization of the initial configuration for both runoff models have not resulted in great discrepancies. TOPKAPI is a distributed and continuous run model, whereas HEC-HMS has been implemented in a semi-distributed and event-based configuration. In the former case, the longer is the calibration time, the more reliable are the simulated flows. In the latter case and for the aim of the present chapter, it has been chosen to perform the calibration process by only selecting a set of events with the greatest similarity to the event under study. Although this approach has demonstrated to be suitable for this case study, it must not be forgotten that within a flood forecasting framework, the use of long rainfall and runoff observed series leads to a great confidence interval for hydrological modeling. In addition, it avoids that the models only work well within a limited range of calibration events.

It is also worth to note that the hydrological models have been forced separately with observed and simulated rainfall fields obtained by two different applications of the kriging method. These methodologies can be considered to have a negligible influence on the subsequent simulated flows. In fact, the impact of the different schemes of the physical processes adopted by the runoff models plays a major role in determining the results. Equivalently, the uncertainties related to the kriging methods can be considered to have a minor role as compared to the uncertainties related to the quantitative precipitation forecasts provided by the NWP models. Furthermore, a sensitivity test to the choice of the variogram has been performed to confirm this hypothesis. It has been selected a linear, an exponential and a Gaussian variogram to spatially distribute the rain-gauges observations. The results (not shown) reveal that very weak differences among the observed patterns have been found.

5.6 Conclusions

This chapter has proposed a hydrometeorological model intercomparison in order to estimate the uncertainties associated with the hydrometeorological forecasting chain for an intense rainfall episode which affected northern Italy on 7-10 November 2003. The flood event which occurred over the upper Reno river basin, a medium size catchment in the Emilia-Romagna Region, has been investigated in detail. To fulfil this aim, the one-way coupled atmospheric-hydrological model simulations have been performed by using the COSMO and MM5 meteorological and the HEC-HMS and TOPKAPI hydrological models. The meteorological runs have been carried out in a research or operational mode depending on the experiment. These simulations have been evaluated by a threefold approach. The first procedure uses a point validation methodology by means of categorical verification indices. This method allows to assess the performance of the simulated rainfall patterns at large scales. The second and third procedures examine the QPFs at catchment scale by using continuous verification scores, and by adopting the coupled atmospheric-hydrological models system as a validation tool. The aim of this study is to investigate which hydrological and meteorological modeling factors could help to enhance the hydrometeorological modeling of such hazardous events in the Western Mediterranean.

The meteorological simulations have shown deficiencies in the forecast of precipitation over the Reno river basin, in terms of timing, location and amount of the rainfall patterns at the catchment scale. These deficiencies have a major impact on the subsequent hydrological chain. However, an enhancement of the horizontal meteorological model resolution has considerably improved the rainfall forecast for one of the experiments. This simulation has benefited also of forecast boundary conditions, which for this case have proved to be more accurate than the analysed ones, and of an initial condition obtained through a mesoscale data assimilation. However, the remaining experiments have shown that the large-scale shift errors on the precipitation patterns can not be corrected by only enhancing the model resolution. In this case the improvement of initial and boundary conditions turns out to play an important role. Furthermore, the one-way nesting methodology adopted by COSMO has proved to introduce broader spread among the different simulations, allowing to obtain more different forecast scenarios, while high- and low-resolution MM5 simulations resemble each other, since a two-way nesting strategy is used. Remarkable differences in the simulated precipitation amounts and their timing and localisation have been found depending on the model itself and in particular on the physical models' parameterizations.

The performance of both hydrological models has shown weak discrepancies, in spite of the differences between their parameterizations, structures and set-up. Concretely, no remarkable differences have been found for flood modeling purposes by using either a distributed and continuous or a semi-distributed and event-based configuration. This issue could be of importance for operational flood forecasting in case of intense, but not extreme, rainfall episode over the Reno river basin. In fact, the characteristics of the rainfall event (i.e. spatial-temporal distribution and intensity) may influence the simulated catchment's response, especially with respect to the modelled soil infiltration mechanism. In addition, the present study has allowed to compare the performance of two hydrologic models, and to evaluate the impact of their different structures in the performance of the proposed flood forecasting chain and in assessing the different sources of uncertainties involved in the forecasting process. The use of two different models, which may be able to reproduce separately different parts of the hydrograph well, makes this intercomparison more valuable for the operational practice.

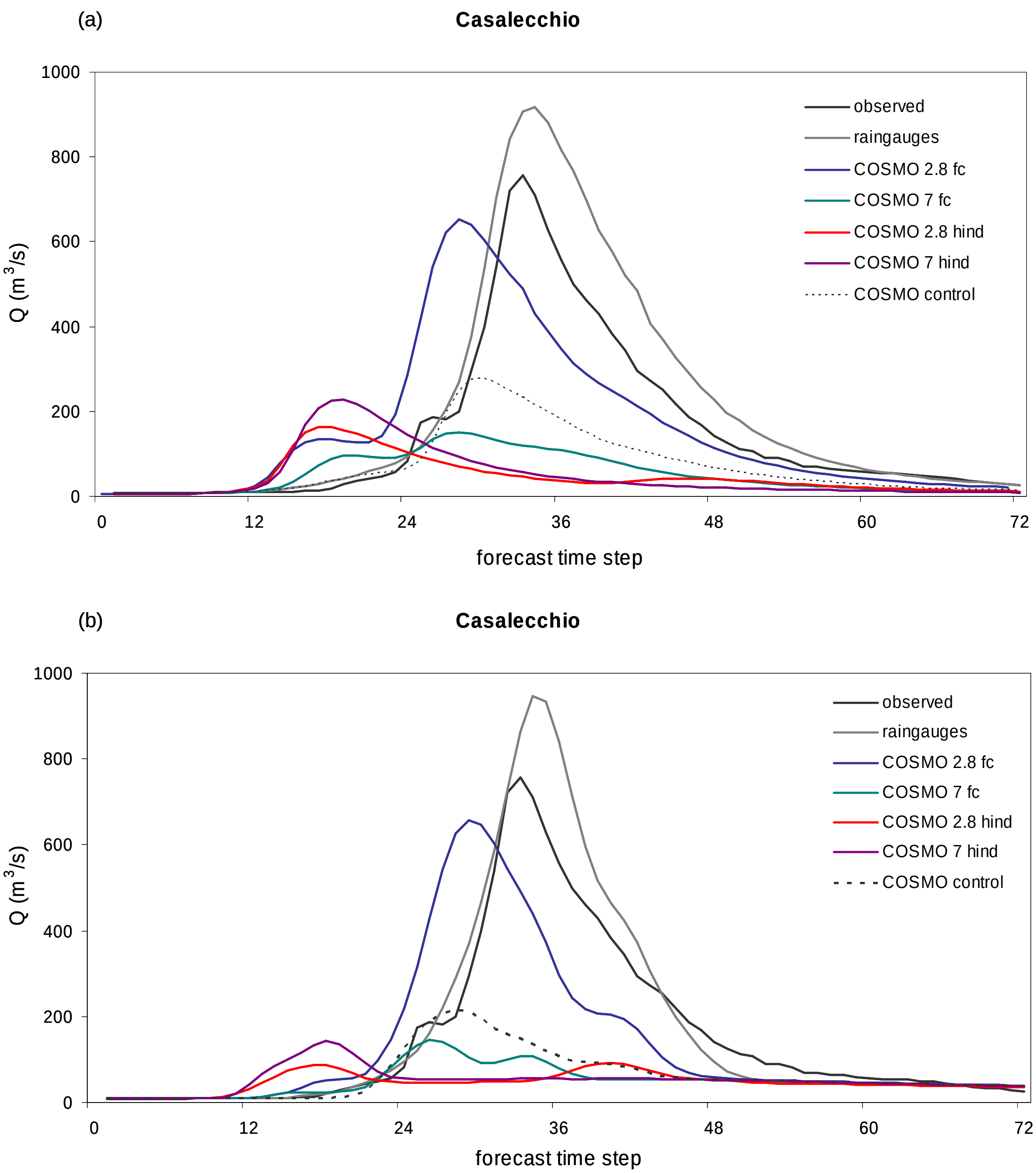

Figure 5.11: (a) Observed and forecasted hourly area-averaged amounts and (b) cumulative hourly area-averaged amounts over the upper Reno river basin provided by the different configurations of MM5 model are displayed from 1300 UTC 7 November 2003 until 00 UTC 09 November 2003

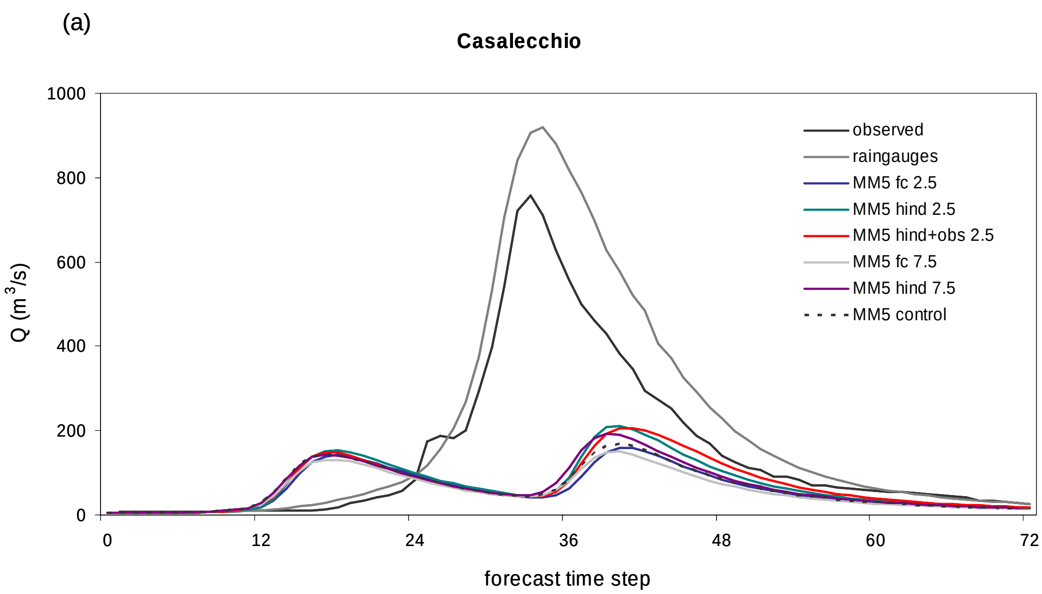

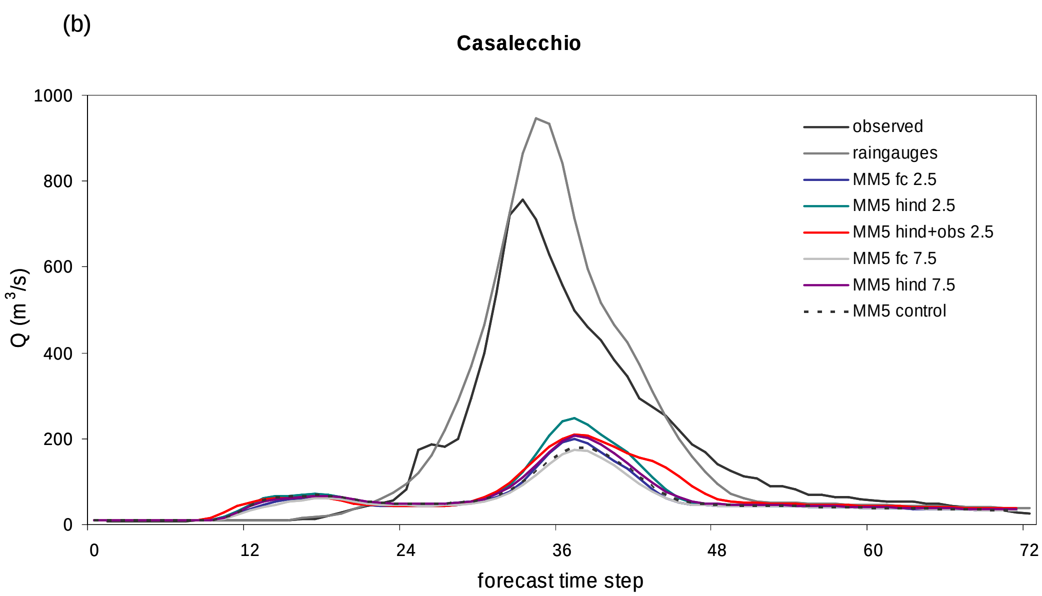

Figure 5.12: (a) TOPKAPI and (b) HEC-HMS runoff simulations driven by the different configurations of MM5, evaluated at Casalecchio outlet

Chapter 6

INFLUENCE OF THE BOUNDARY CONDITIONS RESOLUTION ON DYNAMICAL DOWNSCALING OF PRECIPITATION IN MEDITERRANEAN SPAIN

6.1 Introduction

In this chapter[1], we draw conclusions on the General Circulation Models horizontal and temporal optimum resolution for dynamical downscaling of rainfall in Mediterranean Spain. These results are derived based on the statistical analysis of mesoscale simulations of past events. These events correspond to the 165 heavy rainfall days during 1984-93, which are simulated with the HIRLAM mesoscale model. The model is nested within the ECMWF atmospheric grid analyses. We represent the spectrum of General Circulation Models resolutions currently applied in climate change research by using varying horizontal and temporal resolutions of these analyses. Three sets of simulations are designed using input data with 1^0, 2^0 and 3^0 horizontal resolutions (available at 6 h intervals), and three additional sets are designed using 1^0 horizontal resolution with less frequent boundary conditions updated every 12, 24 and 48 h. The quality of the daily rainfall forecasts is verified against rain-gauge observations using correlation and root mean square error analysis as well as Relative Operating Characteristic curves. Spatial distribution of average precipitation fields are also computed and verified against observations for the whole Mediterranean Spain. This analysis is particularized for six major rain bearing flow regimes that affect the region as well. Starting with a brief description of the mesoscale model used, and of the meteorological and rainfall data bases, section 6.2 explains the methodology followed to assess the simulated rainfall quality as function of input data resolution. Section 6.3 is organized in three main parts: first, results for the whole Mediterranean Spain are presented and discussed; second, the subdomain spatial variability is

[1]The content of this chapter is based on the paper Amengual, A., R. Romero, V. Homar, C. Ramis and S. Alonso, 2007: Impact of the lateral boundary conditions resolution on dynamical downscaling of precipitation in Mediterranean Spain., *Clim. Dyn.*, **29**, 487-499.

examined; and third, the results are evaluated as a function of six characteristic circulation types derived in earlier work (Romero et al., 1999b; Sotillo et al., 2003). To conclude, implications of the obtained results for the dynamical downscaling task in the region are summarized in section 6.4.

6.2 Data base and methodology

This chapter is based on numerical simulations of 165 daily rainfall events in Mediterranean Spain during the period 1984-1993. Romero et al. (1998) used a homogeneous and complete data base comprising daily rainfall series at 410 stations (Fig. 1.8), to show that 1275 significant rain days occurred in the region during that decade. A total of 165 days attained the heavy rainfall threshold as defined in the previous study (2% of the stations registered at least 50 mm). To avoid excessive computer time, then, the study was restricted to this reduced population set, with the hypothesis that the results obtained for the heavy rainfall limit would also apply to categories with lower daily rainfall amounts. Obviously, a heavy rainfall day, in our definition, does not imply heavy rainfall in all parts of Mediterranean Spain, but comprises a spatial range of rainfall intensities, from weak or no rain at all, to large values. The seasonal distribution of the selected events follows the typical pattern of the Mediterranean climate: 45% in autumn, 35% in winter, 15% in spring and only 5% in summer.

Six simulations are performed for each heavy rainfall day by nesting the HIRLAM mesoscale model within large scale analyses (see further details in section 2.3.3). The HIRLAM model is applied over the geographical window comprising from 29.45W to 19.45E and from 20.00N to 59.30N (Fig. 6.1), with a horizontal grid resolution of 0.3^0 (about 30 km). Large-scale meteorological analyses used to nest the model are constructed from the ECMWF ERA-15 spectral reanalysis of geopotential height, temperature, relative humidity and horizontal wind components at eleven standard pressure levels. These analyses are available at 00, 06, 12 and 18 UTC. For the first three experiments, the spectral analyses are gridded onto three different meshes with 1^0, 2^0, and 3^0 horizontal resolutions. Note that the equivalent spatial resolution of the ERA-15 fields is 1.125^0 (approximately 125 km in the region of interest), thus the 2^0 and 3^0 experiments imply a coarsening of the information contained in the reanalyses. An implicit nonlinear normal mode initialization, following Temperton's scheme (Temperton, 1998), is used to remove fast gravity modes from the model integration. Then, the model is run over a 54 hours period, starting at 00 UTC on the day before the cataloged heavy rainfall day. The accumulated precipitation during the last 24 h of simulation is verified against raingauge observations valid for the same 06-06 UTC period. The first 30 h of simulation allow for the boundary condition to spread across the domain and make the sensitivity tests to boundary conditions relevant (Alpert et al., 1996; Homar, 2001; Denis et al., 2002). This resembles the archetype configuration of dynamical downscaling experiments from GCMs, where the memory to the initial conditions in the model is rapidly lost.

Three experiments are thus defined, referred to in the paper as *1^0*, *2^0*, and *3^0* according to the used resolutions for the analyses. These experiments are considered representative of the current range of horizontal resolutions utilized in GCMs for climate simulations. A fourth, fifth and sixth experiments, referred to as *1^0+12h*, *1^0+24h* and *1^0+48h*, are run by using 1^0 resolution input data but less frequent -12, 24 and 48 h apart, respectively- boundary updates for the large-scale meteorological fields. In HIRLAM, the time varying boundary conditions during model

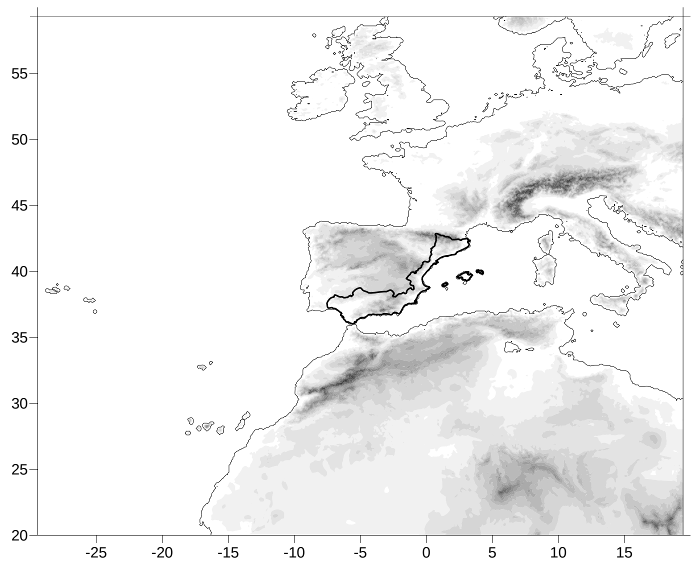

Figure 6.1: Geographical domain considered for the HIRLAM model simulations. The Spanish Mediterranean area is highlighted.

integration are defined by linear interpolation between large scale data at consecutive boundary update times. This last set of experiments attempts to analyze the effects of a low-frequency GCM output system, a characteristic often required owing to data storage limitations. The effects of the LBCs update is probably dependent on the dimension of the integration domain to some extent, in the sense that the smaller the domain, the larger and quicker is the impact of the error arising from the linear interpolation of two boundary conditions too far apart. To explore this issue, a sensitivity analysis of the robustness of the results with respect to integration domain dimension could be carried out, but this kind of analysis is beyond the scope of the study.

Precipitation forecasts are compared against observed rainfall. For each day, observations are interpolated into the 408 model grid points that lie inside the study area, using the kriging method from a network of 410 rain-gauge stations (Fig. 1.8). Several verification scores are derived from these individual comparisons to assess the model performance for experiment: mean spatial correlation and its standard deviation among the 165 modeled and observed precipitation events ($\bar{r}$ and σ_r respectively); analogous, mean spatial and standard deviation of the root mean square error ($\bar{\varepsilon}$ and σ_ε respectively); and the ROC score (further details in Appendix). The event-average of the spatial distribution of precipitation from observations and from the set of experiments are also compared.

The ROC curve method, based on the Signal Detection Theory, is a relatively new approach in Atmospheric Sciences, having been brought into the field as a verification tool by Mason (1982). The method combines False Alarm Rate (F) and Probability of Detection (POD) for a discrete number of predefined thresholds, giving an equal number of points on a graph of POD (vertical axis) against F (horizontal axis) to form the ROC curve (see Appendix). The area under the curve, or ROC score, is then used to assess the skill of the forecast system (Stanski et al., 1989). A perfect system yields an area of 1, whereas a curve lying along the diagonal

(ROC score=0.5) would reflect essentially worthless random forecasts. For the present study, ROC curves were constructed using precipitation thresholds set at 0, 1, 2, 4, 8, 16, 32, 64 and 128 mm.

6.3 Results and discussion

A multiperspective approach has been followed to summarize the model performance for the six types of simulations. First, the overall performance for the bulk of Mediterranean Spain is examined, and then the analysis is refined by taking into account the spatial variability of the results and six heavy rain-bearing flow regimes.

6.3.1 Whole of Mediterranean Spain

The performance of the six sets of simulations is evaluated for all heavy rainfall days and the whole Mediterranean Spain. Results are summarized in Table 6.1 for correlation and root mean square error measures. The mean spatial correlation values for the 165 events do not show large differences among the experiments dealing with the spatial resolution, for all of them the correlation is close to 0.4. However, a small degradation of the forecasts is obtained as the spatial resolution of the input data decreases. Moreover, as the boundary update interval increases the forecasts have less skill, with similar values of correlation for the *3*^{0} and the *1*^{0}*+12h* experiments and significantly lower scores for *1*^{0}*+24h* and *1*^{0}*+48h* experiments.

	Resolution					
	1^0	***2***^{0}	***3***^{0}	***1***^{0}***+12h***	***1***^{0}***+24h***	***1***^{0}***+48h***
$\bar{r}$	0.420	0.410	0.398	0.402	0.371	0.282
σ_r	0.216	0.220	0.224	0.227	0.231	0.253
$\bar{\varepsilon}$	14.117	14.216	14.199	14.271	14.647	15.348
σ_ε	4.772	4.6	4.369	4.569	4.549	4.869

Table 6.1: Average spatial correlation ($\bar{r}$), average root mean square error($\bar{\varepsilon}$, in mm) and their dispersions, σ_r and σ_ε (in mm), for the six experiments with regard to the observed rainfall.

These results suggest that the update frequency of LBCs has larger impact on the downscaling results than their spatial resolution. The values of σ_r do not show high sensitivity to data resolution, although a decrease of this parameter with higher spatio-temporal resolution is observed. Regarding the root mean square error, similar results are obtained. The model is more sensitive to the boundary conditions update frequency than to their horizontal resolution. On the other hand, no significant differences among σ_ε values are obtained among all the set of experiments.

As an alternative and more appropriate verification method, ROC scores for the considered resolutions have been calculated. A single ROC curve is obtained for each experiment after comparing simulations against observations at all grid points and for all events. Figure 6.2 shows the obtained ROC curves for the experimental data sets. All curves lie well above the diagonal, and the only appreciable difference among them is the lower score attained by the *1^0+24h* and *1^0+48h* sets (Table 6.2). To examine the significance of the differences among the curves, a bootstrap test (Diaconis and Efron, 1983) with 1000 repetitions is applied for each experiment. Table 6.2 shows the 95% confidence intervals for the ROC scores, confirming that the *1^0*, *2^0*, *3^0* and *1^0+12h* experiments do not produce significantly different ROC curves, whereas the *1^0+24h* and the *1^0+48h* experiments forecast significantly degraded precipitation fields. Therefore, from the ROC method perspective, it cannot be concluded that a significant improvement of forecast skill in Mediterranean Spain is obtained by initializing the mesoscale model with high resolution meteorological data within the considered spatial range. Rainfall downscaling products might benefit somewhat more from improved boundary conditions frequency. These results can be compared with those obtained by Antic et al. (2004) for the west coast of North America. They examined the sensitivities to spatial resolutions of T30, T60 and T360 (roughly 5^0, 2.5^0 and 0.5^0, respectively) and temporal resolutions of 12, 6 and 3 h. Changes in spatial resolution of driving data from T30 to T60 in their experiments had more repercussion on the downscaling ability than a change from T60 to T360, and the improvements derived from the increase of the LBCs update frequency became more evident when using high spatial resolution (T360) than with the coarser input data.

Resolution	***ROC score***
1^0	0.777 (0.767-0.786)
2^0	0.773 (0.763-0.782)
3^0	0.769 (0.760-0.778)
1^0+12h	0.768 (0.757-0.778)
1^0+24h	0.743 (0.732-0.753)
1^0+48h	0.705 (0.693-0.716)

Table 6.2: ROC scores and the 95% percentile confidence intervals for the six experiments.

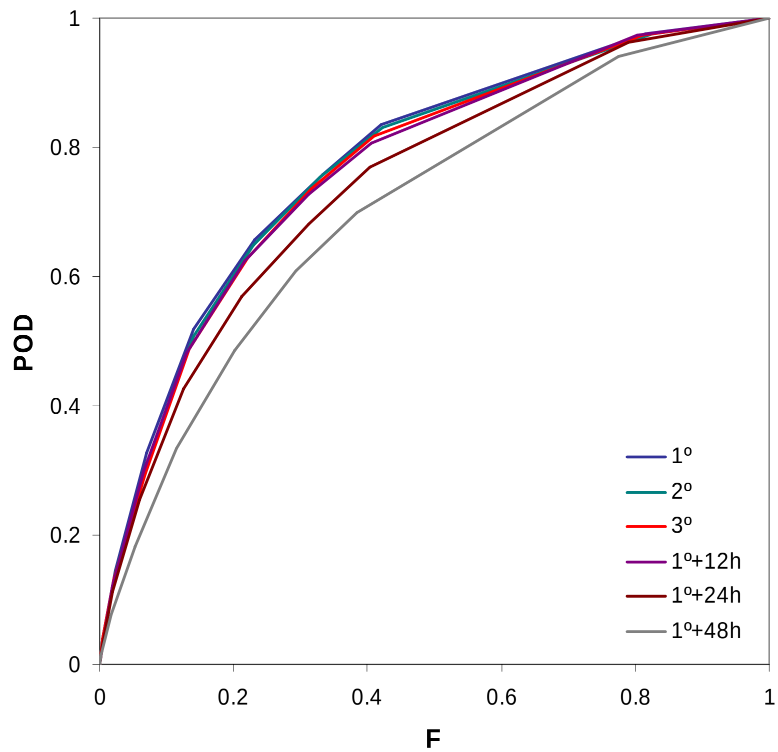

Figure 6.2: ROC curves for 1^0, 2^0, 3^0, 1^0+12h, 1^0+24h and 1^0+48h experiments.

6.3.2 Subdomain Spatial Variability

In this subsection, the quality of the forecasts is examined as a function of location within Mediterranean Spain by computing the ROC curve for each of the 408 model grid points over the area (Fig. 6.3) and by comparing the mean spatial distributions of observed and simulated rainfall fields (Fig. 6.4). A wide range of rainfall enhancement or suppression mechanisms have been identified in the region owing to its complex orography. These processes have high spatial variability and depend on the specific flow type (Romero et al., 1999a and b). Atlantic flows, mostly associated with large-scale low pressure systems, favour rainfall over the western and northern zones but are hardly effective in the east and southeast; Mediterranean air flows, less common and associated with smaller-scale disturbances, encourage rainfall in these latter zones but not in sheltered areas like western and central Andalusia. The northerly flows, often associated with the Genoa gulf cyclogenesis, produce precipitation in the Balearics and eastern Catalonia but do not influence the other areas. Such a diversity of rainfall mechanisms and flow-orography interactions must logically be noted to a certain degree on the spatial variability of the forecast quality.

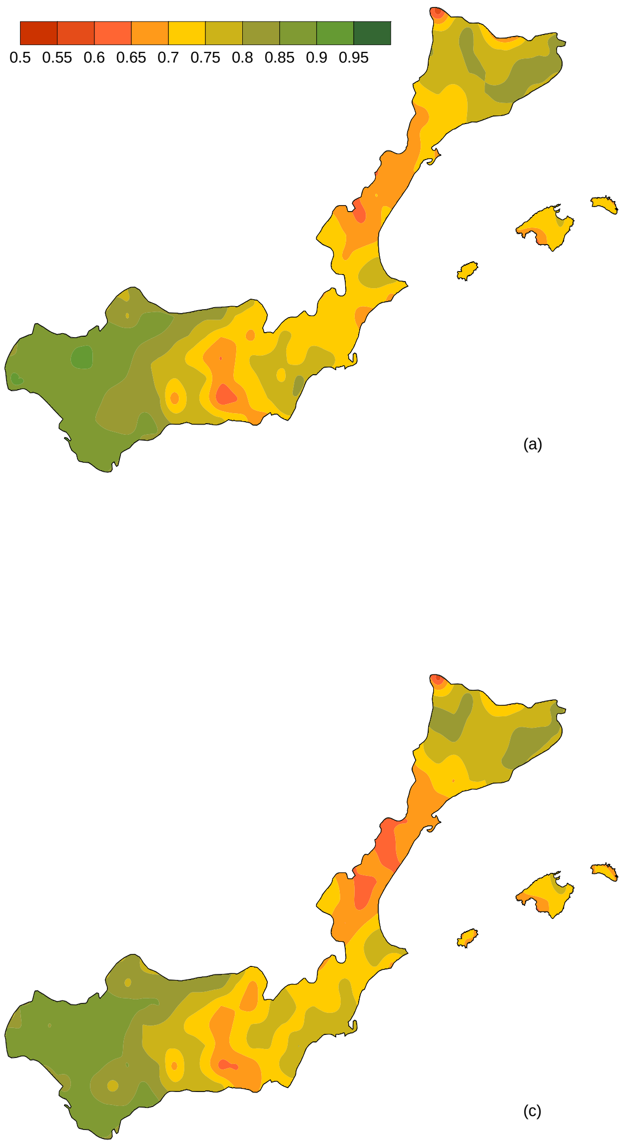
0.5 0.55 0.6 0.65 0.7 0.75 0.8 0.85 0.9 0.95
(a)
(b)
(c)
(d)

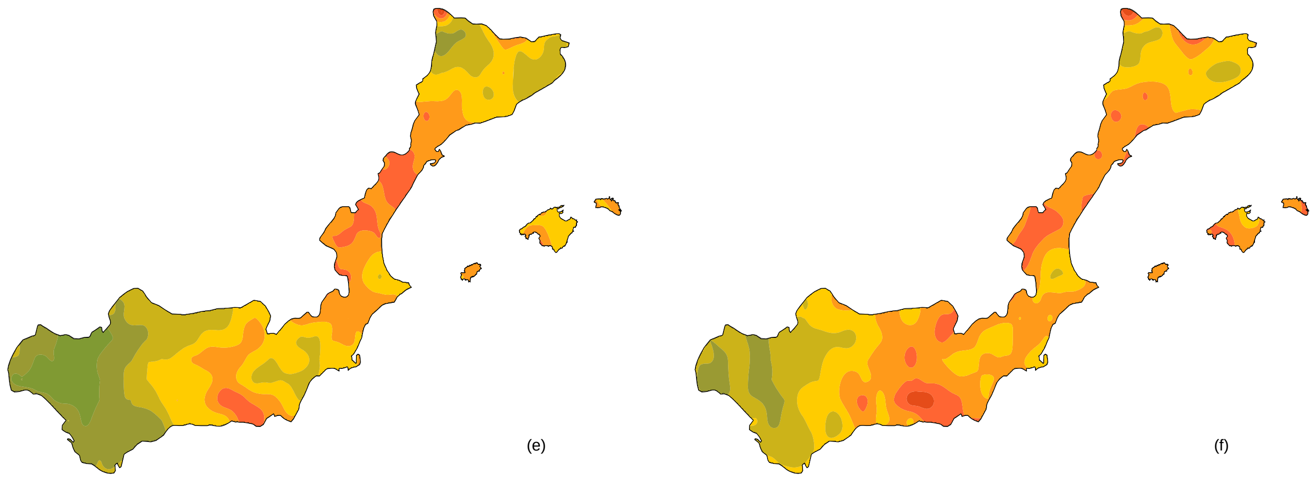

Figure 6.3: Spatial distribution of ROC scores for the 6 sets of experiments: (a) 1^0, (b) 2^0, (c) 3^0, (d) 1^0+12h, (e) 1^0+24h and (f) 1^0+48h.

A direct comparison between the mean observed rainfall distribution (Fig. 6.4a) and the predicted fields (Figs. 6.4b and c) reveals that the model underestimates precipitation across the domain. However, the mean spatial distribution of the forecast fields resembles the observations, except in high mountainous ranges of east Andalusia where the artificial orographic effect in the model is obvious. Comparing Figs. 6.3 and 6.4, it is evident that a direct relationship between model skill expressed in terms of ROC score and in terms of the average precipitation can not be established. For instance, higher ROC scores are found in western Andalusia than in the Aitana range area, but the event-average precipitation is better in the second zone. A detailed analysis of the results reveals that the day by day agreement between model and observations in western Andalusia is quite good, except for a systematic underforecast of rainfall amounts. In contrast, a higher variability in the daily performance of the model is obtained in the Aitana range area, with a great proportion of observed extreme daily rainfall values that the model is not able to reproduce –thus lowering probability of detection– and, on the opposite, some simulated daily values significantly above observations, contributing to increase false alarm rates.

The results for the six sets of experiments (Fig. 6.3) reveal only slight differences among their performance when the spatial resolution is changed or the boundary conditions are 12 h apart. Degradation is clearly visible for the 1^0+24h and 1^0+48h experiments as it was globally observed in last section for the Mediterranean Spain (Table 6.2). This general decrease in ROC scores is partially attributable to the weaker average precipitation amounts obtained as the boundary conditions update frequency decreases (see Fig. 6.4c for 1^0+48h mean precipitation). Regarding the spatial distribution of ROC values, the degradation of the areal-averaged ROC score for 1^0+24h and 1^0+48h experiments is also observed in many subareas, particularly over Catalonia and most of Andalusia (Figs. 6.3e and f).

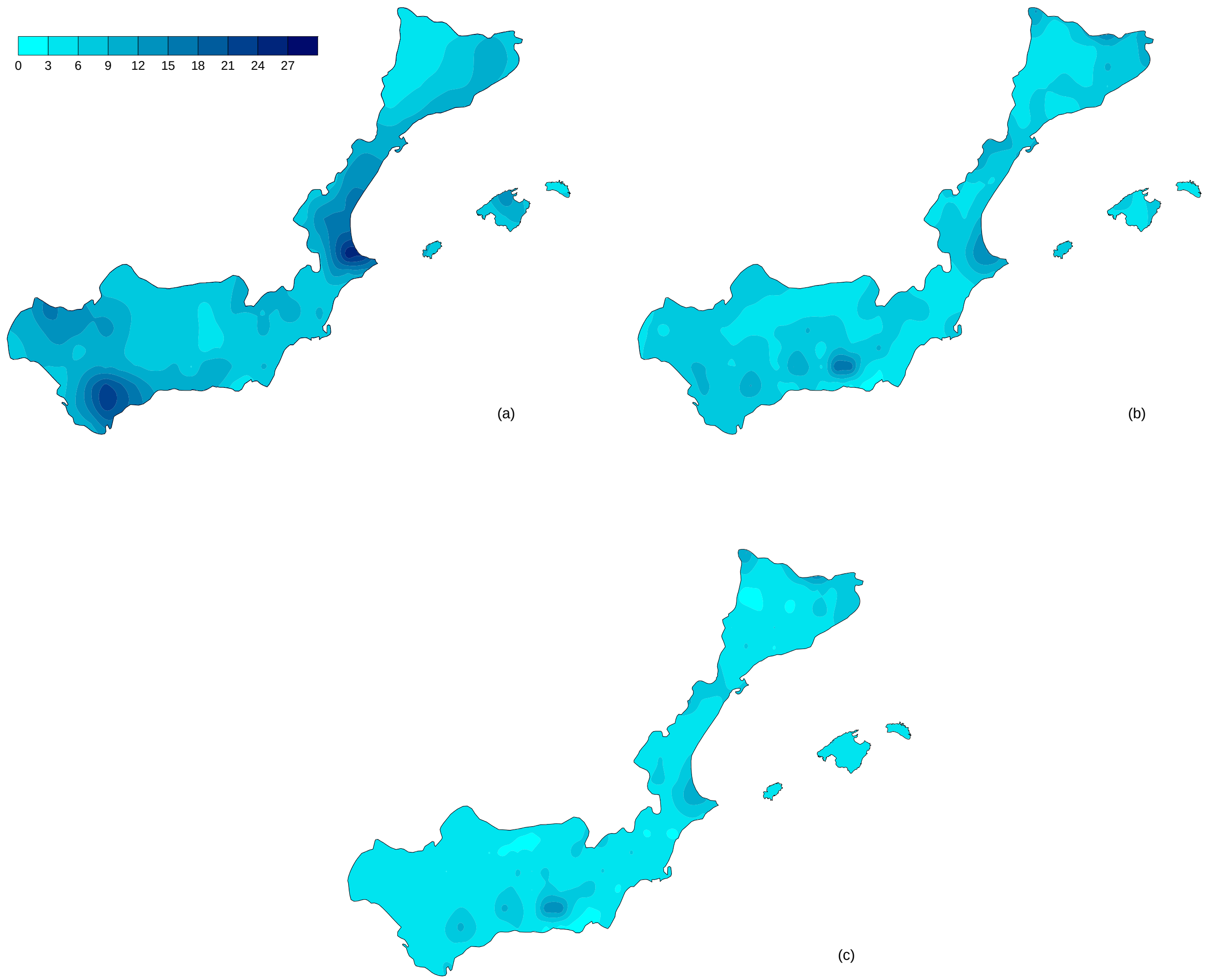

Figure 6.4: Spatial distribution of mean precipitation (in mm) calculated from: (a) observations, (b) 1^0 experiment and (c) 1^0+48h experiment.

Notable contrasts in model performance emerge among different areas in Mediterranean Spain (Fig. 6.3a). The highest scores are obtained over Catalonia, central and western Andalusia, the Balearics and some areas of the southeast (ROC score>0.75). On the contrary, eastern Andalusia and many parts of Valencia are characterized by lower ROC values (ROC score<0.75). The higher ROC scores over the western and northern regions (even exceeding 0.9 in mountainous areas of western Andalusia) can be associated with the relatively high forecast capability for Atlantic flow situations (see next section). These flows are generally associated with large-scale pressure systems which do not suffer appreciable orographic modification as they approach from open oceanic areas. Even if these disturbances contain some analysis or forecast error, and consequently uncertainties in the impinging flow direction are present, no significant effects on the rainfall pattern are likely, especially in western Andalusia, where the exposure to the Atlantic moist flows is effective for a wide range of flow directions. The relatively high scores in central and eastern part of Catalonia and, in a minor measure, in most of the Balearics can also be attributed to the relatively good forecasts of northern Mediterranean cyclones (see next subsection). Many of these cyclones, particularly those developed near the Gulf of Genoa, are the result of Alpine cyclogenesis (Buzzi and Tibaldi, 1978). The main ingredients of these cyclogenesis events, an Atlantic frontal system associated with a baroclinic trough and the extensive Alpine barrier, are well-captured by numerical weather prediction models, resulting frequently in good rainfall forecasts.

In contrast, the lower ROC scores generally found in the east-facing regions of Mediterranean Spain (from eastern Andalusia to south Catalonia) can be attributed to the particular nature of the rainfall systems –often convectively driven– that develop over the Mediterranean sea. Dimitrijevic and Laprise (2005) pointed out similar problems in reproducing the precise timing and location of the convective precipitation events that prevail during the summer season in western North America. Furthermore, Mediterranean disturbances are typically smaller than Atlantic systems, even of mesoscale size, and are often a consequence of the strong disruption of the westerly mid-latitude circulation. In addition, the closed characteristics of the western Mediterranean basin and the prominent surrounding mountain chains strongly modulate the low level flow in the form of pressure dipoles, secondary cyclones and other mesoscale circulations (Reiter, 1975). The mesoscale properties of the Mediterranean circulations and the complex physical processes involved in their genesis affect the predictability of these features. In particular, small errors in the near-surface flow direction can lead to appreciable rainfall modification, owing to the complexity of the orography and coastline pattern. Not surprisingly, then, poorer rainfall forecasts are obtained for Mediterranean rain-bearing flow regimes (see next section), and therefore over the sensitive east-facing areas (Fig. 6.3a).

The distinct model behavior for Atlantic and Mediterranean rain-bearing flow situations might have implications for the downscaling of GCM simulations if major changes in atmospheric pattern frequencies take place. For Mediterranean Spain, Sumner et al. (2003) found, using ECHAM-OPYC3 GCM (Roeckner et al., 1998), marked decreases in frequency for many near-surface circulations with a westerly or northerly component during the twenty first century, whereas a general increase was found for atmospheric patterns with an easterly component. Slightly more uncertain future downscaled precipitation fields are possible therefore, owing to the increase of the relatively poorly-handled easterly regimes.

6.3.3 Major Rain Bearing Flow Regimes

In order to complement the previous results, the data set has been broken down into six major rain bearing flow regimes that affect Mediterranean Spain. These regimes were also considered by Sotillo et al. (2003), after regrouping in a smaller set 19 rainfall-producing atmospheric patterns derived in Romero et al. (1999b) from a large sample of rainy days which included our group of events. The 165 heavy rainfall days simulated are then subdivided into one of the following flow types (Fig. 6.5):

- *A* (Atlantic flows, 53 days), comprising surface circulations from the SW-W produced by Atlantic lows.

- *C* (Cold front passage, 11 days), or winds from the NW-N over the Iberian Peninsula associated with the passage of a cold front.

- *SW* (Southwestern disturbances, 31 days), that is, troughs or cut-off lows at mid-tropospheric levels to the west of Gibraltar Strait, with the surface low near the Gulf of Cadiz which induces winds from the SE-E.
- *S* (Southern disturbances, 30 days), similar to the previous one but with the upper-level disturbance and surface low axis located about Gibraltar Strait.
- *SE* (Southeastern disturbances, 19 days), with the low-level disturbance to the east of Gibraltar Strait.
- *N* (Northerly flows, 21 days), normally associated with low pressure centres located over the western Mediterranean basin.

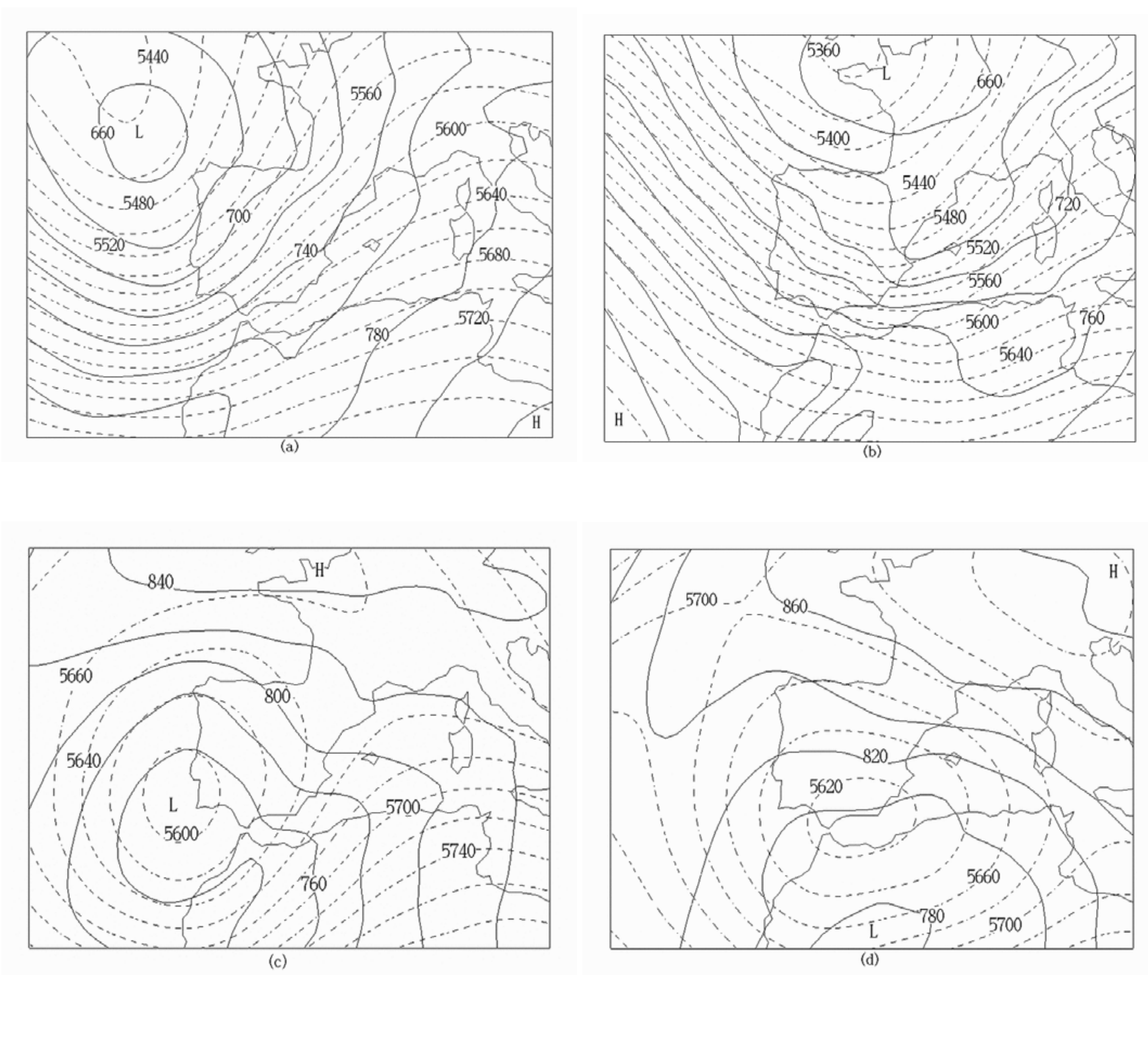

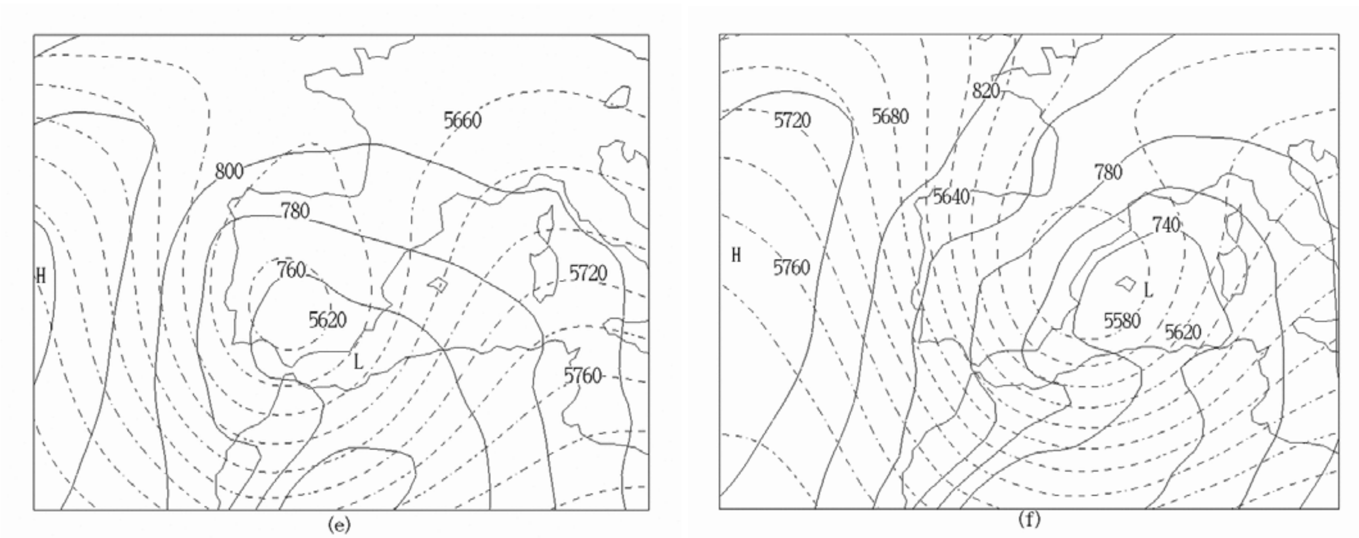

Figure 6.5: Composites of the six major rain bearing flow regimes: (a) Atlantic flows (*A*); (b) Cold front passage (*C*); (c) Southwestern disturbances (*SW*); (d) Southern disturbances (*S*); (e) Southeastern disturbances (*SE*) and (f) Northerly flows (*N*). The continuous lines represent the geopotential height field at 925 hPa (contour interval is 20 m), and the dashed lines that at 500 hPa (same contour interval). Surface lows and highs are indicated.

Model performance results as a function of flow regime are shown in Fig. 6.6 and Table 6.3, corresponding to 1^0 input data resolution experiments. Weak but physically consistent differences emerge among the flow types, with the lowest ROC scores for *SW*, *SE* and *N* situations (0.758, 0.694 and 0.767, respectively). The remaining flow regimes produce scores close to 0.8: *A*(0.789), *C*(0.812) and *S*(0.787). Then, as already emphasized in last subsection a certain distinction can be made between Atlantic or northern Mediterranean disturbances (*A*, *C* and *N*), and low latitude disturbances that induce surface flows with a significant easterly component over Mediterranean Spain (*SW*, *S* and *SE*). The former situations support rainfall distributions of higher predictability; the latter flow types induce more complex rainfall responses, not so easily handled by mesoscale models. An exception to this general rule, however, is indicated by the fact that the southern disturbances exceed in performance the northerly situations. The southern disturbances are typically associated with substantial rainfalls focused around the Aitana range, a highly exposed area (Romero et al., 1999b) where a wide range of flow directions of easterly component lead to essentially the same rainfall responses due to its geographical nature as mountainous cape (Fig 6.4a). Such relative independence to the flow direction benefits the precipitation predictability. On the contrary, our northerly flows category includes, in addition to the highly predictable Genoa-type cyclones, some low-pressure systems located to the south-southeast of the Balearic Islands (see the composite pattern in Fig. 6.5f), resembling the *SE* flow pattern except that the disturbance is located further east. The forecast uncertainty associated to this type of situations penalizes the overall score of the *N* pattern.

	Flow Regimes					
	A	***C***	***SW***	***S***	***SE***	***N***
ROC score	0.789	0.812	0.758	0.787	0.694	0.767

Table 6.3: ROC scores for the six major rain bearing flow regimes (for 1^0 input data resolution).

In analogy with the analysis presented in subsection 6.3.2, the spatial dependence of the forecast accuracy as function of flow type is examined. However, population sizes at domain grid points would be too low to produce useful results on model performance from the ROC statistic computations. In order to alleviate this problem, the circulation types have been further simplified by considering only two categories: *northern disturbances*, associated with a significant Atlantic or northerly component at low levels, composed by *A*, *C* and *N* situations (85 days); and *southern disturbances*, associated with a dominant easterly flow component over Mediterranean Spain, composed by *SW*, *S* and *SE* situations (80 days).

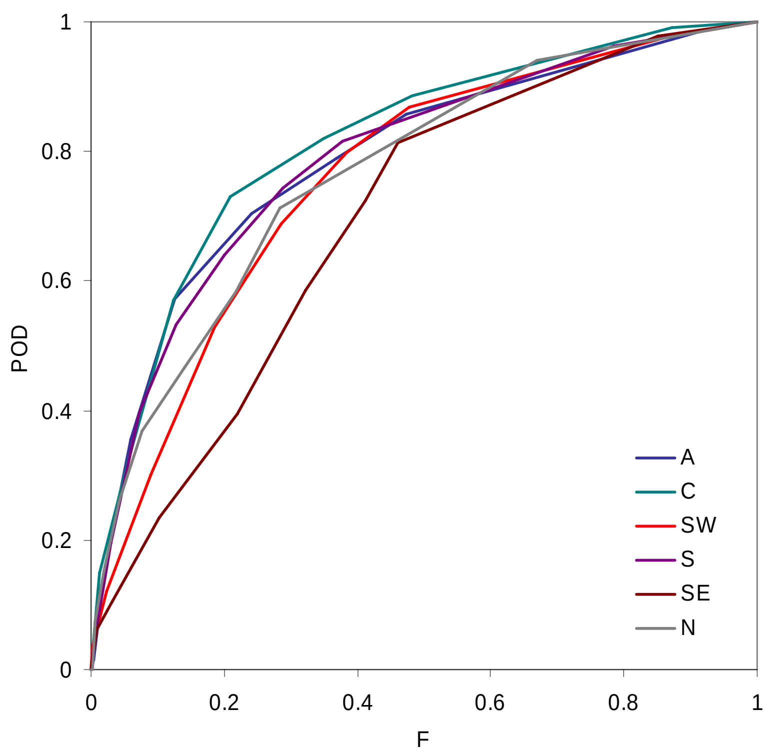

Figure 6.6: ROC curves for the six major rain bearing flow regimes (for 1^0 input data resolution).

Although still not very large, these increased population categories appear to offer interpretable results. First of all, the results in figure 6.7 confirm that the overall skill of mesoscale predictions is favoured under Atlantic flows. The high latitude disturbances (Fig. 6.7a) produce higher ROC scores towards the west and north of Mediterranean Spain, including the Balearic Islands, and some orographic units of the south and east. All these areas are directly exposed to Atlantic and northerly flows. Lower values are found over sheltered areas, such as the Gulf of Valencia and areas of the southeast. In these latter areas, however, the southern disturbances offer better ROC values (Fig. 6.7b), which appears to be consistent with the Mediterranean nature of the associated flows. Nevertheless, the southern disturbances still exhibit the highest ROC values towards the north, some areas of the south-west and the Balearics, not over the more exposed areas of Valencia, Murcia and eastern Andalusia as it would have been expected. A reasonable explanation for this result is that the easterly rainfall regimes typically comprise many convective, low-predictability type events over the previous provinces.

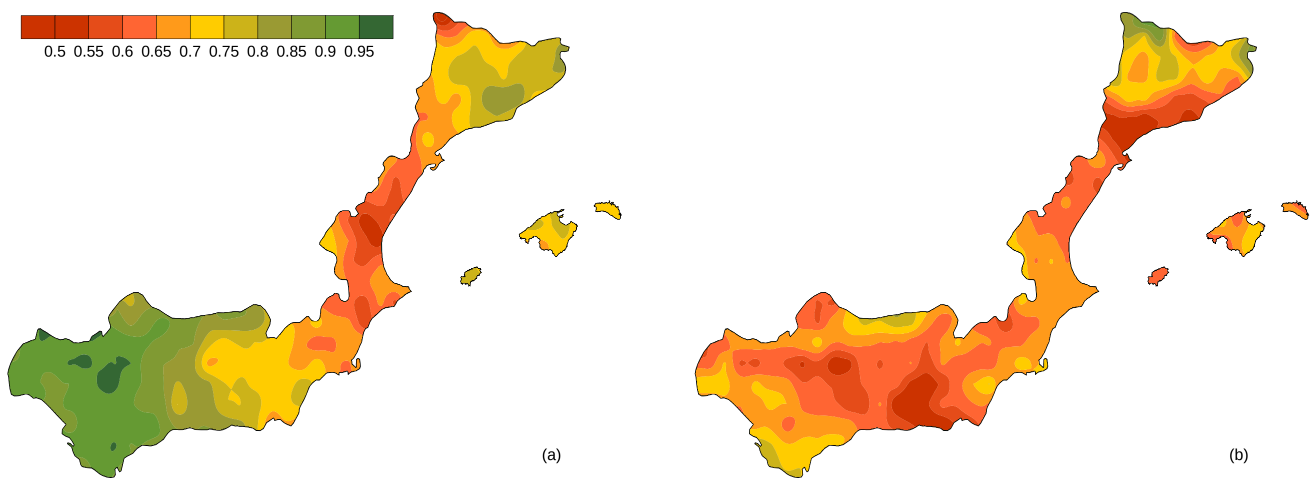

Figure 6.7: Spatial distribution of ROC scores for the two flow categories defined by: (a) Atlantic flows (A), Cold front passage (C) and Northerly flows (N); and (b) Southwestern (SW), Southern (S) and Southeastern (SE) disturbances.

6.3.4 Orographic influence

It has been previously suggested that the degree of low sensitivity to the spatial and temporal resolution of the input datasets can be due to the dominant role of the orography in controlling the rainfall distribution over Mediterranean Spain, to the extent of overcoming the dynamical action induced by sub-synoptic features embedded in the circulation. It would be interesting to verify –or reject– this hypothesis by reproducing the kind of statistical analysis presented in last sections for other remote, smooth orographic regions. This is, of course, beyond the scope of the study, but as an alternative, two additional oceanic regions –besides our study zone (noted as *ZONE* in Fig. 6.8)– have been considered. These regions have been defined over the Atlantic ocean (*ATL*) and the Mediterranean Sea (*MED*) (see Fig. 6.8), with the same areal extent than *ZONE*. If the hypothesis is true, then a greater degradation of the forecast quality with coarser input data resolution should be observed on these non-orographic areas than in the study zone. It is interesting to note that Denis et al. (2003) and Antic et al. (2004) did not found significant differences between western and eastern parts of North America about the sensitivity of downscaled precipitation to the spatial and temporal resolution jumps of LBCs.

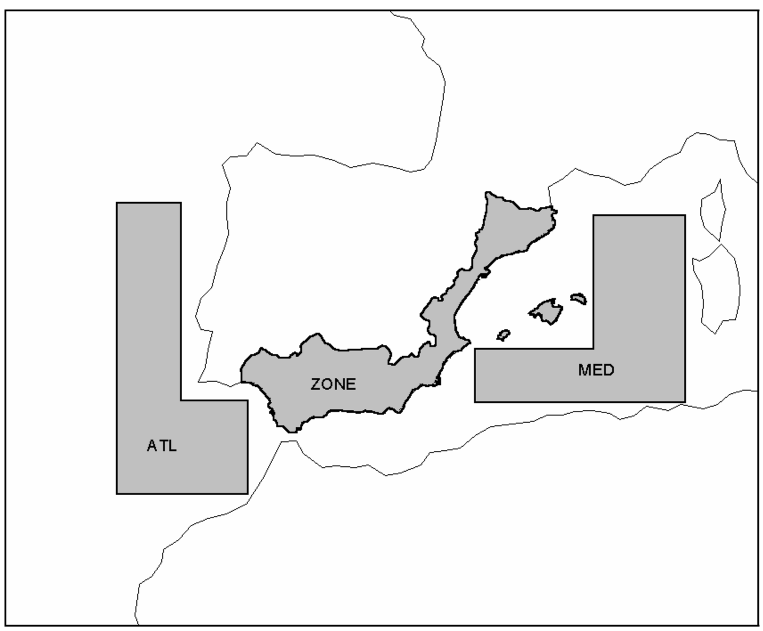

Figure 6.8: Geographical location of the three regions considered for the model performance analysis (see text): Mediterranean Spain (*ZONE*), Atlantic ocean area (*ATL*) and Mediterranean sea area (*MED*).

Since the observed rainfall over the *ATL* and *MED* zones is unknown on any of the 165 simulated days, the analysis has been carried out by considering the 1^0 experiment results as the "truth", and comparing the 2^0, 3^0, 1^0+12h, 1^0+24h and 1^0+48h results with that truth, for each of the three zones. The areal mean precipitation was first examined to ensure that a large fraction of the 165 simulated days yields significant rainfall in both oceanic regions. This important requirement for the statistical significance when comparing results for *ZONE* against those for *ATL* and *MED* could be verified. As a brief summary, the areal mean precipitation values once averaged over the 165 episodes are 6.8, 4.2 and 4.3 mm for *ZONE*, *ATL* and *MED*, respectively.

Results are summarized in Tables 6.4 and 6.5. In terms of spatial correlation averaged over the 165 events under study, higher and more uniform values are found for *ZONE* than for *ATL* and *MED*, and the decrease of this correlation when coarser -in space or time- resolution data is used, is far more appreciable for the oceanic areas than for the study zone (Table 6.4). In terms of the relative root mean square error, lower values are obtained over *ZONE* than over *MED* for all experiments, but interestingly, for all experiments except *2*^{0} and *1*^{0}*+12h*, *ATL* offers lower values than *ZONE*, that is, closer agreement with the *1*^{0} results (Table 6.5). A remarkable feature reflected in both tables is that updating the LBCs at 12 h intervals instead of 6 h has a greater negative impact on the "forecast" than a decrease of horizontal resolution from 1^0 to 2^0 in the input data.

$\bar{r}$	***ZONE***	***ATL***	***MED***
1^0	1	1	1
2^0	0.941	0.834	0.897
3^0	0.883	0.705	0.773
1^0***+12h***	0.900	0.744	0.829
1^0***+24h***	0.785	0.537	0.650
1^0***+48h***	0.610	0.340	0.465

Table 6.4: Average spatial correlation ($\bar{r}$) between the six sets of simulations and the *1*^{0} experiment. The analysis is performed for the three regions shown in Fig. 6.8.

$\bar{\varepsilon_r}$	***ZONE***	***ATL***	***MED***
1^0	0	0	0
2^0	0.390	0.418	0.460
3^0	0.581	0.557	0.714
1^0***+12h***	0.523	0.565	0.575
1^0***+24h***	0.809	0.778	0.886
1^0***+48h***	1.110	1.000	1.184

Table 6.5: Average root mean square "error" relative to the *1*^{0} experiment, normalized by the mean precipitation ($\bar{\varepsilon_r}$), for the six experiments. The analysis is performed for the three regions shown in Fig. 6.8.

6.4 Conclusions

This chapter represents an attempt to examine the problem of dynamical downscaling of precipitation over Mediterranean Spain –a highly vulnerable region according to most of the climate change precipitation scenarios (Meteorological Office, 2001; Watson and Zinyowera, 2001)– with respect to its sensitivity to the spatial and temporal resolution of GCM input fields. The methodological approach to the problem has been determined, first, by the availability of precipitation and meteorological data, and second, by limitations in computer time which prohibited a large number of numerical simulations. Specifically, our conclusions have been outlined from various sets of 165 mesoscale numerical simulations of heavy rainfall events in Mediterranean Spain, initialized with real meteorological grid analyses at six different spatial and temporal resolutions, under the following assumptions: (i) heavy rainfall events are representative of the whole fraction of rainfall days with respect to the model sensitivity –or insensitivity– to input data resolution; (ii) the 6 considered resolutions (1^0, 2^0 and 3^0 in space, plus 1^0+12h, 1^0+24h and 1^0+48h in time) are sufficient to describe the actual envelope of sensitivities of the forecast system; and most importantly, (iii) the use of smoothed meteorological analyses is equivalent to coarse grid GCM outputs.

Hopefully, then, at least a first guess on the effects of GCM resolution for dynamical downscaling tasks in Mediterranean Spain can be derived from this work. The major finding –in general agreement with the results for other regions with complex orography– is that the forecast skill is relatively insensitive to the spatial resolution of the boundary fields, but that it diminishes significantly for updates less frequent than 12h apart, at least for the examined range of spatial and temporal resolutions.

Some implications can be derived from the presented analysis on the spatial variability of model performance and its dependence on flow type. First, the best-behaved areas in terms of forecast accuracy, are those more exposed and dependent on Atlantic and northerly flows (western Andalusia, Catalonia and the Balearics) and highlands in general, whereas many areas of eastern Andalusia and the Iberian eastern flank, often dominated by convective type rainfalls, exhibit relatively large forecast uncertainties. This mapping is a valuable information for improving the definition of spatially-dependent confidence intervals in Mediterranean Spain when dealing with precipitation downscaling products, and also with the real-time numerical model prediction of rainfall events. Second, the analysis has shown that the high latitude disturbances embedded in the midlatitude westerlies generally offer better rainfall forecasts than situations with a strongly negative (i.e. easterly) flow component.

These findings would imply a changed reliability on the downscaled precipitation from GCMs if significant changes in flow type frequencies are to be expected in the area owing to climate change. In this respect, Watson and Zinyowera (2001) and Sumner et al. (2003), among others, note that climate change signal in Mediterranean Spain could be associated with marked decreases in frequency for many near-surface circulations with a westerly or northerly component, and a general increase for easterly component flows.

Chapter 7

CONCLUSIONS AND PERSPECTIVES

In this thesis, efforts have been devoted to gaining knowledge within the framework of Western Mediterranean hydrometeorology. To this aim, several flood events across this geographical area –with a special attention deserved to the Spanish Mediterranean– have been studied through numerical simulations. Furthermore, the use of a hydrometeorological modeling chain as a suitable tool to gain additional lead times for the implementation of warning and emergency procedures before flash-flood situations has been addressed. This methodology could help to mitigate their hazardous effects, since such hazardous events present short recurrence periods in the Mediterranean Spain as a whole. The role of hydrometeorological modeling in a climate change era has been addressed by studying the dynamical downscaling of precipitation from General to Regional Climate Models. It must be remembered that this is the previous fundamental step for the one-way coupling between these latter atmospheric models and the hydrological models. This issue is of the maximum interest owing to the crucial role –for present and future social and economic impacts– of the rainfall amounts in the Spanish Mediterranean. The conclusions derived from this study could help not only to better address the confidence interval in downscaled precipitation products, but the assessment of the possible future climate change scenarios consequences in the magnitude and quantity of the surface, sub-surface and underground water availability from a water resources management point of view.

We have carried out an in-depth study of the 'Montserrat' flash-flood through hydrometeorological model simulations in chapter 3. The spatial and temporal observed rainfall scales have been investigated to answer whether a hydrological model set-up optimizes the basin response for the 'Montserrat' event. It appears that a configuration considering a 39 subbasins segmentation together with a hourly temporal rainfall field discretization results in an optimum reproduction of the hydrological model for this episode. The feasibility of runoff simulations driven by numerical weather prediction mesoscale models over the Llobregat medium-size basin has been addressed. Using ECMWF and NCEP analyses to initialize the hydrometeorological chain, it was possible to obtain, at least at the basin outlet, reasonable runoff simulations with up to 12-48 hours lead times. These control simulations were complemented by an ensemble of driven rainfall-runoff simulations which showed to be useful in order to reduce the biases at the sites where the control simulations would not have produced enough accurate runoff forecasts.

The ensemble of mesoscale simulations was also introduced in attempt to understand the sensitivity of the basin's response to the external-scale forecast errors. The basin rainfall-runoff mechanisms were shown to smooth to a high degree these uncertainties, thus enhancing the predictability of this flash-flood in the Llobregat basin.

Similar arguments have been expounded in chapter 4, where we have studied the feasibility of runoff simulations driven by the MM5 numerical weather mesoscale model over the Albufera small-size basin. This issue has been addressed by studying four intense rainfall events which resulted in floods of varied spatial and temporal scales. It has been possible to obtain reasonable runoff simulations at the basin outlet for some of these episodes. Similarly to chapter 3, a multiphysics ensemble of MM5 simulations has been introduced in order to mitigate the low forecasting skill of the deterministic runoff simulations for the remaining events. The ensemble strategy has been able to further extend the short-range prediction guidance when dealing with flood forecasting situations for the Albufera river basin. The value of a multiphysical model ensemble to convey the uncertainty of the small-scale features in precipitation, and thus, of the discharge forecasts has also been proved.

Chapter 5 has proposed a hydrometeorological model intercomparison in order to estimate the uncertainties associated with the hydrometeorological forecasting chain for an intense rainfall episode which affected the Reno river medium-size catchment. To fulfil this aim, the one-way coupled atmospheric-hydrological model simulations have been performed by using two different meteorological and hydrological models. The multi-NWP model ensemble has been performed by using different initializations and configurations. It has also been possible to highlight some hydrometeorological numerical factors which could help to enhance the hydrometeorological modeling of such hazardous events. In addition, the different infiltration schemes adopted by the hydrological models have shown to play a noticeable role in governing the model's response. The discharge scenarios provided in an independent way by the hydrological models driven by both meteorological models have been regarded as members of an ensemble of discharge predictions, which enable to convey a quantification of the uncertainties involved in the hydrometeorological forecasting chain.

Runoff discharges driven by limited area models have been adopted as an evaluation procedure to assess the performance of the quantitive precipitation forecasts in these previous chapters. Hence, the one-way coupling among the meteorological and hydrological models has been regarded as an advanced complementary tool to evaluate the high-resolution simulated precipitation fields for the verification of the meteorological models' performance.

The impact of the spatial and temporal resolution of the boundary fields on dynamical downscaling of precipitation for the Mediterranean Spain has been examined in chapter 6. It has been found for this complex orographic region that the forecast skill is relatively insensitive for the tested spatial resolutions (1^0-3^0) and for temporal updates up to 12 h. With regard to the spatial variability of the model performance depending on the flow regimes, it has been pointed out those areas of the region with an enhanced or a reduced forecast accuracy. This fact can help to improve the spatial dependent confidence intervals in the Mediterranean Spain when dealing with precipitation downscaling products, especially focussed on climate change, and real-time numerical model forecasts.

A set of general remarks arise from the part of this work directly focussed to the topics of hydrometeorological modeling, which appear to be issues of the maximum priority/interest as future intervention/research lines. First, we have encountered for the Llobregat and Albufera river basins a common problem: the lack of flow data at some flow-gauges for the former catchment and the non existence of these measurements for the latter watershed. In addition, it has also been found an scarcity of automatic pluviometric stations for the Albufera basin. Therefore, it would be desirable to get more information of the future floods affecting the Llobregat river basin by means of an increase in the number of stream-gauges operating in this catchment. With respect to the Albufera river basin, it would be also imperative to get information of future flood events affecting this watershed, with the necessary deployment and increase of the number of automatic stream- and rain-gauges, respectively. These measures will produce an enhancement in the reliability and skill of the rainfall-runoff model before such hazardous episodes for both basins. Further efforts in this direction will permit an improvement of the basins' configuration for the hydrological model, and of the implementation of future alert scheme systems based on runoff forecasts as well.

The methodology presented in this work for the aforementioned basins has been automated, and it is nowadays under test, in order to obtain short-range HEC-HMS runoff forecasts driven by MM5 high-resolution mesoscale predictions currently available in real-time (see, for further details, http://mm5forecasts.uib.es and http://hmsforecasts.uib.es). We believe that the relative good predictability found for the floods under study in the Llobregat and the Albufera basins would also apply to many other hazardous episodes as well as to other Spanish Mediterranean catchments of similar size and physical characteristics. In addition, it must be noted that runoff predictions for use in emergency management directives may not need to match exactly the peak discharges or their timing: these predictions must simply reach suitable thresholds so as to cause the appropriate directives to be enacted.

Another important conclusion that arises from this work is the potential benefits provided by short-range ensemble forecast (SREF) modeling systems aimed at accounting for the forecast variance associated to the diverse external-scale uncertainties. For the cases under study, it has been mentioned that some of the hydrometeorological control simulations exhibited very poor results. If they had been used in a deterministic hydrometeorological system would have missed completely the floods and would have inhibited any standard emergency procedure. These are good examples where simple multi-analyses, multi-physics or multi-models ensemble prediction systems (EPS) would have been found of great value to trigger special flood warnings. The piecewise PV inversion technique has been revealed as a valuable tool to address these external-scale uncertainties, at least for the 'Montserrat' episode. Therefore, additional efforts devoted to study the implementation of ensembles generated from realistic perturbations of upper-level precursor troughs –which could result in floods– within a real-time hydrometeorological forecasting chain framework would be another goal of the maximum interest.

Finally, it is important to remark other problems found when dealing with the different case studies. For the June 2000 episode, we have encountered that the set of driven rainfall-runoff simulations showed the lowest skill at the gauges covering small scales of the basin. None of the members of the ensemble, for example, was able to adequately reproduce the flow of the Anoia river for this episode. For the four intense precipitation events over Majorca, even though the one-way coupled runoff simulations have shown a reasonable skill for most of the evaluated episodes, the 9-10 October 1990 event is a good example of the difficulties encountered for a precise detection of a convectively-driven episode affecting a small size basin, even in the framework of an ensemble strategy. The same difficulties have been found by most of the ensemble members in the precise detection of the precipitation characterising the 7-10

November 2003 episode over the Reno river medium size basin.

The difficult reproduction of the precise timing and location of these convectively-driven events remains as a challenging question that could be addressed by improving the description of both meteorological and hydrological components. For the former, an increase of the members of the meteorological ensemble and of their diversity would be desirable. This can be achieved, for example, by using the ECMWF Ensemble Prediction System to provide initial and boundary conditions or by using a broader multi-model and multi-analysis system to drive the limited-area runs. Furthermore, the hydrometeorological forecast chains have been designed without the intervention of any precipitation assimilation technique connecting the meteorological and hydrological models, but using very high-resolution mesoscale models. Therefore, it would be advisable the implementation of assimilation techniques connecting the one-way coupling among hydrological and meteorological models. Some examples of these techniques are different applications of statistical downscaling (e.g. Hewitson and Crane, 1992; von Storh and Zwiers, 1999; Wilks, 1999; Antolik, 2000; Clark and Hay, 2004) or disaggregation techniques (Deidda et al., 1999; Deidda, 2000; Ferraris et al., 2002).

Another way to reduce the abovementioned limitations would be the introduction of runoff simulations driven by estimated rainfall data from meteorological radars. At this aim, it would be necessary the introduction of distributed rainfall-runoff modeling, in order to take advantage of the benefits of the very high-resolution spatial and temporal structures captured nowadays by the radars. This methodology is very useful when dealing with very small-size basins – where the coherence among the spatial and temporal scales of the features resolved by the numerical mesoscale models and the hydrological models is lost–. All these research lines appear as of the maximum importance for future studies in order to develop the most suitable hydrometeorological chain simulation and forecasting systems upon the Spanish Mediterranean area.

APPENDIX

A.1 Continuous verification statistics

Several skill scores measure the correspondence between the values of the forecasts or simulations and the observations at gridpoints, weather stations, gridcells or subbasins. Next, the statistical indices used in this work are briefly summarized:

- The Nash-Sutcliffe efficiency criterion, *NSE*, can range from $-\infty$ to 1, with higher values indicating a better agreement of the model results with the observations. NSE is defined as:

$$NSE = 1 - \frac{\sum_{i=1}^{n}(x_i - y_i)^2}{\sum_{i=1}^{n}(x_i - \overline{x})^2} \tag{7.1}$$

  where x_i and y_i are the observed and model simulated values, respectively, and $\overline{x}$ is the mean observed value.

- The relative error of total volume, expressed as percentage ($\%EV$), is calculated as:

$$\%EV = (\frac{V_y - V_x}{V_x}) \cdot 100 \tag{7.2}$$

  where V_x and V_y are the observed and simulated runoff volumes, respectively. Therefore, %EV>0 and %EV<0 would indicate an over- and underestimation of the volume by the model, respectively.

- The relative error in percentage to the peak discharge, $\%EP$, can be calculated as:

$$\%EP = (\frac{Q_{p_y} - Q_{p_x}}{Q_{p_x}}) \cdot 100 \tag{7.3}$$

  where Q_{p_x} and Q_{p_y} are the observed and simulated peak discharges. Therefore, $\%EP > 0$ and $\%EP < 0$ would indicate an over- and underestimation of the peak flow by the model, respectively.

- The mean absolute error (MAE) measures the average magnitude of the forecast error, and it is defined as:

$$MAE = \frac{1}{N}\sum_{i=1}^{N}|x_i - y_i| \tag{7.4}$$

- The root mean square error ($RMSE$) measures the error magnitude, and it is defined as:

$$RMSE = \sqrt{\frac{1}{N}\sum_{i=1}^{N}(x_i - y_i)^2} \tag{7.5}$$

- The spatial correlation, r_{xy}, measures the spatial correspondence between forecasted and observed patterns, and it is computed as:

$$r_{xy} = \frac{\sum_{i=1}^{N}(x_i - \overline{x}) \cdot (y_i - \overline{y})}{(N-1) \cdot \sigma_x \cdot \sigma_y} \tag{7.6}$$

- The standard deviation or dispersion, σ_x, is a measure of the spread of the values of a variable, and it is calculated as:

$$\sigma_x = \sqrt{\frac{1}{N-1}\sum_{i=1}^{N}(x_i - \overline{x})^2} \tag{7.7}$$

A.2 Categorical verification statistics

Different scoring techniques measure the correspondence between forecast or simulated and observed occurrence of events at gridpoints, weather stations, gridcells or subbasins. The statistical indices applied in this work are obtained by making use of a contingency table as illustrated in Table A.1.

Forecast	Observed		
	Yes	No	Total
Yes	*a*	*b*	*a+b*
No	*c*	*d*	*c+d*
Total	*a+c*	*b+d*	*a+b+c+d = n*

Table A.1: Schematic contingence table for categorical forecasts of a binary event. The numbers of observations in each category are represented by a, b, c, and d, and n is the total.

This represents a matrix considering the following quantities for any given threshold: a, the number of hits or correct predictions; b, the number of false alarms or wrong predictions; c, the number of misses or non-detected events; d, the number of correct predictions of non-occurrence. The total number of forecasts is then defined as $n = a + b + c + d$. The statistical indices have been calculated by using Table A.1 and the following definitions:

- The threat score, TS, indicates the correct proportion for the rainfall threshold being forecasted when it has been removed the correct no forecasts. $TS = 1$ denotes a perfect skill.

$$TS = \frac{a}{a+b+c} \tag{7.8}$$

- The frequency bias score, $BIAS$, measures the relative frequency of predicted and observed events without regard to forecast accuracy. Unbiased forecasts exhibit $BIAS = 1$.

$$BIAS = \frac{a+b}{a+c} \tag{7.9}$$

- The false alarm ratio, FAR, is the proportion of positive forecasts events that fail to materialize. A perfect forecast has $FAR = 0$.

$$FAR = \frac{b}{a+b} \tag{7.10}$$

- The probability of detection or hit rate, POD, measures the success of the forecast in correctly predicting the occurrence of events. $POD = 1$ denotes a perfect skill.

$$POD = \frac{a}{a+c} \tag{7.11}$$

- The false alarm rate, F, measures the proporcion of non-occurrences that were incorrectly forecast. A perfect forecast has $F = 0$.

$$F = \frac{b}{b+d} \tag{7.12}$$

- The Relative Operating Characteristic (ROC) curve is a graph of hit rate against false alarm rate at varying thresholds (w), with false alarm rate plotted at the X-axis and hit rate as the Y-axis. The location of the whole curve in the unit square is determined by the intrinsic discrimination capacity of the forecasting system, and the location of specific points on the curve is fixed by the decission threshold at which the system is operating. A perfect forecast has $ROC = 1$. Zero skill is indicated by $ROC = 0.5$.

REFERENCES

Agència Catalana de l'Aigua, 2001: *Delimiting of flood plain for the draft of the INUNCAT. Internal Basins of Catalonia. Hydrological calculations and determination of the flood wave discharge. Vol. 2*. Departament de Medi Ambient. Generalitat de Catalunya, 88 pp (in catalan).

Agència Catalana de l'Aigua, 2003: *Technical recommendations for flood studies at local area*. Departament de Medi Ambient. Generalitat de Catalunya, 106 pp (in catalan).

Alpert, P., T. Ben-gai, A. Baharad, Y. Benjamini, D. Yekutieli, M. Colacino, L. Diodato, C. Ramis, V. Homar, R. Romero, S. Michaelides and A. Manes, 2002: The paradoxial increase of Mediterranean extreme daily data in spite of decrease in total values. *Geophys. Res. Lett.*, **20**, 1-4.

Alpert, P., Krichak S.O., Krishnamurty T.N., Stein U., Tsidulko M., 1996: The relatively roles of lateral boundaries, initial conditions and topography in mesoscale simulations of Lee cyclogenesis. *J App Meteor*, **35**, 1091-1099.

Anderson, M.L., Z.Q. Chen, M.L. Kavvas and A. Feldman, 2002: Coupling HEC-HMS with atmospheric models for prediction of watershed runoff. *J. Hydrol. Eng.*, **7**, 312-318.

Anquetin, S., and Coauthors: The 8 and 9 September 2002 flash flood event in France: a model intercomparison. *Nat. Haz. and Earth Sys. Sci.*, **5**, 741-754, 2005.

Antic, S., Laprise R., Denis B., de Elía R., 2004: Testing the downscaling ability of a one-way nested regional climate model in regions of complex topography. *Clim Dyn*, **23**, 473-493.

Antolik, M.S., 2000: An overview of the National Weather Service's centralized statistical quantitative precipitation forecast. *J. Hydrol.*, **239**, 306-337.

Arakawa, A. and V.R. Lamb, 1977: *Computional design of the basic dynamical processes of UCLA general circulation model*, Vol. 17 of Methods in Computational Physics. Academic Press.

Atkinson, S., Woods, R.A. and Sivapalan, M., 2002: Climate and landscape controls on water balance model complexity over changing time scales. *Water Res. Research*, **38(12)**, 1314doi: 10.1029/2002WR001487, pp. 50.1-50.17.

Atkinson, S., Sivapalan, M., Woods, R.A. and Viney, N.R., 2003: Dominant physical controls of hourly streamflow predictions and an examination of the role of spatial variability: Mahurangi catchment, New Zealand. *Adv. in Water Res.*, **26(3)**, 219-235.

Avissar, R. and R. Pielke, 1989: A parameterization of heterogeneous land surfaces for atmospheric numerical models and its impact on regional meteorology. *Mon. Wea. Rev.*, **117**, 2113-2136.

Bacchi, B., A. Buzzi, G. Grossi and R. Ranzi, 2002: Flood forecasting in a midsize catchment in the southern Alps: Recent experiences on the use of couple meteorological and hydrological model. *Proceedings of the third EGS Plinius conference*, Baja Sardinia. Consiglio Nazionale delle Ricerche, Roma, Italy, 201-208.

Bacchi, B. and R. Ranzi, 2003: Hydrological and meteorological aspects of floods in the Alps: an overview. *Hydrol Earth Sys Sci* **7**, 785-798.

Ballard, S.P., B.W. Golding and R.N. Smith, 1991: Mesoscale model experimental forecasts of the Haar of Northeast Scotland. *Mon. Wea. Rev.*, **119**, 2107-2123.

Bellon, A. and I. Zawadzki, 1994: Forecasting of hourly accumulations of precipitation by optimal extrapolation of radar maps. *J. Hydrol.*, **157**, 211-233.

Beck, A., Ahrens, B. and K. Stadlbacher, 2004: Impact of nesting strategies in dynamical downscaling of reanalysis data. *Geophys Res Letters*, **31**, L19101.

Benoit R., P. Pellerin, N. Kouwen, H. Ritchie, N. Donaldson, P. Joe, E.D. Soulis, 2000: Toward the use of coupled atmospheric and hydrologic models at regional scale. *Mon. Wea. Rev.*, **128**, 1681-1706.

Benoit, R., Kouwen, N., Yu, W., Chamberland, S., and P. Pellerin, 2003: Hydrometeorological aspects of the Real-Time Ultrafinescale Forecast Support during the Special Observing Period of the MAP. *Hydrol Earth Sys Sci*, **7**, 877-889.

Betts, A.K. and M.J. Miller, 1986: A new convective adjustment scheme. Part II: single column using GATE wave, BOMEX, ATEX and Artic air-mass data sets. *Quart. J. Roy. Meteor. Soc.*, **112**, 693-709 pp.

Ben Gai, T., Bitan, A., Manes, A. and P. Alpert, 1993: Long-term changes in October rainfall patterns in southern Israel. *Theoretical and Applied Climatology*, **46**, 209-217.

Benjamin, S.G., 1983: Some effects of heating and topography on the regional severe storm environment. *Ph.D. thesis*, The Pennsylvania State University, 265 pp. (Available from University Microfilm, 300 N. Zeeb. Rd., P.O. Box 1346, Ann Arbor, MI 46801-1346.)

Benjamin, S.G. and N.L. Seaman, 1985: A simple scheme for improved objective analysis in curved flow. *Mon. Wea. Rev.*, **113**, 1184-1198.

Blackadar, A.K., 1976: Modeling the nocturnal boundary layer. In *Proc. Third Symp. on Atmospheric Turbulence, Diffusion and Air Quality*, Boston, 46-49 pp. Amer. Meteor. Soc.

Blackadar, A.K., 1979: High resolution models of the planetary boundary layer. *Adv. Environ. Sci. and Eng.*, **1**, 50-85.

Bossard, M., J. Feranec, J. Otahel, 2000: *CORINE Land Cover Technical Guide - Addendum 2000.* Technical Report No. 40, European Environment Agency, Copenhagen, Denmark. 105 pp.

Brémaud, P.J. and Y. Pointin, 1993: Forecasting heavy rainfall from rain cell motion using radar data. *J. Hydrol.*, **142**, 373-389.

Bright, D.R., Mullen, S.L., 2002: The sensitivity of the numerical simulation of the southwest monsoon boundary layer to the choice of PBL turbulence parameterization in MM5. *Wea. Forecasting*, **17**, 99-114.

Burk, S.D. and W.T. Thompson, 1989: A vertically nested regional numerical prediction model with second-order closure physics. *Mon. Wea. Rev.*, **117**, 2305-2324.

Butts, M.B., 2000: Coupling of catchment modelling and meteorological information in flow forecasting. *PIK Report no. 65*, Proc. of European Conf. on advances in flood research, Ed. by Bronsert A, Bismuth C and Menzel C, Potsdam-Institut fr klimafolgenforschung, pp 476-487.

Butts, M.B. , Payne, J.T., Kristensen, M. and Madsen, H., 2004: An evaluation of the impact of model structure on hydrological modelling uncertainty for streamflow simulation. *J. of Hydrol.*, **298**, 242-266.

Buzzi, A. and S. Tibaldi, 1978: Cyclogenesis in the lee of the Alps: A case study. *Quart J Roy Meteo Soc*, **104**, 271-287.

Castelli, F., 1995: Atmosphere modelling and hydrology prediction uncertainty. *Proc. U.S.-Italy Research Workshop on Hydrometeorology: Impacts and Management of Extreme floods*, Perugia, Italy, Water Resources Research and Documentation Center and Colorado State University, 13-17.

Chancibault, K., Anquetin, S., Ducrocq V. and Saulnier, G-M., 2006: Hydrological evaluation of high-resolution precipitation forecast of the Gard flash-flood event (8-9 September 2002). *Q. J. R. Meteorol. Soc.*, **132**, 1091-1117.

Chappell, C.F., 1986: Quasi-stationary convective events. *Mesoscale Meteorology and Forecasting*, P. S. Ray, Ed., Amer. Meteor. Soc., 289-298.

Charney, J.G., 1955: The use of primitive equations of motion in numerical prediction. *Tellus*, **7**, 22-26.

Chow, V.T., D.R. Maidment and L.W. Mays, 1988: *Applied hydrology.* McGraw-Hill International Editions. Civil engineering series. 572 pp.

Clark, M.P. and L.E. Hay, 2004: Use of medium-range numerical weather prediction model output to produce forecasts of stream-flow. *J. Hydrometeor.*, **5**, 243-262.

Conway, B.J. and K.A. Browning, 1988: Weather forecasting by interactive analysis of radar and satellite imagery. *Phil. Trans. Roy. Soc.*, **324**, 299-315.

Conway, B.J. and K.A. Browning, 1988: Weather forecasting by interactive analysis of radar and satellite imagery. *Phil. Trans. Roy. Soc.*, **324**, 299-315.

Cuxart, J., P. Bougeault and J.L. Redelsperger, 2000: A turbulent scheme allowing for meso-scale and large-eddy simulations. *Q. J. R. Meteorol. Soc.*, **126**, 1-30.

Dai, A., Fung, I.Y. and A.D.D Genio, 1997: Surface observed global land precipitation variation during 1900-88. *J. of Climate*, **10**, 2943-2962.

Davis, C.A. and K.A. Emanuel, 1991: Potential vorticity diagnosis of cyclogenesis. *Mon. Wea. Rev.*, **119**, 1929-1953.

Davis, C.A., 1992: A potential vorticity diagnosis of the importance of initial structure and condensational heating in observed extratropical cyclogenesis. *Mon. Wea. Rev.*, **120**, 2409-2428.

Deidda, R., R. Benzi and F. Siccardi, 1999: Multifractal modelling of anomalous scaling laws in rainfall. *Water Resour. Res.*, **35**, 1853-1867.

Deidda, R., 2000: Rainfall downscaling in a space-time multifractal framework. *Water Resour. Res.*, **36**, 1779-1794.

Denis, B., Laprise, R., Caya, D. and J. Côté, 2002: Downscaling ability of one-way nested regional climate models: the Big-Brother Experiment. *Clim. Dyn.*, **18**, 627-646.

Denis, B., Laprise, R. and D. Caya, 2003: Sensitivity of a regional climate model to the resolution of the lateral boundary conditions. *Clim. Dyn.*, **20**, 107-126

Diaconis, P. and B. Efron, 1983: Computer-intensive methods in statistics. *Sci Am*, **248**, 116-130.

Dimitrijevic, M. and R. Laprise, 2005: Validation of the nesting technique in a regional climate model and sensitivity tests to the resolution of the lateral boundary conditions during summer. *Clim. Dyn.*, **25**, 555-580.

Diomede, T., Marsigli, C., Nerozzi, F., Papetti, P., and Paccagnella, T., 2008: Coupling high resolution precipitation forecasts and discharge predictions to evaluate the impact of spatial uncertainty in NWP model output. *Meteor. and Atmos. Phys.* (in press).

Dolciné, L., H. Andrieu, D. Sempere-Torres and D. Creutin, 2001: Flash flood forecasting with coupled precipitation model in mountainous mediterranean basin. *J. Hydrol. Eng.*, **6**, 1-9.

Dooge, J.C.I., 1959: A general theory of the Unit Hydrograph. *J. Geophys. Res.*, **64** (2), 241-256.

Doswell, C.A. 1994: Flash flood-producing convective storms: current understanding and rsearch. *Proceedings from Spain-U.S. joint workshop on natural hazards* Barcelona, Spain, 8-11 June 1993.

Doswell, C.A., H.E. Brooks and R. A. Maddox 1996: Flash flood forecasting: an ingredients-based methodology. *Wea. Forecasting.*, **11**, 560-581.

Doswell, C.A., Ramis, C., Romero, R. ans S. Alonso, 1998: A diagnostic study of three heavy precipitation episodes in the western Mediterranean region. *Wea. Forecasting.*, **13**, 102-124.

Du, J., S.L. Mullen and F. Sanders, 1993: Short-range ensemble forecasting of quantitative precipitation. *Mon. Wea. Rev.*, **125**, 2427-2459.

Ducrocq, V., Lebeaupin, C., Thouvenin, T., and Anquetin, S., 2003: Mesoscale modelling of a cooding storm. Application to the extreme flood of Gard. *5th EGS Plinius conference*, Ajaccio, Corsica, France.

Dudhia, J., 1993: A nonhydrostatic version of the Penn State/NCAR mesoscale model: Validation tests and simulation of an Atlantic cyclone and cold front. *Mon. Wea. Rev.*, **121**, 1493-1513.

Easterling, D.R., Horton, B., Jones, P.D., Peterson, T.C., Karl, T.R., Parker, D.E., Salinger, M.J., Razuvayev, V., Plummer, N., Jamason, P. and C.K. Folland, 1997: Maximum and Minimum Temperature Trends for the Globe. *Science*, **277**, 364-367.

Easterling, D.R., Meehl, G.A., Parmesan, G., Changnon, S.A., Karl, T.R. and L.O Mearns, 2000. Climate extremes: observations, modelling and impacts. *Science*, **289**, 2068-2074.

Elementi, M., Marsigli, C., Paccagnella, T., 2005: High resolution forecast of heavy precipitation with Lokal Modell: analysis of two case studies in the Alpine area. *Nat. Haz. and Earth Sys. Sci.*, **5**: 593-602.

Epstein E.S., 1969: Stochastic dynamic prediction. *Tellus*, **21**, 739-759.

ESRI, 1996: ArcView spatial analyst. Advanced spatial analysis using raster and vector data. Environmental Systems Research Institute, Inc., Redlands, California. 147 pp.

Farmer, D., Sivapalan, M. and Jothityangkoon, C., 2003: Climate, soil and vegetation controls upon the variability of water balance in temperate and semi-arid landscapes: downward approach to hydrological prediction. *Water Res. Research*, **39(2)**, 1035, doi: 10.1029/2001 WR000328.

Ferraris, L., R. Rudari and F. Siccardi, 2002: The uncertainty in the prediction of flash floods in the Northern Mediterranean environment. *J. Hydrometeor.*, **3**, 714-727.

Georgakakos, K.P., Seo, D.-J., Gupta, H., Schaake, J. and Butts, M.B., 2004: Characterising streamflow simulation uncertainty through multimodel ensembles. *J. of Hydrol.*, **298(1-4)**, 222-241.

Gerlinger, K. and Demuth, N., 2000: Operational flood forecasting for the Moselle river basin. *PIK Report no. 65*, Proc. of European Conf. on advances in flood research, ed. by Bronsert A, Bismuth C and Menzel C, Potsdam-Institut fr klimafolgenforschung, pp 562-573.

Giannoni F., J.A. Smith, Y. Zhang, G. Roth, 2003: Hydrologic modeling of extreme floods using radar rainfall estimates. *Adv. Wat. Res.*, **26**, 195-203.

Giorgi, F., 1990: Simulation of regional climate using a limited area model nested in a general circulation model. *J. Clim.*, **3**, 941-963.

Giorgi, F. and L.O. Mearns, 1999: Introduction to special section: Regional climate modeling revisited. *J Geophys Res*, **104 (D6)**, 6335-6352.

Gómez, M. and R. López, 1998: *Rehabilitation of sewer networks in member states. Sant Boi sewer network*. Research Report, European project SPRINT SP-98. (available at: Library of Universitat Politècnica de Catalunya, Barcelona, Spain)

Grell, G.A., J. Dudhia and D.R. Stauffer, 1995: *A description of the fifth-generation of the Penn State/NCAR mesoscale model (MM5)*, NCAR Tech. Note NCAR/TN-398+STR, 117 pp., Boulder, USA.

Grimalt, M., 1992: *Geography of the risk in Majorca. The floods.* PhD thesis. Institut d'Estudis Baleàrics. Conselleria de Cultura, Educació i Esports. Govern de les Illes Balears. 359 pp (in catalan).

Groissman, P.Y., R.T. Karl, D.R. Easterling, R.W. Knight, P.F. Jamason, K.J. Hennessy, R. Suppiah, C.M. Page, J. Wibig, K. Fortuniak, V.N. Razukaev, A. Douglas, E. Førland and P.M. Zhai, 1999: Changes in the probability of heavy precipitation: important indicators od climatic change. *Clim. Chan.*, **42**, 243-283.

Hardaker, P.J., C.G. Collier and C.E. Pierce, 1994: The Gandolf system: A look to the future for operational flood forecasting using satellite and radar measurements. *Proc. British Hydrological Soc. Radar Meeting*, 39-63.

Hearman, A.J. and Hinz, C., 2007: Sensitivity of point scale surface runoff predictions to rainfall resolution. *Hydrol. Earth Syst. Sci.*, **11(2)**, 965-982.

Hewitson, B.C. and R.G. Crane, 1992: Large-scale atmospheric controls on local precipitation in tropical Mexico. *Geophys. Res. Lett.*, **19**, 1835-1838.

Homar, V., 2001: *Synoptic and Mesoscale study of western Mediterranean severe weather events through numerical simulation: Application of factors separation and PV inversion techniques*. Ph D. thesis (available at: Library of Universitat de les Illes Balears, Palma de Mallorca, Spain).

Homar, V., R. Romero, C. Ramis and S. Alonso, 2002: Numerical study of the October 2000 torrential precipitation event over eastern Spain: Analysis of the synoptic-scale stationarity. *Ann. Geophys.*, **20**, 2047-2066.

Hong, S.-Y. and H.-L. Pan, 1996: Nonlocal boundary layer vertical diffusion in a medium-range forecast model. *Mon. Wea. Rev.*, **124**, 2322-2339.

Hoskins, B.J., M.E. McIntyre and A.W. Robertson, 1985: On the use and significance of isoentropic potential vorticity maps. *Quart. J. Roy. Meteor. Soc.*, **111**, 877-946.

IPCC, 2001: *Third assessment report: Climate change 2001 (Synthesis Report).* Watson, R. T. and Core Writting Team (Eds.), IPCC, Geneva, Switzerland, pp. 184.

Janjic, Z.I., 1990: The step-mountain coordinate: Physical package. *Mon. Wea. Rev.*, **118**, 1429-1443.

Janjic, Z.I., 1994: The step-mountain eta coordinate model: Further development of the convection, viscous sublayer, and turbulent closure schemes. *Mon. Wea. Rev.*, **122**, 927-945.

Jansà, A., García-Moya, J.A. and E. Rodríguez, 1991: Numerical experiments on heavy rain and mediterranean cyclones. *WMO/TD 420*, 37-47

Jasper, K. and P. Kaufmann, 2003: Coupled runoff simulations as validation tools for atmospheric models at the regional scale. *Quart. J. Roy. Meteor. Soc.*, **129**, 673-692.

Jensen, S.K. and J.O. Domingue, 1988: Extracting topographic structure from digital elevation data for geographical information system analysis. *Photogrammetric Engrg. and Remote Sensing*, **54 (11)**, 1593-1600.

Jensen, S.K., 1991: Applications of hydrologic information automatically extracted form digital terrain models. *Hydrolog. Processes*, **5 (1)**, 31-44.

Jolliffe I.T., D.B. Stephenson, 2003: *Forecast verification. A practitioner's guide in atmospheric science*. John Wiley and Sons Ltd. Chichester, West Sussex, England. 240 pp.

Jones M.S., B.A. Colle, J.S. Tongue, 2007: Evaluation of a mesoscale short-range ensemble forecats system over the northeast United States. *Wea. Forecasting*, **22**, 36-55.

Kain, J.S. and J.M. Fritsch, 1993: Convective parameterization for mesoscale models: The Kain-Fritsch scheme. The representation of cumulus convection in numerical models. K.A. Emanuel and D.J. Raymond, Eds., *Amer. Meteor. Soc.*, 246 pp.

Kain, J.S., 2004: The Kain-Fritsch convective parameterization: an update. *J. Appl. Meteor.*, **43**, 170-181.

Källén, E., 1996: HIRLAM Documentation Manual, available from SMHI S-60176 Norrkoping. Sweden

Koren, V.I., Reed, S., Smith, M., Zhang, Z. and Seo, D.-J., 2004: Hydrology Laboratory Research Modeling System (HL-RMS) of the National Weather Service. *J. of Hydrol.*, **291**, 297-318.

Kuo, H., 1974: Further studies of the parameterization of the influence of cumulus convection on large-scale flow. *J. Atmos. Sci.*, **31**, 1232-1240.

Kunstmann, H. and Stadler, C., 2003: Operational high resolution meteorological and hydrological analysis as decision support system in integrated water resources management. In IAHS Redbook 'Integrated water resources management: Towards sustainable water utilization in the 21st century'.

Leith, C.E., 1974: Theoretical skill of Monte Carlo forecasts. *Mon. Wea. Rev.*, **102**, 409-418.

Lin, Y-L., R.D. Farley and H.D. Orville, 1983: Bulk parameterization of the snow field in a cloud model. *J. Clim. Appl. Meteor.*, **22**, 1065-1092.

Linsley, R.K., Kohler, M.A. and Paulhus, J.L.H, 1982: *Hydrology for engineers.* 3rd edition. McGraw-Hill, New York, 508 pp.

Liu, Z. and Todini, E., 2002: Towards a comprehensive physically-based rainfall-runoff model, *Hydrol. Earth Syst. Sci.*, **6**, 859-881.

Llasat, M.C., T. Rigo and M. Barriendos, 2003: The 'Montserrat-2000' flash flood event: a comparasion with the floods that have ocurred in the northeast iberian peninsula since the 14th century. *Int. J. Climat.*, **23**, 453-469.

Louis, J.F., 1979: A parametric model of vertical eddy fluxes in the atmosphere. *Bound. Lay. Met.*, **17**, 187-202.

Mariani, S. and Coauthors, 2005: A limited area model intercomparison on the 'Monserrat-2000' flash-flood event using statistical and deterministic methods. *Nat. Haz. and Earth Sys. Sci.*, **5**, 565-581.

Martín, A., R. Romero, V. Homar, A. de Luque, S. Alonso, T. Rigo and M.C. Llasat, 2006: Sensitivities of a flash-flood event over Catalonia: A numerical analysis. *Mon. Wea. Rev.*, **135**, 651-669.

Martín-Vide, J.P., D. Niñerola, A. Bateman, A. Navarro and E. Velasco, 1999: Runoff and sediment transport in a torrential ephemeral stream of the Mediterranean coast. *J. Hydrol.*, **225**, 118-129.

Mason, I., 1982: A model of assessment to weather forecasts. *Aust. Meteo. Mag.*, **30**, 291-303.

Mass C.F. and Y-H Kuo, 1998: Regional real-time numerical weather prediction: current status and future potential. *Bull Amer Meteo Soc*, **79 (2)**, 253-263.

Mazzetti, C. and Todini, E., 2004: *Deliverable 7.1 - Development and application of the block Kriging technique to rain-gauge data*. Resulting from Work package 7, MUSIC Multi-sensor Precipitation calibration and flood forecasting, project supported by the European Commission under Contract No EVK1-CT-2000-00058, (www.geomin.unibo.it/orgv/hydro /music/index2.htm).

Menéndez, M., 1998: *Design discharge calculations and flood plain management*. CEDEX, Madrid. Research Report, European project Flood Aware: prevention and forecast of floods.

Meteorological Office (UK), 2001: *Some recent results from the Hadley Centre*. The Hadley Centre, Met Office, Bracknell, UK

Mlawer, E.J., S.J. Taubman, P.D. Brown, M.J. Iacono and S.A. Clough, 1997: Radiative transfer for inhomogeneous atmosphere: RRTM, a validate correlated-k model for the long wave. *J. Geophys. Rev.*, **102** (D14), 16663-16682.

Murphy, A.H., 1993: What is a good forecast? An essay on the nature of goodness in Weather Forecasting. *Wea. Forecast.*, **8**, 281-293.

MEDIS, 2006: *Towards sustainable water use on Mediterranean Islands: addressing conflicting demands and varing hydrological, social and economic conditions*. Münster, Germany. Final Report, European project Contract No.: EVK1-CT-2001-00092. 285 pp.

Nash, J.E., 1959: Systematic determination of Unit Hydrograph Parameters. *J. Geoph. Res.*, **64** (1), pp 111-115.

Nash, J.E. and J.V. Sutcliffe, 1970: River flow forecasting through conceptual models. Part I: A discussion of principles. *J. Hydrol.*, **10** (3), pp 282-290.

Noilhan, J. and S. Planton, 1989: A simple parameterization of land surface processes for meteorological models. *Mon. Wea. Rev.*, **117**, 536-549.

Obled, C., Djerboua, A., Zin, I. and Garon, R., 2004: A simple probabilistic flood forecasting chain with focus on the use of QPF's. *Proc. of the ESF LESC Exploration Workshop*, Bologna, Italy, Ed. Bios.

Olivera, F. 2001: Extracting hydrologic information from spatial data for HMS modeling. *J. Hydrol. Eng.*, **6 (6)**, pp 524-530.

Orlanski, I. 1975: A rational subdivision of scales for atmospheric processes. *Bull. Amer. Meteor. Soc.*, **56**, pp 527-530.

Pessoa, L.M., R.L. Brass and E.R. Williams, 1993: Use of weather radar for flooding forecasting in the Sieve river basin: A sensitivity analysis.*J. App. Meteor.*, **32**, 462-475.

Pielke, R.A., 1984: *Mesoscale Meteorological Medeling*. Orlando, Florida. Academic Press.

Piervitali, E., Colacino, M. and M. Conte, 1997: Signals of climatic change in the Central-Western Mediterranean catchment. *Theor. Appl. Climatol.*, **58**, 211-219.

Pleim, J.E. and J.S. Chang, 1992: A non-local closure model for vertical mixing in the convective boundary layer. *Atm. Env.*, **26A**, 965-981.

PSU/NCAR Mesoscale Modeling System, 2005: Tutorial class notes and user's guide: MM5 modeling system Version 3. (available from: http://www.mmm.ucar.edu/mm5/mm5-home.htm)

Ramírez, J.A. 2000: Prediction and modeling of flood hydrology and hydraulics. Chapter 11 of *Inland Flood Hazards: Human, Riparian and Aquatic Communities*, Eds. Ellen Wohl: Cambridge University Press.

Ramis, C., S. Alonso and M.C. Llasat, 1994: A comparative study between two cases of extreme rainfall events in Catalunya. *in Hydrometeorological Hazards in a Changing Perspective, Surveys in Geophysics*, **33**, 750.

Ramis, C., Romero, R., Homar, V., Alonso, S. and M. Alarcón, 1998: Diagnosis and numerical simulation of a torrential precipitation event in Catalonia (Spain). *Meteorol. Atmos. Phys.*, **69**, 1-21.

Ranzi, R., Bacchi, B., Grossi, G., Buzzi, A., Malguzzi, P., Ratto, C., and Corazza M., 2000: Previsioni di piena mediante un modello idrologico e un modello meteorologico ad area limitata: alcune esperienze applicative durante l'esperimento MAP-SOP. *Atti del XXVII Convegno di Idraulica e Costruzioni Idrauliche*, Genova, 12-15 settembre 2000, Vol. II, 385-393.

Ranzi, R., B. Bacchi and G. Grossi, 2003: Runoff measurements and hydrological modelling for the estimation of rainfall volumes in an Alpine Basin. *Quart. J. Roy. Meteor. Soc.*, **129**, 653-672.

Raymond, D.J. and K.A. Emmanuel, 1993: *The representation of cumulus convection in numerical models. The Kuo cumulus parameterization.* Chapter 12, Volume 24 of **Meteorological Monographs**. American Meteorology Society.

Refsgaard, J.C. and Knudsen, J., 1996: Operational validation and intercomparison of different types of hydrological models. *Water Res. Research*, **32(7)**, 2189-2202.

Reisner, J., R.J. Rasmussen and R.T. Bruintjes and G., 1998: Explicit forecasting of supercooled liquid water in winter storms using the MM5 mesoscale model. *Quart. J. Roy. Meteor. Soc.*, **124**B, 1071-1107.

Reiter, E.R., 1975: *Handbook for forecaster in the Mediterranean, weather phenomena in the Mediterranean basin.* Monterrey Cal. Tech. Paper, No. 5-75: 344 pp.

Riggs, H.C., 1976: A simplified slope-area method for estimating flood discharges in channels. *J. Res. U.S. Geol. Sur.*, **4**, 285-291.

Ritter, B. and Geleyn, J.F., 1992: A comprehensive radiation scheme for numerical weather prediction models with potential applications in climate simulations. *Mon. Wea. Rev.*, **120**, 303-325.

Roeckner, E., Bengtsson, L., Feichter, J. and Rodhe, H., 1998: *Transient climate change simulations with a coupled atmosphere-ocean GCM including the tropospheric sulphur cycle.* Max Planck Institut fr Meteorologie, Rep 266, Hamburg, Germany.

Romero, R., C. Ramis, S. Alonso, C.A. Doswell III and D.J. Stensrud, 1998a: Mesoscale model simulations of three heavy precipitation events in the western Mediterranean region. *Mon. Wea. Rev.*, **126**, 1859-1881.

Romero, R., Guijarro, J.A., Ramis, C. and S. Alonso, 1998b: A 30 year (1964-1993) daily rainfall data base for the Spanish Mediterranean regions: First exploratory study. *Int. J. Climatol.*, **18**, 541-560.

Romero, R., Guijarro, J.A., Ramis, C. and G. Sumner, 1999a: Daily rainfall affinity areas in the Mediterranean Spain. *Int. J. Climatol.*, **19**, 557-578.

Romero, R., Sumner, G., Ramis, C., and A. Genovés, 1999b: A classification of the atmospheric circulation patterns producing significant daily rainfall in the Spanish Mediterranean area. *Int. J. Climatol.*, **19**, 765-785.

Romero R, Doswell III CA, Ramis C. 2000. Mesoscale numerical study of two cases of long-lived quasistationary convective systems over eastern Spain. *Mon. Wea. Rev.*, **128**, 3731-3751.

Romero, R., 2001: Sensitivity of a heavy rain producing Western Mediterranean cyclone to embedded potential vorticity anomalies.*Quart. J. Roy. Meteor. Soc.*, **127**, 2559-2597.

Romero, R., A. Martín, V. Homar, S. Alonso and C. Ramis, 2006: Predictability of prototype flash flood events in the Western Mediterranean under uncertainties of the precursor upper-level disturbance: the HYDROPTIMET case studies. *Nat. Haz. and Earth Sys. Sci.*, **5**, 505-525.

Savijärvi, H., 1990: Fast radiation parameterization schemes for mesoscale and short range forecast models. *J. Appl. Meteorol.*, **20**, 437-447.

Schultz, P., 1995: An explicit cloud physics parameterization for operational numerical weather prediction. *Mon. Wea. Rev.*, **123**, 3331-3343.

Shafran, P.C., N.L. Seaman and G.A. Gayno, 2000: Evaluation of numerical predictions of boundary layer structure during the Lake-Michigan Ozone Study. *J. Appl. Meteor.*, **39**, 412-426.

Siccardi, F., 1996: Rainstorm hazards and related disasters in the western Mediterranean region. *Rem. Sens. Rev.*, **14**, 5-21.

Simmons, A.J. and D.M. Burridge, 1981: An energy and angular-momentum conserving vertical finite-difference scheme and hybrid vertical coordinates. *Mon. Wea. Rev.*, **109**, 758-766.

Singh, V.P., 1997: Effect of spatial and temporal variability in rainfall and watershed characteristics on stream flow hydrograph. *Hyd. Proc.*, **11**, 1649-1669.

Snyder, F.F., 1938: Synthetic Unit Graphs. *Trans. Am. Geophys. Union*, **19**, 447-454.

Sotillo, M.G., Ramis, C., Romero, R., Homar, V., and S. Alonso, 2003: The role of the orography on the spatial distribution of precipitation over the Spanish Mediterranean zone. *Clim. Res.*, **23**, 247-261.

Stanski, H., Wilson, L.J., and W.R. Burrows, 1989: *Survey of commom verification methods in meteorology.* WMO World Weather Watch Tech Rep 8: 114 pp.

Steinberger, E.H., 1999: *Abstract on Proceedings of the 7th International Conference on Water and Environmental Cooperation for the next Millennium*, June 1999, Jerusalem, 45.

Steinberger, E.H. and N. Gazit-Yaari, 1996: Recent changes in the spatial distribution of annual precipitation in Israel. *J. of Climate*, **9**, 3328-3336.

Stensrud D.J. and J.M Fritsch, 1994a: Mesoscale convective systems in weakly forced large-scale environments. Part II: Generation of a mesoscale initial condition. *Mon. Wea. Rev.*, **122**, 2068-2083.

Stensrud D.J. and J.M Fritsch, 1994b: Mesoscale convective systems in weakly forced large-scale environments. Part III: Numerical simulations and implications for operational forecasting. *Mon. Wea. Rev.*, **122**, 2084-2104.

Stensrud D.J., J-W. Bao, T.T Warner, 2000: Using initial and model physics perturbations in short-range ensemble simulations of mesoscale convective events. *Mon. Wea. Rev.*, **128**, 2077-2107.

Steppeler, J., Doms, G., Schttler, U., Bitzer, H.W., Gassmann, A., Damrath, U., Gregoric, G., 2003: Meso-gamma scale forecasts using the non-hydrostatic model LM. *Meteorol. Atmos. Phys.*, **82**, 75-96.

Sumner, G.N., Romero, R., Homar, V., Ramis, C., Alonso, S. and E. Zorita, 2003: An estimate of the effects of climatic change on the rainfall of Mediterranean Spain by the late 21st century. *Clim. Dyn.*, **20**, 789-805.

Sundqvist, H., E. Berge and J. Kristánsson, 1989: Condensation and cloud parameterization studies with a mesoscale numerical weather prediction model. *Mon. Wea. Rev.*, **121**, 3326-3344.

Tao, W-K., J. Simpson and M. McCumber, 1989: Ice-water saturation adjustment. *Mon. Wea. Rev.*, **117**, 231-235.

Tao, W-K. and J. Simpson, 1993: Goddard Cumulus Ensemble Model. Part I: Model Description. *Terrestrial, Atmospheric and Oceanic Sciences*, **4**, 35-72.

Témez, J.R., 1978: Cálculo hidrometeorológico de caudales máximos en pequeñas cuencas naturales. *MOPU*. Madrid.

Temperton, C., 1988: Implicit normal mode initialization. *Mon. Wea. Rev.*, **116**, 1013-1031.

Tiedtke, M., 1989: A comprehensive mass flux scheme for cumulus parameterization in large-scale models.*Mon. Wea. Rev.*, **117**, 1779-1799.

Todini, E., 1995: *AFORISM – A comprehensive forecasting system for flood risk mitigation and control.* Final report of Contract EPOC-CT90-0023.

Todini, E., 2001: Influence of parameter estimation uncertainty in Kriging. Part 1. Theoretical development. *Hydrol. Earth System Sci.*, **5(2)**, 215-223.

Todini, E. and Ciarapica, L., 2002: *The TOPKAPI model, in Mathematical Models of Large Watershed Hydrology*, edited by Singh, V. P., Frevert, D. K., Water Resources Publications, Littleton, Colorado, USA.

Todini, E., 2007: Hydrological catchment modelling: past, present and future. *Hydrol. Earth Syst. Sci.*, **11(1)**, 468-482.

Tomassetti, B., Coppola, E., Verdecchia, M., and Visconti, G., 2005: Coupling a distributed grid based hydrological model and MM5 Meteorological model for flooding alert mapping. EGU, *Adv. in Geos.*, **2**: 59-63.

Tribbia, J.J. and D.P. Baumhefner, 1988: The reliability of improvements in deterministic short-range forecasts in presence of initial state and modeling deficiencies. *Mon. Wea. Rev.*, **116**, 2276-2288.

US Army Corps of Engineers Hydrologic Engineering Center, 1998: HEC-HMS Hydrologic Modeling system user's manual, USACE-HEC, Davis, California, USA. 188 pp.

US Army Corps of Engineers Hydrologic Engineering Center, 2000: Hydrologic Modeling system HEC-HMS. Technical reference manual. USACE-HEC, Davis, California, USA. 157 pp.

US Army Corps of Engineers Hydrologic Engineering Center, 2003: Geospatial Hydrologic Modeling Extension HEC-GeoHMS user's maual. USACE-HEC, Davis, California, USA. 281 pp.

US Department of Agriculture, 1972: National engineering handbook. Section 4: Hydrology. US Department of Agriculture. Washington DC, USA.

US Department of Agriculture, 1986: Urban hydrology for small watersheds. Technical release 55 of the Nature Resources Conservation Service. US Department of Agriculture. Washington DC, USA.

von Storch, H. and F.W. Zwiers, 1999: *Statistical Analysis in Climate Research.* Cambridge University Press, 494 pp.

Wang, W. and N.L. Seaman, 1997: A comparison study of convective parameterization schemes in a mesoscale model. *Mon. Wea. Rev.*, **125**, 252-278.

Watson, R.T. and M.C. Zinyowera (Eds.), 2001: *The regional impacts of climate change - an assessment of vulnerability.* IPCC Spec. Rep. IPCC, Geneva, Switzerland

Wilks, D., 1999: Multisite downscaling of daily rainfall with a stochastic weather generator. *Clim. Res.*, **11**, 125-136.

Wilks, D.S., 2006: *Statistical methods in the atmospheric sciences. Second edition.* Elsiever Academic Press Publications. International Geophysics Sciences. 627 pp.

Williams, G.P., 1978: Bankfull discharge of rivers. *Water Resour. Res.*, **14(6)**, 1141-1154.

Xopalki, E., 2000: Connection between the large-scale 500 hPa geopotential height fields and precipitation over Greece during wintertime. *Climate. Res.*, **14**, 129-146.

Zhang, D.L. and R.A. Anthes, 1982: A high resolution model of the planetary boundary layer. Sensitivity tests and comparisons with SESAME-79 data. *J. App. Meteor.*, **21**, 1594-1609.

Zhang, D.L. and J.M. Fritsch, 1986: Numerical simulation of the meso-β scale structure and evolution of the 1977 Johnstown flood. Part I: Model description and verification. *J. App. Meteor.*, **43**, 1913-1943.

Zhang, D.L., Chang, H.R., Seaman, N.L., Warner, T.T., and Fritsch, J.M., 1986: A two-way interactive nesting procedure with variable terrain resolution. *Mon. Wea. Rev.*, **114**, 1330-1339.

Zhang D.L. and W.Z. Zheng, 2004: Diurnal cycles of surface winds and temperatures as simulated by five boundary layer parameterizations. *J. App. Meteor.*, **43**, 157-169.

Zhang, Y. and J.A. Smith, 2003: Space-time variability of rainfall and extreme flood response in the Menomonee river basin, Wisconsin. *J. Hydrometeor.*, **4**, 506-517.